2023

Experimental investigation of the interface and wetting characteristics of rock-H2-brine systems for H2 geological storage

Mirhasan Hosseini
Edith Cowan University

Experimental Investigation of the Interface and Wetting Characteristics of Rock-H_2-Brine Systems for H_2 Geological Storage

Mirhasan Hosseini

Thesis for the Degree of Doctor of Philosophy

in

Petroleum Engineering

School of Engineering

Edith Cowan University

November 2023

ABSTRACT

The projected rise in demand for hydrogen (H_2) production is a response to several factors, including greenhouse gas emissions caused by burning fossil fuels, depletion of fossil fuel reserves, and their uneven distribution around the earth. Thus, increased requirement for large-scale hydrogen storage solutions is anticipated to overcome imbalance between energy demand and supply. Deep underground formations such as salt caverns and porous reservoir rocks (e.g., depleted hydrocarbon reservoirs and deep saline aquifers) are necessary to achieve such volumes in practice. This process is known as underground hydrogen storage (UHS) which is technically very similar to underground natural gas storage. Although these two gas types have similar storage mechanisms, their behavior underground differs significantly, and this divergence could affect the efficiency, sustainability, safety, and commercial feasibility of deploying and operating gas storage systems. The interface and wetting characteristics of the various rock/H_2/brine systems are significant physicochemical factors in controlling containment security and storage capacity. These factors demand a thorough assessment. Nevertheless, there exists a literature gap concerning these aspects under diverse geological conditions, encompassing variations in pressure, temperature, organic matter, and salinity.

This study presents experimental data on interfacial tension (IFT) values between H_2 and brine as well as the wettability of different rock/H_2/brine systems under reservoir conditions. The wettability measurements are taken by directly observing the advancing and receding contact angles of water using the pendant drop tilted-plate technique. The experiments are conducted at high pressures (up to 20 MPa), elevated temperatures (up to 353 K) and brine salinities (up to 4.95 $mol.kg^{-1}$) to simulate subsurface conditions commonly encountered in such systems. For the investigation of wettability, various rocks were selected: calcite and Indiana limestone (which are representative of carbonate rocks); shales and evaporate (which are representative of caprocks), and basalt (which is representative of volcanic rocks). The effects of other rock surface properties such as surface roughness by atomic force microscopy (AFM) and organic matter concentration of shale by total organic content (TOC) analyzer on wettability were also investigated in this study. The study employed several other methods to characterize the composition of the rock and fluid samples, which included: 1) energy dispersive spectroscopy (EDS) to determine the elemental composition of the rock surface, 2) x-ray diffraction (XRD) to identify the mineral composition of

the rock sample, and 3) inductively coupled plasma (ICP) to determine the elemental composition of the brine sample. The obtained IFT and contact angle data were utilized to theoretically calculate the IFT of various rock-hydrogen and rock-water systems by the combination of Young's equation and Neumann's equation of state. Additionally, the electrochemical mechanisms controlling the wetting behavior of basalt under various geological conditions were investigated via streaming zeta potential core flooding system.

The results of H_2-brine interfacial tension indicate a linear decrease with increasing pressure and temperature, but a linear increase with increasing salinity over the entire range studied. The findings of the study reveal that in the majority of the rock/H_2/brine systems analyzed, the water advancing and receding contact angles exhibited an increase (more H_2-wet) with increasing pressure, salinity, and organic matter concentration but a decrease (more water-wet) with increasing temperature. Moreover, the samples with a high organic acid concentration showed a decrease in hydrophobicity following treatment with the nanofluid. The rock-hydrogen interfacial tension in shale, evaporite and basaltic rocks decreased with increasing pressure, temperature, and organic matter concentration. Also, the rock-water interfacial tension in these rocks decreased with increasing temperature but increased with increasing organic matter concentration. On the other hand, the calcite-hydrogen interfacial tension decreased with increasing pressure, salinity, and organic acid concentration, while it increased with increasing temperature. The calcite-water interfacial tension showed only minor variations with these parameters. Additionally, according to the findings, the zeta potential of basalt remained stable in response to pressure but showed an increase (less negative) trend as temperature and salinity increased. Conversely, the zeta potential of basalt exhibited a decrease (more negative) trend as the pH level increased.

This thesis offers valuable insights for evaluating the potential of different minerals composing the geological formations as H_2 storage options. The outcomes of this study are especially useful for analyzing the capillary sealing efficiency of caprocks, which can help in identifying the factors that contribute to the leakage of H_2. Furthermore, the information presented can be utilized as a valuable input in the development of H_2/brine flow simulations, which have the potential to provide more accurate predictions and, therefore, reduce the uncertainty associated with H_2 geo-storage projects.

DECLARATION

To the best of my knowledge, this thesis does not include any content that has been previously published by any individual, unless proper acknowledgment has been given. Additionally, this thesis does not incorporate any material that has been accepted for the attainment of another degree or diploma from any university.

Name: Mirhasan Hosseini

Signature 

Date: 20/07/2023

COPYRIGHT

As per the journal article's rights and agreement, I, the primary author of the articles, have the authority to include any of my previously published journal articles in my thesis, as long as they are not published for commercial purposes. In this regard, I am not obligated to seek permission, but I have acknowledged the journals as the original sources.

Name: Mirhasan Hosseini

Signature: 

Date: 20/07/2023

DEDICATION

I would like to dedicate this thesis to my loving family, whose unwavering support and encouragement have been the driving force behind my academic journey, and to my friends, whose friendship and companionship have provided solace, laughter, and motivation throughout this challenging yet rewarding endeavour.

ACKNOWLEDGMENTS

I would like to express my sincere appreciation and gratitude to my principal supervisor, Professor Stefan Iglauer, for his invaluable guidance and unwavering support throughout the journey of completing this thesis. His expertise, wisdom, and commitment to academic excellence have been instrumental in shaping the direction and quality of this research. I am grateful for the collaborative and supportive environment fostered by my co-supervisors Dr. Alireza Keshavarz and Dr. Jalal Fahimpour. Their approachability, responsiveness to queries, and willingness to offer guidance and resources have greatly facilitated the progression of my research. I am truly fortunate to have had Dr. Muhammad Ali for his invaluable assistance in editing and publishing the papers that form the foundation of this thesis. His expertise, meticulous attention to detail, and dedication to excellence have significantly contributed to the quality and impact of my research. I am immensely thankful to Dr. Muhammad Arif for his exceptional editorial skills, which have played a vital role in refining the clarity, coherence, and overall presentation of my first publication during my PhD journey.

I am deeply grateful to the executive management of ECU's School of Engineering, particularly Professor Daryoush Habibi and Associate Professor Iftikhar Ahmed as well as Associate Professor Mehdi Khiadani, for their continuous support and guidance. Their commitment to excellence has been instrumental in fostering a conducive academic environment. I would also like to extend my appreciation to the technical support staff, especially Dr. Guanliang Zhou, Dr. Hamed Akhondzadeh, and Mr. Farhad Farivar, for their unwavering assistance in the maintenance and troubleshooting of the equipment.

I would like to seize this opportunity to express my gratitude to my collaborators and co-authors, Dr. Faisal Ur Rahman Awan, Dr. Nilesh Kumar Jha, Dr. Rossen Sedev, and Dr. Mujahid Ali for their invaluable contributions to the research conducted in this thesis. I extend my heartfelt thanks to all co-authors of the papers published during my PhD journey, but not forming part of the thesis.

Specifically, I would like to extend a heartfelt expression of gratitude to the examiners of this thesis, Associate Professor Ryosuke Okuno and Dr. Kejian Wu as well as the anonymous reviewers who provided valuable feedback and expert recommendations to improve the quality of the publications incorporated in this thesis.

CONTENTS

LIST OF FIGURES

LIST OF TABLES

LIST OF SCHEMES

OUTPUTS DURING THE RESEARCH

- ***Journal publications forming part of the thesis as standalone chapters***

1. **Hosseini, M.**, Fahimpour, J., Ali, M., Keshavarz, A., Iglauer, S., 2022. H_2-brine interfacial tension as a function of salinity, temperature, and pressure; implications for hydrogen geo-storage. Journal of Petroleum Science and Engineering 213, 110441. https://doi.org/10.1016/j.petrol.2022.110441

2. **Hosseini, M.**, Fahimpour, J., Ali, M., Keshavarz, A., Iglauer, S., 2022. Hydrogen wettability of carbonate formations: Implications for hydrogen geo-storage. Journal of Colloid and Interface Science 614, 256-266. https://doi.org/10.1016/j.jcis.2022.01.068

3. **Hosseini, M.**, Fahimpour, J., Ali, M., Keshavarz, A., Iglauer, S., 2022. Capillary Sealing Efficiency Analysis of Caprocks: Implication for Hydrogen Geological Storage. Energy&Fuels 36,7, 4065-4075. https://doi.org/10.1021/acs.energyfuels.2c00281

4. **Hosseini, M.**, Ali, M., Fahimpour, J., Keshavarz, A., Iglauer, S., 2022. Basalt-H_2-brine wettability at geo-storage conditions: Implication for hydrogen storage in basaltic formations. Journal of Energy Storage 52, 104745. https://doi.org/10.1016/j.est.2022.104745

5. **Hosseini, M.**, Ali, M., Fahimpour, J., Keshavarz, A., Iglauer, S., 2022. Assessment of rock-hydrogen and rock-water interfacial tension in shale, evaporite and basaltic rocks. Journal of Natural Gas Science and Engineering 106, 104743. https://doi.org/10.1016/j.jngse.2022.104743

6. **Hosseini, M.**, Ali, M., Fahimpour, J., Keshavarz, A., Iglauer, S., 2023. Calcite-fluid interfacial tension: H_2 and CO_2 geological storage in carbonates. Energy&Fuels. https://doi.org/10.1021/acs.energyfuels.3c00399

7. **Hosseini, M.**, Sedev, R., Ali, M., Ali, M., Fahimpour, J., Keshavarz, A., Iglauer, S., 2023. Hydrogen-wettability alteration of Indiana limestone in the presence of organic acids and nanofluid. International Journal of Hydrogen Energy 48,90, 35220-35228. https://doi.org/10.1016/j.ijhydene.2023.05.292

8. **Hosseini, M.**, Awan, F.U.R., Jha, N.K., Keshavarz, A., Iglauer, S., 2023. Streaming and zeta potentials of basalt as a function of pressure, temperature, salinity, and pH. Fuel 351, 128996. https://doi.org/10.1016/j.fuel.2023.128996

- ***Related journal publications not forming part of the thesis***

1. Esfandyari, H., **Hosseini, M**., Ali, M., Iglauer, S., Haghighi, M., Keshavarz, A., 2023. Assessment of the interfacial properties of various mineral/hydrogen/water systems. Journal of Energy Storage, 60, p.106637. https://doi.org/10.1016/j.est.2023.106637

2. Isfehani, Z.D., Sheidaie, A., **Hosseini, M**., Fahimpour, J., Iglauer, S. and Keshavarz, A., 2023. Interfacial tensions of (brine+ H_2+ CO_2) systems at gas geo-storage conditions. Journal of Molecular Liquids, p.121279. https://doi.org/10.1016/j.molliq.2023.121279

3. Zeng, L., **Hosseini, M.**, Keshavarz, A., Iglauer, S., Lu, Y., Xie, Q., 2022. Wettability in Carbonate Reservoirs: Implication for Underground Hydrogen Storage from Geochemical Perspective. International Journal of Hydrogen Energy 47, 25357-25366. https://doi.org/10.1016/j.ijhydene.2022.05.289

- ***Non-related journal publications not forming part of the thesis***

1. **Hosseini, M.**, Arif, M., Keshavarz, A., Iglauer, S., 2021. Neutron scattering: A subsurface application review. Earth-Science Reviews 221, 103755. https://doi.org/10.1016/j.earscirev.2021.103755

2. Ali, M., Yekeen, N., **Hosseini, M.**, Abbasi, G.R., Alanazi, A., Keshavarz, A., Finkbeiner, T. and Hoteit, H., 2023. Enhancing the CO_2 trapping capacity of Saudi Arabian basalt via nanofluid treatment: Implications for CO_2 geo-storage. Chemosphere, p.139135. https://doi.org/10.1016/j.chemosphere.2023.139135

3. Ali, M., Yekeen, N., Ali, M., **Hosseini, M.**, Pal, N., Keshavarz, A., Iglauer, S., Hoteit, H., 2022. Effects of Various Solvents on Adsorption of Organics for Porous and Nonporous Quartz/CO_2: Implications for CO_2 Geo-Storage. Energy & Fuels. https://doi.org/10.1021/acs.energyfuels.2c01696

- ***Related conference papers and poster competitions not forming part of the thesis***

1. **Hosseini, M.**, Ali, M., Fahimpour, J., Keshavarz, A., Iglauer, S., 2023. Solid Surface Energy of Limestone-H_2-Brine Systems: Effect of Organic Acids and Nanofluids. EAGE Conference on Future of Energy, 12-13 September, Kuala Lumpur, Malaysia. https://doi.org/10.3997/2214-4609.202372006

2. **Hosseini, M.**, Keshavarz, A., Iglauer, S., 2023. Interface and Wetting Characteristics of Rock-H_2-Water systems for H_2 geological storage. SPE Asia Pacific Hydrogen Week, 18–22 September, Perth, Australia.

3. **Hosseini, M.**, Keshavarz, A., Iglauer, S., 2022. H_2-brine interfacial tension as a function of salinity, temperature, and pressure. Poster Competition for Australia's 4th Annual National Hydrogen Day Celebration, 15 September, Murdoch University, WA, Australia.

Chapter 1 Introduction

1.1 Background

The increase in the average temperature of the planet, also known as global warming, is causing significant apprehension because of its direct influence on the climate and, as a result, on the standard of living (Rahmstorf, 2007, Hsiang et al., 2013, Costello et al., 2009, Pachauri et al., 2014). Greenhouse emissions' critical element, carbon dioxide (CO_2), makes a significant contribution to global warming (Knorr, 2009, Le Quéré et al., 2015). According to the analysis conducted by National Oceanic and Atmospheric Administration's (NOAA's) Global Monitoring Lab, the average atmospheric CO_2 levels worldwide in April 2023 reached a new record high of 424 parts per million (ppm) (Canadell et al., 2007, National Oceanic and Atmospheric Administration, (n.d.).). This represents a 51% increase since the beginning of the Industrial Age (1760) when the concentration was roughly 280 ppm. Numerous methods have been suggested for reducing CO_2 emissions, including CO_2 geological storage (CGS) as well as renewable energy sources like wind and solar energy that don't emit carbon (Riahi et al., 2007, Hong, 2022). While wind and solar energy rely heavily on weather conditions like sunlight and wind velocity and direction, hydrogen is viewed as a promising renewable energy option (Zivar et al., 2021). Hydrogen which can be produced by several methods (i.e., steam methane reforming (SMR), electrolysis, partial oxidation, biomass gasification, and photoelectrochemical (PEC) water splitting) has the potential to reduce the carbon footprint of energy-intensive industries, heavy transport, and the construction sector (Weger et al., 2021, Wang et al., 2023). However, compared to other fuels, hydrogen has a low energy density, which means that a larger volume is needed to store the same amount of energy as a denser fuel (Züttel et al., 2010, Bhandari and Shah, 2021). Moreover, hydrogen gas is highly combustible and can be challenging to confine (Depken et al., 2022). In comparison with other surface methods for hydrogen storage (see Chapter 2), UHS is a secure, affordable, and adaptable way of storing significant amounts of hydrogen, which can help address these challenges (Tarkowski, 2019). This can be done by utilizing geological structures like depleted natural gas reservoirs, coal seams, salt caverns, basaltic formations and aquifers to

hold compressed or liquefied hydrogen (Epelle et al., 2022). Hydrogen withdrawal typically occurs during periods of high demand or when the price of hydrogen is favorable. The rate of withdrawal is dependent on the capacity of the UHS facility and the demand for hydrogen (Pan et al., 2021b, Gabrielli et al., 2020). It has been recognized that UHS is an essential technology for managing large-scale energy supply and demand due to its unparalleled capacity and performance, and there are few alternatives that can match it (Ugarte and Salehi, 2022, Tarkowski and Uliasz-Misiak, 2022).

The specific trapping mechanisms of UHS include:

1. Physical trapping: Occurring when the pore spaces of the reservoir rock physically confine hydrogen molecules. Capillary forces and surface tension play a role in holding the hydrogen in place (Ugarte and Salehi, 2022).

2. Adsorption trapping: Taking place when hydrogen molecules are adsorbed onto the surface of the reservoir rock, held in position by weak van der Waals forces (López-Chávez et al., 2020).

3. Chemical trapping: Occurring when hydrogen undergoes a chemical reaction with minerals within the reservoir rock, leading to the formation of stable compounds such as metal hydrides. In this scenario, hydrogen becomes chemically bound to the mineral, preventing its escape (Miocic et al., 2023).

One of the significant mechanisms for UHS is structural trapping beneath a caprock (i.e. shale, evaporate, and basalt) as it can significantly reduce the risk of hydrogen leakage (Iglauer, 2022). In this context, the interface and wetting characteristics of rock/H_2/brine systems are important physicochemical factors that have significant impacts on the structural storage capacity. The equilibrium between the upward buoyancy force exerted on hydrogen by brine, and the downward capillary force due to surface tension at the interface of the two fluids is obtained by a capillary force-buoyancy force balance (Iglauer et al., 2015b):

$$h = \frac{2\gamma \cos\theta_r}{\Delta\rho g r}, \tag{1.1}$$

where, h represents the maximum height of the H_2 column that can be permanently trapped beneath the caprock, γ stands for the interfacial tension between H_2 and brine, θ_r is the water receding contact angle which determines the wettability, $\Delta\rho$ represents the density difference between H_2 and brine, g is the gravitational acceleration, and r denotes the average pore throat radius. Obviously, γ and θ_r directly affect the structural storage capacity. In term of a storage rock, wettability controls H_2 flow pattern in porous rock (Iglauer et al., 2015b). Therefore, it is crucial to precisely determine these two parameters under relevant physicochemical conditions to obtain a precise estimation of the H_2 geological storage capacity and flow pattern. Several factors, including pressure, temperature, and salinity can affect the interface and wetting characteristics of the rock/H_2/brine system. Moreover, surface roughness, rock type, and surface chemistry of the rock can also significantly influence wettability.

The equilibrium contact angle (θ_e) for a rock/gas/water system is related to three different interfacial forces between rock and fluids (see Fig. 1-1), including rock-gas interfacial tension ($\gamma_{rock\text{-}gas}$), rock-liquid interfacial tension ($\gamma_{rock\text{-}liquid}$), and liquid-gas interfacial tension ($\gamma_{liquid\text{-}gas}$) as follows (Young, 1805):

$$\cos\theta_e = \frac{\gamma_{rock-gas} - \gamma_{rock-liquid}}{\gamma_{liquid-gas}}. \tag{1.2}$$

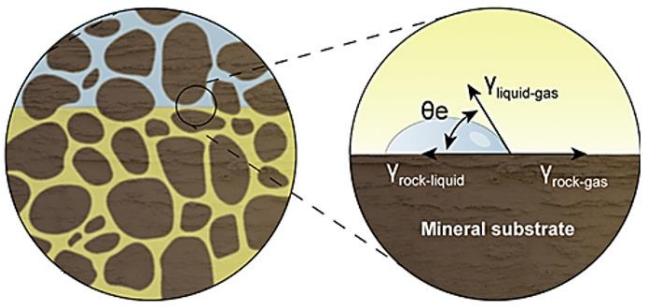

Fig. 1-1 Relation between θ_e and interfacial forces between rock and fluids for a rock/gas/water system

Fluid-fluid interfacial tension is the measurement of the amount of force per unit length between two immiscible fluids, which is caused by the molecular forces of the fluids differing at their interface. It is the energy needed to increase the area of the interface between the two fluids

(Adamson and Gast, 1967). There are several experimental methods for measuring the fluid-fluid interfacial tension, including spinning drop method, drop volume method, and pendant drop method (Hartland, 2004). However, there is no independent experimental technique to measure the rock-fluid interfacial tension (Arif et al., 2016b), and it can be calculated via indirect methods such as Neumann's equations of state (Neumann et al., 1974) and molecular dynamic simulation (Good and Girifalco, 1960). Wettability is defined as the ability of a liquid to evenly spread over a solid surface (Bico et al., 2002). There are several methods for measuring wettability, including Amott method, U.S. Bureau of Mines (USBM) method, and contact angle measurement (Donaldson and Alam, 2013). The pendant drop method and contact angle measurement are of the most commonly used techniques for fluid-fluid interfacial tension and wettability measurements, respectively. These two methods are often preferred due to their simplicity and ability to provide direct quantitative measurements (Sanchez, 2013). However, other methods may be suitable for certain applications (Kwok and Neumann, 1999). Note that unlike fluid-fluid interfacial tension and wettability, rock-fluid interfacial tension cannot be experimentally measured due to a lack of mobility at the rock interface (Li and Neumann, 1992).

In the context of UHS in porous media, it is considered to investigate the interface and wetting characteristics in geological rocks (i.e., sedimentary and volcanic rocks). Thus, the assessment of the salt cavern (which is artificially formed by dissolving salt deposits in injected water) is not the subject of this study. Moreover, hydrogen wettability of quartz has been studied by (Hashemi et al., 2021b, Iglauer et al., 2021b), thus it is not the primary focus of this current study. It is also important to note that analyzing thermodynamic (e.g., classical thermodynamic parameters like entropy and enthalpy), empirical and numerical methods was out of the scope of the thesis. Moreover, the use of equation (1.2) to calculate surface forces was a component of the present analysis but did not extend to the displacement mechanisms of fluids, as this was not the subject of the research. Thus, the objective is to provide valuable experimental insights and data that could be useful for the modelling and further theoretical work in the field. The novelty of the present experimental study lies in the following aspects: The existing body of literature on hydrogen wettability primarily focuses on sedimentary rocks, particularly quartz, but lacks sufficient information on other types of sedimentary rocks such as calcite (representative of carbonate rocks found in caprock and reservoir rock), shale, evaporate (common caprocks), and volcanic rocks like basalt in geostorage conditions. A comprehensive understanding of hydrogen wettability in these

rocks is crucial for assessing their structural storage capacity. Additionally, there is a scarcity of information on how to enhance hydrogen storage capacity and recovery during withdrawal by improving hydrogen wettability. The interpretation of hydrogen flow patterns in reservoir rock based on hydrogen wettability is also underexplored in the literature. Another gap pertains to the interfacial tension between fluid-fluid (e.g., H_2-brine) and rock-fluid (e.g., rock-H_2 and rock-brine). Furthermore, investigating the key determinants of wettability (e.g., zeta potential) in geo-storage conditions is essential.

1.2 Research objectives

This compilation consists of experimental data gathered under broad range of geological conditions, encompassing the H_2-wettability characteristics of different types of rocks such as calcite, caprocks, and basalt. It also covers the H_2-wettability alteration observed in Indiana limestone, the interfacial tension between H_2 and brine, and the streaming zeta potential, which serves as a key factor in determining wettability of basalt. Moreover, it reports IFT data for various rock-hydrogen and rock-water systems.

The subsequent enumeration outlines the precise aims and goals of this study:

1. Interfacial tension of H_2-brine as a function of pressure (2.76–34.47 MPa), temperature (298.15–423.15 K) and salinity (0–4.95 $mol.kg^{-1}$).

2. Wettability characterization of calcite/H_2/brine system as a function of different parameters, including pressure (0.1–20 MPa), temperature (298–353 K), salinity (0–4.95 $mol.kg^{-1}$), organic acid concentration (10^{-9} - 10^{-2} mol/L), tilting plate angle (0^o - 45^o) and surface roughness (RMS = 341 nm, 466 nm, and 588 nm).

3. Capillary sealing efficiency analysis of caprocks (shales and evaporite) under various pressures (0.1–20 MPa), temperature (298–353 K), organic acid concentrations (10^{-9} - 10^{-2} mol/L), total organic contents (TOC, 0.01 – 14 wt%), pore throat sizes (5 and 10 nm) and mineralogies.

4. Wettability characterization of basalt/H_2/brine system as a function of different parameters, including pressure (5–20 MPa), temperature (308–343 K), organic acid concentration (10^{-9} - 10^{-2} mol/L).

5. Assessment of rock-hydrogen and rock-water interfacial tension in shale, evaporite and basaltic rocks under various pressures (5–20 MPa), temperature (298–353 K), TOC (0.01 – 14 wt%) and mineralogy.

6. Calcite-fluid interfacial tension for calcite/H_2/brine systems as a function of different parameters, including pressure (5–20 MPa), temperature (298–353 K), salinity (0–4.95 mol.kg^{-1}), organic acid concentration (10^{-9} - 10^{-2} mol/L).

7. Hydrogen-wettability alteration of Indiana limestone in the presence of organic acids (hexanoic acid, lauric acid, and stearic acid) and nanofluid (various concentrations of 0.1 wt%, 0.25 wt%, and 0.5 wt%) at ambient (298 K and 0.1 MPa) and reservoir (323 K and 8.27 MPa) conditions.

8. Streaming zeta potential measurement (a wettability-determinant) in basalt as a function of pressure (1.72–6.9 MPa), temperature (298 K and 323 K), salinity (1–3.5 wt% NaCl), and pH (4 - 10).

1.3 Thesis organization

The thesis consists of a total of eleven chapters, each serving a specific purpose. In Chapter 1, the introduction to the thesis is presented. Chapter 2 provides a comprehensive literature review that is pertinent to the thesis. Chapters 3, 4, 5, 6, 9, and 10 encompass the experimental methodology, materials, results, discussions, and implications derived from the gathered data. Chapters 7 and 8 discuss on theoretical calculation of rock-fluid interfacial tension and its implications. The layout of the thesis objectives and structure, as depicted in Figure 1-2, illustrates the framework of the aforementioned objectives covered in Chapters 3 to 10. The order of these chapters was carefully designed and they were classified into three categories: a) H_2-brine interfacial tension discussed in Chapter 3, b) wettability of rock/H_2/brine systems (carbonate, caprock and basalt) discussed in Chapters 4 to 6, and c) factors responsible for the wettability alteration (rock-fluid IFT, effect of nanoparticle, and effect of surface charge) discussed in Chapters 7 to 10. Specifically, Chapter 3 addresses the interfacial tension between H_2 and brine. Chapters 4, 5, and 6 delve into the measurement of H_2-wettability for calcite, caprocks, and basalt, respectively. Chapter 7 investigates rock-hydrogen and rock-water interfacial tension in shale, evaporite and basaltic rocks. Chapter 8 evaluates calcite-fluid interfacial tension for calcite/H_2/brine systems. Chapter 9

focuses on elucidating the H_2-wettability alteration observed in Indiana limestone. Chapter 10 is dedicated to the measurement of streaming zeta potential, a determinant of wettability, specifically in basalt. Lastly, Chapter 11 serves as the conclusion of the thesis and provides recommendations for future research prospects. It should be noted that Chapters 3 to 10 are individual publications by the author, reproduced here as separate chapters. Readers may choose to read them independently, and certain illustrations in the text may be repeated in multiple places.

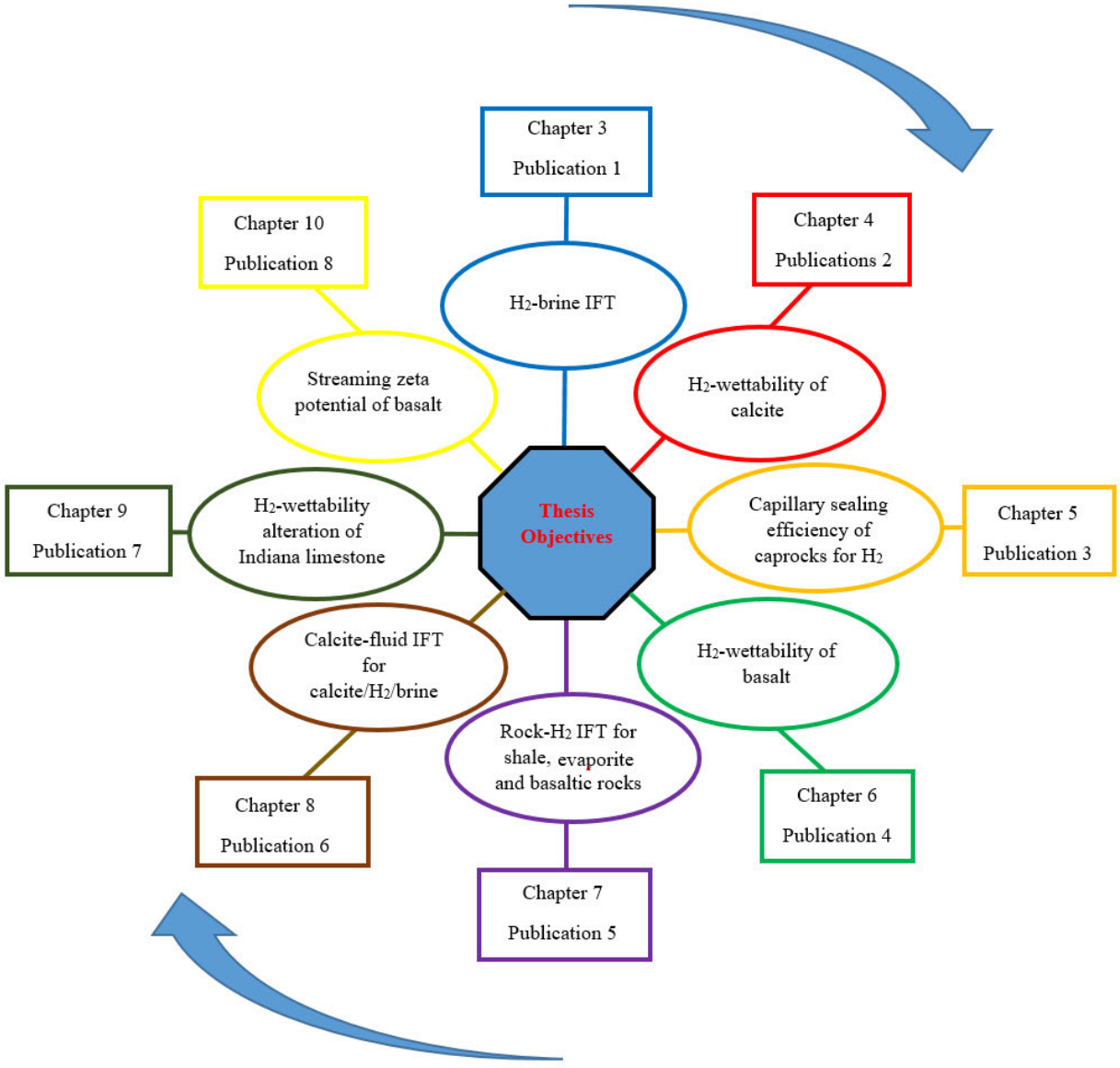

Fig. 1-2 Flowchart of thesis structure

Chapter 2 Literature review

2.1 Introduction

Hydrogen, often hailed as the "fuel of the future," has garnered considerable attention as a potential solution to various global energy challenges. Being a clean, versatile, and abundant energy carrier, hydrogen holds great promise in combating climate change and facilitating the transition to a sustainable energy system. However, one of the main hurdles lies in its low density, which means it occupies a large volume compared to its energy content. This presents difficulties in terms of storage and transportation since substantial volumes are required to store significant amounts of hydrogen. While compressing hydrogen gas can increase its energy density, it necessitates specialized equipment and may result in energy losses. In order to tackle these challenges, UHS has emerged as a promising approach for large-scale hydrogen storage. The viability of UHS relies on two crucial factors: the presence of a storage rock with favorable porosity and permeability, and a caprock with effective sealing properties. When hydrogen is introduced into a storage medium, it encounters the rock matrix and the surrounding fluids, typically brine. The interactions within a rock/hydrogen/brine system are intricately linked to the interface and wetting characteristics of the system. A thorough comprehension of these characteristics under in-situ conditions is crucial for establishing optimal operating conditions and selecting suitable formations for hydrogen storage. This chapter initiates the discussion by exploring the properties and applications of hydrogen, along with various methods for hydrogen production and storage. It then specifically centers on UHS sites and mechanisms, delving into the examination of interface and wetting characteristics in rock/hydrogen/brine systems under in-situ conditions to address existing knowledge gaps.

2.2 Hydrogen properties and applications

Hydrogen, the most abundant element in the universe, is primarily found as a diatomic molecule (H_2) and constitutes approximately 75% of the elemental mass (Jain, 2009). At standard temperature and pressure (STP), it is a colorless, odorless, and tasteless gas (Saxena et al., 2008).

Hydrogen gas is exceptionally lightweight, possessing a density of approximately 0.0899 grams per liter (g/L) at STP (Luconi et al., 2019). It has a melting point of -259.16 ºC (-434.49 ºF) and a boiling point of -252.87 ºC (-423.17 ºF). Although hydrogen gas is sparingly soluble in water, around 0.41 milligrams of hydrogen gas dissolves in one liter of water at 25 ºC. Notably, hydrogen exhibits high thermal conductivity, making it valuable in cooling applications and as a fuel in rocket engines (Korte et al., 2016).

Hydrogen gas is highly flammable and readily combustible when exposed to air. Its combustion produces a pale blue flame and releases a substantial amount of heat energy (Zivar et al., 2021). Due to its high reactivity, hydrogen can engage in various chemical reactions with a wide range of elements, including metals, nonmetals, and halogens, resulting in the formation of diverse compounds (Gilbert and Parsons, 2002). Chemically, hydrogen gas serves as an excellent reducing agent, capable of donating electrons during chemical reactions (Luidold and Antrekowitsch, 2007). In the presence of a catalyst like platinum, hydrogen reacts with oxygen to form water (H_2O) through either combustion or hydrogenation processes. Moreover, when hydrogen gas dissolves in water, it forms hydronium ions (H_3O^+), contributing to the acidity of aqueous solutions (Akitt, 1973).

Hydrogen finds wide-ranging applications across various industries and sectors. It can serve as a fuel for fuel cell electric vehicles (FCEVs), powering their electric motors with generated electricity (Li and Taghizadeh-Hesary, 2022). Additionally, hydrogen offers a solution for storing excess energy from renewable sources. Surplus electricity from solar or wind power can be used to produce hydrogen via electrolysis, which can later be converted back into electricity or heat during times of high demand or low renewable energy availability (Sorgulu and Dincer, 2018). Moreover, hydrogen plays a vital role in industrial processes. It serves as a feedstock for manufacturing ammonia, methanol, and other chemicals (Matzen et al., 2015), while also finding use in oil refining and metal refining as a reducing agent (Ramachandran and Menon, 1998). Fuel cells utilizing hydrogen are also employed to generate electricity for stationary power needs, serving as backup power sources, distributed power generation units, and potential replacements for conventional power plants in the future (Lubitz and Tumas, 2007, Dincer, 2007). Establishing hydrogen fueling infrastructure is pivotal for facilitating the widespread adoption of hydrogen-powered vehicles, enabling convenient and accessible refueling at hydrogen fueling stations

(Turoń, 2020, Hosseini and Butler, 2020). These examples merely scratch the surface of the diverse applications of hydrogen. As hydrogen technology continues to advance, its possibilities are expected to expand, driving the transition towards a cleaner and more sustainable energy future.

2.3 Hydrogen production

Hydrogen is not freely available in its pure form in nature and must be produced from various primary sources (Alpaslan et al., 2023). Methods for hydrogen production encompass a varied array of techniques involving the extraction of hydrogen from various feedstocks and its conversion into usable forms. These methods can be broadly categorized into three main groups: fossil fuel-based processes, renewable energy-based processes, and biological processes. Each method comes with its distinct advantages, limitations, and applicability. Understanding the characteristics of these methods is essential in determining the most suitable approach for hydrogen production in a given context.

2.3.1 Fossil fuel-based processes

Fossil fuel-based processes have historically been the primary methods for hydrogen production due to their cost-effectiveness and well-established infrastructure (Kannah et al., 2021). These processes utilize fossil fuels, such as natural gas and coal, as feedstocks to generate hydrogen (known as grey hydrogen). One of the most widely used fossil fuel-based methods is SMR which involves reacting methane, the primary component of natural gas, with steam in the presence of a catalyst to produce hydrogen and carbon monoxide. This process is typically carried out at high temperatures and pressures (Kenard Jr, 1962). The resulting mixture, known as synthesis gas or "syngas" is further processed to separate hydrogen from the carbon monoxide, leaving behind CO_2 as a by-product (Memon et al., 2021). SMR is currently the most cost-effective method for large-scale hydrogen production, accounting for the majority of global hydrogen output (Parkinson et al., 2018). Another fossil fuel-based method is coal gasification, which involves converting coal into a hydrogen-rich gas through a series of chemical reactions. Coal gasification can utilize various coal types, including sub-bituminous, bituminous, and lignite (Midilli et al., 2021, Stiegel

and Ramezan, 2006). The process involves heating coal in a controlled environment with a limited oxygen supply to produce a mixture of hydrogen, carbon monoxide, carbon dioxide, and other species. The gas is then cleaned, and hydrogen is separated from the other components (Seyitoglu et al., 2017). Similar to SMR, coal gasification results in the release of CO_2, making it necessary to capture and store or utilize the emitted carbon to reduce environmental impacts (Man et al., 2014).

2.3.2 Renewable energy-based processes

These methods offer a more sustainable alternative to fossil fuel-based methods for hydrogen production (Wang et al., 2019). Electrolysis is a key method in this category, which involves passing an electric current through water to split it into hydrogen and oxygen gases through two separate reactions (Godula-Jopek, 2015). If the electricity used in the process is sourced from renewable sources like solar or wind power, the resulting hydrogen is considered "green" and completely free of carbon emissions (Abad and Dodds, 2020). Other renewable methods, such as thermochemical processes and PEC systems, are also being explored and developed to produce hydrogen efficiently and sustainably (Balat, 2008, Cheng et al., 2021). Thermochemical processes utilize high-temperature heat from renewable sources to drive chemical reactions that produce hydrogen from water or other feedstocks. These processes include water splitting using metal oxides or metal hydrides, and sulfur-based cycles like the sulfur-iodine cycle or hybrid sulfur cycle (Harries et al., 2011). PEC systems combine semiconductor materials with sunlight to directly produce hydrogen from water. PEC devices utilize the energy from solar radiation to drive the water-splitting reaction, offering a direct conversion of sunlight into hydrogen (Moss et al., 2021).

2.3.3 Biological processes

These methods including bioconversion and fermentation, utilize microorganisms and biological reactions to produce hydrogen from organic matter (Saravanan et al., 2022). These methods can utilize biomass, agricultural waste, or even algae to generate hydrogen through biological pathways (Ren et al., 2009, Sarma et al., 2012, Chu et al., 2011). While still in the early stages of

development, biological processes offer the potential for producing hydrogen from renewable feedstocks while minimizing carbon emissions as they involve the capture and utilization of biogenic carbon dioxide during hydrogen production (Levin and Chahine, 2010). However, these processes often have lower hydrogen production rates and yields compared to conventional methods. The optimization of microbial strains and process conditions is necessary to improve efficiency (Singh and Wahid, 2015, Zhao et al., 2012). Additionally, scaling up biological hydrogen production systems can be complex, and the economics of these processes need further exploration to ensure their commercial viability (Ren et al., 2011).

As the world strives to reduce carbon emissions and transition to a clean energy future, there is a growing emphasis on advancing renewable energy-based and biological hydrogen production methods, which hold the promise of decarbonizing the hydrogen sector.

2.4 Hydrogen storage

Hydrogen storage is crucial for the integration of renewable energy, enabling the efficient use of excess energy, facilitating clean transportation, ensuring grid stability, and supporting various industrial applications (Graetz, 2009). It helps overcome the challenges associated with intermittent energy sources and provides a pathway towards a more sustainable and resilient energy future. In the following, some common hydrogen storage techniques have been discussed.

2.4.1 High-pressure gas cylinders

Storing hydrogen gas involves subjecting it to elevated pressures, typically falling within the range of 200 to 700 bar, depending on its intended application. The compressed hydrogen is then stored in durable tanks constructed from materials such as carbon fiber-reinforced composites or metal alloys. While this approach enables high storage density, it necessitates robust and weighty containers. Widely employed, particularly for portable applications. (Mori and Hirose, 2009).

2.4.2 Insulated tanks or dewars

Hydrogen can be stored as a cryogenic liquid, referred to as LH2, in specially designed tanks or dewars that are insulated to sustain extremely low temperatures below its boiling point. Storing hydrogen as a liquid provides the benefit of higher energy density compared to compressed gas (Klell, 2010). However, this approach requires specialized storage and handling procedures due to the involvement of cryogenic temperatures (Stetson et al., 2016).

2.4.3 Metal hydride storage

Metal hydrides are solid materials capable of absorbing and releasing hydrogen through the formation of chemical bonds with metal atoms, resulting in hydrides. The storage of hydrogen takes place through this bonding mechanism. Metal hydrides offer the advantage of a high capacity for hydrogen storage, and they can be transported and handled more conveniently than compressed or liquid hydrogen. However, it's essential to acknowledge that the absorption and release of hydrogen in metal hydrides may occur at a slower rate compared to other storage methods (Sakintuna et al., 2007).

2.4.4 Chemical hydride storage

Chemical hydrides are compounds that integrate hydrogen into their molecular structure through chemical bonding, providing the capability to store and release hydrogen through reversible chemical reactions (Biniwale et al., 2008). Chemical hydrides present the advantage of substantial storage capacity for hydrogen. However, the process of releasing and reabsorbing hydrogen from chemical hydrides often requires the use of additional reactants or catalysts to facilitate the reactions (Zhu and Xu, 2015).

2.4.5 Carbon-based materials

Hydrogen can be stored in particular carbon-based materials, such as activated carbon, carbon nanotubes, and graphene. These materials have the capability to adsorb hydrogen onto their surfaces, facilitating reversible storage (Xia et al., 2013). Carbon-based materials exhibit potential for high hydrogen storage capacity and the added advantage of being lightweight. Nevertheless,

additional research is needed to optimize and enhance their storage capabilities (Gopalsamy and Subramanian, 2014).

2.4.6 Underground storage

Underground hydrogen storage offers a potential solution for large-scale hydrogen storage due to the significant storage capacity of underground formations (Hassannayebi et al., 2019, Hassanpouryouzband et al., 2021, Heinemann et al., 2021). This method requires suitable geological formations that can safely and efficiently hold the gas. These formations can include depleted natural gas fields, salt caverns, porous rock formations (e.g., aquifers), or abandoned mines (Tarkowski, 2019). The choice of formation depends on factors such as porosity, permeability, geological stability, and containment integrity (Zivar et al., 2021). This method utilizes the existing infrastructure and knowledge developed for natural gas storage. However, modifications may be necessary to ensure compatibility with hydrogen, address safety considerations, and optimize performance for hydrogen storage (Epelle et al., 2022). Hydrogen is injected into the formation through drilled wells during periods of excess supply or low demand, and it can be withdrawn when needed (Lord et al., 2014). Prior to injection, hydrogen gas is compressed to the required pressure for storage. The compressed hydrogen is then transported through pipelines to the storage site and injected into the underground reservoir using specialized equipment (Tarkowski, 2019). The injection process carefully manages the pressure and flow rates to ensure safe and efficient storage. Underground storage formations must have proper containment and sealing properties to prevent hydrogen leakage or migration. Depending on the type of formation, various sealing mechanisms such as cap rocks, impermeable layers, or engineered seals may be employed to maintain the integrity of the storage reservoir (Zivar et al., 2021). The layout in Fig. 2-1 shows the main steps required for UHS projects.

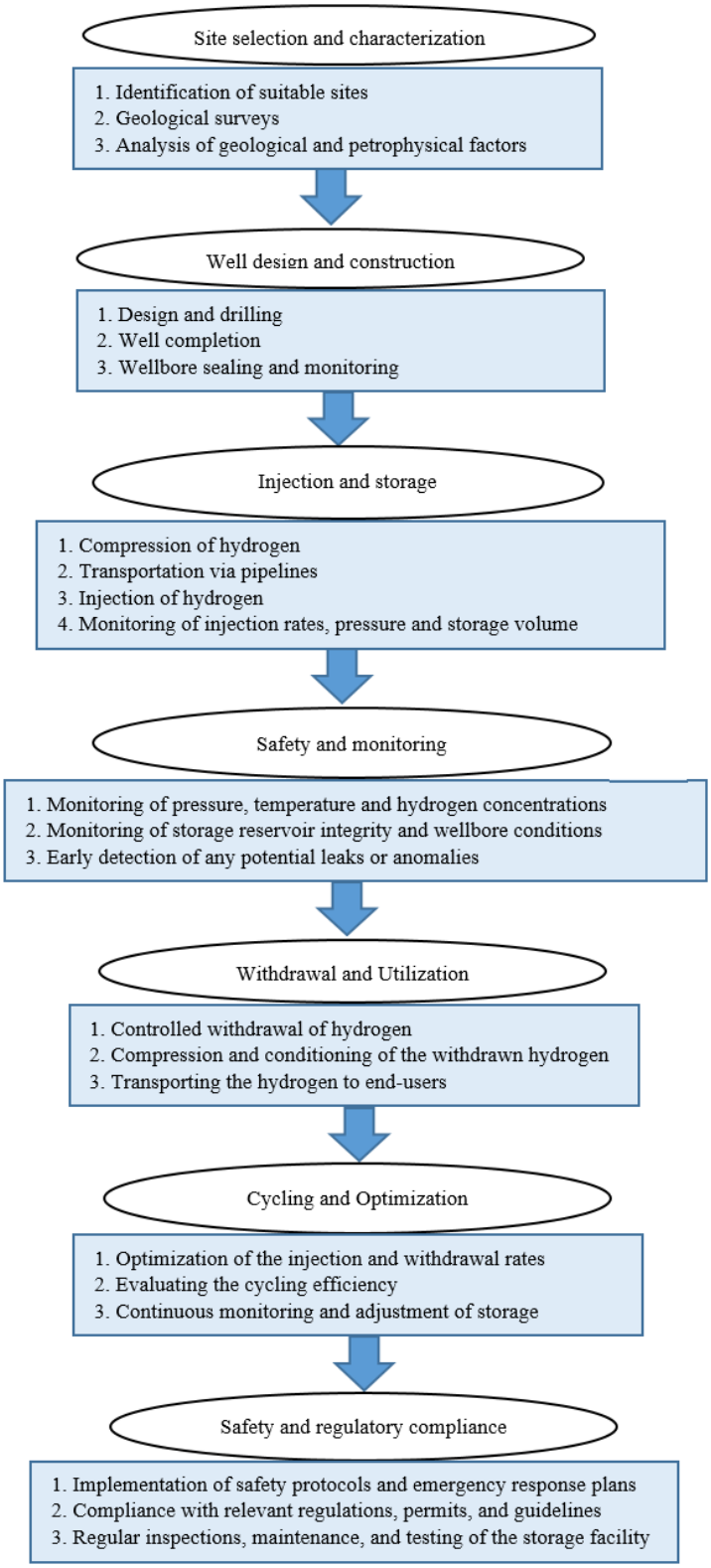

Fig. 2-1 Main steps and subsets involved in UHS projects (modified after (Groenenberg et al., 2020)).

2.5 UHS sites

UHS sites play a crucial role in enabling the large-scale storage and distribution of hydrogen, supporting its integration into energy systems and facilitating its availability for various applications. Conventional storage sites encompass depleted natural gas fields, salt caverns, and aquifers (see Fig. 2-2), while unconventional storage sites include unmineable coal seams and basalt formations. Table 2-1 presents a list of past, present and planned UHS projects in conventional storage sites. Currently, commercially operated underground storage sites specifically designed for storing pure hydrogen are predominantly limited to salt caverns. The subsequent sections will delve into the UHS sites, providing further insights into their characteristics and applications.

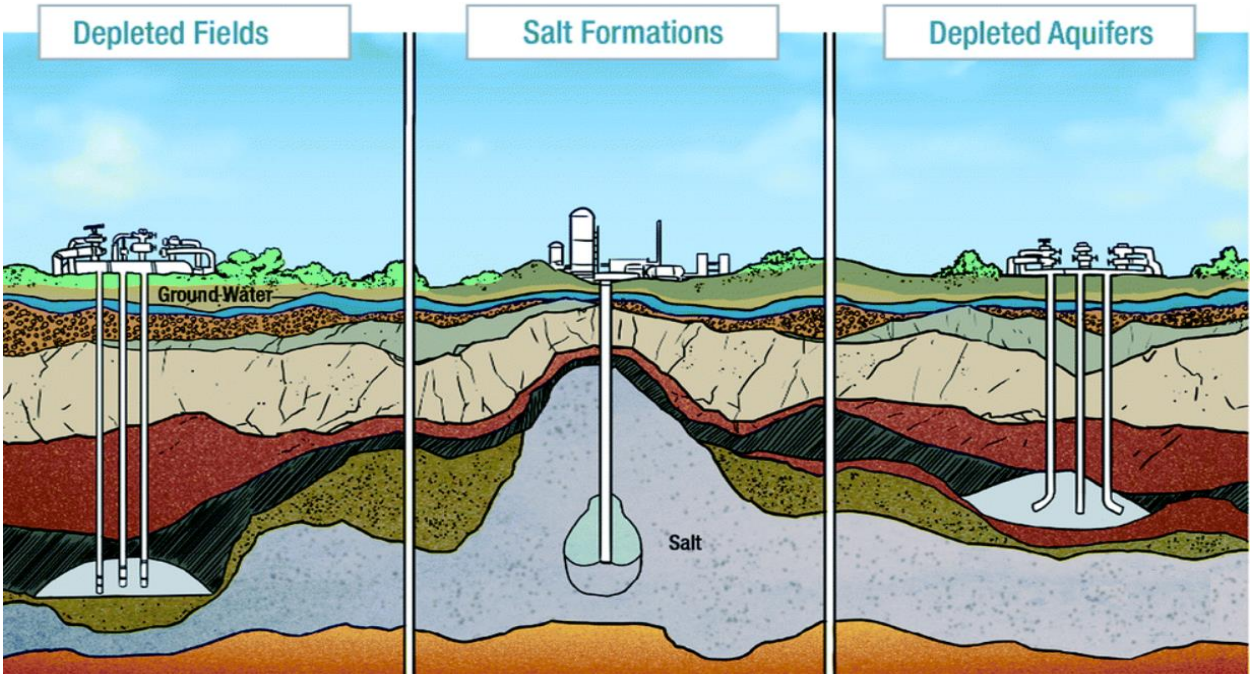

Fig. 2-2 Schematic representation for general UHS sites (reproduced from (Epelle et al., 2022) with permission from Royal Society of Chemistry)

Table 2-1 Some H_2 geostorage projects worldwide (reproduced after Hydrogen TCP-Task#42, 2023 (TCP-Task#42, 2023))

Project	Storage site	Expected capacity (GWh)	Development status
Green hydrogen @Kinsale, Ireland	Depleted gas field	3000	Pre-feasibility
SunStorage, Austria	Depleted gas field	Unknown, testing only	Testing completed
Loenhout Hydrogen, Belgium	Aquifer	Unknown, testing only	Pre-feasibility
Green Hydrogen Hub, Denmark	Salt cavern	200	Pre-feasibility
Bad Lauchstädt, Germany	Salt cavern	150	Pre-feasibility
Teeside, UK	Salt cavern	27	Operational
Advanced clean energy storage, USA	Salt cavern	300	Feed

2.5.1 Depleted natural gas fields

Depleted natural gas fields are underground storage sites that were previously used for extracting natural gas but have reached a stage where the gas reserves have been significantly depleted (Muhammed et al., 2023, Perera, 2023, Hemme and Van Berk, 2018). These fields offer potential for repurposing and utilizing the existing infrastructure such as wells, pipelines, and surface facilities, providing a cost-effective advantage for the storage of hydrogen (Hemme and Van Berk, 2018). Thus, the existing infrastructure with the known reservoir characteristics provide attractive opportunities for hydrogen storage in these fields. While the remaining natural gas in the depleted reservoir can act as a cushion gas for H_2, this also reduces the H_2 purity (Zivar et al., 2021).

2.5.2 Salt caverns

Salt caverns are commonly utilized for storing hydrogen underground (Caglayan et al., 2020, Portarapillo and Di Benedetto, 2021, Lankof and Tarkowski, 2020). These caverns are formed through a process called solution mining, in which water is injected into underground salt

formations to dissolve the salt and create large cavities. The impermeable nature of the salt walls acts as a barrier, minimizing the risk of leakage and maintaining the integrity of the stored hydrogen. Moreover, salt formations possess desirable physical characteristics such as stability and resistance to corrosion, making them well-suited for long-term storage (Ozarslan, 2012). However, the process of solution mining and cavern creation can be intricate and expensive. It is vital to thoroughly evaluate and ensure the stability of the salt walls to prevent any potential leaks or collapses. Careful monitoring and maintenance of the caverns are required to ensure the safety and security of the stored hydrogen (Takach et al., 2022).

2.5.3 Depleted and deep saline aquifers

Underground aquifers, which are natural porous rock formations capable of holding water, can be used for hydrogen storage (Tarkowski, 2019, Heinemann et al., 2021, Luboń and Tarkowski, 2023). Hydrogen can be injected into these formations, displacing the water and occupying the pore spaces. Aquifers used for hydrogen storage require suitable cap rocks or sealing layers above them (Sáinz-García et al., 2017). Several phenomena can impact the process of hydrogen storage in aquifers, including undetected fault leakage, biochemical reactions, and hydrogen reactions with minerals in the reservoir rock (Raad et al., 2022, Raad et al., 2023).

2.5.4 Unmineable coal seams

Unmineable coal seams are coal deposits that cannot be economically extracted using conventional mining techniques (Shi and Durucan, 2005). However, these seams can be repurposed for alternative uses like hydrogen geostorage. The coal's porosity enables it to adsorb and retain hydrogen within its structure (Liu and Liu, 2023). It is important to note that hydrogen geostorage in unmineable coal seams is still in the research and development stage. Various technical and environmental obstacles must be overcome, including efficient hydrogen storage and mitigating the risk of gas leakage (Jiang et al., 2022).

2.5.5 Basalt formations

Certain basalt formations, which are volcanic rocks, have the potential to store hydrogen (Al-Yaseri and Jha, 2021). The hydrogen can be stored within the pore spaces and fractures within the basalt rock. Research and pilot projects are currently underway to evaluate the feasibility, technical viability, and economic viability of using basalt formations for hydrogen storage (e.g., see Chapters 6 and 10).

2.6 Wettability of rock/H_2/brine systems

Wettability describes how the liquid phase (here brine) spreads or adheres to the solid surface (here rock) in the presence of another immiscible phase (here H_2 gas). It affects the flow, distribution and residual saturation of fluids during UHS process, thereby impacting the capillary pressure and relative permeability curves (Chaudhary et al., 2013, Pentland et al., 2011, Jackson et al., 2005). In a rock/H_2/brine system, wettability can be categorized into three primary types: water-wet, gas-wet, and intermediate-wet. In a water-wet system, the rock surface inherently attracts water, facilitating its spread and adhesion to the rock surface. This creates favorable conditions for displacing and pushing the gas phase through the porous rock matrix. Conversely, a gas-wet system occurs when the rock surface favors gas over water. As a result, the water phase faces challenges in spreading and penetrating into the rock pores, while the gas phase tends to adhere to the rock surface. Intermediate-wet wettability falls between the two extremes of water-wet and gas-wet. The rock surface exhibits some affinity for both water and gas, resulting in a mixed wetting behavior (Iglauer, 2017).

2.6.1 Quantitative wettability measurement

In petroleum industry, there are several preferred methods which can quantitatively analyze wettability. These methods are preferred (compared to other methods such as Wilhelmy plate method, capillary-rise method, and capillary penetration method) due to the possibility of the measurements at HPHT conditions. One of these preferred methods is the Amott method which is a relatively simple and widely used technique to gain insights into the wettability behavior of

subsurface rocks (Amott, 1959). The Amott method is based on conducting core flooding experiments and involves the calculation of an index derived from the capillary pressure versus water saturation curve (e.g. see Fig. 2-3; note that this figure illustrates a rock/oil/brine system, but similar principles can be applied to a rock/gas/brine system):

$$\text{Amott\_index} = \frac{\overline{BC}}{\overline{BD}} - \frac{\overline{DE}}{\overline{DB}} \tag{2.1}$$

where $\overline{BC}$ and $\overline{DE}$ are the brine spontaneous imbibition and brine spontaneous drainage processes, respectively. In this context, if the index falls between 0.3 and 1, the system is considered gas wet. If the index falls between -0.3 and 0.3, the system is neutrally wet, and if the index falls between -1 and -0.3, the system is considered water wet (Amott, 1959). Another wettability index known as the USBM index can be calculated based on the information depicted in Fig. 2-3. The USBM index is defined as the logarithm of the ratio of A_1 to A_2 ($\log(A_1/A_2)$). In this case, if the USBM index is close to 1, the system is classified as gas wet. If the USBM index is close to 0, the system is considered neutrally wet. And if the USBM index is close to -1, the system is categorized as water wet (Donaldson and Alam, 2013).

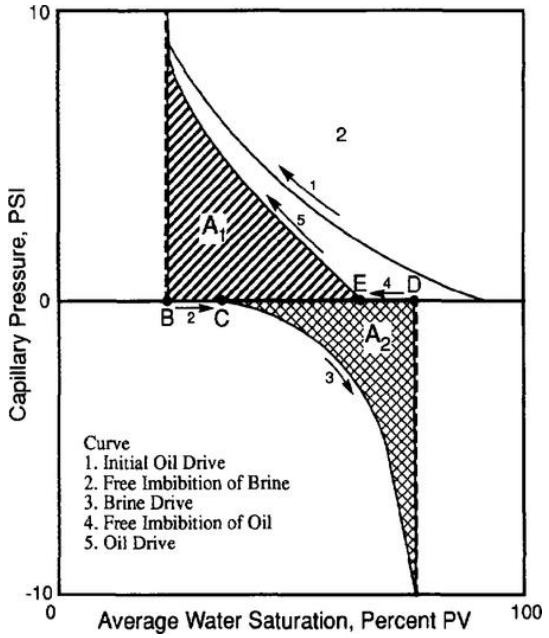

Fig. 2-3 Wettability analysis via Amott and USBM methods (reproduced from (Anderson, 1986) with permission from SPE Publishing)

The most effective method for quantifying wettability in rock/fluid systems is through contact angle (θ) measurement, as advocated by (Giraldo et al., 2013). Several indirect methods for quantifying θ exist, including the Wilhelmy plate method, capillary-rise method, and capillary penetration method (Aslannezhad et al., 2023). In the petroleum industry, direct measurement of θ is commonly achieved using the captive bubble method and the sessile drop method (Anderson, 1986). The captive bubble method specifically focuses on determining the contact angle of a rock surface submerged in a liquid. This method involves injecting a gas bubble into a chamber filled with the liquid, and the bubble adheres to the desired rock surface. Utilizing an imaging technique, such as a high-resolution camera, allows for the capture of the bubble's shape and dimensions, facilitating the measurement of the contact angle (Sakurovs and Lavrencic, 2011).

On the other hand, the sessile drop method entails carefully placing a liquid droplet onto the rock surface rather than using a gas bubble. The contact angle is then measured by analyzing the droplet's shape. The sessile drop method, especially through a tilted plate, is particularly advantageous for wettability assessment as it enables the simultaneous measurement of both advancing and receding contact angles (Lander et al., 1993) (see Fig. 2-4). In a system involving rock, gas (e.g., CO_2 and H_2), and brine, when θ falls below 50°, the system displays a strong water-wet characteristic. Within the range of 50-70°, it exhibits weak water-wetting behavior. For θ values spanning 70-110°, the system is categorized as intermediate-wet. As θ increases to 110-130°, the system transitions into a weak gas-wet state, and for θ values ranging from 130-180°, it becomes strongly gas-wet (Iglauer et al., 2015b)

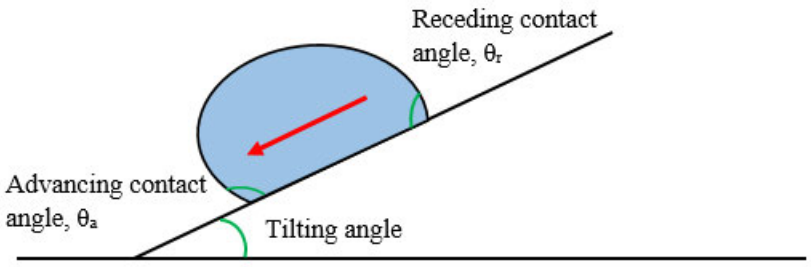

Fig. 2-4 Schematic of advancing and receding contact angles using the sessile drop through a tilted plate

2.6.2 Wettability studies of the rock/H_2/brine systems

Several research studies have examined the impact of various factors on the wettability of rock/H_2/brine systems. These factors encompass pressure, temperature, salinity, mineralogy, as well as the presence of organic acid and cushion gas. Subsequent analysis is dedicated to exploring the influence of each factor, drawing from a review of existing literature.

2.6.2.1 Effect of pressure on the wettability of rock/H_2/brine systems

Most studies have shown that the hydrogen wettability of rocks increases with increase in pressure. The research conducted by (Iglauer et al., 2021b) and (Ali et al., 2021d) demonstrated this trend for quartz and mica (pure and stearic-aged) samples, respectively. Similarly, (Ali et al., 2021c) and (Ali et al., 2022c) observed the same trend for quartz and mica substrates (aged in different organic acids), respectively. Moreover, (Al-Yaseri et al., 2021c, Al-Yaseri and Jha, 2021) used a semi-empirical thermodynamic model to determine the wettability of clay/H_2/brine and basalt/H_2/brine systems at typical geo-storage conditions and observed an increase in hydrogen wettability with an increase in pressure. This behavior was attributed to the increase in the intermolecular interaction between gas and rock at elevated pressure for rock/H_2/brine systems (Iglauer et al., 2012).

However, some contradictions were reported by some scholars. (Al-Mukainah et al., 2022) observed a slight decrease in hydrogen wettability with increase in pressure for shale/H_2/brine systems. They pointed out that the change in density of H_2 gas with increase in pressure is not adequate for increase in hydrogen wettability. Also, (Hashemi et al., 2021b) did not observe any change in the wettability of quartz with pressure. Similarly, (Higgs et al., 2022) observed no correlation between wettability of sandstone and pressure at constant temperature. Therefore, further investigations are necessary to understand the impact of pressure on the wettability of rock/H_2/brine systems.

2.6.2.2 Effect of temperature on the wettability of rock/H_2/brine systems

The effect of temperature on the wettability of various rock/H_2/brine systems has been limitedly reported in the literature. For sandstone rock, (Iglauer et al., 2021b) discovered that the hydrogen wettability of quartz increases as the temperature rises. This effect was attributed to the breaking of hydrogen bonds between water molecules and silanol groups on the quartz surface (Chen et al., 2015b). However, (Hashemi et al., 2021b) did not observe any correlation between quartz wettability and temperature. In the case of caprock, (Ali et al., 2021d) observed a decrease in the hydrogen wettability of mica as the temperature increased. This decline was attributed to the reduction in intermolecular forces and interfacial energy between the gas and the rock (Arif et al., 2017a). Additional research is needed to explore the impact of temperature on the hydrogen wettability of less-studied rocks, particularly carbonate and basaltic rocks, which have limited information available in the literature.

2.6.2.3 Effect of salinity on the wettability of rock/H_2/brine systems

The presence of ions in the brine can lead to ion adsorption on the rock surface, affecting the distribution of charges and altering the wettability behavior (Al-Yaseri et al., 2016). However, the specific effects of salinity on hydrogen wettability can vary depending on the rock type. (Higgs et al., 2022) examined the effect of brine salinity on hydrogen wettability of quartz. They found a weak correlation at low pressures (i.e. hydrogen wettability increased with salinity), but no correlation was observed at high pressures. These observations were attributed to the limited solubility of hydrogen in water, resulting in minimal alterations in surface energies. Similarly, (Hashemi et al., 2021b) and (Esfandyari et al., 2022) did not observe a meaningful and significant change in the hydrogen wettability of the rocks. (Hou et al., 2023) explored the impact of salinity on the hydrogen wettability of carbonate/H_2/brine systems. The results of their study revealed that the hydrogen wettability increased with salinity. Additionally, they found that the type of ions in the solution influenced the hydrogen wettability. Specifically, the presence of potassium (K^+) ions induced greater surface de-wetting compared to sodium (Na^+) ions, which was attributed to the larger atomic size of K^+ ions causing increased compression of the electrostatic double layer compared to Na^+ ions. Furthermore, the presence of divalent ions had a more pronounced effect on the hydrogen wettability of carbonate rock surfaces. This difference was attributed to the more electropositive nature of divalent cations and their higher degree of adsorption on the carbonate

rock surface compared to monovalent ions. Further research is needed to investigate the influence of salinity on the hydrogen wettability of subsurface rocks in order to address the inconsistencies found in the existing literature.

2.6.2.4 Effect of organic acid and TOC on the wettability of rock/H_2/brine systems

A few studies have shown that the specific effects of organic acids on hydrogen wettability can vary depending on factors such as the concentration and type of the organic acid regardless of rock type. (Iglauer et al., 2021b), (Ali et al., 2021d), (Ali et al., 2021c) and (Ali et al., 2022c) observed that the hydrogen wettability of rock increases with organic acid concentration. They attributed this trend to the adsorption of organic acid on the rock surface. (Al-Mukainah et al., 2022) and (Al-Yaseri et al., 2022c) observed that shale samples with higher TOC content exhibited increased contact angles, indicating higher hydrophobicity. This suggests that the presence of higher TOC in shale contributes to its enhanced water repellence.

Moreover, (Ali et al., 2021c) and (Ali et al., 2022c) examined the effect of different organic acids on the hydrogen wettability of rocks and found that the hydrogen wettability of rock increases with increase in alkyl chain length of organic acid due to the increased standard energy of adsorption, resulting in a stronger interaction with the rock substrate.

2.6.2.5 Effect of mineralogy on the wettability of rock/H_2/brine systems

The composition of rock minerals significantly influences the rock's wettability, which, in turn, affects the ability of the geological medium to trap hydrogen. When comparing the findings of (Ali et al., 2021c) regarding the wettability of the quartz/H_2/brine system with those of (Ali et al., 2022c) regarding the mica/H_2/brine system, it was observed that mica exhibited higher hydrogen wettability compared to quartz under similar experimental conditions. This difference was attributed to the presence of a greater number of silanol groups on the surface of quartz compared to mica. (Esfandyari et al., 2022) discovered that at a temperature of 80 °C and a pressure of 10 bar, the hydrogen wettability of the examined rocks followed the sequence: gypsum > quartz > anhydrite > calcite > shale > dolomite > granite > basalt. However, the precise mechanism behind

the influence of rock mineralogy on the system's wettability was not clarified in the study. According to the findings of (Hou et al., 2023), the hydrogen wettability of three distinct rock types exhibited the following order: carbonate > shale coal > sandstone. However, the study did not provide an explanation for these observed differences in wettability. Furthermore, the hydrogen wettability of different clay minerals (e.g. kaolinite, illite and montmorillonite) was examined by (Al-Yaseri et al., 2021c) using a semi-empirical thermodynamic model. All the clay samples displayed characteristics of water-wetting behavior. The order of water wetness on the clay surfaces in the presence of hydrogen was determined to be as follows: kaolinite > illite > Montmorillonite. The higher water wetness observed on the surface of kaolinite clay, as indicated by a lower water contact angle, was attributed to its hydrophilic nature. This hydrophilicity is linked to the composition of kaolinite clay, which consists of a 1:1 arrangement of tetrahedral siloxane (T-sheet) and octahedral hydroxide surface (O-sheet) (Tunega et al., 2004). On the other hand, illite and montmorillonite clays belong to the category of 2:1 clays, where the O-sheets are positioned between two T-sheets (Tunega et al., 2002). Further research is required to investigate the hydrogen wettability of different rocks in detail at geo-storage conditions.

2.6.2.6 Effect of cushion gas on the wettability of rock/H_2/brine systems

In hydrogen geostorage, cushion gas can be used to maintain a certain pressure level to ensure the stability and safety of the stored hydrogen (Kanaani et al., 2022, Zivar et al., 2021). However, there are only a few works in the literature examining the effect of the mixture of H_2 with cushion gas on the hydrogen wettability. An instance of this is when (Mirchi et al., 2022) conducted contact angle experiments on oil-wet sandstone and limestone, utilizing the captive bubble method, with H_2/CH_4 mixtures. They found that the wettability of the oil-wet rocks changed to weak water-wetting states in the presence of the cushion gas, thereby recommending CH_4 as a favorable cushion gas option for the UHS purposes. Similarly, (Hashemi et al., 2022) employed a captive bubble arrangement to evaluate the contact angle of Bentheimer sandstone with H_2/CH_4 mixtures. Their results demonstrated a predominantly water-wet state. Additionally, their findings indicated that the measured contact angle remained unchanged by the examined reservoir pressure, temperature, and salinity variations. (Alanazi et al., 2023) recently conducted a study using the tilted plate contact angle method to investigate how CH_4 as a cushion gas affects wettability of

organic-oil-rich shale source rocks in Jordan. The researchers focused on examining the influence of different gas types (pure CH_4, pure H_2, and H_2/CH_4 mixtures) on the wettability at geo-storage conditions. The results demonstrated that the hydrogen wettability of the examined gases followed the sequence: $CH_4 > H_2/CH_4$ mixture $> H_2$. These results were attributed to the density differences between the gases which followed the same sequence as the wettability.

2.7 H_2-water interfacial tension

For two immiscible fluids, the interfacial tension is quantified as the force required to overcome the intermolecular forces at the interface per unit length (Wu, 1971, Shariat et al., 2012). Understanding and managing interfacial tension is crucial for analyzing the capillary sealing efficiency of caprocks, structural storage capacity beneath caprocks, and fluid flow and distribution pattern in the storage rock (Arif et al., 2016a).

2.7.1 Quantitative modelling techniques for IFT

Several modelling techniques of IFT with many empirical or semi-empirical techniques serving as standard models within commercial simulators have been put forth in the field of petroleum industry. The widely employed approaches encompass the Parachor method (Macleod, 1923, Sugden, 1924), the scaling law (Lee and Chien, 1984), the corresponding-states theory (Guggenheim, 1945, Zuo and Stenby, 1997, Queimada et al., 2006), thermodynamic methods (Girifalco and Good, 1957, Winterfeld et al., 1978), and various empirical correlations (Sutton, 2009, Argaud, 1992). Among these methodologies, the Parachor method (Weinaug and Katz, 1943, Macleod, 1923) and the scaling law (Lee and Chien, 1984) have garnered considerable attention due to their straightforwardness and precision in characterizing the IFT of vapor-liquid interfaces in hydrocarbon systems. It's worth noting that although a Parachor value has been established for water, it is not recommended for predicting IFT in aqueous interfaces (Danesh, 1998, Firoozabadi and Ramey Jr, 1988). Instead, a more reliable and accurate model for estimating interfacial tension in hydrocarbon + water systems was introduced by (Firoozabadi and Ramey Jr, 1988). In their research, the authors successfully established a correlation between IFT and the density of the interacting phases across a wide spectrum of conditions. Subsequently, (Argaud,

1992) and (Sutton, 2009) refined the original (Firoozabadi and Ramey Jr, 1988) correlation, adapting it to encompass a broader range of compounds and a larger dataset. Although these approaches yielded favorable outcomes, they do exhibit limitations in terms of their transferability and predictive capabilities.

Various robust approaches grounded in statistical thermodynamics consider the molecular distribution at the interface. These techniques encompass perturbation theory (Nordholm et al., 1980), integral and density functional theories (Nordholm et al., 1980, Evans, 1979, Almeida and Telo da Gama, 1989, Bongiorno and Davis, 1975), the Linear Gradient Theory (LGT) (Zuo and Stenby, 1996a, Zuo and Stenby, 1996b), and the Square Gradient Theory (SGT) or Density Gradient Theory (DGT) (Cahn and Hilliard, 1958, Rowlinson, 1979). The latter has been widely applied in predicting IFT across a diverse range of systems, including spanning hydrocarbons (Cumicheo et al., 2014, Nino-Amezquita et al., 2010), alcohols (Cornelisse et al., 1998, Oliveira et al., 2008), esters (Oliveira et al., 2011, Freitas et al., 2011), glycols (Enders and Quitzsch, 1998), polymers (Poser and Sanchez, 1979, Sauer and Dee, 1994), near-critical systems (Fisk and Widom, 1969, Sahimi and Taylor, 1991), petroleum mixtures (Miqueu et al., 2008, Nilssen et al., 2010), and more recently, aqueous systems containing gases like CO_2, CH_4, and N_2 (Chow et al., 2016a, Miqueu et al., 2011, Li et al., 2008). Additionally, Molecular Dynamics (MD) and Monte Carlo (MC) computer simulations have successfully characterized IFT as well (Müller and Mejía, 2014, Biscay et al., 2009, Iglauer et al., 2012).

For accurate IFT estimation, it is crucial to represent the composition and density of bulk phases accurately using a thermodynamic phase behavior model. Classical cubic equations of state (EoSs) such as the Soave-Redlich-Kwong 1972 (SRK72) EoS (Soave, 1972) and the Peng-Robinson 1978 (PR78) EoS (Robinson and Peng, 1978) are suitable for simple systems consisting of gases and hydrocarbons. In contrast, systems with polar and associating compounds like water, alcohols, and glycols, featuring strong hydrogen bonding interactions, benefit from theoretically sound EoSs like the Statistical Associating Fluid Theory (SAFT) EoS (Chapman et al., 1989, Huang and Radosz, 1990) and the Cubic-Plus-Association (CPA) EoS (Kontogeorgis et al., 2006a, Kontogeorgis et al., 2006b).

2.7.2 Quantitative experimental techniques for IFT

There are some experimental techniques to quantitatively analyze IFT. The most popular techniques are Wilhelmy plate method, Du Noüy ring method, Maximum bubble pressure method, capillary rise method, spinning drop method, drop volume method, and pendant drop method. Among these methods, some are preferred due to their simplicity and ease of implementation at high pressure and high temperature. One of these preferred methods is spinning drop method, with which a small droplet of one fluid is suspended within another fluid in a tube and spun at a constant speed (see Fig. 2-5). The IFT is calculated by balancing the centrifugal force acting on the droplet with the interfacial tension force. By assuming $l > 8r$, the IFT can be quantified by the Vonnegut equation (Princen et al., 1967):

$$\gamma = \omega^2 r^3 \frac{\Delta\rho}{4}, \tag{2.2}$$

where γ is the interfacial tension between heavy fluid (with the density of ρ_1) and light fluid (with the density of ρ_2), ω is the rotational speed of the tube, r is the radius of the drop, and $\Delta\rho = \rho_1 - \rho_2$ is the density difference between the fluids.

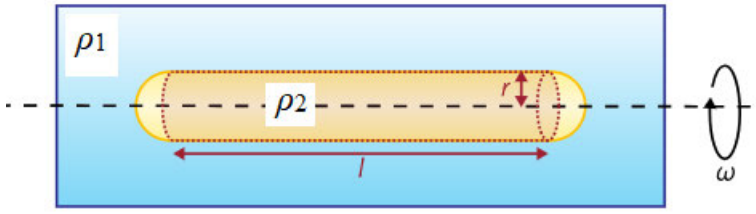

Fig. 2-5 Schematic of the spinning drop method for IFT measurement

Another preferred method for quantitative measurement of the IFT is the drop volume method. In this method, the weight (W) or volume (V) of a drop falling from a capillary tube with the radius of r' correlates with the IFT as follows (Drelich et al., 2002):

$$W = V\Delta\rho g = 2\pi r'\gamma f\left(\frac{r'}{\sqrt[3]{V}}\right), \tag{2.3}$$

where g is the gravitational acceleration and f is a correction factor for the released drop which is tabulated by (Harkins and Brown, 1919).

The most effective approach for measuring interfacial tension (IFT) in fluid-fluid systems under high pressure and high temperature (HPHT) conditions is the pendant drop method, which is the preferred and recommended technique (Stauffer, 1965). In this method (which the same apparatus for the contact angle measurement is also used here), a droplet of one fluid is suspended from a needle or capillary tube, which is immersed in the other fluid. The shape of the droplet is analyzed using the axisymmetric shape drop analysis (ASDS) technique to determine the IFT. The ASDS technique relies on matching the actual shape of a liquid droplet with a calculated shape generated by numerically integrating the Young-Laplace equation (note: more in-depth discussion of the theoretical foundations in the context of the Young-Laplace equation was not a central part of the thesis). To determine this theoretical profile, one can utilize the solution of the following equations, considering the lengths and angles as defined in Fig. 2-6 (Georgiadis et al., 2010):

$$\frac{d\theta}{dS} = 2 - \beta Y - \frac{\sin\theta}{X}, \tag{2.4}$$

$$\frac{dX}{dS} = \cos\theta, \tag{2.5}$$

$$\frac{dY}{dS} = \sin\theta, \tag{2.6}$$

where $X = x/R_0$, $Y = y/R_0$, and $S = s/R_0$ represent non-dimensional coordinates of a point labelled P on the droplet's shape profile. R_0 stands for the radius of curvature at the highest point of the droplet, while β is a non-dimensional shape parameter that correlates with interfacial tension through the following equation:

$$\gamma = \frac{\Delta\rho g R_0^2}{\beta}, \tag{2.7}$$

where γ represents interfacial tension, $\Delta\rho$ signifies the density difference between the drop and the surrounding medium, and g stands for gravity acceleration. In this analysis, the objective is to determine, through a process of trial or alternative methods, the optimal values of R_0 and β that

closely match with the observed drop profile. Once the values of R_0 and β are established, and a specific $\Delta\rho$ is known, γ is then calculated using equation (2.7).

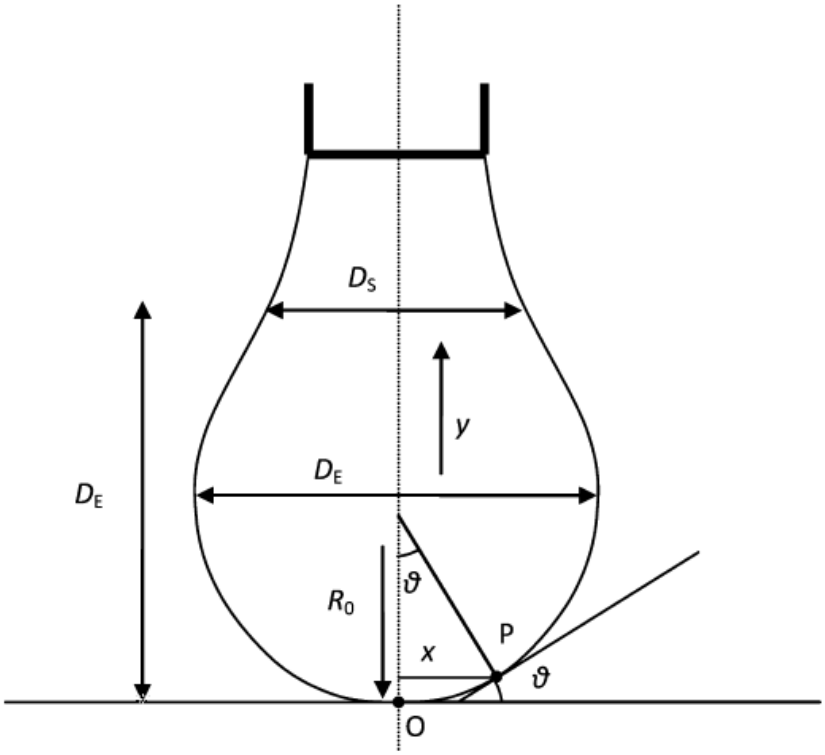

Fig. 2-6 Schematic of a hanging liquid droplet's shape, illustrating the coordinate system referenced in the text. At the highest point O, R_0 represents the radius of curvature, while *s* denotes the arc length between O and the location P. Additionally, *y* and *x* represent the vertical and horizontal positions, respectively, in relation to the origin located at point O (reproduced from (Li et al., 2012a) with permission from American Chemical Society)

The literature review on H_2-water IFT suggests that an empirical equation is required to allow for the prediction of the IFT as a function of pressure, temperature, and brine molality (see Chapter 3).

2.7.3 IFT studies of the H_2-water systems

A few research studies have investigated the effects of different factors on IFT of H_2-brine systems. These factors include pressure, temperature, salinity, and cushion gas. The following analysis focuses on understanding the individual impact of each factor, utilizing a comprehensive review of existing literature.

2.7.3.1 Effect of pressure on the IFT of H_2-water systems

Research findings indicate that the IFT of H_2-water systems tends to decrease as pressure increases. (Slowinski Jr et al., 1957) and (Massoudi and King Jr, 1974) observed slight decrease in IFT for H_2-H_2O systems at a temperature of 298 K when pressure increased up to 10 MPa. Similar slight reduction in IFT of similar system was obtained by (Esfandyari et al., 2022) for the same pressure increase at different temperatures. (Chow et al., 2018) also noted a slight decrease in IFT for H_2-H_2O and H_2-CO_2-H_2O systems as pressure increased up to 45.2 MPa at different temperatures. Similarly, (Fukuzawa et al., 2018) observed a linear decrease in IFT for H_2-CO_2-H_2O systems as pressure increased up to 7 MPa. (Al-Mukainah et al., 2022) and (Higgs et al., 2022) observed a similar slight reduction in IFT with pressure for H_2-brine systems. These observations were attributed to the slight increase in H_2 density with pressure, resulting in a minor decrease in the density difference between H_2 and water and, consequently, a slight decrease in IFT. Further experimentation and modelling investigations are necessary to gain a comprehensive understanding of the influence of pressure on IFT of H_2-water systems.

2.7.3.2 Effect of temperature on the IFT of H_2-water systems

There are a few studies showing that the IFT of H_2-water systems tends to decrease as temperature increases. (Chow et al., 2018) observed a considerable decrease in IFT for H_2-H_2O and H_2-CO_2-H_2O systems as temperature increased up to 448 K. This reduction was nonlinear according to a molecular simulation study conducted by (van Rooijen et al., 2023). However, (Fukuzawa et al., 2018) observed a weak temperature dependency of the IFT at temperatures ranging from $T = 271.2$ K to 280.2 K. In the case of H_2-brine systems, (Esfandyari et al., 2022) observed a slight reduction in the IFT with temperature. The similar slight reduction in the IFT was also observed by (Mirchi et al., 2022) for H_2-CH_4-brine systems. The reduction in the IFT with temperature was

attributed to the reduction in the density difference between gas and water. However, more research is needed to elucidate the effect of temperature on IFT of H_2-water systems.

2.7.3.3 Effect of salinity on the IFT of H_2-water systems

There is a lack of research in existing literature on the impact of salinity on the IFT of H_2-water systems. Previous studies by (Higgs et al., 2022) and (Esfandyari et al., 2022) examined this influence by comparing the results of distilled water and brine under varying pressures and temperatures, but they did not establish any correlations. Therefore, further investigation is necessary to gain a better understanding of this effect.

2.7.3.4 Effect of cushion gas on the IFT of H_2-water systems

IFT can be significantly influenced by cushion gas as a result of changes in gas composition and relevant physical and chemical properties. However, there is a limited number of research available on this particular effect. (Chow et al., 2018) discovered that the IFT between a gas mixture of 70% H_2 and 30% CO_2 and water is lower than the IFT between pure H_2 and water. Similarly, (Mirchi et al., 2022) conducted a similar analysis using varying percentages of CH_4 in the gas mixture and observed that the IFT decreases as the concentration of CH_4 increases. Additionally, (Alanazi et al., 2023) observed that the sequence of IFT for different gas compositions is as follows: pure H_2 > 50% H_2 + 50% CH_4 gas mixture > pure CH_4. These observations can be attributed to an increase in gas density resulting from the addition of cushion gas, which in turn leads to a decrease in the density of the gas mixture and the corresponding IFT.

2.8 Rock-fluid interfacial tension

Unlike the direct experimental determination of IFT between fluids, there is a current absence of available experimental methods for accurately estimating the IFT between rocks and fluids. Consequently, semi-empirical approaches and correlations, such as Young's equation and Neumann's equation of state, are employed to ascertain the IFT between rocks and fluids. Chapters 7 and 8 provide a comprehensive description of the methodology.

2.8.1 Studies on rock-fluid IFT in rock/H_2/water systems

A restricted number of researchers have computed the IFT of rock-H_2 and rock-water in rock/H_2/water systems by employing a combination of Young's equation and Neumann's equation of state (e.g. (Ali et al., 2022b, Pan et al., 2021a, Yekeen et al., 2022)). In the following, the impact of pressure, temperature, organic acid concentration, and rock mineralogy is examined.

2.8.1.1 Effect of pressure and temperature on rock-fluid IFT

The research indicates that the IFT between rock and H_2 diminishes with increasing temperature and pressure. (Pan et al., 2021a) discovered that the rock-H_2 IFT for quartz and basalt experiences a reduction with elevated pressure and temperature. Similar reductions in rock-H_2 IFT were observed for mica, as well as clay minerals, by (Yekeen et al., 2022). They attributed the pressure effect to the rise in gas density and intermolecular forces between the rock and gas. Furthermore, they noted that with increasing temperature, the kinetic energy of H_2 gas intensifies, resulting in heightened mobility and less available time for interaction with the solid surface.

2.8.1.2 Effect of organic acid concentration on rock-fluid IFT

Studies, such as those conducted by (Pan et al., 2021a) for quartz and (Ali et al., 2022b) for mica, propose that the IFT between rock and H_2 decreases with an increase in organic acid concentration. This trend was attributed to the enhanced hydrophobic properties of the system in the presence of organic acid, preventing water from adhering to the surface. In contrast, H_2 gas readily forms bonds with the rock surface due to its lack of an external dipole moment, requiring less energy for interaction. Conversely, these studies noted that the IFT between rock and water increases with organic acid concentration. This was linked to the polar nature of water, which experiences strong repulsion from the hydrophobic surface, necessitating more energy for water to spread on the surface.

2.8.1.3 Effect of mineralogy on rock-fluid IFT

The mineral composition of rocks significantly influences the IFT between rock and fluids. (Pan et al., 2021a) noted that, under the same pressure and temperature conditions, the quartz-H_2 IFT exceeds the basalt-H_2 IFT, attributed to the presence of organic matter in the basaltic rock, altering its wettability from hydrophilic to hydrophobic. Similarly, (Yekeen et al., 2022) investigated the impact of rock mineralogy on rock-fluid IFT, focusing on quartz and three different clay surfaces (montmorillonite, kaolinite, and illite). They observed a higher quartz-H_2 IFT compared to clay-H_2 IFT, ascribed to the greater presence of silanol functional groups on the quartz surface, limiting interaction sites with H_2. In contrast, the IFTs between H_2 and the three clays were similar, indicating that variations in clay composition do not significantly affect rock-H_2 IFT.

The literature review on rock-fluid IFT in rock/H_2/water systems suggests a need for further research on the impact of other parameters, such as salinity and shale-TOC, on rock-fluid IFT. This is particularly relevant for different types of caprocks (e.g., shale, evaporite, and basaltic rocks, as discussed in Chapter 7) and calcite (as explored in Chapter 8).

Chapter 3 H_2–brine interfacial tension as a function of salinity, temperature, and pressure; Implications for hydrogen geo-storage

Published in *Journal of Petroleum Science and Engineering*, Elsevier 2022, 301, 102595
DOI: https://doi.org/10.1016/j.petrol.2022.110441

Abstract

Hydrogen as a clean fuel source compared to hydrocarbons has attracted many attentions to mitigate anthropogenic greenhouse gas emissions and meet global energy demand. However, high volatility and compressibility of hydrogen make a challenge for its storage. In this regard, the surface-based hydrogen storage facilities (e.g. aerospace, cryogenic tanks, high-pressure gas cylinders, etc.) have been in operation for decades. Moreover, H_2 geo-storage is an effective way to store vast volume of hydrogen in deep underground formations where it can be withdrawn again to generate energy when the need arises. The interaction between the injected hydrogen and resident formation fluids (e.g. water), can strongly influence the H_2-flow pattern and storage capacity. In this regard, interfacial tension (γ) between hydrogen and brine is a key parameter that influences hydrogen displacement within the geological porous medium. As there is a serious lack of literature on this important subject, we measured H_2-brine interfacial tension at various geo-storage conditions for a wide range of pressure, temperature, and brine salinity, using the pendant drop technique. The results of the study indicate that γ declined linearly with increasing pressure when temperature and salinity are kept constant. Moreover, a linear reduction in γ with increasing temperature was observed under constant salinity and pressure conditions. The results also clearly demonstrate that γ increased linearly with brine molality over the whole range investigated. An empirical equation was also developed with which γ as a function of pressure, temperature, and brine molality can be predicted. The predictions for data points of this work had a maximum deviation of 2.13 % from the experimental data. This work thus provides fundamental data for H_2 geo-storage projects, and aids in the implementation of an industrial-scale hydrogen economy.

Keywords

Hydrogen geo-storage; interfacial tension; hydrogen; brine salinity; reservoir conditions; high pressure

3.1 Introduction

Hydrogen production from renewable resources can potentially drastically reduce anthropogenic CO_2 emissions, and therefore, contribute to climate change mitigation (Caglayan et al., 2020, Moradi and Groth, 2019, Tarkowski, 2019, Bauer et al., 2015, Pan et al., 2021b, Zivar et al., 2021). Solar thermochemistry, electrolytic, biomass gasification, and steam methane reforming processes are used to produce hydrogen (H_2), which can again generate energy at peak demand times (Boretti et al., 2021, Cao et al., 2020, Wang et al., 2021, Mohanty et al., 2021). Besides, H_2 has many applications in liquid-propellant vehicles, fuel cell, and refinery (Nazir et al., 2020a, Nazir et al., 2020b, Wang et al., 2012). One key problem, however, is large-scale H_2 storage, which is currently limited (Al-Yaseri et al., 2021c, Ali et al., 2021d, Iglauer et al., 2021b, Ali et al., 2021c, Hosseini et al., 2022c, Ali et al., 2022c, Hashemi et al., 2021b).

Thus geological formations, e.g. depleted oil and gas reservoirs (Hemme and Van Berk, 2018, Lemieux et al., 2019, Pfeiffer and Bauer, 2015), deep saline aquifers (Hassannayebi et al., 2019, Sáinz-García et al., 2017), basaltic formations (Al-Yaseri et al., 2021b), organic-rich shales (Arif et al., 2017b), and coal seam gas reservoirs (Iglauer et al., 2021a, Keshavarz et al., 2022) have been suggested as potential H_2 and CO_2 storage mediums. However, so far, only salt caverns have been operated at an industrial scale as storage sites for pure hydrogen (100 % H_2) storage (Lankof and Tarkowski, 2020). Other examples of hydrogen geo-storage projects include the storage of a mixture of hydrogen with other gases (e.g. town gas) in aquifers (e.g. Lobodice in Czechoslovakia (50 % H_2) and Beynes in France (50 % H_2) (Panfilov et al., 2006)) and depleted gas reservoirs (e.g. Underground Sun Storage in Austria (10 % H_2) (Pichler, 2019)).

A key parameter relevant to gas storage in sedimentary rocks (e.g. sandstone or limestone formations) is the interfacial tension (γ) between the injected gas and resident reservoir brine which influences the H_2 storage capacity and containment security (Zivar et al., 2021). The maximum

column height or storage height (h) of H_2 which can be permanently trapped in a formation, can be estimated as follows (Aggelopoulos et al., 2011):

$$h = \frac{2\gamma \cos\theta}{\Delta\rho g R}, \tag{3.1}$$

where θ is the receding contact angle, $\Delta\rho$ is the H_2-brine density difference, g is the gravitational acceleration, and R is the mean pore throat radius. Equation (3.1) shows that H_2 column height is a function of γ. The H_2 column height can be used to calculate the H_2 storage capacity, defined as the maximum mass of H_2 that can be stored safely in the formation (Shah et al., 2008):

$$M_{H_2} = \rho_{H_2} h\phi(1 - S_w), \tag{3.2}$$

where M_{H2} is the mass of H_2 per unit area of the formation, ρ_{H2} is the density of H_2, S_w is the residual water saturation in the formation, and ϕ is the porosity. Thus γ determines H_2 storage capacity and H_2 containment security (Broseta et al., 2012, Farokhpoor et al., 2013, Shah et al., 2008).

While γ measurements of CO_2 and brine for geo-storage purposes have been extensively studied (Aggelopoulos et al., 2011, Arif et al., 2016a, Arif et al., 2016b, Li et al., 2012a, Li et al., 2012b, Pereira et al., 2016), γ data is scarce for H_2 and brine systems at elevated temperatures, high pressures, and high salinities. Thus far, a limited number of studies have reported the interfacial tension of hydrogen with other rock/fluid systems (Jander et al., 2021, Massoudi and King Jr, 1974, Pan et al., 2021a, Slowinski Jr et al., 1957, Chow et al., 2018). A semi-empirical method was used by (Pan et al., 2021a) to calculate rock-gas interfacial tension ($\gamma_{rock\text{-}gas}$) for H_2, CH_4 and CO_2, and the results showed that $\gamma_{rock\text{-}gas}$ follows the order $H_2 > CH_4 > CO_2$. Slowinski et al. (1957) and Massoudi and King (1974) reported interfacial tension of ($H_2O + H_2$) system at pressures up to 10 MPa and temperature of 298 K. Furthermore, Chow et al. (2018) reported interfacial tensions of ($H_2O + H_2$) and ($H_2O + CO_2 + H_2$) systems at pressures up to 45 MPa and temperatures of (298 to 448) K (with the average standard deviation of 0.3 %). Interfacial tension measurement of liquid organic hydrogen carriers (LOHCs) and hydrogen system at pressures up to 7 MPa and temperatures up to 523 K was also reported by Jander et al. (2021).

Nevertheless, formation water invariably contains dissolved salt, with saturations reaching very high levels, even attaining maximum and surpassing them (Bjørlykke and Gran, 1994). The

primary compositions of formation salts include Na^+, K^+, Ca^{2+}, Mg^{2+}, Cl^-, CO_3^{2-}, SO_4^{2-}, and HCO_3^-. Among these ions, Na^+, K^+, and Cl^- exhibit the highest concentrations, ranging from 103 to 105 mg/liter in formation water (Wan, 2011).

In this study, we, therefore, measured γ between hydrogen and brine system of [0.864 NaCl + 0.136 KCl] (aq) as a function of pressure, temperature, and water salinity. This work thus provides fundamental physico-chemical data, which will aid in the implementation of a large-scale hydrogen economy.

3.2 Experimental Methodology

3.2.1 Materials

NaCl (purity ≥ 0.99 mole fraction), KCl (purity ≥ 0.99 mole fraction), and H_2 (purity ≥ 0.99 mole fraction) were used in the experiments. Deionized water (electrical conductivity = 0.02 $mS.cm^{-1}$) was used for preparing all electrolyte solutions. All solutions were prepared gravimetrically and then filtered using filter paper to remove potential impurities.

3.2.2 Experimental Procedure

To conduct the experiments, a high-pressure-high-temperature (HPHT) optical cell was utilized, with operational conditions set at 40 MPa and 433 K. Figure 3-1 illustrates the schematic of the apparatus employed for interfacial tension measurement. The measurements were carried out by imaging pendant drops of the desired phase injected through a stainless steel capillary tube (1.5875 mm outer diameter) into the surrounding bulk phase. A Dino-Light camera with a resolution of 1280 × 1024 (1.3 MP) captured high-quality images of the pendant droplets. The view cell was filled with H_2-saturated brine, and a pendant H_2 bubble was injected from the bottom to the top (average volume = 10 μL ± 1 μL) through the capillary tube at the cell's bottom. To ensure equilibrium conditions, the surrounding liquid phase (deionized water or brine) was saturated with H_2 gas before interfacial tension measurements. An H_2 gas cap at the optical cell's ceiling, continuously in contact with the bulk liquid phase under the desired test pressure and temperature, facilitated this saturation process. Occasional manual shaking of the cell expedited equilibration,

with a waiting period of four to five hours for the system to reach equilibrium at the desired test pressure and temperature. System pressure, monitored throughout the test, was used as an indication of equilibrium. Once the pressure stabilized, the system was considered in equilibrium. Acquired images of pendant drops were analyzed using DSA-100 software to determine corresponding γ values. Measurements were conducted for H_2–deionized water (molality = 0) and H_2–brine [0.864 mole fraction NaCl + 0.136 mole fraction KCl] systems. Four different salinities (m = 0, 1.05, 3.15, 4.95 mol·kg^{-1}) were tested, along with four isotherms (T = 298.15, 323.15, 373.15, 423.15 K) for each salinity. In each isotherm, four pressure points (p = 2.76, 13.79, 27.58, 34.47 MPa) were measured, resulting in testing 64 thermo-physical states. Notably, the critical pressure and temperature of hydrogen are 1.3 MPa and 33.3 K, respectively. However, the minimum pressure and temperature used in this study are 2.76 MPa and 298 K, respectively. Thus, H_2 was in the supercritical state under all experimental conditions.

To check the repeatability and reliability of our measurements, a minimum of four individual drops were generated and analyzed for each data point. The relative standard deviation $\sigma(\gamma)/\gamma$ for all state points was < 0.5 % and the average standard deviation was found to be 0.2 %. The relative standard uncertainty (u_r) of interfacial tension is determined by the relative standard deviation of the interfacial tension and the relative standard uncertainties of temperature, pressure, salinity, and density difference. This value is calculated based on the relationship (Chow et al., 2018, Li et al., 2012a):

$$u_r^2 = \left[\frac{1}{\gamma}\left(\frac{\partial\gamma}{\partial T}\right)_{p,m} u(T)\right]^2 + \left[\frac{1}{\gamma}\left(\frac{\partial\gamma}{\partial p}\right)_{T,m} u(p)\right]^2 + \left[\frac{1}{\gamma}\left(\frac{\partial\gamma}{\partial m}\right)_{p,T} u(m)\right]^2 + \left[\frac{u(\Delta\rho)}{\Delta\rho}\right]^2 + \left[\frac{\sigma(\gamma)}{\gamma}\right]^2, \quad (3.3)$$

where it is 0.1 mN.m^{-1}, and the expanded uncertainty at 95 % confidence is 0.2 mN.m^{-1} (with a coverage factor of k = 2 and the relative standard uncertainties of 1 K for temperature, 0.1 psi for pressure, 0.02 mol.kg^{-1} for molality, and 0.15 kg.m^{-3} for density difference).

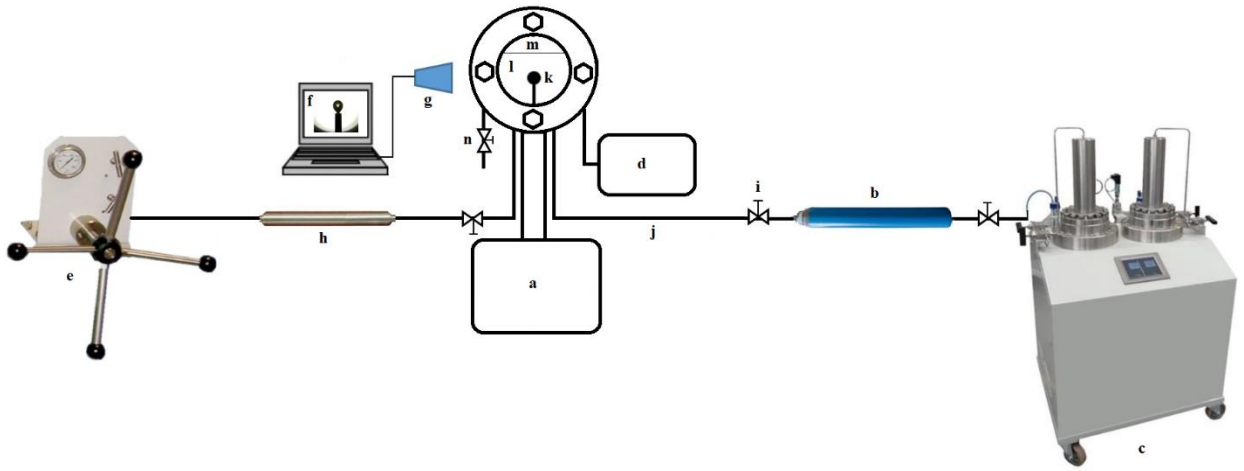

Fig. 3-1 Experimental configuration for interfacial tension measurement used in this study: (a) HPHT optical cell, (b) H_2 cylinder, (c) dual pump, (d) electrical heater, (e) high pressure manual pump, (f) DSA-100 software, (g) dino-light camera, (h) brine vessel, (i) control valve, (j) flow line, (k) capillary tube with H_2 bubble, (l) brine, (m) H_2, (n) relief valve.

3.2.3 Data Analysis

The interfacial tension can be determined by mathematical analysis of the asymmetric droplet shape (see Chapter 2) as follows (Georgiadis et al., 2010):

$$\gamma_{\mathrm{H_2\text{-}brine}} = \frac{\Delta\rho g}{\left(\beta k_{\mathrm{apex}}\right)^2}, \tag{3.4}$$

where $\Delta\rho$ is the H_2-brine density difference, g is the gravitational acceleration, β is the characteristic shape parameter (dimensionless), and k_{apex} is the interface curvature at the apex point of the drop. Thus, to calculate γ, the H_2-brine density difference needs to be known. The density difference between the pure compounds was assumed to be the density difference between two phases as the mutual solubility of the two phases is very limited (De Lucia et al., 2015, Leachman et al., 2009). Therefore, the density values of H_2 and deionized water were obtained from (Kunz and Wagner, 2012, Leachman et al., 2009, Wagner and Pruß, 2002). The density values of brines at the desired temperatures (T = 298.15, 323.15, 373.15, 423.15 K), pressures (p = 2.76, 13.79,

27.58, 34.47 MPa), and brine molalities (m = 1.05, 3.15, 4.95 mol·kg^{-1}) were obtained from (Al Ghafri et al., 2012).

3.2.4 Validation

To validate the correctness of the measurements, γ of (H_2O + air) was measured at ambient pressure and T = 298.15 K, and it was found to be 71.6 ± 0.26 mN.m^{-1}, confirming to the published values of 71.99 ± 0.05 mN.m^{-1} (Pallas and Harrison, 1990) and 71.9 ± 0.1 mN.m^{-1} (Li et al., 2012a).

3.3 Results and Discussion

As real geological conditions are expected to change considerably between different depths and formations, it is necessary to determine 'γ' as a function of pressure, temperature, and salinity. The obtained results are further analyzed and discussed below.

3.3.1 H_2-water interfacial tension as a function of pressure

γ always slightly decreased linearly with increasing pressure (at constant molalities of 0, 1.05, 3.15, 4.95 mol·kg^{-1} and constant temperatures of 298.15, 323.15, 373.15, 423.15 K), Fig. 3-2 This trend can be explained by the increasing intermolecular forces between H_2 and water at elevated pressure (due to the higher gas densities) (Iglauer et al., 2012). According to Equation (3.4), γ is proportional to the H_2-brine density difference. The variations of gas density (ρ_{gas}) and gas-water density difference ($\Delta\rho_{\text{gas-water}}$) with pressure at T = 373.15 K are shown in Figs. 3-3 and 3-4, respectively.

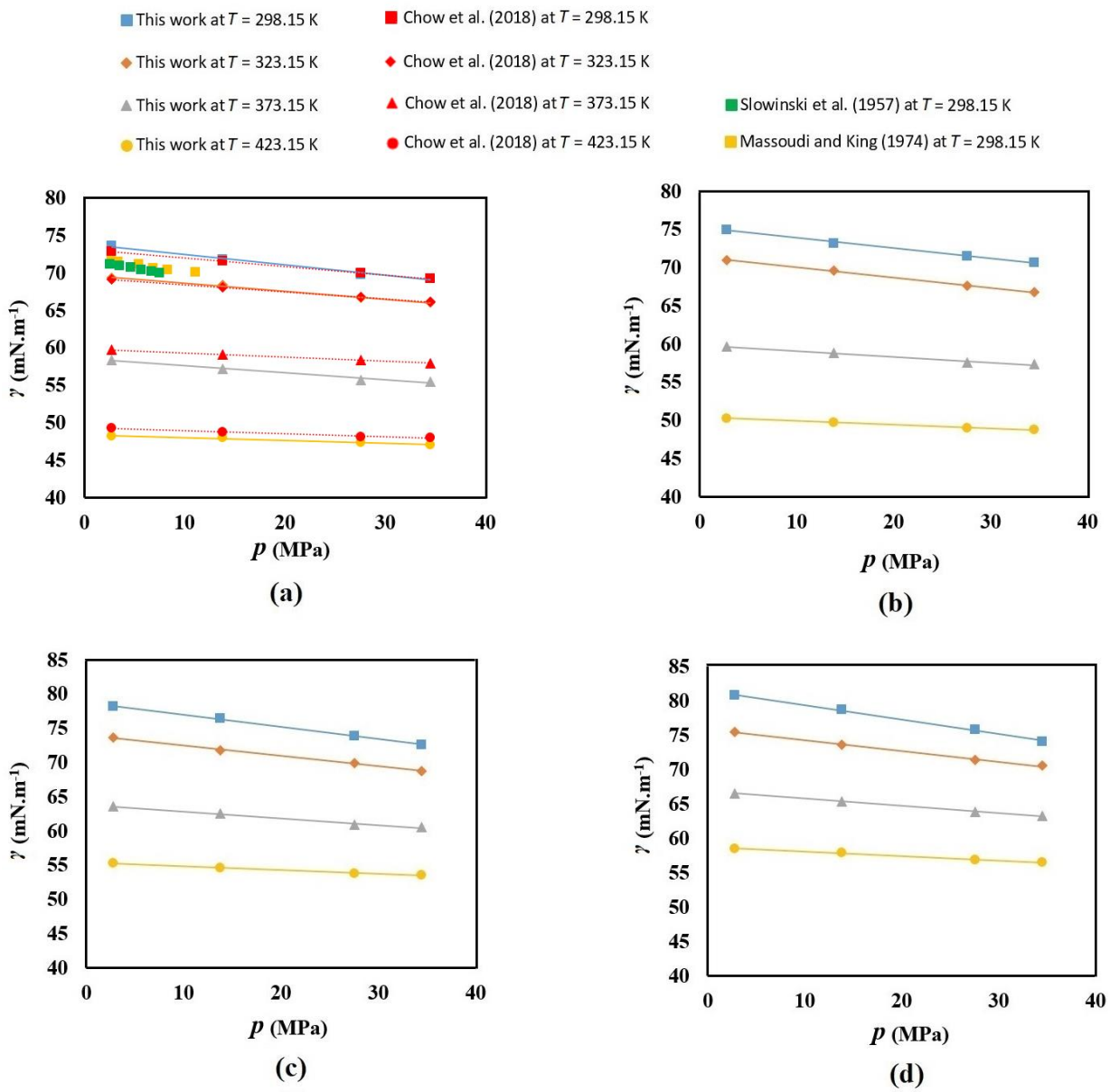

Fig. 3-2 Interfacial tensions versus pressure. Four isotherms are shown, for (a) (H_2 + H_2O; m = 0 mol.kg^{-1}), (b) (H_2 + brine; m = 1.05 mol.kg^{-1}), (c) (H_2 + brine; m = 3.15 mol.kg^{-1}), (d) (H_2 + brine; m = 4.95 mol.kg^{-1}).

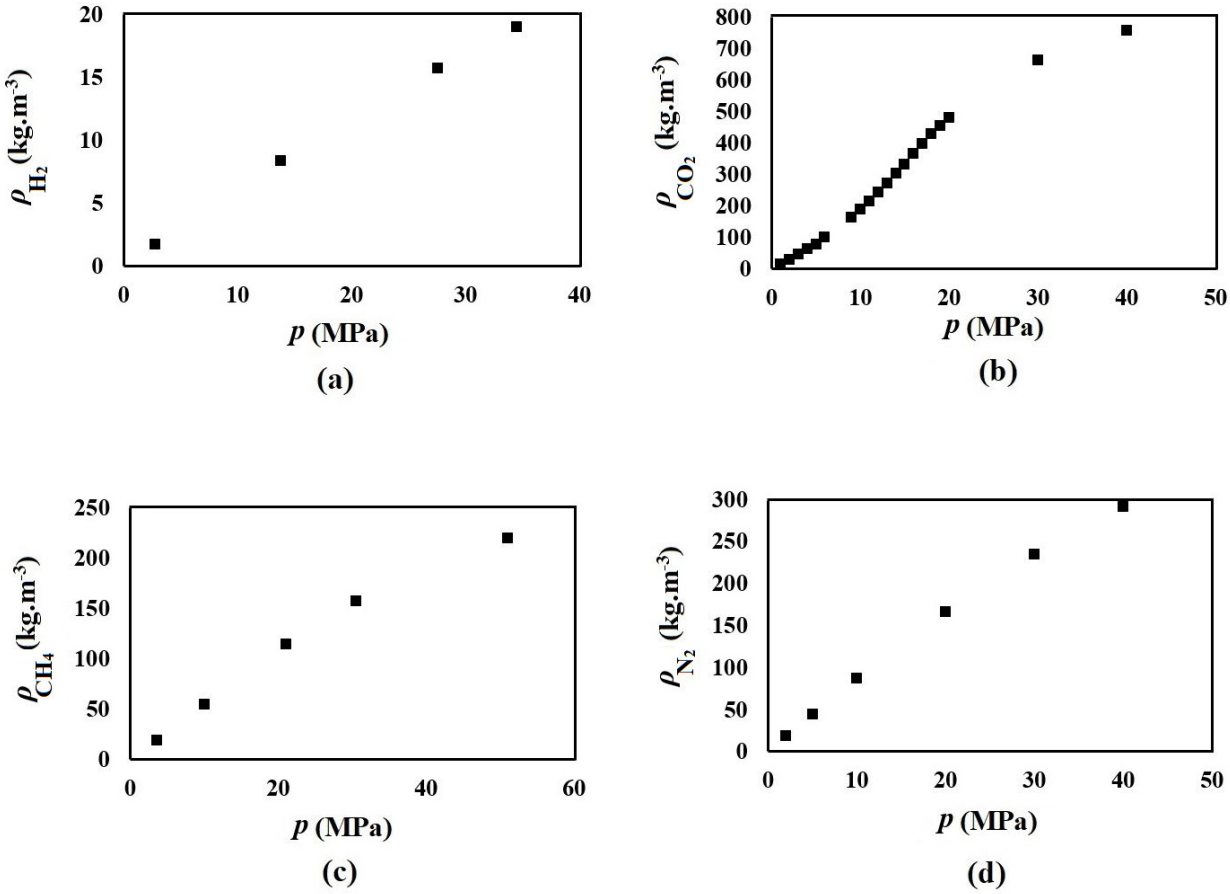

Fig. 3-3 Gas density versus pressure at T = 373.15 K for different gases.

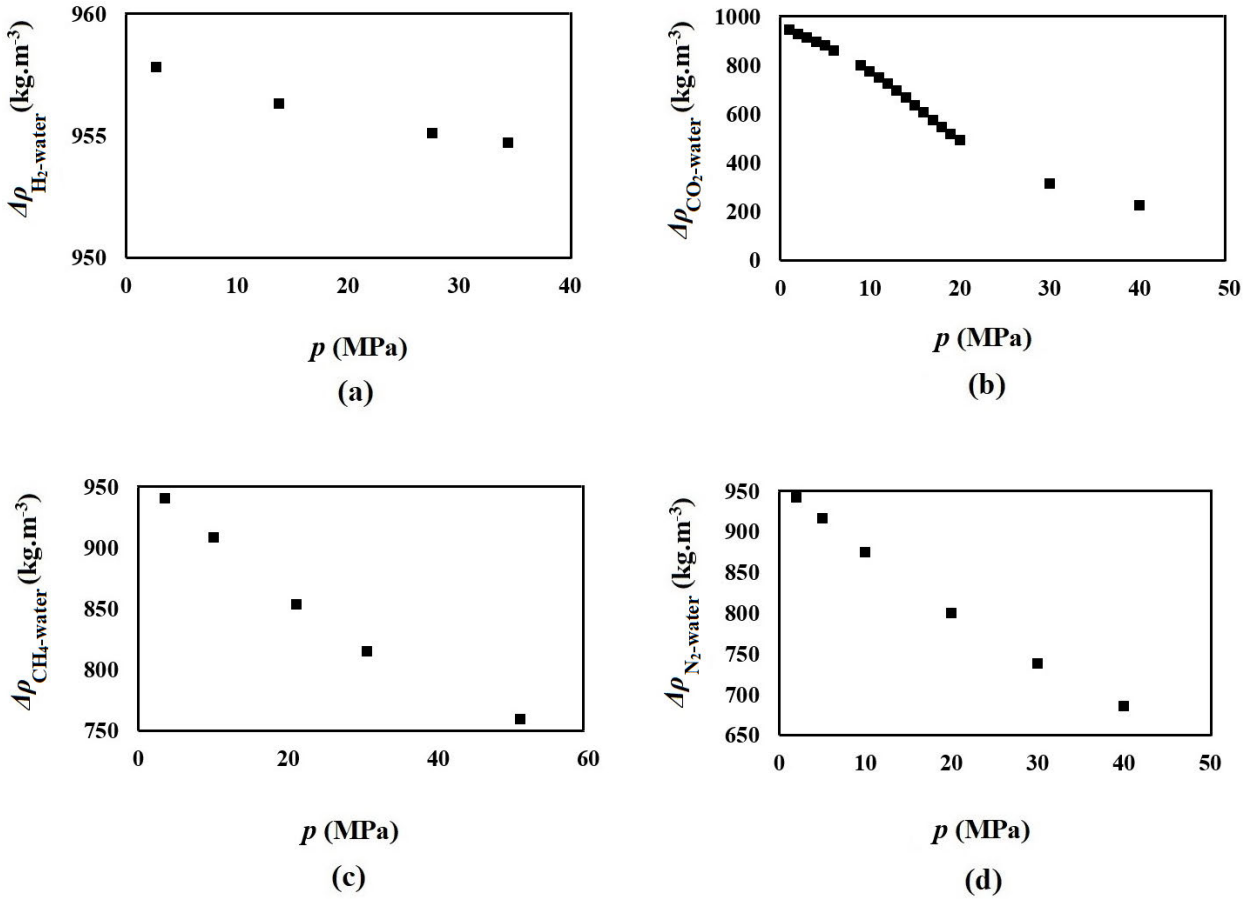

Fig. 3-4 Gas-liquid density difference versus pressure at T = 373.15 K for (a) (H_2 + H_2O), this work; (b) (CO_2 + H_2O), data taken from (Georgiadis et al., 2010); (c) (CH_4 + H_2O), data taken from (Kashefi et al., 2016); (d) (N_2 + H_2O), data taken from (Chow et al., 2016b).

For an isotherm, pressure compresses the gas and reduces its volume, and then increases the ρ_{gas}. This increase in ρ_{gas} is different for various gases. For example, when compared to CO_2, the variations are slight and linear for H_2. Also, at constant salinity and temperature, water density slightly increases with pressure as it is essentially incompressible (e.g. the maximum increase in water density is ~15 kg.m^{-3} when pressure is increased by 30 MPa). It was shown previously that ρ_{gas} correlates with cos(θ), where θ is the contact angle between gas, water, and mineral surface (Al-Yaseri et al., 2016). According to the Young-Laplace equation, the θ for a solid/gas/liquid system is related to solid-gas interfacial tension (γ_{sg}), solid-liquid interfacial tension (γ_{sl}), and liquid-gas interfacial tension (γ_{lg}) as follows (Young, 1805):

$$\cos\theta = \frac{\gamma_{sg} - \gamma_{sl}}{\gamma_{lg}}. \quad (3.5)$$

Thus we correlated here ρ_{gas} with γ. As shown in Fig. 3-5a, H_2–water interfacial tension slightly decreased linearly with gas density (decrease in $\Delta\rho_{\text{gas-water}}$) and hence ρ_{gas} is a good predictor for γ. This effect is similar for N_2 and CH_4 gases, although ρ_{N2} and ρ_{CH4} show a stronger effect on γ, Fig. 3-5 (c, d) as ρ_{N2} and ρ_{CH4} change more than ρ_{H2} with pressure (see Fig. 3-3). However, when compared with CO_2, the interfacial tension of CO_2-water decreases more strongly with ρ_{CO2}, especially with an initial increase in ρ_{CO2} (Fig. 3-5b). This is due to CO_2's strong quadrupole moment (Buckingham and Longuet-Higgins, 1968); CO_2 thus undergoes stronger Debye interactions with water, especially at high CO_2 molecular density (i.e. high ρ_{CO2}), and to CO_2's capability to undergo weak hydrogen bonding with hydroxyl (-OH) groups (Fujii et al., 2002).

Furthermore, interfacial tension variation with pressure was different for different salinities, from 46.97 to 73.57 $mN.m^{-1}$ for m = 0 $mol.kg^{-1}$ – in close agreement with the literature (Chow et al., 2018) – to 56.46 to 80.77 $mN.m^{-1}$ for m = 4.95 $mol.kg^{-1}$ when pressure increased from 2.76 – 34.47 MPa – this is further discussed below. It is notable that while a good agreement with (Chow et al., 2018) was observed, some discrepancies were evident when compared to the results of (Massoudi and King Jr, 1974, Slowinski Jr et al., 1957) for m = 0 $mol.kg^{-1}$. The outcomes reported by these authors consistently indicated lower values, even in the case of other analogous systems involving gases like nitrogen and argon. Therefore, this inconsistency can be attributed to differences in the experimental setup or procedures employed by these researchers.

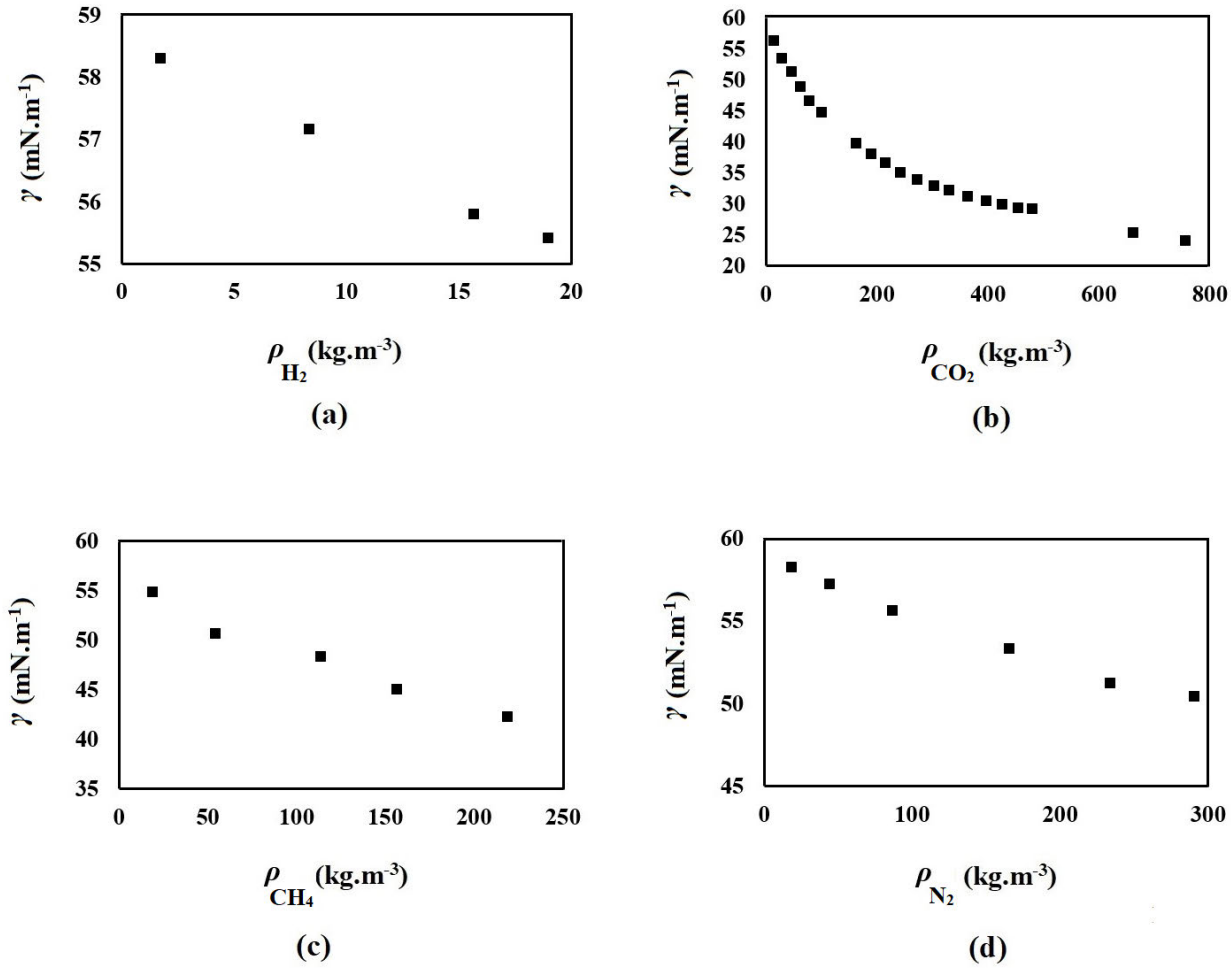

Fig. 3-5 Interfacial tensions versus gas density at T = 373.15 K for (a) (H_2 + H_2O), this work; (b) (CO_2 + H_2O), data taken from (Georgiadis et al., 2010); (c) (CH_4 + H_2O), data taken from (Kashefi et al., 2016); (d) (N_2 + H_2O), data taken from (Chow et al., 2016b).

3.3.2 H_2-water interfacial tension as a function of temperature

γ decreased substantially and also linearly with increasing temperature (at constant molalities of 0, 1.05, 3.15, 4.95 mol·kg^{-1} and constant pressures of 2.76, 13.79, 27.58, 34.47 MPa), Fig. 3-6 The effect of temperature is more significant than the pressure effect (e.g. the maximum decrease in γ was ~3 mN/m when pressure increased by 30 MPa, while γ decreased by a substantial ~26 mN/m when temperature increased from 298 K to 423 K).

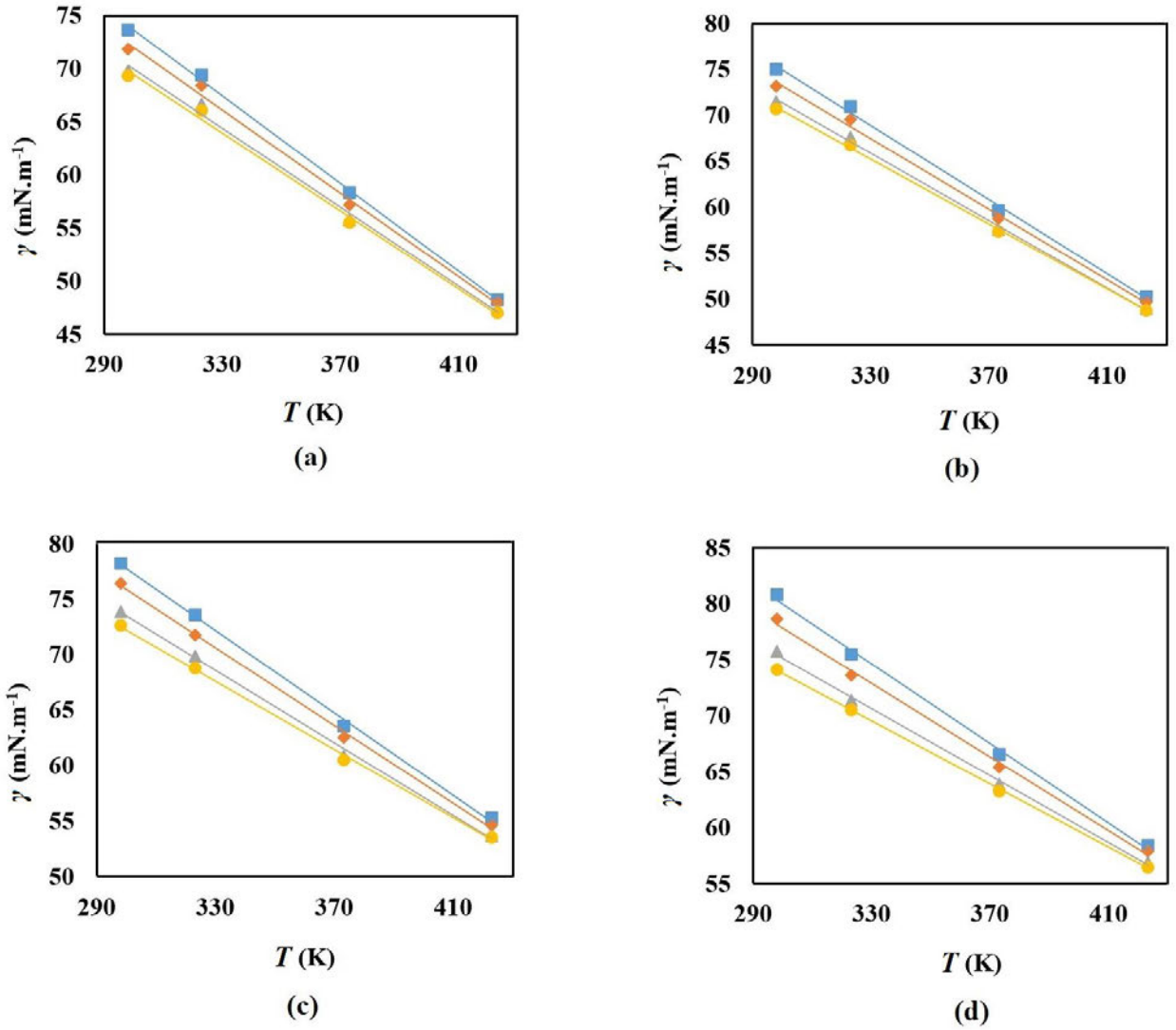

Fig. 3-6 Interfacial tensions measured versus temperature. Data for four isobars is shown, (a) (H_2 + H_2O), (b) (H_2 + brine; m = 1.05 mol.kg^{-1}), (c) (H_2 + brine; m = 3.15 mol.kg^{-1}), (d) (H_2 + brine; m = 4.95 mol.kg^{-1}). Experimental data points for p = 2.76 MPa: ■; p = 13.79 MPa: ◆; p = 27.58 MPa: ▲; p = 34.47 MPa: ● are indicated.

Fig. 3-7a shows that ρ_{H2} decreases slightly with the temperature at p = 20 MPa. Also, at constant molalities (e.g. m = 0, 1.05, 3.15, 4.95 mol·kg^{-1}) and constant pressures (e.g. p = 2.76, 13.79, 27.58, 34.47 MPa), water density decreases with temperature (e.g. it decreased from 1003 to 925 kg.m^{-3} when water temperature increased from 298 to 423 K at p = 13.79 MPa). Therefore, both gas and liquid phases are strongly influenced by temperature. Thus we correlated γ with $\Delta\rho_{gas\text{-}water}$,

which shows different results for various gases. For example, Fig. 3-8a shows that $\Delta\rho_{H2\text{-water}}$ decreases substantially with temperature. This is because the water density decreases more than hydrogen density with temperature. However, $\Delta\rho_{CO2\text{-water}}$ increases substantially with temperature (Fig. 3-8b) as a substantial decrease in CO_2 density with temperature can be seen in Fig. 3-7b. As shown in Fig. 3-9a, H_2−water interfacial tension substantially increased linearly with $\Delta\rho$; however, CO_2 shows an inverse trend (Fig. 3-9b) as the dependence of CO_2−water interfacial tension on temperature is intricate (Aggelopoulos et al., 2011, Li et al., 2012a). Also, the trend for N_2 is not changed regularly (Fig. 3-9d).

Moreover, while the change in $\gamma_{H2\text{-brine}}$ with temperature (when temperature increased from 298.15 to 423.15 K) is effectively the same for different salinities (+ 25 mN/m; e.g. 46.97 to 73.57 mN.m^{-1} for m = 0 mol.kg^{-1} and 56.46 to 80.77 mN.m^{-1} for m = 4.95 mol.kg^{-1}), higher salinity resulted in significantly higher γ, see section 3.3.3.

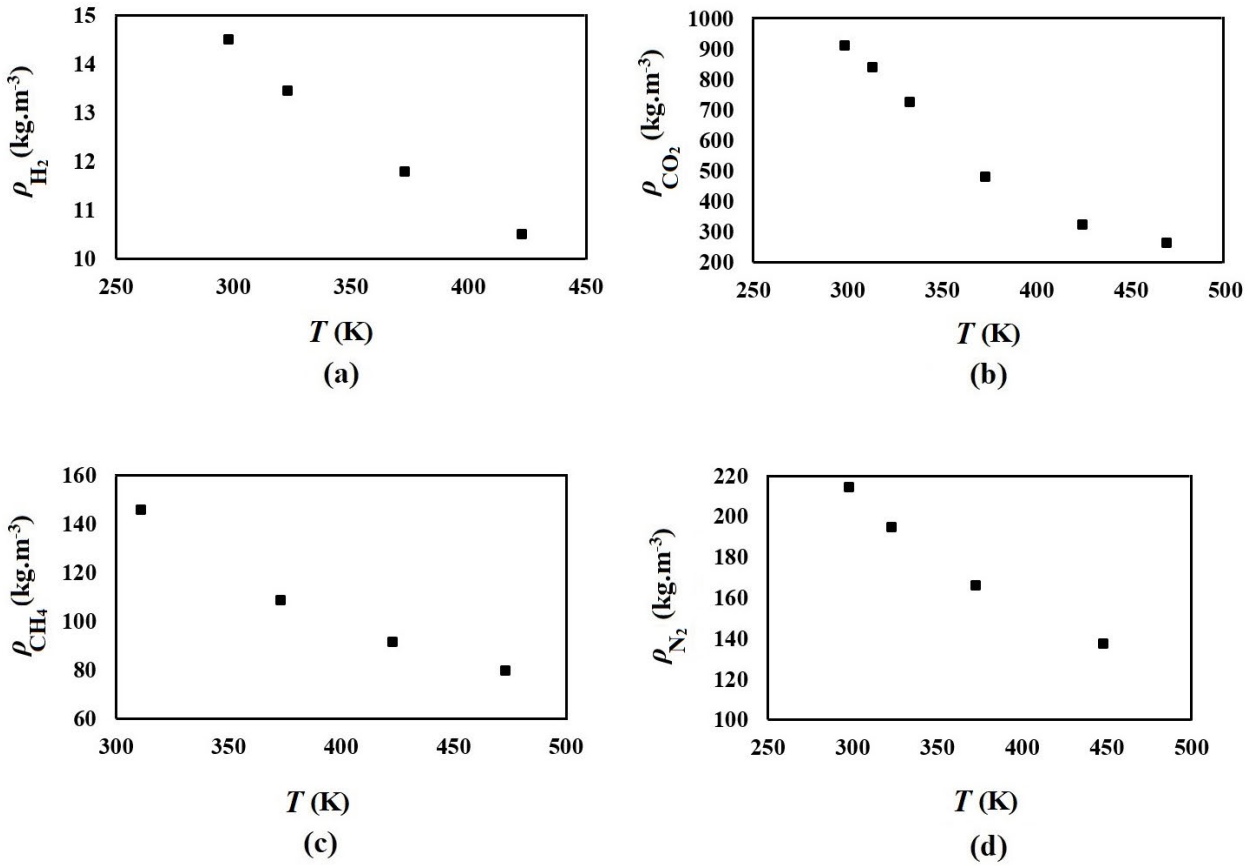

Fig. 3-7 Gas density versus temperature at p = 20 MPa for different gases.

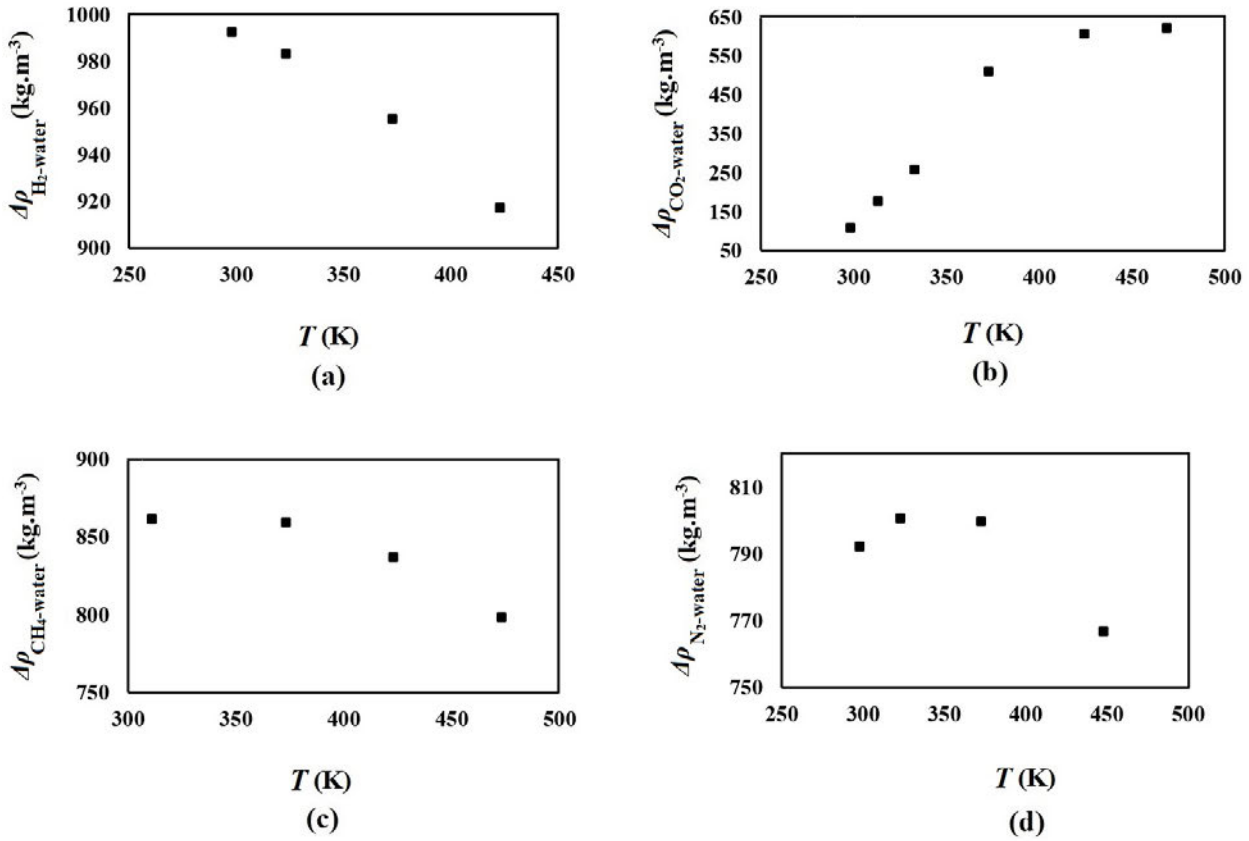

Fig. 3-8 Gas-liquid density difference versus temperature at p = 20 MPa for (a) (H_2 + H_2O), this work; (b) (CO_2 + H_2O), data taken from (Pereira et al., 2016); (c) (CH_4 + H_2O), data taken from (Kashefi et al., 2016); (d) (N_2 + H_2O), data taken from (Chow et al., 2016b).

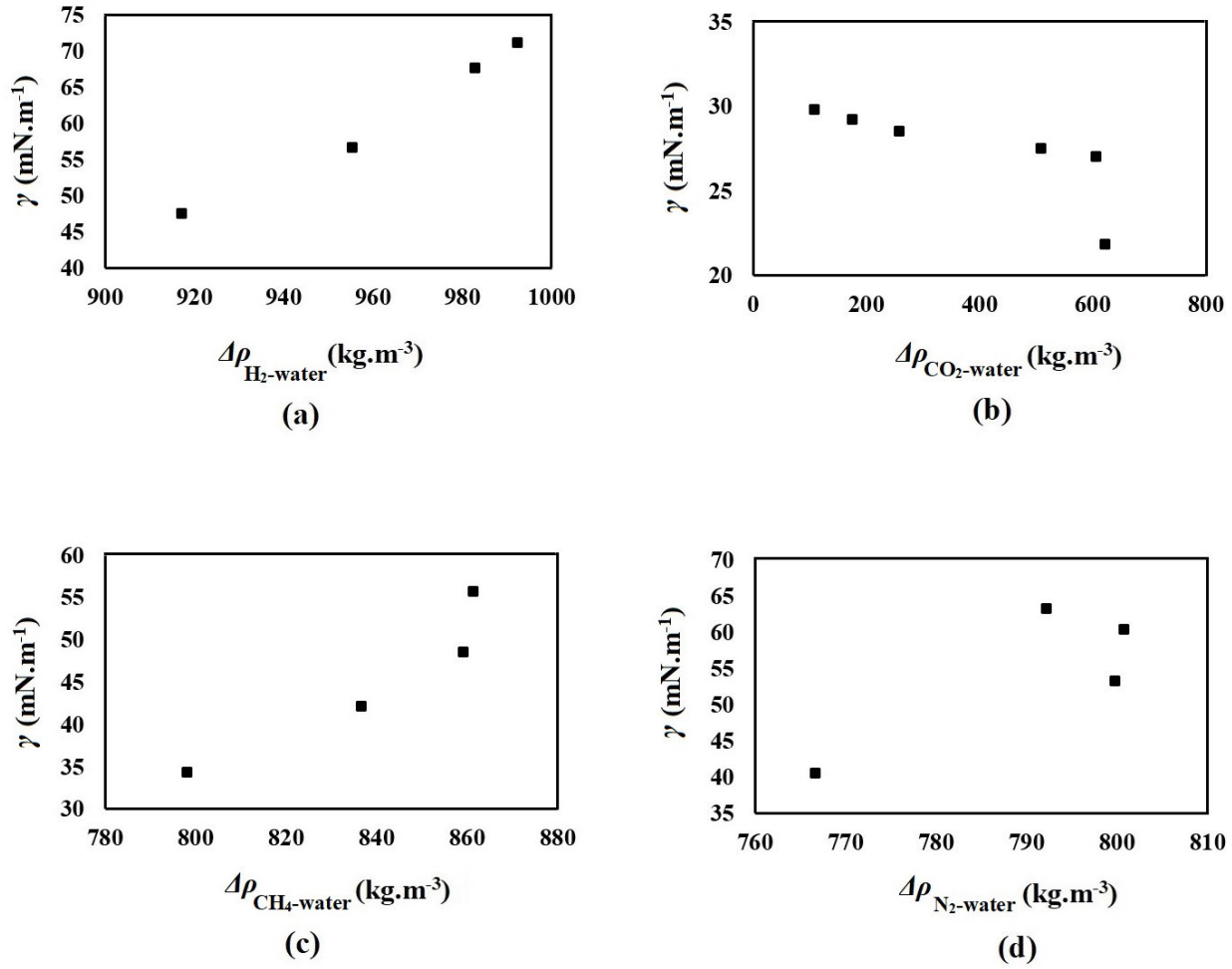

Fig. 3-9 Interfacial tensions versus gas-liquid density difference at p = 20 MPa for (a) (H_2 + H_2O), this work; (b) (CO_2 + H_2O), data taken from (Pereira et al., 2016); (c) (CH_4 + H_2O), data taken from (Kashefi et al., 2016); (d) (N_2 + H_2O), data taken from (Chow et al., 2016b).

3.3.3 H_2-water interfacial tension as a function of salinity

γ increased significantly and also linearly with increasing salinity (at constant pressures of 2.76, 13.79, 27.58, 34.47 MPa and constant temperatures of 298.15, 323.15, 373.15, 423.15 K), Fig. 3-10. This is consistent with the behavior of CO_2 and CH_4 (Aggelopoulos et al., 2011, Kashefi et al., 2016, Li et al., 2012a, Li et al., 2012b).

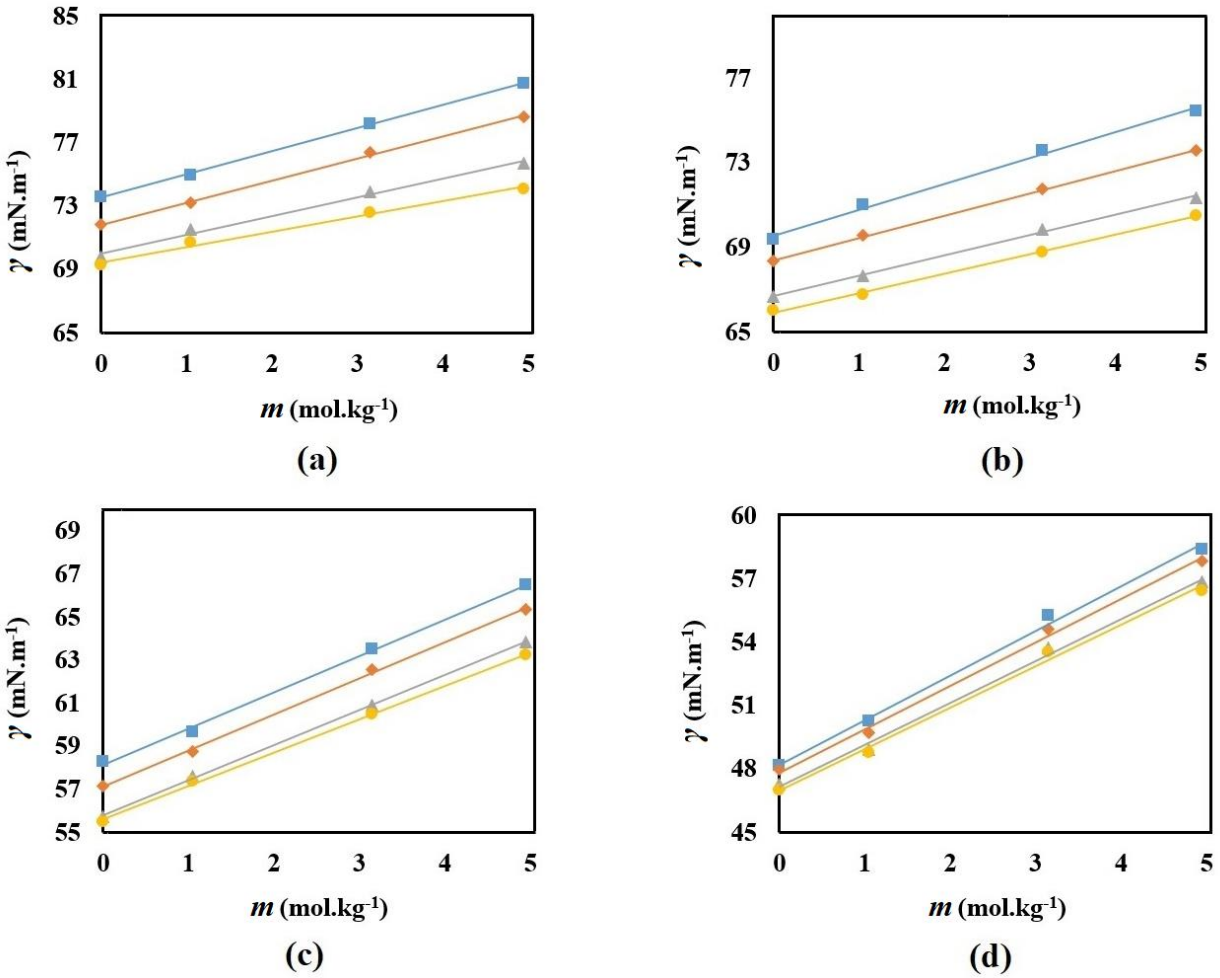

Fig. 3-10 Interfacial tensions of H_2 + [0.864 mole fraction NaCl + 0.136 mole fraction KCl] brine versus salinity at (a) T = 298.15 K, (b) T = 323.15 K, (c) T = 373.15 K, (d) T = 423.15 K: ■, p = 2.76 MPa; ◆, p = 13.79 MPa; ▲, p = 27.58 MPa; ●, p = 34.47 MPa.

Thus the interfacial tension variation with salinity is proportional to the surface excess concentration of the dissolved ions (Soleymanzadeh et al., 2021). Crucially, cations exhibit a greater ability to arrange water dipoles (hydrogen bonding network) in the aqueous bulk phase compared to anions, as depicted in Fig. 3-11. As a consequence, cations experience repulsion from the gas-water interface, while anions become adsorbed at the interface, as discussed by (Hribar et al., 2002, Leroy et al., 2010, Manciu and Ruckenstein, 2003). The resulting depletion of cations from the interface leads to an increased requirement for work to expand the interfacial area, as outlined by (Aggelopoulos et al., 2011).

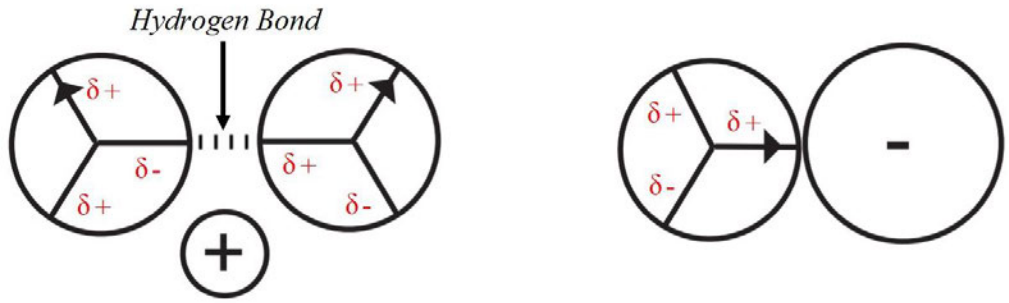

Fig. 3-11 Schematic of the structure-making cations (left side) and structure-breaking anions (right side). Structure-making cations (e.g. Na^+) can better organize the water dipoles (hydrogen bonding network) in the aqueous bulk phase. Structure-breaking anions (e.g. Cl^-) increase interactions between the ion and the neighboring water molecules. [Reproduced from (Leroy et al., 2010) with permission from Elsevier and (Hribar et al., 2002) with permission from American Chemical Society.]

Furthermore, salinity can significantly increase brine density as there is more salt packed into the water (Fig. 3-12a). This figure indicates that the brine densities utilized in this study align with those employed by (Kashefi et al., 2016, Li et al., 2012a). Nevertheless, under constant pressure and temperature, H_2 exhibits a lower density, resulting in a higher $\Delta\rho$, and consequently, a higher interfacial tension compared to CH_4 and CO_2 (see Figs. 3-12b and 3-13). Overall, salinity had a more significant effect than pressure, but a lower effect than temperature.

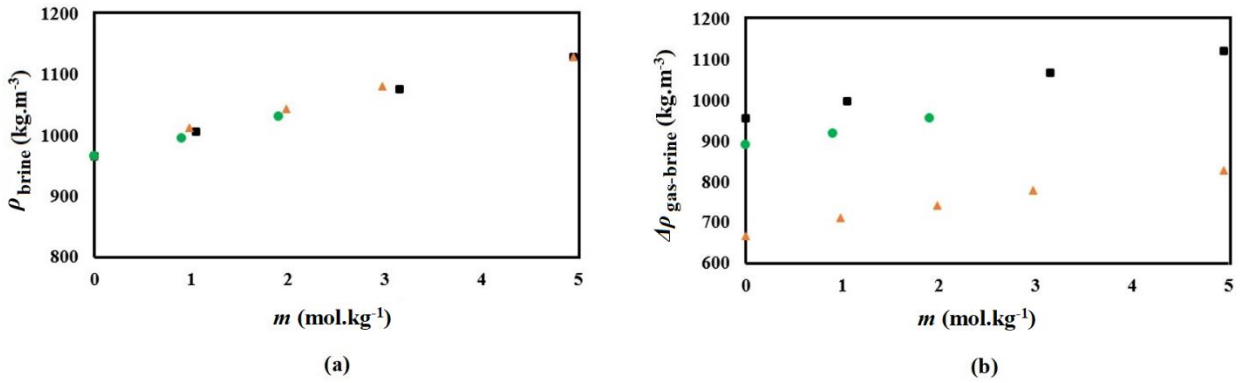

Fig. 3-12 Cross plot of (a) brine density, and (b) gas-brine density difference versus salinity at p = 14 MPa and T = 373.15 K: ■, H_2 + [0.864 NaCl + 0.136 KCl] brine, this work; ▲, CO_2 + [0.864 NaCl + 0.136 KCl] brine, taken from (Li et al., 2012a); ●, CH_4 + NaCl (aq) taken from (Kashefi et al., 2016).

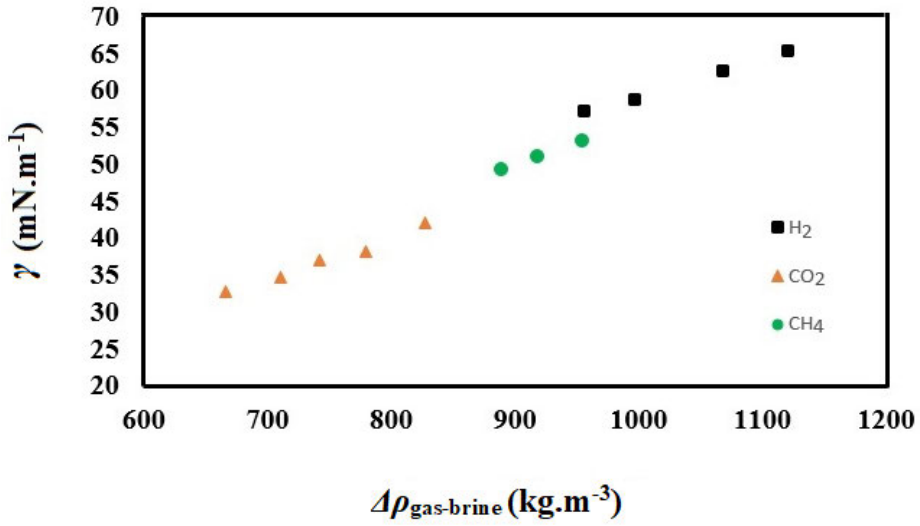

Fig. 3-13 Interfacial tensions versus density difference between gas and brine at p = 14 MPa and T = 373.15 K: ■, H_2 + [0.864 mole fraction NaCl + 0.136 mole fraction KCl] brine: m = 0, 1.05, 3.15, 4.95 mol.kg^{-1}, this work; ▲, CO_2 + [0.864 mole fraction NaCl + 0.136 mole fraction KCl] brine: m = 0, 0.98, 1.98, 2.97, 4.95 mol.kg^{-1}, taken from (Li et al., 2012a); ●, CH_4 + brine: 0, 5, 10 wt% NaCl, taken from (Kashefi et al., 2016).

3.3.4 Empirical Equation

As illustrated in Fig. 3-10, it is evident that γ (mN.m^{-1}) undergoes linear changes with salinity across various pressure and temperature values:

$$\gamma = Am + B, \tag{3.6}$$

where A is a linear function of T (K) and p (MPa) since γ exhibits linear variations with this parameters,

$$A = a_0 + a_1 p + a_2 T, \tag{3.7}$$

and B represents γ (mN.m^{-1}) for the (H_2 + H_2O) system (m = 0); B is the product of two linear functions (of T and p; as γ has a linear variation with T and p, see discussion above). B is thus given by a bilinear interpolation as follows (note: the empirical equation developed by (Georgiadis et al., 2010) pertains to the (H_2O + CO_2) system, which differs, particularly in the non-linear change of B with pressure and temperature):

$$B=\sum_{i=1}^{2}\sum_{j=1}^{2}b_{ij}p^{i-1}T^{j-1}=b_{11}+b_{21}p+b_{12}T+b_{22}pT. \tag{3.8}$$

The model (Equation (3.6)) was validated by the γ values measured in this work and γ values taken from (Chow et al., 2018). This unique model is thus valid at $298.15 \leq T$ (K) ≤ 423.15, $2.76 \leq p$ (MPa) ≤ 34.47 MPa, and molalities up to about 5 mol.kg^{-1} [$0 \leq m$ (mol.kg^{-1}) ≤ 4.95], and other researchers can validate their results with this model at the specified p, T and m. Following the fitting process with the acquired data, all seven parameters in Equations (3.7) and (3.8) were computed, leading to the development of the empirical equation. The seven fitting parameters are listed in Table 3-1 The average absolute relative deviation ΔAAD for the entire data set (80 in number) is 0.83 % (0.72 % for 64 data points from this work and 1.26 % for 16 data points from (Chow et al., 2018)), which is calculated as follows:

$$\Delta AAD=\frac{1}{N}\sum_{i=1}^{N}\left(\frac{\Delta\gamma}{\gamma}\right)_i\times 100, \tag{3.9}$$

where N is the number of data points and $\Delta\gamma$ is the difference between γ values obtained from the experiment and model. As γ increases with salinity, the accuracy of the model also increases with salinity (Table 3-2). The predictions for all 80 data points has a maximum deviation of 2.59 % ($\Delta\gamma$ = ± 1.5 mN.m^{-1}) from the experimental data (Fig. 3-14). The predictions for data points of this work has a maximum deviation of 2.13 % ($-1.19 \leq \Delta\gamma$ (mN.m^{-1}) ≤ 0.78, Fig. 3-14a), while the predictions for data points of (Chow et al., 2018) has a maximum deviation of 2.59 % ($-1.06 \leq \Delta\gamma$ (mN.m^{-1}) ≤ 1.5, Fig. 3-14b) from the experimental data, implying that data from (Chow et al., 2018) has more deviation than this work in general.

Table 3-1 Fitting parameters in Equation (3.6) required for predicting γ between H_2 and brine.

Parameter	Value
a_0	-0.47876
a_1	-0.01004
a_2	0.00593
b_{11}	135.41479
b_{21}	-0.38368
b_{12}	-0.20520
b_{22}	0.00084

Table 3-2 The effect of salinity on the accuracy of the model.

m (mol kg^{-1})	ΔAAD
0	1.14
1.05	0.85
3.15	0.53
4.95	0.49

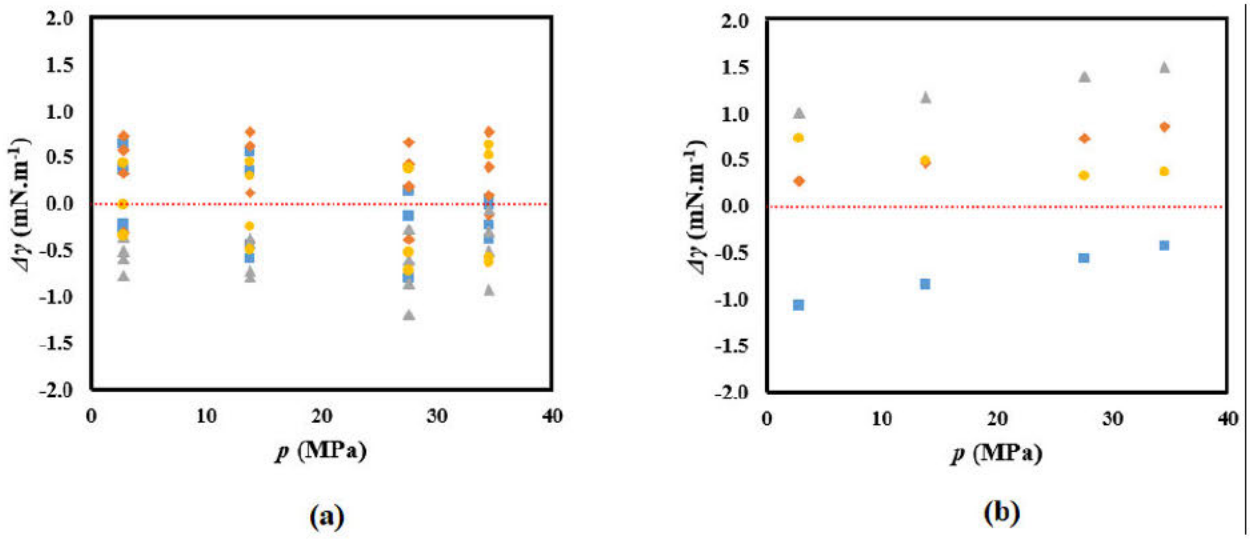

Fig. 3-14 Deviations between experimental and predicted γ data for (a) this work and (b) (Chow et al., 2018) at four isotherms: ■, T = 298.15 K; ◆, T = 323.15 K; ▲, T = 373.15 K; ●, T = 423.15 K.

3.4 Conclusions

H_2–brine interfacial tension (γ) as one of the key thermos-physical parameters for H_2 geo-storage was measured over wide ranges of temperatures (298.15-423.15 K), pressures (2.76-34.47 MPa), and molalities (0-4.95 mol.kg^{-1}). Clearly, γ declined linearly with increasing pressure and temperature. We observed a satisfactory agreement with the findings of (Chow et al., 2018), but discrepancies were noted in comparison to the results reported by (Massoudi and King Jr, 1974, Slowinski Jr et al., 1957) for m = 0 mol.kg^{-1}. The outcomes reported by these authors consistently appeared lower, even when considering other similar systems like nitrogen and argon gases.

Moreover, a linear increase in γ was observed with increasing salinity. From the experimental data of this work and (Chow et al., 2018), an empirical equation was developed and validated with an average absolute relative deviation of 0.83 % for the entire data set (80 in number). The predictions for all 80 data points has a maximum deviation of 2.59 % ($\Delta\gamma$ = ± 1.5 mN.m^{-1}) from the experimental data.

In addition to its impact on the storage capacity and containment security, γ also influences capillary pressure (P_c), a crucial input for reservoir-scale modelling (Yekta et al., 2018). The variation of γ with pressure, temperature, and salinity leads to changes in P_c under reservoir conditions. The effect on P_c is more pronounced for temperature and salinity as the results showed that γ has substantial variations with these two variables compared to pressure. Consequently, the pore-network upscaled functions utilized in reservoir-scale modelling (Hashemi et al., 2021a) are expected to be sensitive to reservoir conditions. This work thus gives fundamental physio-chemical data, which will aid in successful implementation of a large-scale hydrogen geo-storage project.

3.5 Supporting Information

Table S3-1 Interfacial tension for (H_2O + H_2) systems at different temperatures and pressures.

T (K)	p (MPa)	$\Delta\rho$ (kg.m^{-3})	γ (mN.m^{-1})
298.15	2.76	972.2	73.57 ± 0.09
298.15	13.79	993.9	71.81 ± 0.01
298.15	27.58	991	69.75 ± 0.28
298.15	34.47	990	69.25 ± 0.11
323.15	2.76	987.2	69.37 ± 0.20
323.15	13.79	984.3	68.33 ± 0.12
323.15	27.58	981.9	66.66 ± 0.13
323.15	34.47	981	66.01 ± 0.05
373.15	2.76	957.8	58.30 ± 0.20
373.15	13.79	956.3	57.16 ± 0.14
373.15	27.58	955.1	55.71 ± 0.16
373.15	34.47	954.7	55.49 ± 0.23
423.15	2.76	916.7	48.17 ± 0.22
423.15	13.79	917	47.95 ± 0.04
423.15	27.58	917.6	47.28 ± 0.03
423.15	34.47	918.1	46.97 ± 0.04

Table S3-2 Interfacial tension for H_2 + (0.864 NaCl + 0.136 KCl) brine systems at different temperatures and pressures at a total salt molality of m = 1.05 mol.kg^{-1}.

T (K)	p (MPa)	$\Delta\rho$ (kg m^{-3})	γ (mN.m^{-1})
298.15	2.76	1038.3	74.97 ± 0.03
298.15	13.79	1034.3	73.17 ± 0.14
298.15	27.58	1030.6	71.49 ± 0.01
298.15	34.47	1029.4	70.68 ± 0.09
323.15	2.76	1028	71.00 ± 0.12
323.15	13.79	1024.7	69.54 ± 0.29
323.15	27.58	1021.7	67.65 ± 0.20
323.15	34.47	1020.6	66.77 ± 0.09
373.15	2.76	998.8	59.67 ± 0.22
373.15	13.79	996.6	58.76 ± 0.12
373.15	27.58	994.9	57.58 ± 0.25
373.15	34.47	994.3	57.37 ± 0.09
423.15	2.76	960	50.27 ± 0.07
423.15	13.79	959.4	49.68 ± 0.08
423.15	27.58	959.2	48.92 ± 0.04
423.15	34.47	959.4	48.79 ± 0.04

Table S3-3 Interfacial tension for H_2 + (0.864 NaCl + 0.136 KCl) brine systems at different temperatures and pressures at a total salt molality of m = 3.15 mol.kg^{-1}.

T (K)	p (MPa)	$\Delta\rho$ (kg m^{-3})	γ (mN.m^{-1})
298.15	2.76	1111.6	78.21 ± 0.10
298.15	13.79	1107.1	76.37 ± 0.15
298.15	27.58	1103	73.87 ± 0.08
298.15	34.47	1101.4	72.60 ± 0.14
323.15	2.76	1099.7	73.57 ± 0.18
323.15	13.79	1095.9	71.76 ± 0.13
323.15	27.58	1092.4	69.84 ± 0.17
323.15	34.47	1091.1	68.76 ± 0.30
373.15	2.76	1070.2	63.52 ± 0.01
373.15	13.79	1067.5	62.53 ± 0.19
373.15	27.58	1065.2	60.89 ± 0.06
373.15	34.47	1064.5	60.49 ± 0.18
423.15	2.76	1033.4	55.26 ± 0.14
423.15	13.79	1032.4	54.61 ± 0.15
423.15	27.58	1031.5	53.70 ± 0.03
423.15	34.47	1031.3	53.54 ± 0.10

Table S3-4 Interfacial tension for H_2 + (0.864 NaCl + 0.136 KCl) brine systems at different temperatures and pressures at a total salt molality of m = 4.95 mol.kg^{-1}.

T (K)	p (MPa)	$\Delta\rho$ (kg.m^{-3})	γ (mN.m^{-1})
298.15	2.76	1166.6	80.77 ± 0.26
298.15	13.79	1161.8	78.65 ± 0.18
298.15	27.58	1157.2	75.71 ± 0.14
298.15	34.47	1155.4	74.08 ± 0.11
323.15	2.76	1153.5	75.46 ± 0.06
323.15	13.79	1149.4	73.58 ± 0.23
323.15	27.58	1145.6	71.36 ± 0.05
323.15	34.47	1144.1	70.51 ± 0.23
373.15	2.76	1123.4	66.50 ± 0.33
373.15	13.79	1120.6	65.34 ± 0.18
373.15	27.58	1117.9	63.84 ± 0.17
373.15	34.47	1117	63.22 ± 0.02
423.15	2.76	1088.2	58.41 ± 0.16
423.15	13.79	1086.5	57.85 ± 0.04
423.15	27.58	1085	56.86 ± 0.18
423.15	34.47	1084.8	56.46 ± 0.28

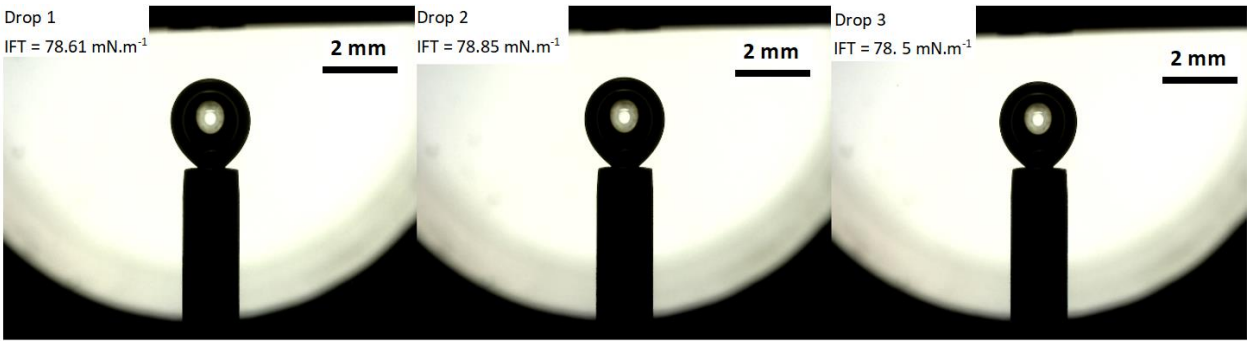

Fig. S3-1 Example recorded images of hydrogen drop in brine (m = 4.95 mol.kg^{-1}) at T = 298.15 K and p = 13.79 MPa, γ = 78.65 ± 0.18 mN.m^{-1}.

Chapter 4 Hydrogen wettability of carbonate formations: Implications for hydrogen geo-storage

Published in *Journal of Colloid and Interface Science*, Elsevier 2022, 614, 256-266
DOI: https://doi.org/10.1016/j.jcis.2022.01.068

Abstract

Hypothesis: The mitigation of anthropogenic greenhouse gas emissions and increasing global energy demand are two driving forces toward the hydrogen economy. The large-scale hydrogen storage at the surface is not feasible as hydrogen is very volatile and highly compressible. An effective way for solving this problem is to store it in underground geological formations (i.e. carbonate reservoirs). The wettability of the rock/H_2/brine system is a critical parameter in the assessment of residual and structural storage capacities and containment safety. However, the presence of organic matters in geo-storage formations poses a direct threat to the successful hydrogen geo-storage operation and containment safety.

Experiments: Given the scarcity of literature (modelling and experimental data) on hydrogen wettability in calcite-rich formations, this study measured advancing (θ_a) and receding (θ_r) contact angles in water/H_2/calcite systems under various parameters. These parameters included pressure (0.1-20 MPa), temperature (298-353 K), salinity (0-4.95 mol.kg^{-1}), stearic acid concentration (representative of organic acid, ranging from 10^{-9} to 10^{-2} mol/L), tilting plate angle (0º - 45º), and surface roughness (RMS = 341 nm, 466 nm, and 588 nm).

Findings: The results of the study show that at ambient conditions, the system was strongly water-wet, but became intermediate wet at high pressure. The water contact angle strongly increased with stearic acid concentration making the calcite surface H_2-wet. Moreover, the contact angle increased with salinity and tilting plate angle but decreased with temperature and surface roughness. We conclude that the optimum conditions for de-risking H_2 storage projects in carbonates are low pressures, high temperatures, low salinity, and low organic surface

concentration. Therefore, it is essential to measure these effects to avoid overestimation of hydrogen geo-storage capacities and containment security.

Keywords

Contact angle, wettability, hydrogen, hydrogen geo-storage, calcite-rich formation

4.1 Introduction

Hydrogen as a clean energy has recently gained lots of attention worldwide as it can be potentially used instead of fossil fuels to strongly reduce anthropogenic CO_2 emissions and meet increasing global energy demand (Tarkowski, 2019, Zivar et al., 2021). Hydrogen can be produced through several processes, including the electrolytic process (Kumar and Himabindu, 2019, Wang et al., 2021), steam methane reforming (Chen et al., 2020, Mohanty et al., 2021), biomass gasification (Cao et al., 2020, Shayan et al., 2018), and solar thermochemistry (Arribas et al., 2018, Boretti et al., 2021). However, in implementing a full-scale hydrogen economy, because of high volatility and compressibility of hydrogen, its large volume storage for a long time becomes a challenge at the surface (Lemieux et al., 2020, Zhang et al., 2016). A prominent way for solving this problem is to store hydrogen in deep underground formations known as underground hydrogen storage (UHS) due to their vast storage capacities and cheap associated operations (Ali et al., 2020a, Ali et al., 2020b, Caglayan et al., 2020, Iglauer et al., 2021a, Iglauer et al., 2021b, Pfeiffer and Bauer, 2015, Iglauer, 2022). Unlike CO_2 which is permanently stored in geological formations (Ali et al., 2022a), the stored hydrogen can be withdrawn again to generate energy/electricity at peak demand times (Ali et al., 2020b, Ali et al., 2022c, Keshavarz et al., 2022).

Deep saline aquifers, basaltic formations, coal seams, depleted oil/gas reservoirs, and salt caverns have been suggested as potential hydrogen geo-storage sites (Al-Khdheeawi et al., 2021, Al-Rubaye et al., 2021, Al-Yaseri and Jha, 2021, Ali et al., 2021c, Dahraj et al., 2016, Mahesar et al., 2020a, Mahesar et al., 2020b, Ozarslan, 2012, Yekta et al., 2018, Memon et al., 2020, Akhondzadeh et al., 2020, Akhondzadeh et al., 2021). However, salt caverns have been the only storage site operated thus far where pure hydrogen has been stored at an industrial scale

(Tarkowski, 2019, Zivar et al., 2021). For UHS in an aquifer, two rock categories are required: 1) a permeable reservoir rock for accumulation of hydrogen and 2) an impermeable layer (caprock) for sealing the hydrogen (Zivar et al., 2021). Various storing mechanisms (e.g. structural, residual, adsorption, and dissolution/mineral trapping) can be used to permanently trap the gas in geological formations (Al-Khdheeawi et al., 2021, Ali et al., 2020a, Arif et al., 2017a, Arif et al., 2017b, Iglauer et al., 2015a, Iglauer et al., 2021b). However, residual and structural trapping are considered as the most significant gas geo-storage mechanisms, where there are strong correlations between capillary and buoyancy forces (Abdulelah et al., 2021, Al-Yaseri et al., 2021b, Ali et al., 2020a, Iglauer et al., 2015b). For example, calcite, serving as a representative for carbonate formations, is prevalent in both reservoir rock and caprock (Ali et al., 2019a, Haldar, 2020, Trueman et al., 2019). Consequently, the interplay of structural trapping (in the context of a calcite-rich caprock) and residual trapping (in the case of a calcite-rich reservoir rock) mechanisms holds significance for hydrogen storage in calcite-rich formations (Arif et al., 2017a). Rock-fluid and fluid-fluid interfacial tensions and rock wettability are critical parameters in gas geo-storage, which can be significantly affected by geo-storage conditions (e.g. pressure, temperature, and salinity) (Al-Yaseri et al., 2021a, Ali et al., 2021c, Crotogino et al., 2010, Haghighi et al., 2020, Hashemi et al., 2021b, Iglauer et al., 2021a, Iglauer et al., 2021b, Nazarahari et al., 2021). Moreover, organic matters can be found in geo-storage formations, specifically where sediments are deposited in anoxic conditions (Iglauer et al., 2021b, Ali et al., 2021a, Ali et al., 2019a, Ali et al., 2019b, Ali et al., 2021b, Ali et al., 2021c, Ali et al., 2020b). Even minute existence of the organic matters can change the wettability, which may affect the hydrogen geo-storage capacities and containment security (Ali et al., 2021a, Ali et al., 2019a, Ali et al., 2019b, Ali et al., 2021b, Ali et al., 2021c).

The thermos-physical parameters such as rock-fluid and fluid-fluid interfacial tensions and wettability depends on the gas type (e.g. CO_2, CH_4, H_2) (Pan et al., 2021a). The literature data on the H_2-wettability of rocks at geological conditions are scarce (Shi et al., 2020). The reported H_2-wettability of minerals is limited to a few studies, concerning the hydrogen wettability of sandstone and shale. For example, (Yekta et al., 2018) conducted a core flooding test in which hydrogen was injected into a brine-saturated sandstone core sample. They reported only two contact angle values of 21.56^o and 34.9^o at two different temperature (T) and pressure (p) values of (20 C, 50 bar) and (45 C, 100 bar), respectively. Moreover, the tilted plate method was used by (Iglauer et al., 2021b)

for measuring θ_a and θ_r (at T = 296-343 K and p = 0.1-25 MPa) to determine the H_2-wettability of pure and stearic acid-aged quartz substrates. Another contact angle measurements of the brine/H_2/sandstone system (at p = 20-100 bar and T = 20-50 C) using the captive-bubble method was performed by (Hashemi et al., 2021b). More recently, the H_2-wettability of mica substrates (aged with stearic acid) was determined by (Ali et al., 2021d) at p = 0.1-25 MPa and T = 296-343 K. Also, the hydrogen wettability of clays (at p = 5-20 MPa and T = 333 K) was mathematically derived and interpreted by (Al-Yaseri et al., 2021c) using empirical correlations.

Unfortunately, there is an intensive lack of data for H_2-wettability of carbonate-rich formations (calcite, a representative mineral for carbonates) at geo-storage conditions. In this study, we, therefore, measured the H_2-wettability of calcite and examined the effect of different parameters, including pressure, temperature, salinity, organic surface concentration, fluids equilibration, tilting plate angle, and surface roughness on the wettability. For this purpose, we measured both advancing and receding contact angles using the tilted plate method. This work thus gives basic data for UHS in carbonates.

4.2 Experimental Methodology

4.2.1 Materials

In this study, pure calcite, $CaCO_3$ (56.03% CaO and 43.97% CO_2, sample dimensions = 1 cm × 1 cm × 0.4 cm), was selected and quite cleaved for the experiments. Although the effect of cleavage on wettability may be considerable (e.g. (Lai et al., 2015)), we did not consider this effect in our measurements. Methanol solvent (purity ≥ 0.99 mole fraction) was used for cleaning the mineral substrate. Also, stearic acid (purity ≥ 0.99 mole fraction) was applied for the aging of the calcite surface. Deionized water (electrical conductivity = 0.02 $mS.cm^{-1}$), a mixture of 0.864 mole fraction NaCl and 0.136 mole fraction KCl (purities of NaCl and KCl ≥ 0.99 mole fraction) for simulating some natural formation water as Na^+, K^+, and Cl^- have the highest concentration (103-105 mg/liter) among the ions in the formation water (Li et al., 2012a, Wan, 2011), H_2 (99.9 mol%), and CO_2 (99.9 mol%) were used in this study for contact angle measurements.

4.2.2 Surface roughness

The atomic force microscope (AFM, model DSE 95-200 from Semilab) was used to measure the surface roughness of the samples before conducting the experiments. Three calcite samples of varying surface roughness were used for the experiments. A sample with the root mean square (RMS) surface roughness value of 466 nm was used for investigating the influences of temperature, pressure, tilted plate angle, and fluids equilibration on wettability. The effects of aging and salinity were also tested on the samples with RMS surface roughness values of 568-588 nm and 341 nm, respectively. Also, the effect of surface roughness on contact angle was tested and has been discussed in section 4.3.7.

4.2.3 Surface cleaning procedure

Firstly, deionized water was utilized to wipe the calcite substrates to remove contaminations on the surfaces. Then, the water film on the surfaces was wiped off by nitrogen (99.9 mol%) blowing and the surfaces were put in an oven to be dried at 338 K for 60 minutes (Ali et al., 2020a). Finally, calcite samples were placed in air plasma for 15 mins to eliminate the organic impurities (Iglauer et al., 2014).

4.2.4 Aging procedure

To simulate carbonate rock in a geological formation, the following strategy was used (Davis, 1982, Kleber et al., 2015, Ulrich et al., 1988, Zullig and Morse, 1988): At first, we ionized the calcite surface by immersing in 2 wt% NaCl brine for 30 mins at ambient conditions (Ali et al., 2021a, Ali et al., 2021c, Ali et al., 2020b). The brine acidity was also retained at pH = 4 by adding HCl acid (concentration = 37.5 vol%) droplets. In this way, the adsorption rate of stearic acid onto the calcite surface increases (Al-Anssari et al., 2020, Ali et al., 2019a, Ali et al., 2019b, Jardine et al., 1989, Madsen and Ida, 1998, Stalker et al., 2013). Subsequently, ultra-pure nitrogen was used to clean the remaining water film from the surface. The mineral substrates were then aged in toluene/stearic acid solutions (highly diluted stearic acid concentrations: 10^{-9} - 10^{-2} mol/L) for a week to simulate disposal to organic compounds over geological times as stearic acid exists in

geological formations (Ali et al., 2019a, Ali et al., 2019b, Jardine et al., 1989, Madsen and Ida, 1998, Stalker et al., 2013). The stearic acid makes the calcite surfaces strongly hydrophobic by esterifying the hydroxyl groups on the surfaces (Al-Anssari et al., 2016, Ali et al., 2019a, Ali et al., 2019b), the schematic has been shown in (Ali et al., 2019a).

4.2.5 Contact angle measurements

The contact angle test is the technique of choice to quantitatively determine the wetting characteristics of a fluid/rock system (Chiquet et al., 2007). The contact angle measurements in this study were conducted employing a high pressure-high temperature optical cell (with a working temperature and pressure of 433 K and 40 MPa, respectively) utilizing the tilted plate technique (Al-Anssari et al., 2016, Lander et al., 1993). The tilted plate method is considered a routinely used technique for quantifying the contact angle hysteresis effect by measuring receding and advancing contact angles, simultaneously (Lander et al., 1993). The calcite substrate (clean or aged) was then placed on the tilted plate (angle = 15º) inside the optical cell. To ensure the tests are conducted under equilibrium conditions (to eliminate the effect of mass transfer between fluids on the measurements), a few milliliters of water was injected into the bottom of the cell (beneath the sample's plate). Setting the setup on desired test temperature, the optical cell was pressurized with H_2 gas and adequate time was given for the system to reach equilibrium. Upon the system equilibration, a droplet of aqueous phase (average volume = 5 μL ± 1 μL) was dispensed onto the calcite surface through a stainless steel capillary tube (with outer diameter of 1.5875 mm) mounted vertically on the cell's ceiling. The receding and advancing contact angles were measured at the trailing and leading edge of the droplet, respectively, and the measurements were conducted just before the droplet movement (Lander et al., 1993). A dino-light camera with a resolution of 1280 × 1024 (1.3 MP) was used for recording high-quality images of the droplets. Finally, the acquired images were analyzed using DSA-100 software to determine the corresponding θ_a and θ_r values.

In this study, we evaluated the influence of different parameters on the H_2 wettability of the calcite surface. The effects of pressure and temperature were evaluated at five pressure (p = 0.1, 5, 10, 15, 20 MPa) and three temperatures (T = 298, 323, 353 K) values, where the DI-water was used as the liquid phase. Furthermore, the influence of salinity for three different molalities (m = 1.05, 3.15, 4.95 mol·kg^{-1}) were investigated at T = 323 K and p = 15 MPa. We also assessed the influence of

organic compounds' adsorption on the H_2-wettability of the calcite surface at T = 323 K and p = 10 MPa. The effect of fluids equilibration on wettability was also analyzed for two measurements at T = 323 K, p = 5 MPa, and T = 323 K, p = 15 MPa with DI-water. Also, the influence of tilting angle on the contact angle hysteresis was investigated at three different angles (15º, 30º, 45º) at T = 323 K and p = 10 MPa with DI-water. Finally, the influence of solid surface roughness on wettability was scrutinized for three samples with different roughness values at T = 323 K and p = 15 MPa with DI-water. To check the reproducibility of the results, the measurements were repeated at least thrice (each time, same sample was cleaned carefully and a fresh H_2/water system was used, while the lines and pressure cell of the setup were cleaned) and the average values were calculated and reported here. The standard deviation of the measurements was ± 2º.

4.2.6 Validation

To validate the correctness of the measurements, water contact angles of clean calcite/CO_2/deionized (DI) water system at p = 0.1, 5, 10, 15, 20 MPa and T = 298 K as well as aged calcite/CO_2/DI water system for five stearic acid concentrations of 10^{-2}, 10^{-3}, 10^{-5}, 10^{-7} and 10^{-9} mol/L at p = 10 MPa and T = 323 K were measured. The water contact angle values in CO_2 were found to be higher than that in H_2 as CO_2 has a higher density than H_2 (e.g. (Ali et al., 2021d, Iglauer et al., 2021b); see sections 4.3.1 and 4.3.4).

4.3 Results and discussion

H_2-wettability of calcite is a critical parameter for determining containment security and storage capacity of carbonate formations as it controls the maximum column height or storage height (Aggelopoulos et al., 2011, Shah et al., 2008). When hydrogen is injected in an aquifer, it displaces water which is correlated to the receding contact angle (θ_r) and corresponds to structural storage capacities (Broseta et al., 2012). If $\theta_r > 90°$, capillary leakage could take place (Iglauer et al., 2015b). When hydrogen is withdrawn again, water displaces hydrogen, which is associated with the advancing contact angle (θ_a) which is correlated to residual trapping at $\theta_a < 50°$ (Al-Menhali and Krevor, 2016, Chiquet et al., 2007, Rahman et al., 2016). Thus a true understanding of different parameters affecting θ is crucial from a safe and economic H_2 storage perspective. Some of these

parameters, studied in this work, include pressure, temperature, salinity, organic surface contamination, fluids equilibration, tilted plate angle, and surface roughness.

4.3.1. Effect of pressure

The contact angles (θ_a and θ_r) increased with pressure (decrease in water wettability of calcite at constant temperatures of 298, 323, 353 K), Fig. 4-1. For instance, θ_a increased from 0º (water wet) at ambient conditions (0.1 MPa and 298 K), which confirms literature results, e.g. (Arif et al., 2016a, Arif et al., 2016d, Grate et al., 2012, Iglauer et al., 2021b, Iglauer et al., 2014, Sarmadivaleh et al., 2015), to 83.6º (intermediate wet) at 298 K and 20 MPa. This increase is consistent with literature data, e.g. (Arif et al., 2017a, Broseta et al., 2012, Chiquet et al., 2007, Iglauer et al., 2014, Jung and Wan, 2012, Saraji et al., 2013a, Yang et al., 2008). This trend can be explained by the increased intermolecular forces between H_2 and calcite at elevated pressure (due to the higher gas densities; e.g. (Iglauer et al., 2012)). We also observed similar trends for the calcite/CO_2/water system (Fig. 4-1). For example, it is seen that by increasing pressure from 5 MPa to 20 MPa at 298 K, θ_a and θ_r for the calcite/CO_2/water system increased from 78.29° to 106.14° and 75.6° to 102.56°, respectively. It is also seen that the CO_2 system has higher values of contact angle as CO_2 has higher density than H_2 (Al-Yaseri and Jha, 2021, Ali et al., 2021d, Iglauer et al., 2021b). For example, at 298 K and 20 MPa, CO_2 and H_2 densities are 914.9 kg/m^3 and 14.5 kg/m^3, respectively (Iglauer et al., 2021b, Leachman et al., 2009, Span and Wagner, 1996). This trend was also reported for brine/H_2/quartz and brine/H_2/mica systems (Ali et al., 2021d, Iglauer et al., 2021b), where the contact angles for these systems is lower than that of brine/H_2/calcite system (Fig. 4-1). This is consistent with CO_2 systems such as brine/CO_2/quartz (Sarmadivaleh et al., 2015), brine/CO_2/mica (Arif et al., 2016a), and brine/CO_2/calcite (Arif et al., 2017a) systems.

4.3.2 Effect of temperature

The contact angles (θ_a and θ_r) decreased with temperatures (water wettability increased, Fig. 4-1). For instance, at 15 MPa, θ_a and θ_r decreased from 80.35° to 57.85° at 298 K and 76.6° to 53.15° at 353 K, respectively (the analogous trend was reported for CO_2 e.g. (Arif et al., 2017a, Yang et al., 2008)). This can be due to the fact that H_2 gas density decreases with temperature (Ali et al.,

2021d). Another reason for the reduction of the contact angle with temperature is that rock/H_2 interfacial tension increases with temperature as the difference between the molecular cohesive energy density of rock and H_2 increases (when temperature increases, the molecular cohesive energy density decreases for H_2 but remains constant for the rock) (Arif et al., 2017a). In other words, increasing temperature leads to higher collision and accelerated diffusion of the H_2 gas molecules as their kinetic energy also increases (fast motion). Thus, the molecular interactions between the calcite surface and H_2 decreases and this results in the increase in water wettability (reduction in water contact angle) with temperature. This trend is consistent with brine/H_2/mica (Ali et al., 2021d), while brine/H_2/quartz contact angles increased with temperature due to higher silanol groups on the surface (Iglauer et al., 2021b). These observations suggest that analogous to the brine/H_2/mica system the wettability of brine/H_2/calcite system highly depend on H_2 density, while the wettability of brine/H_2/quartz system depend on hydrogen bonding between silanol groups and water molecules on the quartz surface which is broken at high temperatures (Al-Yaseri et al., 2016, Chen et al., 2015b).

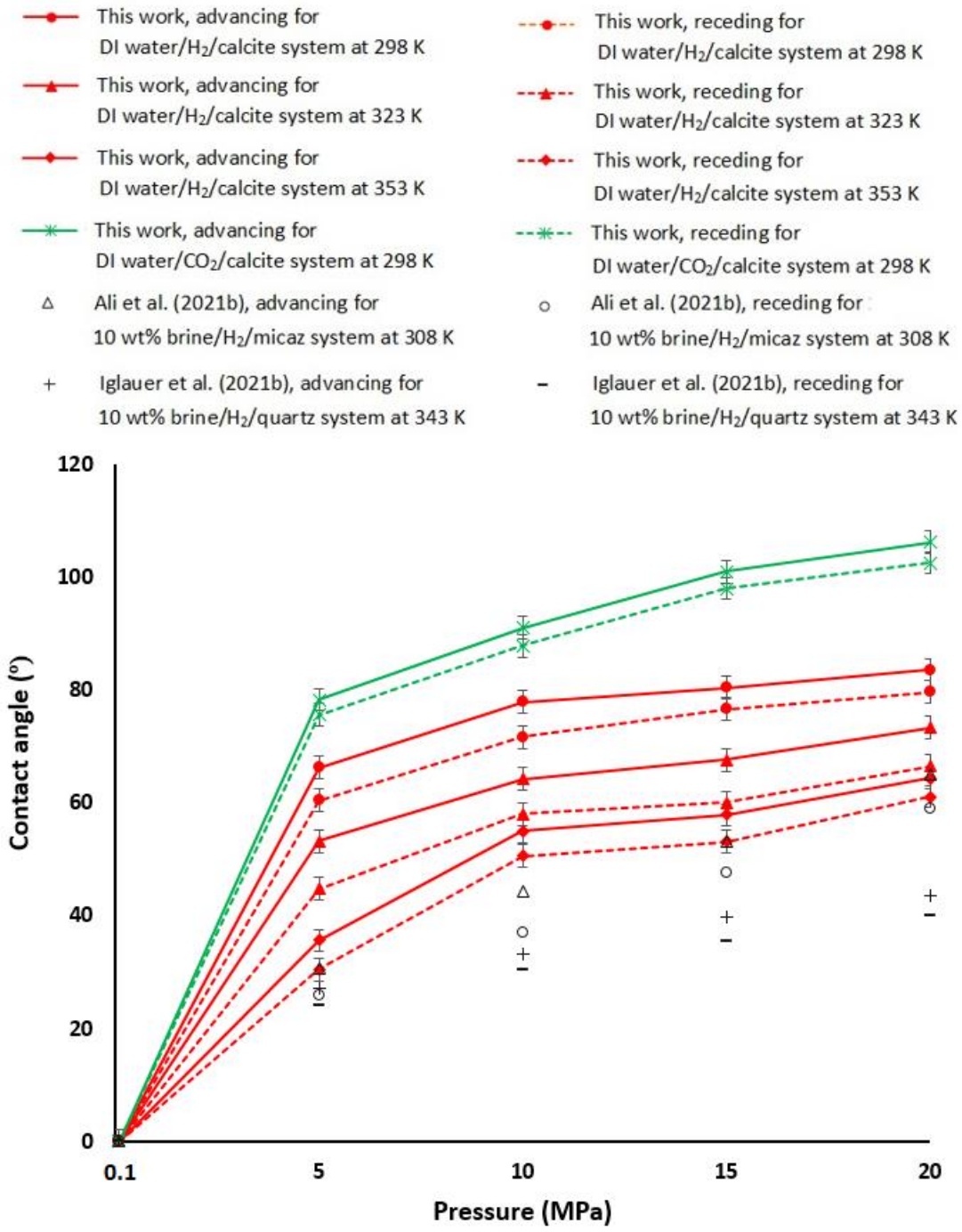

Fig. 4-1 Water/H_2/calcite contact angles as a function of pressure and temperature, and comparison with other water/gas/rock systems: green and red lines represent this work for CO_2 and H_2, respectively (solid: advancing, dotted: receding). Gray symbols represent literature measurements.

4.3.3 Effect of salinity

Both θ_a and θ_r contact angles slightly increased with salinity (decrease in water wettability of calcite, Fig. 4-2). For instance, at 323 K and 15 MPa, by increasing salinity from 0 mol.kg^{-1} to 4.95 mol.kg^{-1}, θ_a increased from 69.8º to 80.65º and θ_r also increased from 63.35º to 73.3º. The decrease in water wettability with salinity is consistent with CO_2 systems such as brine/CO_2/quartz (Espinoza and Santamarina, 2010), brine/CO_2/mica (Arif et al., 2016a), brine/CO_2/coal (Arif et al., 2016c), and brine/CO_2/calcite (Arif et al., 2017a). When the salinity increases, the number of ions needed for neutralizing the surface charge of the sample also increases (reduced surface polarity), which promotes de-wetting of the surface (Arif et al., 2016a, Arif et al., 2017a, Iglauer, 2017). This effect can also be investigated for divalent ions. For example, Al-Yaseri et al. (2016) showed that divalent ions have more increase in θ_a and θ_r than monovalent ions. When salt concentration or ion valency increases, zeta potential also increases (Arif et al., 2016d, Arif et al., 2017a). Therefore, higher electrolyte concentrations result in more efficient shielding and potent de-wetting of the surface (Kaya and Yukselen, 2005, Saraji et al., 2013b). It is notable that minimal dissolution of the calcite in the brine is expected as the calcite surface had minimal exposure to the brine during the contact angle tests.

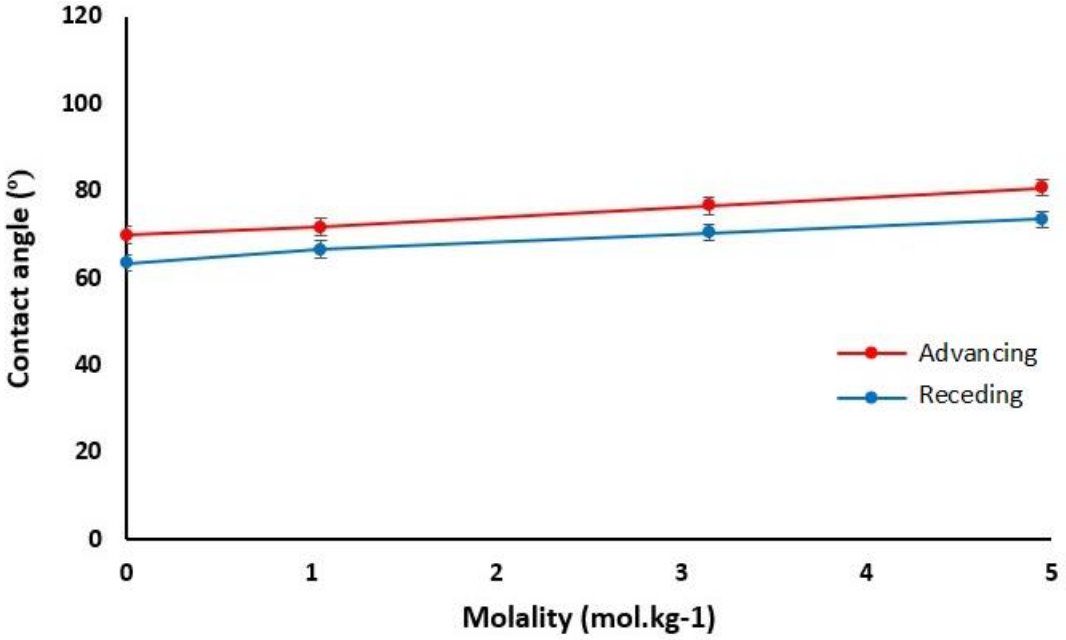

Fig. 4-2 Variation of brine/H_2/calcite contact angle with salinity at 323 K and 15 MPa.

4.3.4 Effect of organic surface concentration

To simulate the realistic scenario of a geological formation, organic acids are subjected to the rock surface for a given time (Ali et al., 2019a, Ali et al., 2019b, Ali et al., 2021b, Ali et al., 2021c, Ali et al., 2021d, Iglauer et al., 2021b, Ali et al., 2022c). The contact angles (θ_a and θ_r) substantially increased with stearic acid concentration (decrease in water wettability of calcite, Fig. 4-3). For example, at 10 MPa and 323 K, advancing and receding θ increased from 75.85° and 68.7° (intermediate wet) to 115.85° and 110.85° (weakly H_2-wet), when the stearic acid concentration increased from 10^{-9} mol/L to 10^{-2} mol/L. Also, the extremely low stearic acid concentration of 10^{-9} mol/L had a considerable effect on contact angle (θ_a = 75.85° and θ_r = 68.7°, versus θ_a = 64.6° and θ_r = 55.4° for chemically clean calcite surface). This is because the hydrophobicity of the rock surface increases by adsorption of organic acid on the surface, which results in higher water contact angles, e.g. (Abramov et al., 2019, Iglauer et al., 2021b). We observed similar trends for calcite/CO_2/water system at 323 K and 10 MPa so that by increasing stearic acid concentration from 10^{-9} mol/L to 10^{-2} mol/L, θ_a and θ_r increased from 90.4° to 130.69° and 84.2° to 123.12°, respectively (Fig. 4-3). The decrease in water wettability with increasing stearic acid concentration is also consistent with brine/H_2/quartz (Iglauer et al., 2021b) and brine/H_2/mica (Ali et al., 2021d), where the degree of contact angles for these systems is lower than that of brine/H_2/calcite system (Fig. 4-3). This is because calcite has a less hydrophilic surface compared to mica and quartz (Ali et al., 2021d); therefore, it is expected to have higher contact angles (lower rock/H_2 interfacial energies) for calcite.

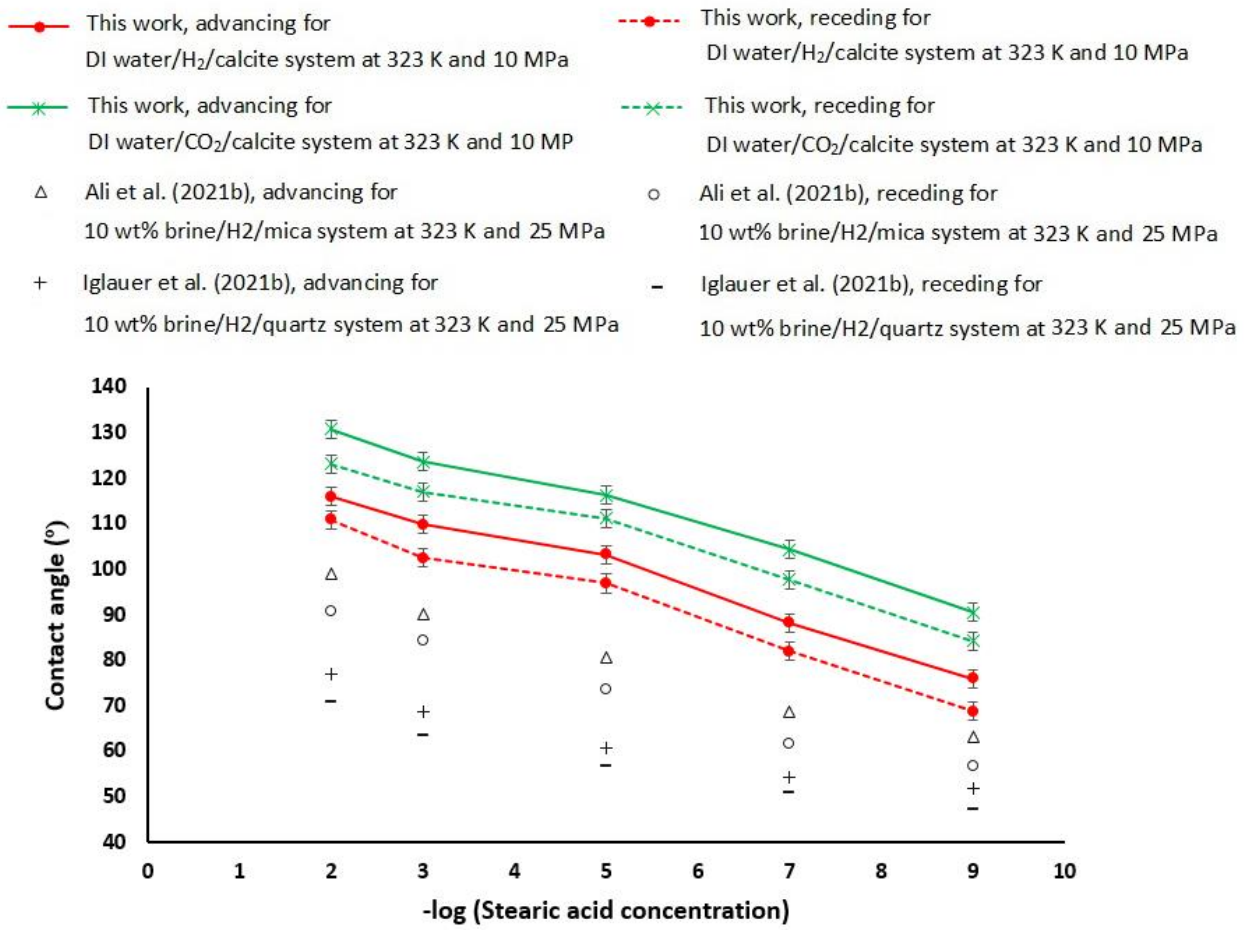

Fig. 4-3 Effect of organic surface concentration on DI water/H_2/calcite contact angle at 323 K and 10 MPa, and comparison with other water/gas/rock systems: green and red lines represent this work for CO_2 and H_2, respectively (solid: advancing, dotted: receding). Gray symbols represent literature measurements.

4.3.5 Effect of fluids equilibration

To minimize dissolution effects during the measurements, we conducted all the experiments with thermodynamically equilibrated H_2/brine phases and the equilibration lasted for about 60 minutes for each measurement. Fig. 4-4 shows that the contact angle at (353 K, 20 MPa) is not considerably changed by the equilibration during the first 300 s (θ_a decreased from 68.6º to 64º and θ_r decreased from 66.5º to 62.3º after 300 s). The effect of such fluids equilibration on contact angles was investigated by conducting two measurements (323 K, 5 MPa) and (323 K, 15 MPa) using non-

equilibrated fluids. The results showed that at (323 K, 5 MPa), θ_a was 50.5° and θ_r was 44.1° for non-equilibrated fluids compared to equilibrated fluids (θ_a = 53.2° and θ_r = 44.8°). Analogously, at (323 K, 15 MPa), θ_a was 65.5° and θ_r was 59.2° for non-equilibrated fluids compared to equilibrated fluids (θ_a = 67.6° and θ_r = 60°). Thus we observed that the difference in θ values with non-equilibrated fluids was ~2-3° for θ_a and < 1º for θ_r compared to equilibrated fluids, which is an insignificant change. This is consistent with CO_2 systems such as brine/CO_2/quartz (Al-Yaseri et al., 2016, Sarmadivaleh et al., 2015), brine/CO_2/mica (Arif et al., 2016a), and brine/CO_2/calcite (Arif et al., 2017a). This is because the measurements of contact angles were conducted by dispensing a droplet of brine into the gas atmosphere, where water has relatively low diffusion coefficients in H_2 and CO_2 (Arif et al., 2017a).

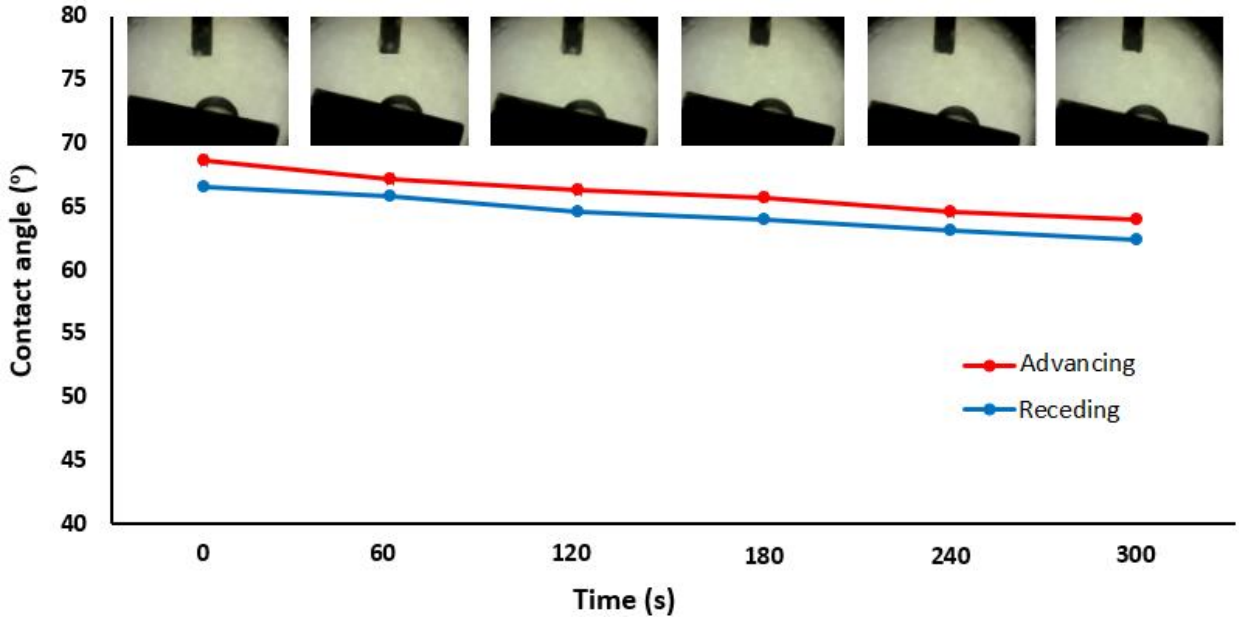

Fig. 4-4 Development of the contact angle with time for thermodynamically equilibrated H_2/water phases at 353 K and 20 MPa.

4.3.6 Effect of tilted plate angle

Although all the measurements in this study used a tilted plate angle of 15º, the tilted plate method can be challenging in practice for systems with high (>30º) or low (<10º) tilted plate angle as it

can affect contact angles (Pierce et al., 2008). Fig. 4-5a shows that θ_a significantly increased with tilted plate angle (at 323 K and 10 MPa, θ_a increased from 56.6° to 77.65°, when the tilted plate angle increased from 0° to 45°). However, θ_r smoothly increased with tilted plate angle (at 323 K and 10 MPa, θ_r increased from 56.6° to 60.9°, when the tilted plate angle increased from 0° to 45°). This trend can be explained by the balance between gravity and interfacial forces which is expressed as follows (Furmidge, 1962):

$$\sin(\alpha) = \gamma \frac{Rk}{mg}(\cos\theta_r - \cos\theta_a), \tag{4.1}$$

where α is the tilting plate angle, γ is the interfacial tension between hydrogen and water, R is a length scale (generally taken as the droplet's radius), k is a shape constant for the contour of the droplet (a fitting parameter based on the experimental data), m is the droplet's mass, and g is the gravitational acceleration. Our results are consistent with Equation (4.1), where the cross plot of ($\cos\theta_r - \cos\theta_a$) versus sin ($\alpha$) yields a linear change with a slope of $mg/Rk\gamma$ = 0.37, Fig. 4-5b. If k =1 and γ = 68 mN/m (taken from (Chow et al., 2018)), the value of $mg/Rk\gamma$ = 0.36 is calculated for a droplet with the volume of 5 µL and the radius of 2 mm.

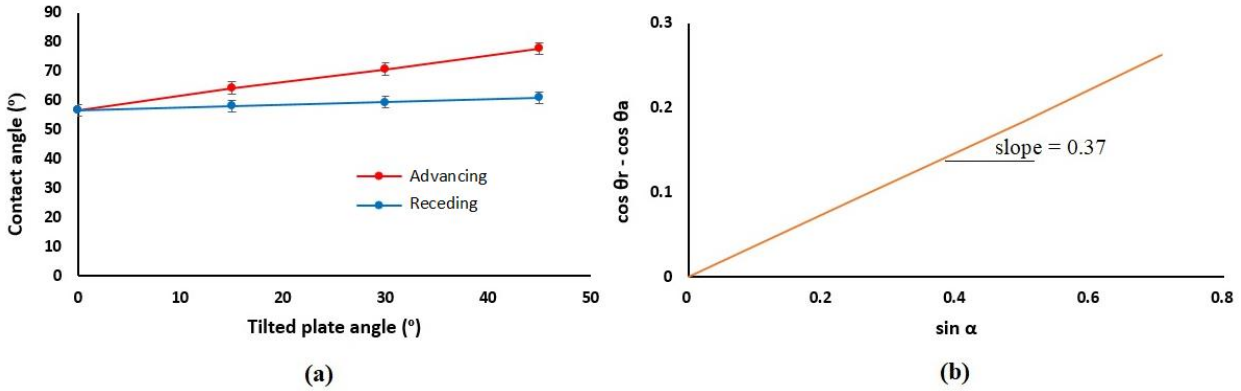

Fig. 4-5 Effect of tilting plate angle on calcite/H_2/DI-water contact angle at 323 K and 10 MPa.

4.3.7 Effect of surface roughness

The surface roughness affects wetting behavior within reservoir rocks/caprocks and hence controls the parameters relevant to the hydrogen storage and recovery processes such as the fluid flow pattern, the geometry of displacement front in H_2/brine displacement process, and the capillary

trapping efficiency (Sari et al., 2020, Morrow, 1975, Zulfiqar et al., 2020). To study the variation of θ with surface roughness, three pure calcite substrates with different surface roughness values (RMS = 341, 466, 588 nm) were selected. Fig. 4-6 shows the AFM images (2D and 3D) from the surfaces of these three samples. Both θ_a and θ_r smoothly decreased with RMS roughness value at 323 K and 15 MPa in DI water (Fig. 4-7). For instance, for 341 nm roughness surface, θ_a and θ_r were 69.8° and was 63.35°, respectively. However, for 588 nm roughness surface, θ_a and θ_r decreased to 64.6° and 55.4°. The decrease in water contact angle with surface roughness is consistent with brine/CO_2/quartz (Al-Yaseri et al., 2016) and brine/CO_2/calcite (Arif et al., 2017a), implying that smooth surfaces are less water-wet than rougher surfaces. This can be explained by Wenzel's equation which is expressed as follows (Wenzel, 1936):

$$\cos\theta_{rough} = r\cos\theta_{smooth}, \tag{4.2}$$

where θ_{rough} is the actual θ measured on the rough surface, θ_{smooth} is the ideal θ measured on the 100% mathematically smooth surface, and r is the roughness ratio between the ideal and actual surfaces. For ideal and rough surfaces, $r = 1$ and $r > 1$, respectively (Al-Yaseri et al., 2016). This effect is due to liquid penetrating into the grooves on the surface (Marmur, 2006, Swain and Lipowsky, 1998). Therefore, adding surface roughness will raise the wettability caused by the surface chemistry, although other surface factors such as surface shape, energy dissipation, and adsorption/desorption may also affect the wettability.

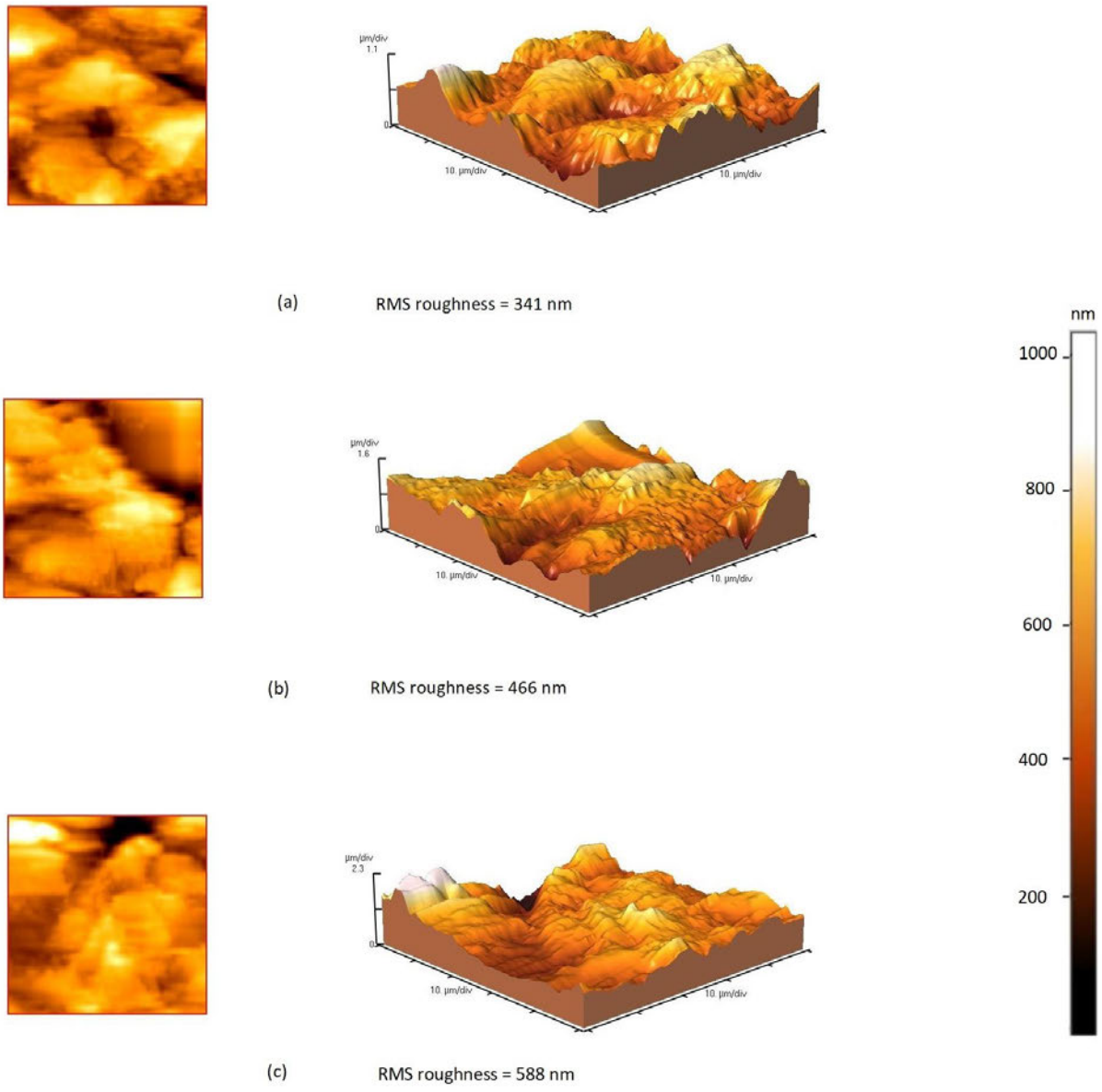

Fig. 4-6 Atomic force microscope (AFM) images from the surfaces of three different calcite substrates investigated (a, b, and c): 2D (left) and 3D (right).

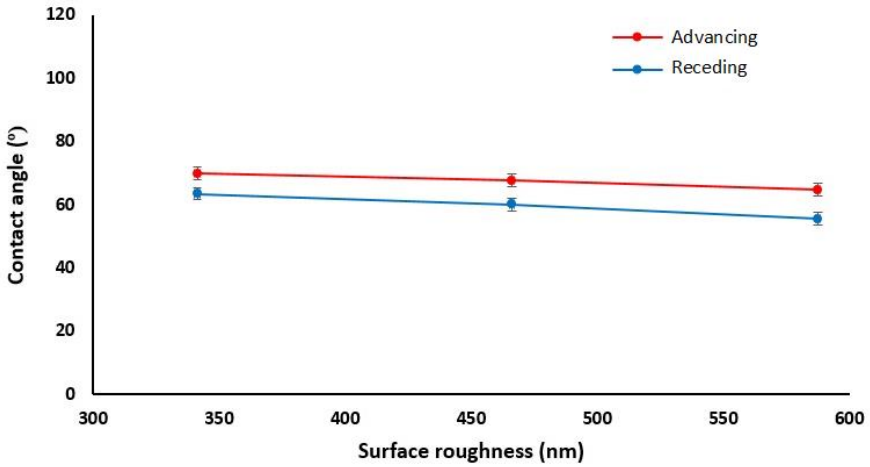

Fig. 4-7 Variation of calcite/H_2/DI-water contact angle with surface roughness at 323 K and 15 MPa.

4.4 Implications

Wettability is helpful for the interpretation of pore-scale flow dynamics (e.g. imbibition process by θ_r), residual H_2 saturation for residual trapping (e.g. by θ_a) and relative permeability-saturation relationships. For example, increasing H_2-relative permeability with temperature at a constant water saturation implies that the system becomes water-wet with temperature. Calcite, serving as a representative mineral for carbonates, is prevalent in both caprock and reservoir rock (Haldar, 2020, Tonnet et al., 2011, Trueman et al., 2019). Thus, wettability characterization of calcite is crucial for H_2 geo-storage capacity assessments in carbonates as it strongly influences both the structural trapping (in case of a calcite-rich caprock) and residual trapping (in case of a calcite-rich reservoir rock, e.g. (Arif et al., 2016a, Arif et al., 2016d, Iglauer et al., 2015a, Iglauer et al., 2015b, Rahman et al., 2016)). For example, an H_2-wet calcite-rich rock results in low structural trapping capacity (as upward suction force is made, which leads to leakage through the caprock, e.g. (Iglauer et al., 2015a, Iglauer et al., 2015b)) and residual trapping capacity (as an advancing wetting phase cannot residually trap the non-wetting phase, e.g. (Krevor et al., 2015)). However, when the calcite-rich reservoir rock is H_2-wet, high structural storage capacity is expected as most of the pore volumes are occupied by H_2, making a thicker H_2 column. In this study, no H_2-wet state was observed for chemically clean calcite surface at various temperatures (298-353 K) and pressures (0.1-20 MPa). However, we found a diverse wetting behavior (intermediate wet changed

to weakly H_2-wet), when the concentration of stearic acid on calcite surface reached 10^{-2} mol/L (which simulates a real deep aquifer, e.g. (Akob et al., 2015, Lundegard and Kharaka, 1994, Stalker et al., 2013)) at 323 K and 10 MPa. Under such conditions, capillary leakage of H_2 will result in a significant reduction in structural storage (in case of a calcite-rich caprock), and reduced residual trapping (in case of a calcite-rich reservoir rock, although high structural storage capacity is expected due to a thicker H_2 column). Therefore, a precise knowledge of storage conditions such as organic acid concentration is essential for safe and effective H_2 geological storage in carbonate formations. However, it should be noted that the current data applies for calcite-rich carbonate formations, and that we investigated the salinity effect with only one brine (composed of monovalent ions) as well as the organic surface effect with only one organic acid (stearic acid). Therefore, to acquire better insights on the wettability of carbonate formations, consideration of a wide range of carbonate mineralogy, organic acids, and brines (especially those composed of divalent ions) can be helpful. The contact angle measurements in this study mainly reflect in-situ surface chemistry. Considering the cyclic nature of UHS procedures involving both hydrogen imbibition and drainage, wettability for both phases is crucial. The presented data is exclusive to in-situ conditions representative of hydrogen storage in carbonate reservoirs. Thus, conducting hydrogen core flooding experiments on carbonates is recommended to capture dynamic wettability during both storage and extraction processes, contributing to predicting wetting transitions and interface stability throughout the carbonates. It is also notable that the analysis of critical point pressure (1.3 MPa) was omitted because it lacks relevance for UHS under HPHT conditions. Additionally, the experiment was conducted at ambient conditions to supplement the trend analysis. At ambient conditions, as depicted in the Fig. 4-1, hydrogen is in a gaseous state and exhibits a strongly water-wet characteristic. As pressure increases and transitions into the supercritical state, hydrogen wettability also intensifies. Consequently, it is anticipated that the wettability at the critical pressure should align with the observed variation.

4.5 Conclusions

The wettability of rock is a key parameter that regulates the spread of gas (H_2 in this case) in a formation (Al-Khdheeawi et al., 2017a, Al-Khdheeawi et al., 2017b). It determines the gas flow rates (during injection (Arif et al., 2016c, Iglauer, 2017) and withdrawal (Al-Yaseri and Jha, 2021,

Ali et al., 2021c, Iglauer et al., 2021b, Jha et al., 2021) steps), fluid-flow behavior (Iglauer, 2017, Iglauer et al., 2015a), and storage capacity (Arif et al., 2017a, Iglauer et al., 2015a, Iglauer et al., 2015b) and reduces the uncertainty (Ali et al., 2021a, Jha et al., 2019, Jha et al., 2020). Thus a true understanding of different parameters affecting wetting characteristics (e.g. pressure, temperature, salinity, organic surface contamination, fluids equilibration, tilted plate angle, and surface roughness) is crucial from a safe and economic H_2 storage perspective (Akob et al., 2015, Al-Yaseri and Jha, 2021, Ali et al., 2021c, Caballero et al., 2003, Iglauer et al., 2021a, Iglauer et al., 2021b, Jha et al., 2021, Lundegard and Kharaka, 1994, Stalker et al., 2013). However, literature data lacks in term of the influence of various parameters on the H_2-wettability of carbonates and the relevant structural (in case of a calcite-rich reservoir rock) and residual (in case of a calcite-rich caprock) storage capacities as the investigation of the feasibility of hydrogen geo-storage from the wettability perspective is a new field of research that should be assessed carefully. Therefore, we measured the H_2-wettability of calcite using the tilted plate method and examined the effect of different parameters on the wettability.

Our results depict that at ambient conditions, the calcite/H_2/water system was extremely water-wet which became intermediate wet at higher physio-thermal conditions. The clear decrease in both advancing and receding θ with temperature suggests that low-temperature carbonate rocks have less water wettability than high-temperature carbonate rocks. Moreover, θ slightly increased with salinity but decreased with surface roughness. The effect of the tilting plate angle was insignificant for θ_a and θ_r. Furthermore, the water contact angle strongly increased with stearic acid concentration, making the calcite surface H_2-wet at 10 MPa and 323 K.

We conclude that the optimum conditions for de-risking H_2 storage projects in carbonates are low pressures, high temperatures, low salinity, and low organic surface concentration, although intermediate wettability at low organic surface concentration does not still guarantee safe storage. A comparison between this work and previously published works on brine/H_2/quartz (Iglauer et al., 2021b) and brine/H_2/mica (Ali et al., 2021d) shows that at realistic conditions calcite-rich formations have a higher risk than other formations for H_2 storage projects. Therefore, to have successful H_2 geo-storage projects, it is necessary to gauge the influencing parameters. Results of this study significantly provide a fundamental comprehension of the factors responsible for hydrogen wettability variation in carbonate formations.

Chapter 5 Capillary-sealing efficiency analysis of caprocks: Implication for hydrogen geological storage

Published in *Energy & Fuels*, ACS Publications 2022, 36, 7, 4065–4075
DOI: https://doi.org/10.1021/acs.energyfuels.2c00281

Abstract

In hydrogen geological storage, capillary sealing efficiency analysis of caprocks is very important for containment security. In this work, the H_2 wettability of three shales and one evaporite under various pressures (0.1, 5, 10, 15 and 20 MPa), temperatures (298 and 353 K), and organic acid concentrations (10^{-9} - 10^{-2} mol/L) were measured using the tilted plate method and their effects on the capillary sealing efficiency of the caprocks were analyzed. Furthermore, two oil shales were tested to see the effect of their total organic content (TOC) on the wettability at two different pressure (5 and 15 MPa) and temperature (323 and 353 K) values, since the TOC dramatically varies in shales and can significantly influence the wetting characteristics, thus, the sealing efficiency. The results of this study indicate that the H_2 wettability of the caprocks increased with pressure, organic acid concentration and TOC but decreased with temperature. However, the sealing efficiency and H_2 column height of the caprocks decreased with all the varying parameters but increased with temperature for oil shales. Furthermore, small pore sizes (i.e. r = 5 nm as a typical value for this study) and evaporites (e.g. gypsum) have the most efficient conditions for sealing for increased storage capacity. Overall, this work provides a deep understanding of the sealing efficiency of caprocks, which will aid in the successful implementation of hydrogen geo-storage and its associated structural trapping capacities.

Keywords

Capillary-sealing efficiency, H_2 wettability, H_2 geo-storage, capillary entry pressure, H_2 column height, caprocks

5.1 Introduction

In the geological context, caprock is defined as an impermeable layer (seal formation) overlying a permeable (e.g. reservoir) rock, which traps fluids such as oil, water and gas thus preventing them from upward migration (Haldar, 2020, Wollenweber et al., 2009). Shales and evaporites are two common types of caprock due to their low permeability (< 10^{-21} m^2) and porosity in sedimentary basins (Aplin et al., 2006, Hangx et al., 2011, Hangx et al., 2010, Ma et al., 2018). Shale, as the most common sedimentary rock (Okeke and Okogbue, 2011), can also be identified as unconventional source rock (e.g. oil/gas shales) (Law and Curtis, 2002, Yu et al., 2018, Li et al., 2019a, Li et al., 2021, Memon et al., 2021, Memon et al., 2020, Li et al., 2019b), a geothermal energy resource (Dickson and Fanelli, 2013) and storage site for different gases such as CH_4, CO_2, and H_2 (Arif et al., 2017b, Busch et al., 2008, Kang et al., 2011, Ali et al., 2022c) and nuclear wastes (Mallants et al., 2001). Anhydrite or anhydrous calcium sulfate ($CaSO_4$) and gypsum ($CaSO_4.2H_2O$) are evaporite minerals formed by the evaporation of a huge volume of seawater, abundantly found in sedimentary basins in the form of interbedded layers often along with limestone and halite (Haldar, 2020). When exposed to water, anhydrite converts to gypsum ($CaSO_4.2H_2O$) (Templeton and Rodgers, 1967). Thus, the characterization of caprock is crucial for the sealing efficiency for gas storage in geological formations (Hildenbrand and Krooss, 2003, Carles et al., 2010, Fleury et al., 2010, Shukla et al., 2010).

In this context, hydrogen geo-storage is a highly promising way to achieve a large-scale hydrogen economy that mitigates greenhouse gas emissions caused by burning fossil fuels and meets global energy demand (Tarkowski, 2019, Zivar et al., 2021, Mohanty et al., 2021). The key influencing parameters on the capillary sealing efficiency of the caprocks are the interface, pore and wetting characteristics of the rock/H_2/water system. The small pore throat radius of caprocks implies that a very high capillary entry pressure is needed for gas penetration in the pore (Al-Bazali et al., 2005, Li et al., 2005). The Laplace equation for capillary pressure is given as follows:

$$P_c = \frac{2\gamma \cos\theta}{r}, \tag{5.1}$$

where γ is the interfacial tension between gas and water, θ is the receding contact angle which determines the wettability of the rock/gas/water system, and r is the pore throat radius of the caprock. Thus, the capillary sealing efficiency of a caprock which depends on caprock/gas/brine

wettability provides a better understanding of the structural storage and successful long-term containment safety such as when caprock is water-wet (Law and Curtis, 2002, Tarkowski, 2019, Yu et al., 2018).

While there have been frequent studies on the CO_2 wettability of caprock such as shale (Arif et al., 2017b, Borysenko et al., 2009, Guiltinan et al., 2017, Pan et al., 2018, Iglauer et al., 2015a), only a few studies have investigated the H_2 wettability of caprocks under geological conditions. For example, (Ali et al., 2021d, Ali et al., 2022c) studied the H_2 wettability of mica at pressures up to 25 MPa, temperatures up to 343 K, and organic acid concentrations of 10^{-9} - 10^{-2} mol/L, however, the mineral used in these studies is not fully representative of the real geological formation. Also, (Al-Yaseri et al., 2021c) used empirical correlations to mathematically derive and interpret the hydrogen wettability of kaolinite, illite, and montmorillonite at pressures up to 20 MPa and T = 333 K. These works studied the wettability of a caprock consisting of only one mineral as a benchmark. However, a caprock may consist of various minerals. For example, shale may constitute of clay, feldspar, quartz, calcite, etc. (Arif et al., 2017b, Arif et al., 2021). Moreover, there is a clear lack of data on the effect of TOC on the hydrogen wettability of shales as TOC and organic acids can strongly affect the wetting characteristics of caprocks (Arif et al., 2017b, Guiltinan et al., 2017, Pan et al., 2018, Pan et al., 2020b, Yekeen et al., 2021). There is also no study on the hydrogen wettability of evaporites in the literature.

Here, we measured the H_2-wettability of different caprock samples using the tilted plate method and analyzed the effect of different parameters, including pressure, temperature, organic acid concentration, and TOC on the wettability and capillary sealing efficiency of the caprocks. This work provides fundamental data for understanding the wetting characteristics, sealing efficiency of caprock and containment security issues, which are critical for underground hydrogen storage (UHS).

5.2 Experimental Procedure

5.2.1 Materials and preparation

Three clean shales (with very low TOCs of 0.08, 0.1 and 0.09 wt %), two oil shales (with medium TOC of 4.95 wt % and high TOC of 14 wt %), and one clean evaporite sample (with very low

TOC of 0.01 wt %) were analyzed as listed in Table 5-1. The rocks were cut into 1 cm × 1 cm × 0.4 cm dimensions and their surfaces were uniformly polished to minimize the surface roughness effects on the contact angle measurements. Our previous study on calcite/H_2/water (Hosseini et al., 2022e) showed a smooth variation of the contact angle with surface roughness as it is widely reported in the wettability studies that surface roughness less than 1 micro meter does not have any significant impact on the contact angles (Al-Yaseri et al., 2016, Marmur, 2006). H_2 gas (99.9 mol%) and 1.05 M brine (0.864 mole fraction NaCl + 0.136 mole fraction KCl) prepared by mixing the salts (purities of NaCl and KCl ≥ 0.99 mole fraction) with deionized water (electrical conductivity = 0.02 $mS.cm^{-1}$) were used for the experiments. To clean contaminants from the mineral surface, we firstly washed the samples with deionized water (Ali et al., 2021b). Then, ultra-pure nitrogen (99.9 mol%) was used to wipe off the water film from the surfaces, which were then dried in an oven at 338 K for 60 minutes (Ali et al., 2020a). Finally, to remove the residual organic contaminants, the samples were placed in an air plasma cleaner for 15 min (Iglauer et al., 2014, Ali et al., 2020a). To simulate real geological samples exposed to formation fluid over geological times, stearic acid (purity ≥ 0.99-mole fraction) was applied for the aging of caprock samples with very low TOC values based on the following strategy conducted in four steps (Davis, 1982, Kleber et al., 2015, Ulrich et al., 1988, Zullig and Morse, 1988, Ali et al., 2021a): a) ionizing the surfaces by immersing in rock-equilibrated 2 wt % NaCl brine for 30 min at ambient conditions (Ali et al., 2021a), b) maintaining the acidity of the brine at pH = 4 by adding droplets of aqueous hydrochloric acid (HCl concentration = 37.5 vol%) and increasing the adsorption rate of stearic acid onto the rock surface (Al-Anssari et al., 2020, Jardine et al., 1989, Madsen and Ida, 1998), c) cleaning the remaining water from the rock surface using ultra-pure nitrogen to remove contaminants, and d) aging the substrates in toluene/stearic acid solutions (highly diluted stearic acid concentrations of 10^{-2}, 10^{-3}, 10^{-5}, 10^{-7} and 10^{-9} mol/L) for a week (Ali et al., 2022c).

5.2.2 Contact angle measurements

The wetting properties of a rock/fluid system can be quantitatively assessed through the contact angle test (Chiquet et al., 2007). To simultaneously measure both receding and advancing contact angles, accounting for the hysteresis effect, we utilized a tilted plate within a high-pressure, high-temperature optical cell, with a maximum working pressure and temperature of 40 MPa and 433

K, respectively (Lander et al., 1993). The sample (clean or aged) was then placed on the tilted plate with an angle of 15º inside the optical cell at the desired temperature. Subsequently, the optical cell was pressurized with H_2 gas. A droplet of brine (average volume of 5 μL ± 1 μL) was then dispensed onto the caprock surface by a needle (outer diameter of 1.5875 mm) mounted vertically on the cell's ceiling. The receding (θ_r) and advancing (θ_a) contact angles were measured at the trailing and the leading edge of the droplet, respectively, just before the droplet's movement (Lander et al., 1993). A dino-light camera with a resolution of 1280 × 1024 (1.3 MP) was used to record high-quality images of the droplets, which were then used for determining the corresponding θ_a and θ_r angles using ImageJ software. Fig. 5-1 is a schematic of the experimental setup. At a specific pressure and temperature, the contact angles did not considerably change during the first 300 s as H_2 and brine were thermodynamically equilibrated before the measurements to minimize dissolution effects.

In this study, the H_2 wettability of caprocks was analyzed with different parameters. The effects of pressure and temperature were investigated at five pressure (0.1, 5, 10, 15 and 20 MPa) and two temperatures (298 and 353 K) values. The effect of organic acid concentration in the range of 10^{-9} - 10^{-2} mol/L on the H_2 wettability of caprocks was assessed at T = 323 K and p = 15 MPa. Two oil shales with medium-TOC of 4.95 wt % and high-TOC of 14 wt % were also measured to assess the effect of TOC on the H_2 wettability at two pressure (5 and 15 MPa) and two temperature (323 and 353 K) values. Every measurement at a single point was repeated thrice from which the average value was computed and reported here. The standard deviation of the measurements was ± 3º.

Table 5-1 Rock samples analyzed.

Rock sample	Composition from XRD		TOC (wt %)
	Mineral	wt %	
Shale A	Quartz	28	0.08
	Dolomite	3	
	Calcite	58	
	Muscovite-illite	8	
	Chlorite	2	
	Hematite	1	
Shale B	Quartz	30	0.1
	Kaolinite	7	
	Siderite	6	
	Muscovite-illite	33	
	Chlorite	16	
	Anatase	1	
	Albite	4	
	Potassium feldspar	1	
	Goethite	2	
Shale C	Quartz	25	0.09
	Chlorite	20	
	Siderite	2	
	Muscovite-illite	27	
	Amorphous	10	
	Anatase	1	
	Albite	10	
	Smectite Group	5	
Evaporite	Anhydrite	1	0.01
	Gypsum	99	
Oil shale A	Pyrite	6	4.95
	Calcite	28	
	Dolomite	30	
	Quartz	12	
	Potassium feldspar	4	
	Illite	15	
	Amorphous	5	
Oil shale B	Pyrite	3	14
	Calcite	56	
	Dolomite	3	
	Quartz	9	
	Potassium feldspar	4	
	Gypsum	1	
	Amorphous	20	
	Clay mineral	4	

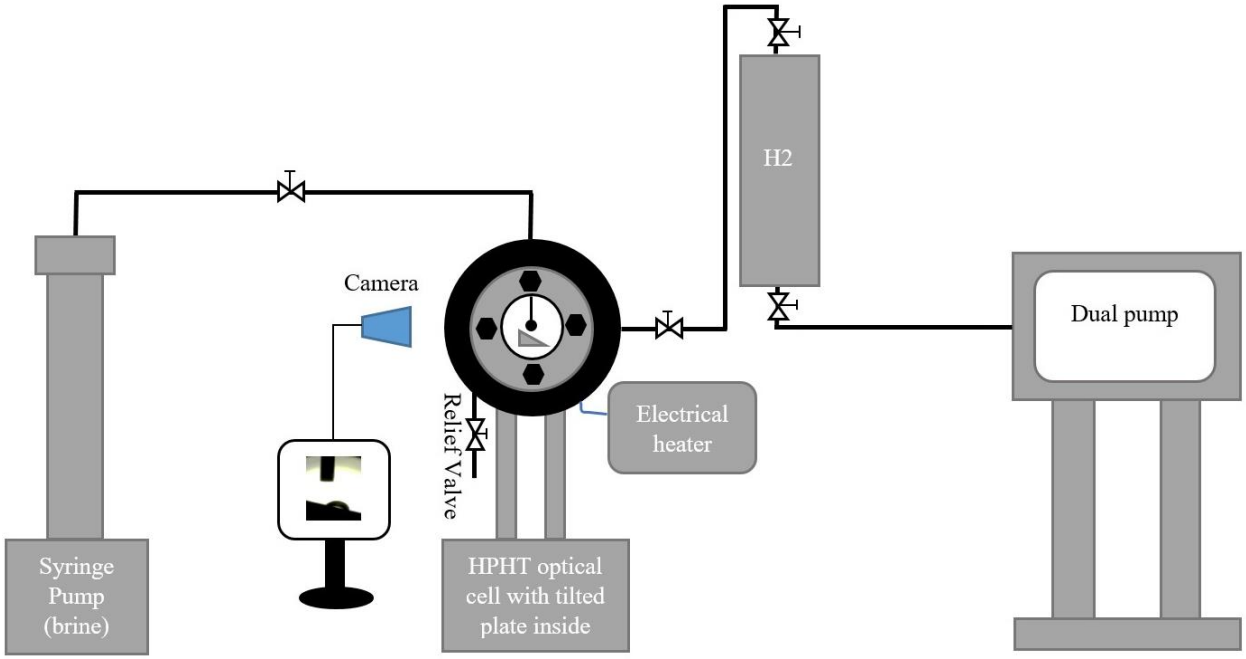

Fig. 5-1 Schematic of the high pressure-high temperature (HPHT) experimental setup for contact angle measurements.

5.3 Results and discussion

The capillary entry pressure (p_{ce}) is the minimum capillary pressure that is required for hydrogen to penetrate the largest pore throat of a caprock (Iglauer et al., 2015b). Thus, it is a critical parameter for the sealing efficiency of the caprock and the successful structural storage of hydrogen (Al-Bazali et al., 2005, Espinoza and Santamarina, 2017, Rezaeyan et al., 2015). Here, we therefore discuss the effect of various geological conditions such as pressure, temperature, organic acid concentration, and TOC on the wettability and capillary sealing efficiency of caprocks. The capillary sealing efficiency was computed for caprocks with two typical pore throat radius values of 10 and 5 nm (Armitage et al., 2010, Espinoza and Santamarina, 2017, Watson et al., 2005). Also, data for γ was taken from (Hosseini et al., 2022d), while wettability data was measured for the various caprock samples.

5.3.1 Effect of pressure and temperature on H_2-wettability and capillary sealing efficiency

The advancing (θ_a) and receding (θ_r) contact angles increased with pressure for all the caprocks (that is, a decrease in water wettability at the constant temperatures of 298 and 353 K) as shown in Fig. 5-2, which is in close agreement with the results in the literature for hydrogen (Ali et al., 2021d, Al-Yaseri et al., 2021c). For instance, θ_r for shale A increased from 0º (high water wettability) at ambient conditions of 298 K and 0.1 MPa to 41.8º (low water wettability) at 298 K and 20 MPa. However, at the same temperature and pressure conditions, θ_r for evaporite sample had a lower increase from 0º to 13.15º. This is because the intermolecular forces between gas and rock increase with pressure (Iglauer et al., 2012). However, both θ_a and θ_r contact angles showed a decrease with temperature for all the caprocks (that is, an increase in water wettability, see Fig. 5-2), consistent with (Ali et al., 2021d). For instance, at 20 MPa, θ_r for shale A decreased from 41.8° to 27.59° as the temperature increased from 298 K to 353 K, respectively. However, under the same temperature and pressure conditions, θ_r for the evaporite sample showed a smaller decrease from 13.15º to 9.44º. The decrease in water contact angles with temperature is attributed to the decreased intermolecular forces and interfacial energy between gas and rock (Arif et al., 2017a). It is worth mentioning that the examination of the critical point pressure (1.3 MPa) was excluded as it is not pertinent to UHS in HPHT conditions. Nonetheless, there is an expectation that the wettability at the critical pressure should correspond with the observed variation.

At both temperatures of 298 and 353 K, p_{ce} decreased with pressure for the caprocks as shown in Fig. 5-3. For instance, p_{ce} for shale A with a typical pore size of r = 10 nm at T = 353 K decreased from 12.40 MPa to 11.08 MPa when the pressure increased from 5 MPa to 20 MPa, implying a decrease in capillary sealing efficiency of the shale with pressure. Furthermore, at the same pore size, temperature, and pressure increase, the p_{ce} for the evaporite sample slightly decreased from 12.74 MPa to 12.33 MPa. This decrease can be attributed to the decrease in γ and water wettability with pressure at a constant temperature. However, p_{ce} for all the caprocks showed a decrease with temperature as shown in Fig. 5-3. For instance, at 10 MPa and r = 10 nm, p_{ce} for shale C decreased from 14.38 MPa to 12.50 MPa when the temperature increased from 298 K to 353 K, implying a decrease in capillary sealing efficiency of the shale with temperature. At the same pore size, pressure, and temperature increase, the decrease in p_{ce} for the evaporite sample was very close to shale C (14.58 MPa to 12.61 MPa). Although both γ and θ decreased with temperature, γ was more

effective than θ (decrease in $\gamma\cos\theta$), leading to a decrease in p_{ce} with temperature. For instance, at 10 MPa and r = 10 nm for shale C, γ decreased from 74.26 mN/m to 63.54 mN/m and cos θ increased from 0.968 to 0.983, leading to a decrease in $\gamma\cos\theta$ from 71.88 mN/m to 62.46 mN/m thus decrease in p_{ce}.

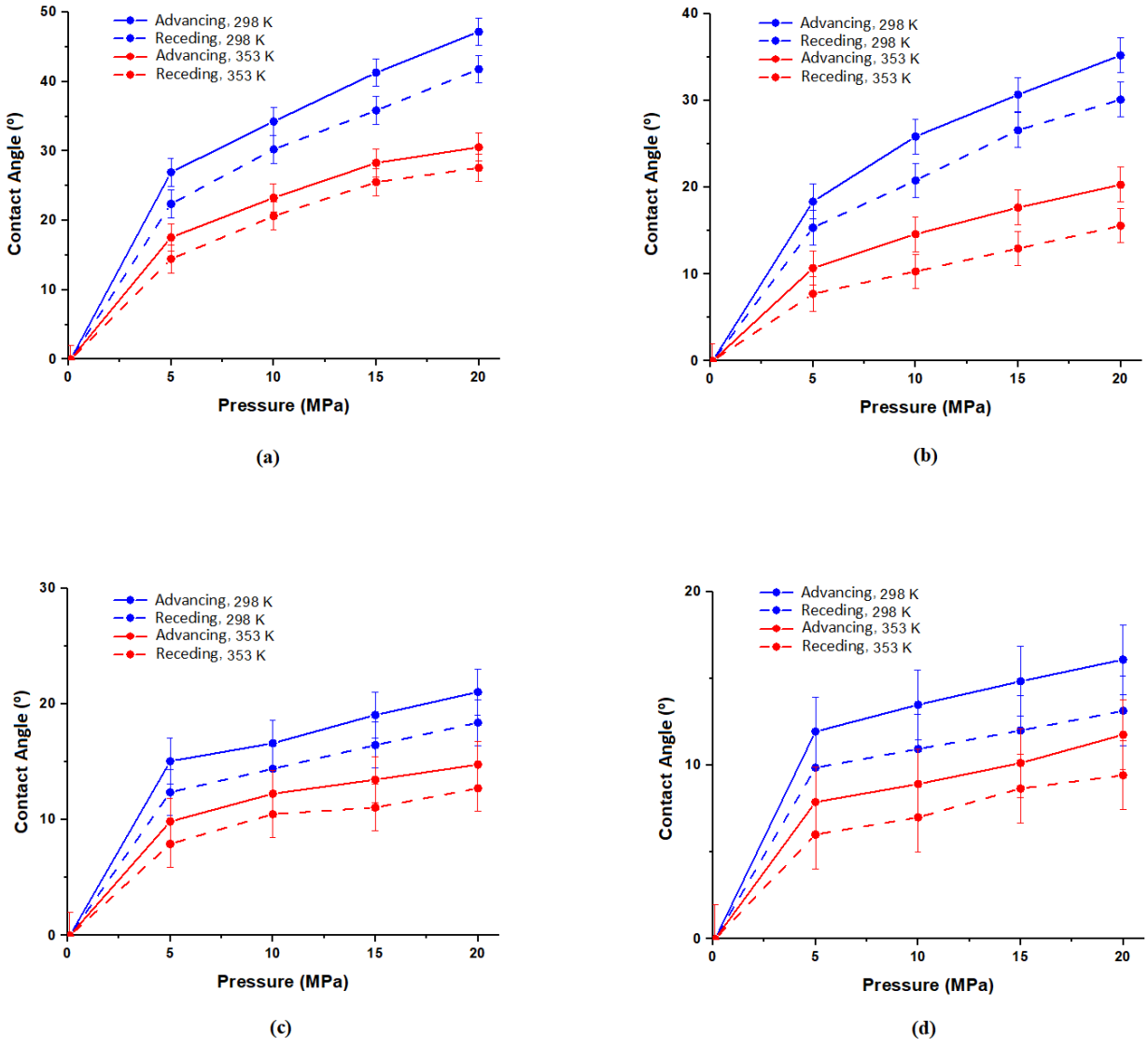

Fig. 5-2 Caprock/H_2/brine contact angles at two different temperatures as a function of pressure: (a) shale A, (b) shale B, (c) shale C, and (d) evaporite sample.

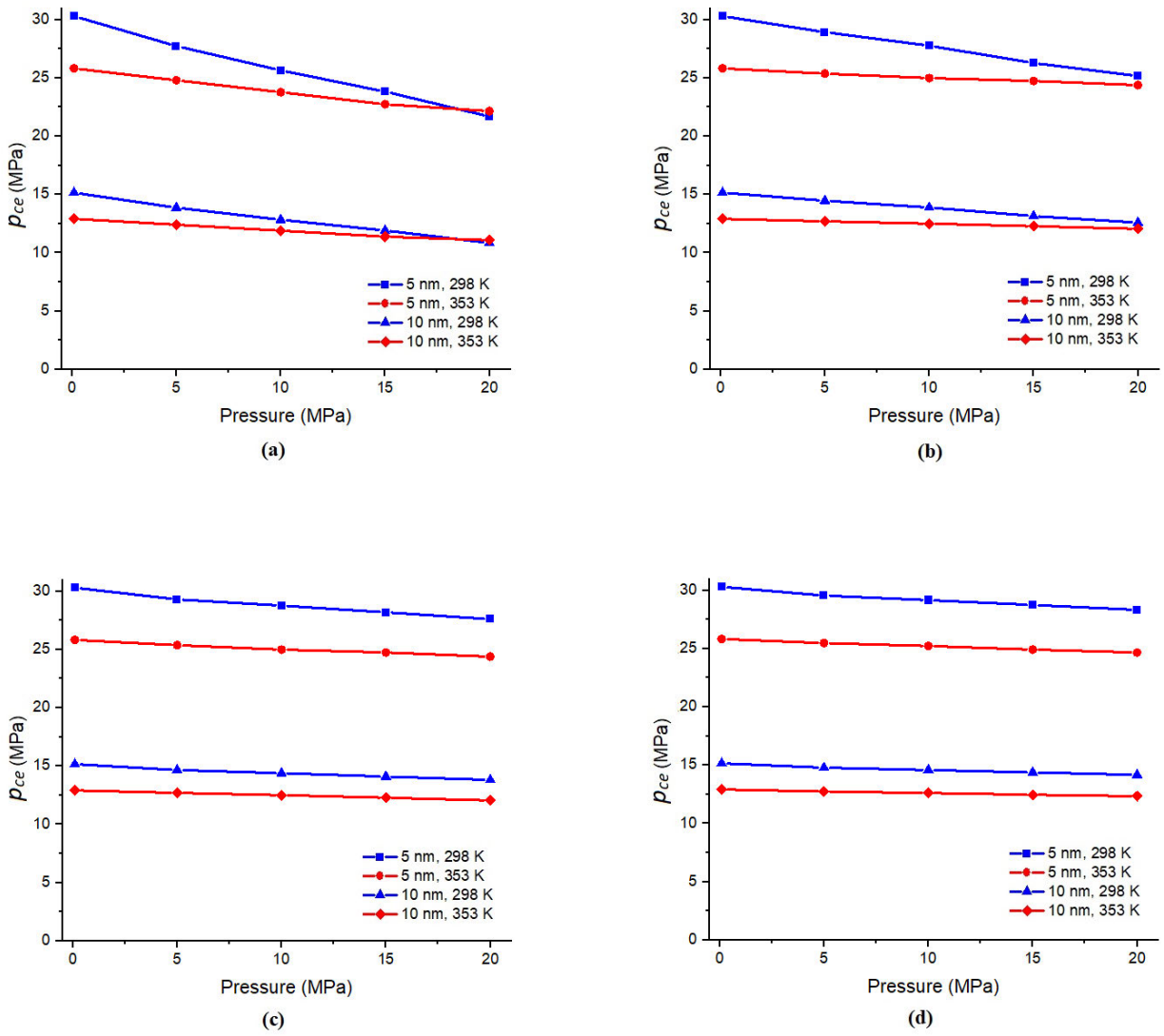

Fig. 5-3 Capillary entry pressure as a function of pressure for two typical pore sizes at two different temperatures: (a) shale A, (b) shale B, (c) shale C, and (d) evaporite sample.

5.3.2 Effect of organic acid concentration and TOC on H_2-wettability and capillary sealing efficiency

It is widely reported in the literature that geological formations including caprocks have organic molecules in their structure which can significantly affect the wetting characteristics (Arif et al., 2017b, Stalker et al., 2013, Lundegard and Kharaka, 1994, Akob et al., 2015, Ali et al., 2022c).

Therefore, we analyzed the effect of organic acid concentration (for clean caprocks) and TOC (for oil shales) on the wettability and capillary sealing efficiency of the caprocks.

For all the aged caprocks tested, both θ_a and θ_r increased with stearic acid concentration (that is, a decrease in water wettability, see Fig. 5-4), consistent with (Ali et al., 2021d). For instance, at 15 MPa and 323 K, θ_r for shale A increased from 34.94º (low wettability) to 69.51º (intermediate wettability) when the concentration of stearic acid rose from 10^{-9} mol/L to 10^{-2} mol/L. However, at the same temperature and pressure and increase in organic acid concentration, θ_r for the evaporite sample showed a lower increase from 11.81º to 40.57º, implying that it remained weakly water-wet. This decrease in water wettability is attributed to the increased hydrophobicity of the rock surface (surface de-wetting) induced by organic acid adsorption (Abramov et al., 2019). The effect of TOC on the wettability at the three pressure and temperature conditions of 5 MPa and 323 K, 15 MPa and 323 K, and 15 MPa and 353 K, were also measured. Both θ_a and θ_r under these conditions increased with TOC (that is, showed a decrease in water wettability, see Fig. 5-5), consistent with (Arif et al., 2017b, Guiltinan et al., 2017, Pan et al., 2018, Pan et al., 2020b). For instance, at 15 MPa and 323 K, θ_r increased from 31.77º (low wettability) to 82.4º (intermediate wettability), when the TOC increased from 0.09 wt % to 14 wt %, respectively. This decrease in water wettability can also be attributed to the increased hydrophobicity of the rock surface (surface de-wetting) induced by the high organic content of the oil shales (Arif et al., 2017b). Fig. 5-5 also shows an increase in water wettability with temperature and a decrease in water wettability with pressure, implying that the effect of TOC on wettability depends on the formation pressure and temperature.

At 15 MPa and 323 K, p_{ce} decreased with stearic acid concentration for the caprocks (for both the typical pores sizes) as shown in Fig. 5-6. For instance, p_{ce} for shale A with a typical pore size of r = 5 nm decreased from 22.54 MPa to 9.62 MPa when the stearic acid concentration increased from 10^{-9} mol/L to 10^{-2} mol/L, respectively, implying a decrease in capillary sealing efficiency of the shale with stearic acid concentration. At the same typical pore size and increase in the stearic acid concentration, the p_{ce} for the evaporite sample slightly decreased from 26.91 MPa to 20.89 MPa. Also, p_{ce} decreased with TOC (for both the typical pores sizes) as shown in Fig. 5-7. For instance, at 15 MPa and 323 K, p_{ce} for the caprock with a typical pore size of r = 5 nm decreased from 23.38 MPa to 3.64 MPa when the TOC increased from 0.09 wt % to 14 wt %, respectively. These

decreases in p_{ce} can be attributed to the decrease in water wettability with stearic acid concentration and TOC at constant pressure and temperature (γ remains constant).

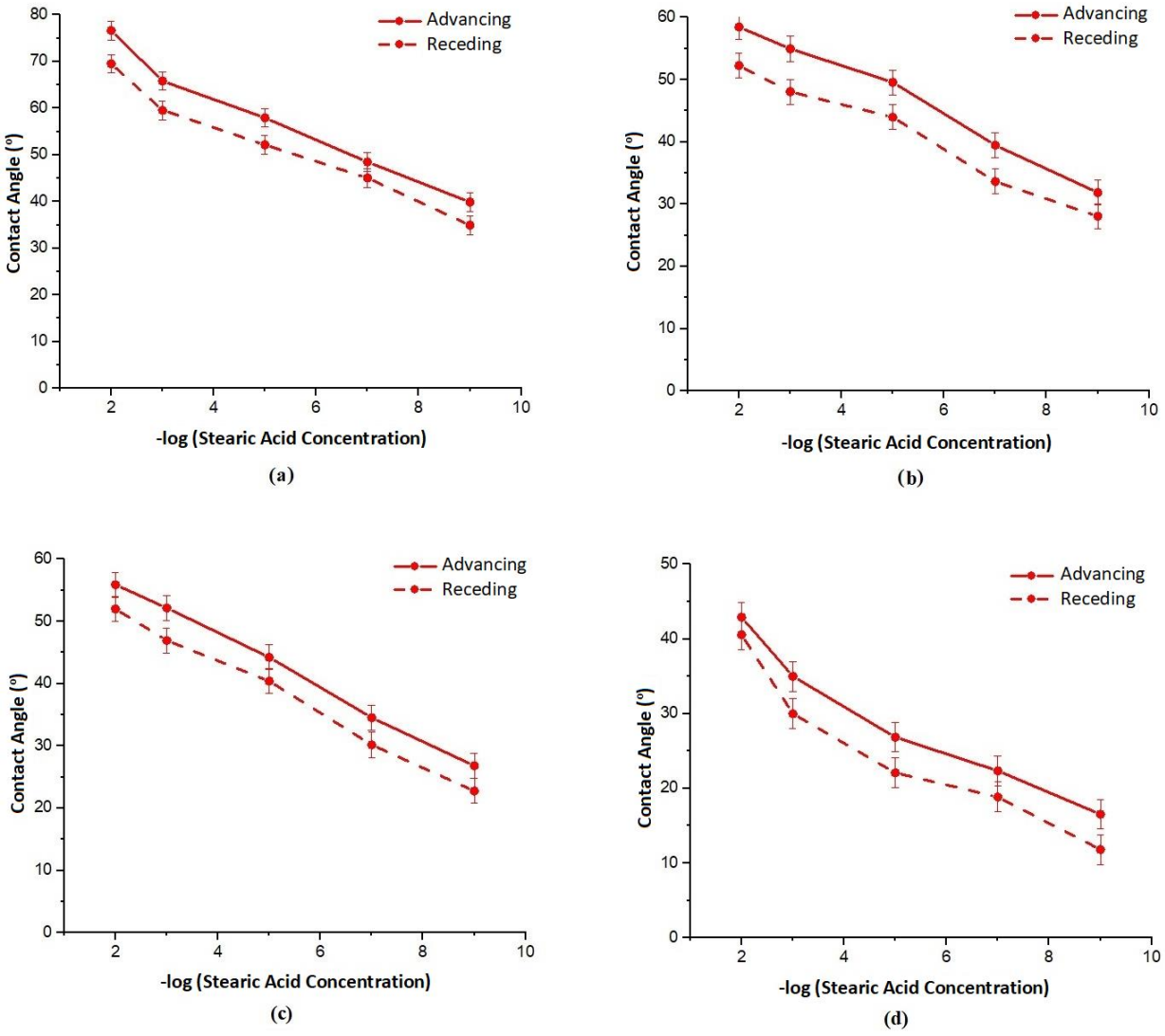

Fig. 5-4 Effect of organic acid concentration on brine/H_2/caprock contact angle at 15 MPa and 323 K: (a) shale A, (b) shale B, (c) shale C, and (d) evaporite sample.

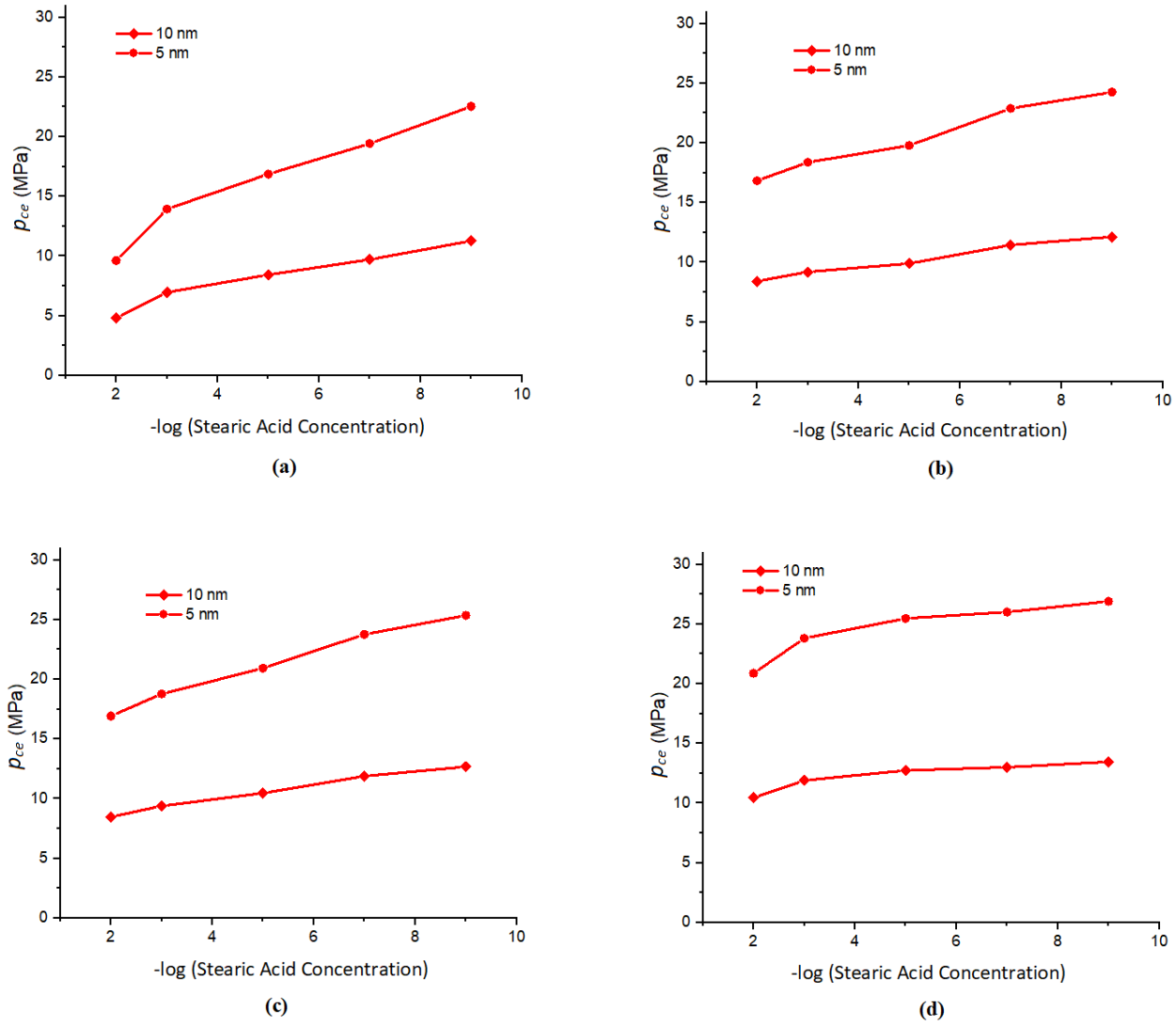

Fig. 5-5 Capillary entry pressure as a function of stearic acid concentration for two typical pore sizes at 323 K and 15 MPa: (a) shale A, (b) shale B, (c) shale C, and (d) evaporite sample.

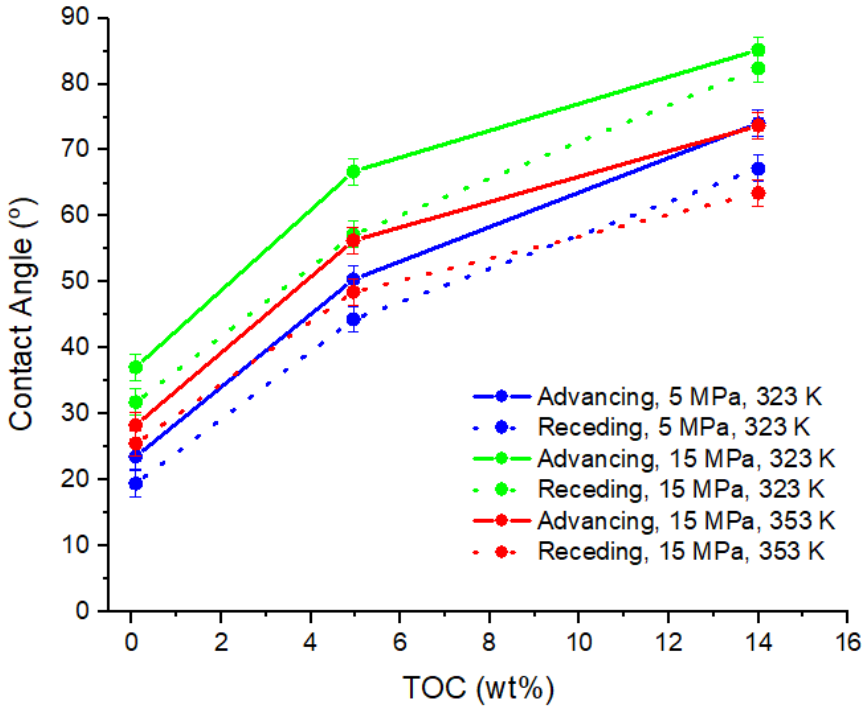

Fig. 5-6 Effect of TOC on oil shale/H_2/brine contact angle as a function of temperature and pressure.

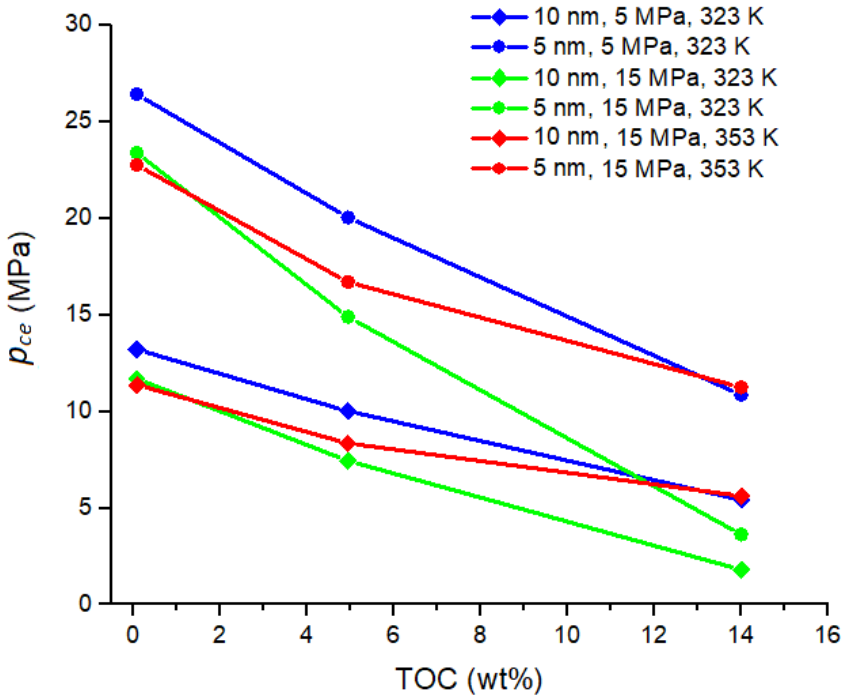

Fig. 5-7 Capillary entry pressure as a function of TOC for two typical pore sizes at two different pressures and temperatures.

5.3.3 Effect of mineralogy on H_2-wettability and capillary sealing efficiency

Hydrogen wettability of pure minerals such as quartz (Iglauer et al., 2021b), mica (Ali et al., 2021d), and calcite (Hosseini et al., 2022e) have been reported in the literature. However, because of the complexity in the mineralogy of caprocks (specifically, shales), their composition should be precisely identified to assess the hydrogen wettability. For example, clays (chlorite, kaolinite, illite), mica (muscovite), calcite, quartz, and feldspars can all be the mineral constituents of shales. Thus, the shale hydrogen wettability can be significantly influenced by the mineral dominance, and this particularly refers to low-TOC shales as the wettability of the high-TOC shales (oil shales) is significantly influenced by their TOC (Arif et al., 2017b). For instance, a high H_2-wetting nature (higher θ) of shale A compared to shale B and shale C is attributed to the calcite dominance (58%, Table 5-1) in the mineralogy due to the high hydrophobicity of the calcite. Also, the higher θ in shale B compared to shale C is attributed to clay + mica dominance in shale B (55% in shale B versus 47% in shale C) (Pan et al., 2020c). Notably, the dominant mineral for shale A and oil shale B is calcite with 58% and 56%, respectively. Thus, these rocks are more H_2-wet than other rocks, and the higher hydrogen wettability of oil shale B compared to shale A is attributed to the remarkable difference in TOC. The evaporite sample which constitutes 99% gypsum has a high water wettability, implying that evaporites have higher capillary sealing efficiency compared to shales.

5.3.4 H_2 column height in caprocks

To evaluate the structural trapping capacity, the maximum gas column height or storage height which can be permanently stored beneath the caprock is predicted using the equilibrium between buoyancy and capillary forces (Iglauer et al., 2015b):

$$h = \frac{P_c}{\Delta\rho g} = \frac{2\gamma \cos\theta_r}{\Delta\rho g r}, \tag{5.2}$$

where $\Delta\rho$ is the density difference between gas and water (taken from (Al Ghafri et al., 2012, Kunz and Wagner, 2012, Leachman et al., 2009, Wagner and Pruß, 2002)) and g is the gravitational acceleration. Figure 5-8 shows the calculated maximum H_2 column height for the mean pore throat radius of r = 1 nm (note: attaining the maximum column height in shale and evaporite caprocks

requires the smallest possible radius for micropores, e.g. (Armitage et al., 2010)) as a function of pressure, temperature, organic acid concentration, and TOC. The column height decreases with pressure and temperature (Fig. 5-8a), implying that lower volumes of H_2 can be stored in the hotter and higher pressure reservoirs due to the decrease in p_c with pressure and temperature. For instance, at 353 K, the H_2 column height for shale A decreased by 1298 m with increasing pressure from 5 MPa to 20 MPa. However, with the same increase in pressure at T = 353 K, the H_2 column height for shale B, shale C, and evaporate sample decreased by 620 m, 459 m, and 372 m, respectively. This implies that the lowest impact of the pressure on the H_2 column height is for the evaporite sample as p_c was reduced by 3 MPa (Fig. 5-3d), while the highest impact is for shale A as p_c was reduced by 8.6 MPa (Fig. 5-3a). Also, the column height decreases for clean caprocks (due to the more effect of γ) but increases for oil shales (due to the more effect of θ) with temperature. For instance, at 10 MPa when temperature increased from 298 K to 353 K for shale C, γ decreased from 74.26 mN/m to 63.54 mN/m, cos θ increased from 0.968 to 0.983 and $\Delta\rho$ decreased from 1035.6 kg/m^3 to 1012.86 kg/m^3, leading to a decrease in $\gamma\cos\theta/\Delta\rho$ from 0.069 mN.m^2/kg to 0.062 mN.m^2/kg thus the decrease in h and implying that lower volumes of H_2 can be stored in the hotter reservoirs with low TOC caprocks (Fig. 5-8a). However, at 15 MPa when temperature increased from 323 K to 353 K for the oil shale with medium TOC (TOC = 4.95 wt %), γ decreased from 68.74 mN/m to 63.03 mN/m, cos θ increased from 0.542 to 0.662 and $\Delta\rho$ decreased from 1024.5 kg/m^3 to 1011.9 kg/m^3, leading to an increase in $\gamma\cos\theta/\Delta\rho$ from 0.036 mN.m^2/kg to 0.041 mN.m^2/kg thus the increase in h and implying that higher volumes of H_2 can be stored in the hotter reservoirs with high TOC caprocks (Fig. 5-8c). Furthermore, the column height decreases with organic acid concentration (Fig. 5-8b) and shale-TOC (Fig. 5-8c), suggesting that caprocks with lower organic acid concentration and TOC may securely trap larger volumes of H_2. For instance, at 15 MPa and 323 K, the H_2 column height for shale A decreased by 6426 m when the concentration of stearic acid increased from 10^{-9} mol/L to 10^{-2} mol/L. However, with the same increase in the organic acid concentration at 15 MPa and 323 K, the H_2 column height for shale B, shale C, and evaporite sample decreased by 3699 m, 4194 m, and 2999 m, respectively. This also implies that the lowest impact of the organic matter on the H_2 column height is for the evaporite sample as p_c was reduced by 6 MPa (Fig. 5-3d), while the highest impact is for shale A as p_c was reduced by 12.9 MPa (Fig. 5-3a). Thus, the results suggest that under varying subsurface conditions, evaporite caprocks can provide higher H_2 storage capacity compared to other caprocks.

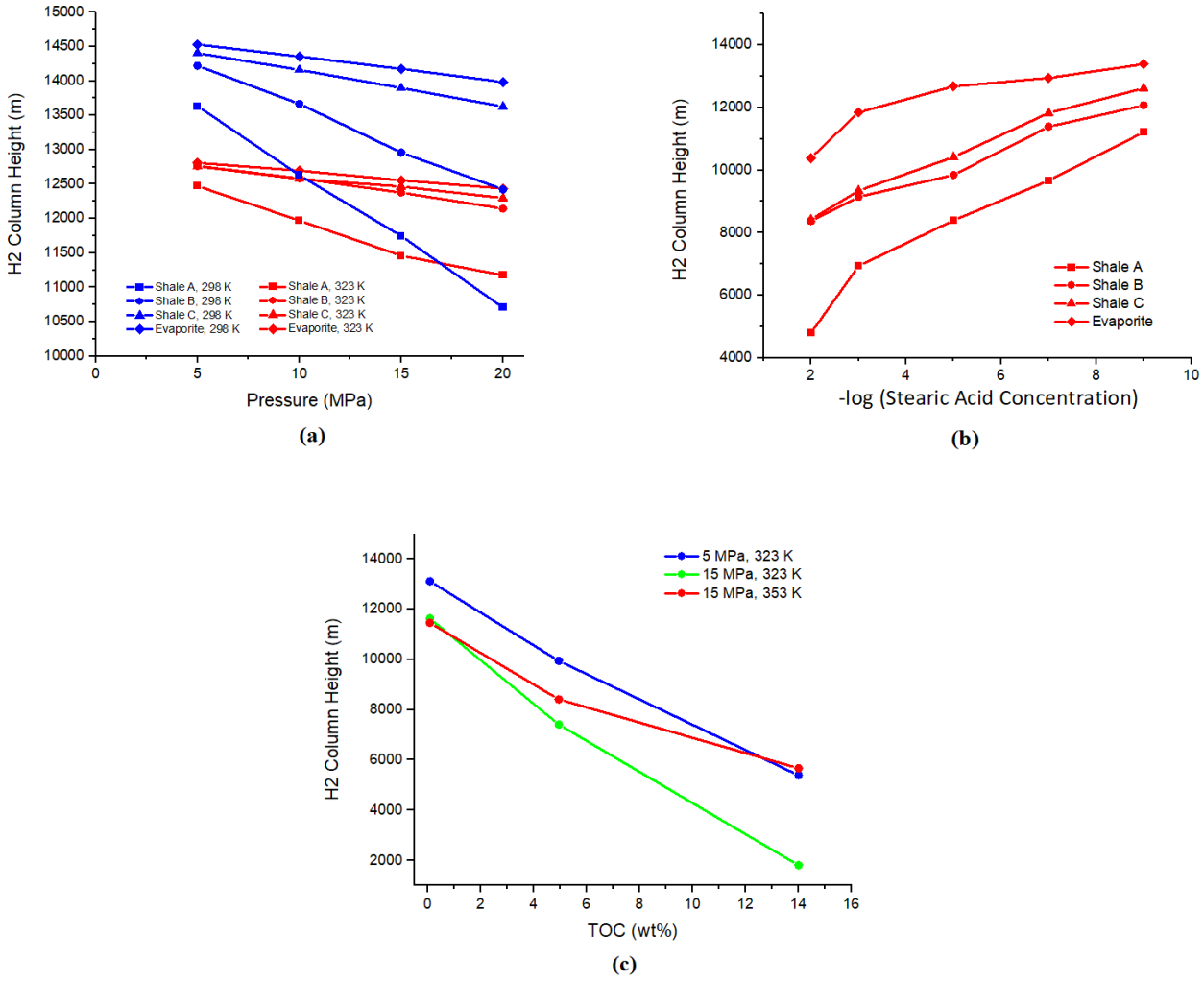

Fig. 5-8 H_2 column height as a function of a) pressure and temperature, b) organic acid concentration, and c) TOC for a typical pore size of r = 1 nm.

5.4 Implications

Capillary sealing efficiency of caprocks at geo-storage conditions can be analyzed by calculating the capillary entry pressure (p_{ce}), which is a function of γ, θ, and r. In this regard, the wettability of caprocks for gas/water systems at geo-storage conditions strongly affects the structural storage capacity (Iglauer et al., 2015b) (i.e. gas column height). The present study agrees with literature (e.g. (Iglauer, 2018, Arif et al., 2017b, Al-Yaseri et al., 2021c)) that the capillary sealing efficiency of caprocks for preventing gas leakage increases with water wettability. The main operating

paramters influencing on the caprock wettability include, but are not limited to, temperature, pressure, mineralogy and TOC (Pan et al., 2020c, Ali et al., 2022c). It is worth noting that surface contamination and roughness can affect the contact angle measurements and thus the wettability (Iglauer, 2017, Sari et al., 2020). Therefore, appropriate surface cleaning and polishing methods must be taken to reduce their effects on the contact angle measurements.

In addition to the calculation of H_2 column height by the p_{ce}, the gas penetration into the rock pores can be identified. According to Fig. 5-3 for the clean (low TOC) caprocks, it is assumed that the p_{ce} changes linearly with the prevailing reservoir pressure (p) as follows:

$$p_{ce} = ap + b, \tag{5.3}$$

where a (slope) and b (intercept) are constants determined by linear fitting at each T and r. Effective sealing occurs when the capillary entry pressure (p_{ce}) exceeds the existing reservoir pressure (p); otherwise, gas may readily infiltrate the larger pores in the caprock. Consequently, the maximum permissible reservoir pressure ($p_{\max}$) for safely storing hydrogen beneath a caprock at a given T and r is determined as follows:

$p_{ce} \geq p \rightarrow ap + b \geq p \rightarrow p\,(1 - a) \leq b$ and considering that $(1 - a) > 0$, the following equation is derived:

$$p_{\max} = \frac{b}{1-a}. \tag{5.4}$$

Table 5-2 gives the calculated p_{max} for the clean caprocks at two T and two r values. For example, for all the clean caprocks with r = 10 nm, gas can easily penetrate the pores when the reservoir pressure is more than about 15 MPa (Fig. 5-3). However, for pores with r = 5 nm, gas will not be able to penetrate the pores as the relevant values for p_{ce} are greater than the reservoir pressure (due to the small pore size). For the caprocks aged in stearic acid at 15 MPa and 323 K, gas can easily penetrate the pores with r = 10 nm for all the acid concentrations (Fig. 5-5). However, for pores with r = 5 nm, gas will not be able to penetrate the pores for all the acid concentrations, except at concentrations of 10^{-3} mol/L and 10^{-2} mol/L for shale A (this is due to the effect of mineralogy). For high-TOC oil shale, the computed p_{ce} for both r = 10 nm and r = 5 nm is lower than 15 MPa, implying that gas can easily enter the pores (Fig. 5-7), however, for medium-TOC and low-TOC oil shales with r = 5 nm, gas will not be able to penetrate the pores.

Table 5-2 The maximum prevailing reservoir pressure (p_{max}) for the clean caprocks at two T and two r values.

Rock sample	T (K)	r (nm)	p_{max} (MPa)
Shale A	298	5	21.13
	353	5	21.67
	298	10	15.26
	353	10	11.77
Shale B	298	5	24.05
	353	5	23.78
	298	10	13.41
	353	10	12.38
Shale C	298	5	26.66
	353	5	24.08
	298	10	14.15
	353	10	12.45
Evaporite	298	5	27.55
	353	5	24.39
	298	10	14.40
	353	10	12.54

One of the most important factors affecting sealing efficiency is pore structure of the caprocks (specifically, shales) which varies significantly under different lithofacies, thermal evolution and structural conditions (Xu et al., 2020, Gou et al., 2021, Li et al., 2019a). Moreover, shale micro-fractures are clearly important for sealing efficiency analysis of shales (Gou et al., 2019). In this investigation, we considered two standard pore sizes for analyzing the capillary sealing efficiency of caprocks, as our laboratory lacks the necessary advanced equipment to directly measure them (note: caprocks typically exhibit complex and variable pore networks. Their heterogeneous nature makes it challenging to obtain a representative pore size distribution, and conducting tests such as Mercury Injection Capillary Pressure (MICP) can be problematic due to the potential for sample damage or distortion). Thus, full-scale pores and micro-fractures characterization of the caprocks using advanced techniques such as X-rays, infrared spectroscopy, and neutron scattering (NS) (Hosseini et al., 2021) are needed for future research to have better understanding of their sealing efficiency. The effects of connectivity, maturity and distribution of organic matter on caprock

wettability and thus capillary sealing are another aspect for future research that need to be carefully examined. It is also important to note that while the accurate assessment of wettability typically involves coreflooding experiments, conducting conventional core flooding for caprock is impractical, if not exceedingly challenging, due to the nanopore structure inherent in caprocks.

5.5 Conclusions

The capillary entry pressure (p_{ce}) is a critical parameter for the sealing efficiency analysis of caprocks in the structural trapping of hydrogen (Espinoza and Santamarina, 2017, Iglauer et al., 2015b, Rezaeyan et al., 2015). However, there is a scarcity of information on the effect of different parameters such as pressure, temperature, organic acid concentrations, and TOC on the hydrogen sealing efficiency of caprocks such as shales and evaporites. Thus, we used the θ (measured in this study), γ (taken from (Hosseini et al., 2022d)), and r (two typical values of r = 10 nm and 5 nm) to compute the p_{ce} and analyze the sealing efficiency of the caprocks. The key findings of the study are as follows:

1. The water wettability of the caprocks decreased with pressure, organic acid concentration, and TOC, while it increased with temperature.
2. The capillary sealing efficiency of the caprocks decreased with all geo-storage conditions but increased with temperature for oil shales. Although both γ and θ decreased with temperature, γ was more effective than θ for clean caprocks (decrease in $\gamma\cos\theta$), leading to a decrease in p_{ce} with temperature. However, when temperature increased for oil shales (high TOC), θ was more effective than γ (increase in $\gamma\cos\theta$), leading to an increase in p_{ce}.
3. The results showed more efficient sealing and storage capacity for small pore sizes and evaporites.

We can therefore conclude that it is essential to accurately determine the γ, θ, r, and mineralogy to have a better analysis of the capillary sealing efficiency of the caprocks, which will aid in the successful implementation of hydrogen geo-storage projects.

Chapter 6 Basalt-H_2-brine wettability at geo-storage conditions: Implication for hydrogen storage in basaltic formations

Published in *Journal of Energy Storage*, Elsevier 2022, 52, Part A, 104745
DOI: https://doi.org/10.1016/j.est.2022.104745

Abstract

Among all gas geo-storage sites, basaltic formations have attracted limited attentions in recent years, specially for large-scale storage of CO_2. However, the suitability of the basaltic formations for large-scale H_2 storage is completely unknown. Wettability of these geological formations is an important parameter for gas geo-storage process as it determines the capacity of gas to spread throughout the pore matrix. To comprehend the wetting characteristics of natural and ideal basaltic rocks in geological conditions, we have measured the basalt-H_2-brine contact angles with and without presence of organics under various physio-thermal conditions (5-20 MPa and 308-343 K). Further, H_2 column heights which can be safely stored in basaltic formations were calculated based on the contact angle experimental data. Moreover, acquired hydrogen wettability data was compared with that of CO_2 for validation purposes. The results showed that the basalt-H_2-brine system was strongly water-wet at lower pressures (5 and 10 MPa), but it turned to weakly water-wet at higher pressures (15 and 20 MPa). The increase in temperature and organic acid concentrations also showed negative effect so that basalt-H_2-brine system completely turned to intermediate-wet (affinity of basalt for both water and gas). The H_2 column height calculations have suggested that unlike CO_2 which may show leakage above depth of 1100 meters, H_2 could be safely trapped in basaltic formation even up to 2000 meters. The presented data in this work is highly crucial, which will aid in the successful implementation of H_2 storage in basaltic formations.

Keywords

Contact angle, H_2 wettability, H_2 geo-storage, H_2 column height, basalt formation

6.1 Introduction

Continuous increase in atmospheric CO_2 concentration caused by burning fossil fuels has persuaded countries to make plans for low-carbon energy production (Hassanpouryouzband et al., 2021, Tarkowski, 2019, Energy, 2014). Hydrogen as low-carbon energy carrier produced from renewable resources has attracted many attentions to be a substitute for fossil fuels (Hosseini et al., 2022e). However, the fluctuations of renewable energy sources (e.g. sunlight duration, wind direction, and wind power) can lead to imbalance in energy demand and supply (Turner, 2004). Thus, hydrogen storage is required to provide a reliable energy supply (Zivar et al., 2021). In this regard, the surface-based hydrogen storage facilities have been used for decades, however, they have low storage capacity due to very low density of hydrogen (Hosseini et al., 2022d, Lemieux et al., 2020). Underground hydrogen storage (UHS) is a prominent way to store millions of tons of hydrogen in geological formations where the storage capacity is vast and the associated operations are cheap (Pfeiffer and Bauer, 2015, Iglauer et al., 2021b).

Many subsurface geological formations have been proposed as mediums for the large-scale UHS, where the hydrogen can be withdrawn again for utilization at peak demand times (Muhammed et al., 2022, Zivar et al., 2021, Ali et al., 2022a). Although salt formations have been practically used for hydrogen storage for many decades (Caglayan et al., 2020, Lankof and Tarkowski, 2020, Lemieux et al., 2019), other porous geological formations have also been proposed as potential mediums for large-scale hydrogen storage (Tarkowski, 2019). In this regard, sedimentary formations such as aquifers and depleted oil/gas reservoirs have attracted most attentions for the large-scale hydrogen storage due to their higher capacity and sealing efficiency (Iglauer et al., 2021b, Pfeiffer, 2017, Sáinz-García et al., 2017, Yekta et al., 2018, Ali et al., 2021d). Volcanic rocks such as basalts known as an unconventional storage medium with vast storage capacity have attracted limited attention (Gislason and Oelkers, 2014, Gislason et al., 2010, Al-Yaseri et al., 2021b, Al-Yaseri and Jha, 2021, Abdulelah et al., 2021). However, basaltic rocks with their relatively large thicknesses are abundantly found on Earth's surface (approximately 10% of the continents and two-third of the ocean floor) (Gislason and Oelkers, 2014, le Roex, 1998). Therefore, similar to the sedimentary formations, it is highly recommended to explore basaltic formations for gas storage purposes (Goldberg et al., 2018). Specifically, two successful CO_2 storage projects including the Carbfix Project in Iceland (Gislason et al., 2010) and the Columbia

River Basalt Project in Washington State (McGrail et al., 2017) have proved the suitability of the basaltic formations for long-term H_2 storage.

The storage of hydrogen as a working gas is performed with a cushion gas to pre-pressurize the formation and prevent brine production (Zivar et al., 2021). For example, CO_2 is considered as a cushion gas during H_2 storage because CO_2 has high compressibility and can be safely stored as a greenhouse gas (Pfeiffer and Bauer, 2015, Oldenburg, 2003). The mixing of these two gases at desired mole fractions is determined by differences in their thermodynamic and transport properties such as density, viscosity, vapor-liquid equilibria, thermal capacity and conductivity, and molecular diffusion (Hassanpouryouzband et al., 2020). For example, higher mole fractions of CO_2 lead to higher density and viscosity values as the density and viscosity of CO_2 are considerably higher than H_2 (Kondepudi, 2008).

One crucial parameter for gas storage in basaltic formations is the wettability of basalt-gas-brine which controls gas spreading in the rock's pore network (Blunt, 2017). The wettability at geo-storage conditions is very crucial for an accurate estimation of H_2 column heights and storage capacity (Hassanpouryouzband et al., 2021, Hosseini et al., 2022c). There are a few researchers who reported the wettability of basalt-CO_2-brine (Al-Yaseri et al., 2021b, Iglauer et al., 2020, Matter et al., 2007), however, wettability data for the basalt-H_2-brine is scarce in the literature. The only data for basalt-H_2-brine wettability was reported by (Al-Yaseri and Jha, 2021) who used empirical correlations for its prediction.

Analogous to sedimentary rocks, basalts may also contain organic matter which can be added to the basalts via seawater circulation, or trapped and fossilized in the altered igneous rocks (Türke et al., 2018, Furnes and Staudigel, 1999, Furnes et al., 2001). Thus, organic matter can adsorb on the rock surface to some extent due to diagenesis of organic matter and fossil biodegradation (Lundegard and Kharaka, 1994, Akob et al., 2015, Jones et al., 2008) although its concentration is normally low (Stalker et al., 2013). However, this low concentration adsorbed to the rock surface is sufficient to affect the rock wettability, and thus the storage capacity and containment safety (Gomari and Hamouda, 2006, Standnes and Austad, 2003, Ali et al., 2019b, Al-Khdheeawi et al., 2017a). Accordingly, finding the optimum organic matter concentration is very important for the investigation of storage capacity and containment safety. In this regard, research scientists have used modern analytical methods such as mass spectroscopy and gas chromatography to separate

organic acids (carboxylic or fatty acids) from the crude oil stream and proved the presence of these fatty acids (recognizable fossils) in numerous geological formations ranging from the Precambrian age (before the development of geological formations) to the recent age (Akob et al., 2015, Kvenvolden, 1967, Lundegard and Kharaka, 1994). These organic acids may range in various carbon number of items (C_2 to C_{26}) (Kvenvolden, 1967) and in different concentrations. In this study, we used stearic acid (C_{18}, at various concentration thresholds) which is commonly found in the geological formations (Akob et al., 2015, Lundegard and Kharaka, 1994, Stalker et al., 2013) for measuring its effects on hydrogen wettability.

Therefore, in this study, we have experimentally determined the basalt-H_2-brine wettability by measuring both advancing and receding contact angles at various physio-thermal geo-storage conditions for ideal (pure basalt) and anoxic (organic-aged basalt) geological conditions. Thereafter, H_2 column heights were calculated based on wettability data and was compared to that of CO_2 for validation purposes. Being the first work in the literature for basalt-H_2-brine systems, the presented data will open the new boundaries for the exploration of underground hydrogen storage (UHS) in basaltic formations.

6.2 Experimental Procedure

6.2.1 Materials and preparation

One basalt rock sample (provided by GSI) with very low TOC value (0.05 wt %) was selected for the experiment. The mineralogy of the sample, as detailed in Table 6-1, underwent analysis using the Bruker Model D8 Discover XRD technique, which utilizes X-ray diffraction complemented by an ATLAS goniometer. The analysis revealed that anorthite, a plagioclase feldspar, predominates in the sample. The sample was cut into 1 cm × 1 cm × 0.4 cm dimensions using a high-speed diamond blade. Then, its surface was uniformly polished with 400 and 1200 grit sandpaper to minimize the surface roughness effects on the contact angle measurements. H_2 gas (99.9 mol%, from BOC Australia) and 1.05 M synthetic reservoir brine (0.864 mole fraction NaCl + 0.136 mole fraction KCl) prepared by mixing the salts (purities of NaCl and KCl ≥ 0.99 mole fraction, from Chemlab) with deionized water (electrical conductivity = 0.02 mS.cm-1, from David Gray) were used for the experiment. To assure that the rock surface is dust-free, we firstly washed

the sample with deionized water (Iglauer et al., 2021b). Then, ultra-pure N_2 gas (99.9 mol%, from BOC Australia) was used to remove the water thin film from the rock surface, which was then dried in an oven at 338 K for 60 minutes (Arif et al., 2017a). Finally, the sample was placed in an air plasma cleaner for 15 min to remove the residual organic contaminants (Iglauer et al., 2014).

To simulate the basaltic rock in a geological formation, we aged the clean basalt surface with stearic acid (purity ≥ 0.99 mole fraction, from Sigma Aldrich) under the following strategy in four steps (Davis, 1982, Kleber et al., 2015, Ulrich et al., 1988, Zullig and Morse, 1988): 1) the rock surface was ionized by immersing in rock-equilibrated 2 wt % NaCl brine for 30 min at ambient conditions (Ali et al., 2021a), 2) both maintaining the acidity of the brine at pH = 4 and increasing the adsorption rate of the stearic acid onto the rock surface were performed by adding droplets of aqueous hydrochloric acid (HCl concentration = 37.5 vol%, from Sigma Aldrich) (Jardine et al., 1989, Madsen and Ida, 1998), 3) the ultra-pure N_2 gas was then used to remove the contaminants from the rock substrate, and finally 4) the substrates were aged in toluene/stearic acid solutions (highly diluted stearic acid concentrations of 10^{-2}, 10^{-3}, 10^{-5}, 10^{-7} and 10^{-9} mol/L) for a week (Ali et al., 2019b).

Table 6-1 Mineralogy of the sample via XRD technique.

Mineral	Formula	wt %
Anorthite	$CaAl_2Si_2O_8$	55
Augite	$Ca(Fe,Mg)Si_2O_6$	25
Orthoclase	$KAlSi_3O_8$	16
Lizardite	$Mg_3(Si_2O_5)(OH)_4$	4

6.2.2 Contact angle measurements

To quantitatively analyze the wetting characteristics of the basalt-H_2-brine system, the tilted plate method was used for simultaneous measurements of the receding and advancing contact angles (Marmur, 2006). The basalt sample (clean or aged) was placed on the tilted plate with an angle of 15º inside a high pressure-high temperature optical cell (with a maximum working pressure and temperature of 40 MPa and 433 K, respectively) at the desired temperature (Lander et al., 1993). The optical cell was then pressurized with H_2 gas at the desired pressure. A needle (with outer

diameter of 1.5875 mm mounted vertically on the cell's ceiling) was then used to dispense a droplet of brine (average volume of 5 µL ± 1 µL) onto the basalt surface. The receding and advancing contact angles were measured at the back and the front edge of the droplet, respectively, just before the droplet initiated a movement. A dino light camera (with a resolution of 1280 × 1024 (1.3 MP)) was used to record high-quality images of the droplets which were then used for determining the corresponding contact angles using ImageJ software. Fig. 6-1 is a schematic of the contact angle system.

The measurements were conducted for typical storage pressures (5, 10, 15 and 20 MPa) and two temperatures (308 and 343 K). The effect of organic acid concentration in the range of 10^{-9} - 10^{-2} mol/L on the H_2 wettability of basalt was assessed at T = 323 K and p = 15 MPa. Based on the repeated measurements (three times for every measurement at a single point), the average value was computed and reported here. The average standard deviation of the measurements was ± 3º (with the relative standard uncertainties of 1 K for temperature and 0.1 psi for pressure).

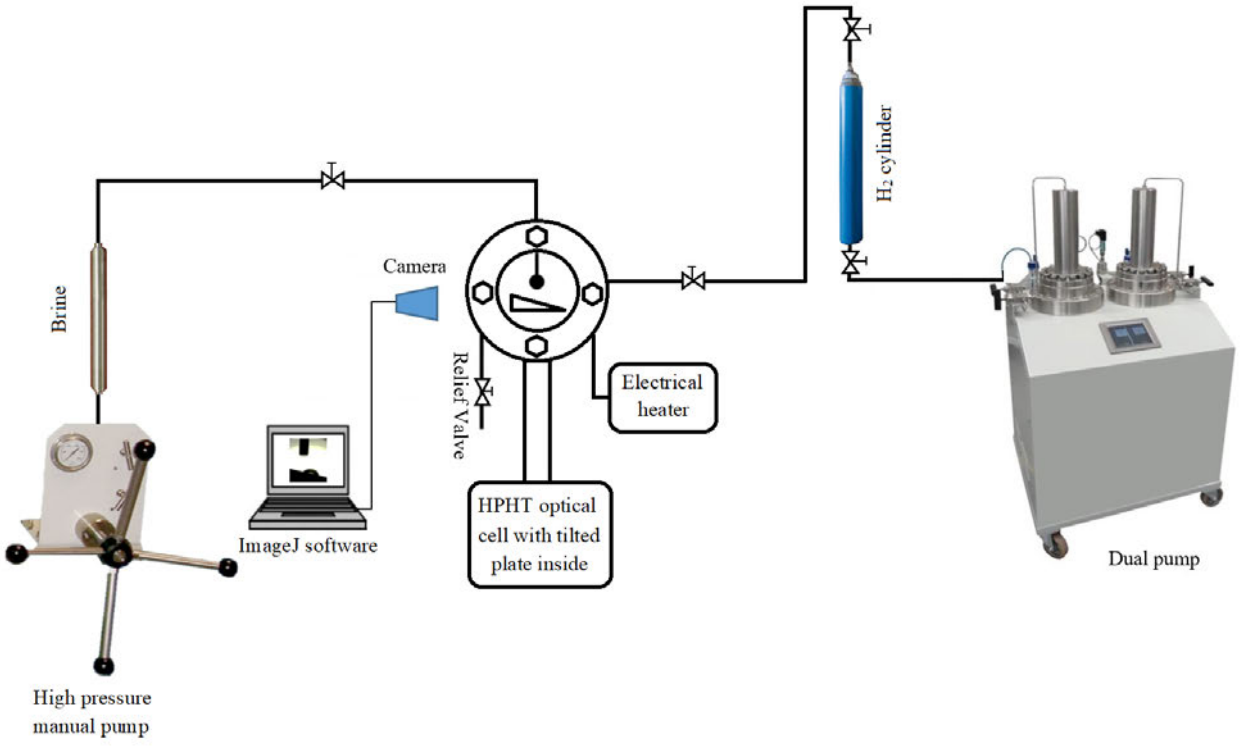

Fig. 6-1 Schematic of the HPHT experimental setup for contact angle measurements.

6.3 Results and discussion

It is notable that depending on the petrophysical properties (i.e., porosity and permeability) of the basalt, it can be considered as both storage and seal rock. However, basaltic rock as a storage rock may rarely happen due to high heterogeneity and poor connectivity of pores in the rock. Thus, in this study, the basaltic rock was considered as a seal rock, and the relevant maximum column height beneath the rock was calculated based on the available data. H_2-wettability of basalt is a key factor to evaluate the storage capacity via the maximum column height or storage height beneath the basaltic formations (Al-Yaseri et al., 2021b). In an aquifer, the water displacement by H_2 (i.e. during hydrogen injection) is known as a drainage process which is referred to the receding contact angle (θ_r) (Broseta et al., 2012), while the H_2 displacement by water (i.e. during hydrogen withdrawal) is known as an imbibition process which is referred to the advancing contact angle (θ_a) (Chiquet et al., 2007). As the contact angles and associated storage capacity vary with geological conditions (Ali et al., 2021d), we thus discuss the effect of pressure, temperature, and organic surface concentration on the H_2 wettability and column height of the basaltic rock.

6.3.1 Effect of pressure, temperature and organic surface concentration on basalt-H_2-brine wettability

The water wettability decreased with pressure at the constant temperatures of 308 and 343 K (increase in θ_a and θ_r, Fig. 6-2) due to the increased intermolecular forces between basalt and hydrogen (Iglauer et al., 2012), which is consistent with literature data for various rock surfaces tested with hydrogen (Ali et al., 2021d, Iglauer et al., 2021b, Hosseini et al., 2022e). However, some authors did not find obvious correlation between wettability and pressure for rock/H_2/water system (e.g. (Hashemi et al., 2021b, Hashemi et al., 2022)). These discrepancies were attributed to the differences in the experimental conditions, methodologies, and sample preparation (Hashemi et al., 2021b).

At 308 K, the basalt surface was strongly water-wet at 5 MPa (θ_a = 32.29º) and became weakly water-wet at 20 MPa (θ_a = 59.31º). At 343 K, we observed a similar result, strongly water-wet at 5 MPa (θ_a = 47.86º) and weakly water-wet at 20 MPa (θ_a = 68.61º). The basalt surfaces are often silica-rich, especially those located at mid-ocean ridges, subduction zones and large igneous

provinces (Selley et al., 2005). Analogous to the brine/H_2/quartz system the wettability of brine/H_2/basalt system highly depends on hydrogen bonding between silanol groups and water molecules on the rock surface (Iglauer et al., 2021b). However, in our previous work, the wettability of brine/H_2/calcite system was attributed to the gas density as there are no silanol groups in calcite (Hosseini et al., 2022e). The decrease in water wettability with temperature shown in Fig. 6-2 can thus be explained by breaking hydrogen bonds between water molecules and silanol groups on the basalt surfaces at high temperatures (Chen et al., 2015b). The broken hydrogen bonds at elevated temperatures lead to a decrease in affinity between water and basalt and thus decrease in hydrophilicity and water wettability of the basalt.

Also, we compared our results with the literature data for two basalt-CO_2-brine systems (Fig. 6-2), including Western Australian basalt (WAB) (Al-Yaseri et al., 2021b) and Icelandic Carbfix basalt (Iglauer et al., 2020), and observed that the CO_2 systems have higher contact angles as CO_2 has higher density and solubility and lower IFT than H_2 (Al-Yaseri and Jha, 2021, Hassanpouryouzband et al., 2021), leading to a weaker intermolecular forces between H_2 and basalt compared to CO_2 and basalt. It is noteworthy that the contact angles of the WAB are greater than those of the Icelandic Carbfix basalt (Al-Yaseri et al., 2021b), primarily because the WAB is more hydrophobic. This heightened hydrophobicity can be attributed to its higher plagioclase mineral content (Khan et al., 2014), which is 80% in the WAB compared to 59% in the Icelandic basalt (Al-Yaseri et al., 2021b).

For the aged basalt tested, both θ_a and θ_r increased with stearic acid concentration (decrease in water wettability, see Fig. 6-3), consistent with (Ali et al., 2021d). For instance, at 15 MPa and 323 K, θ_r increased from 67.09º to 86.28º (turned from weakly water-wet to intermediate water-wet) when the concentration of stearic acid increased from 10^{-9} mol/L to 10^{-2} mol/L. This decrease in water wettability is attributed to the surface de-wetting due to the organic acid adsorption on the basalt surface (Abramov et al., 2019).

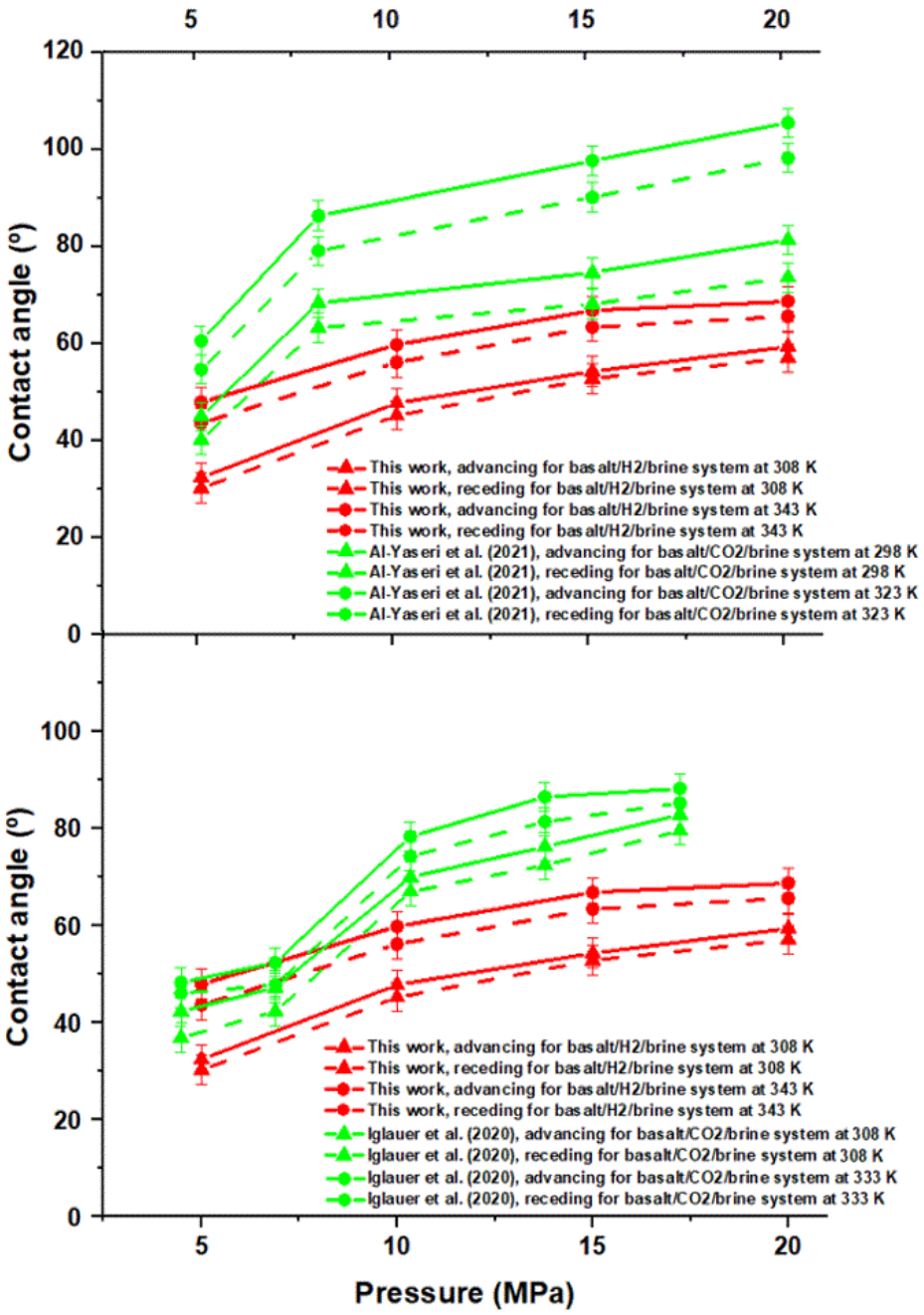

Fig. 6-2 Basalt-H_2-brine contact angles (red lines) as a function of pressure and temperature, and comparison with basalt-CO_2-brine contact angles (green lines) of Western Australian basalt (top) and Icelandic Carbfix basalt (bottom). The solid and dashed lines show advancing and receding contact angles, respectively.

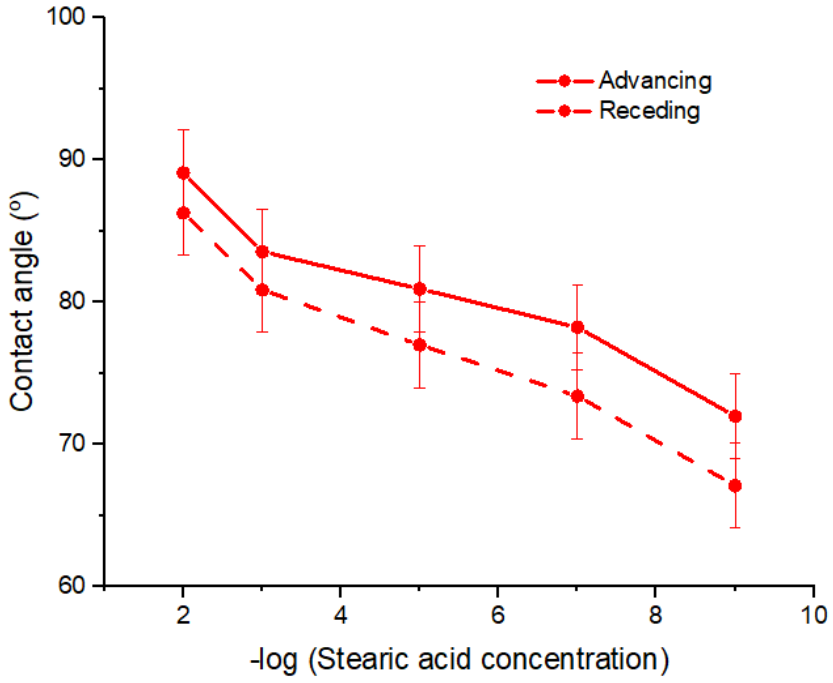

Fig. 6-3 Effect of organic surface concentration on basalt-H_2-brine contact angle at 323 K and 15 MPa.

6.3.2 Effect of pressure, temperature and organic surface concentration on H_2 column height

To evaluate the sealing capacity of basaltic rocks, the maximum H_2 column height or storage height that can be safely stored under basalts is predicted using the following equation (Dake, 1983):

$$h = \frac{2\gamma \cos\theta_r}{\Delta\rho g r}, \tag{6.1}$$

where γ is the interfacial tension between hydrogen and brine (taken from (Hosseini et al., 2022d)), θ_r is the receding contact angle of the basalt-H_2-brine system (measured in this study), $\Delta\rho$ is the density difference between hydrogen and brine (taken from (Al Ghafri et al., 2012, Kunz and Wagner, 2012, Leachman et al., 2009, Wagner and Pruß, 2002)), g is the gravitational acceleration and r is the mean pore throat radius in basalt (typical value of 29 nm taken from (Al-Yaseri et al., 2021b)). The H_2 column height can be used to calculate the hydrogen storage capacity or maximum mass of hydrogen that can be safely stored in basaltic rock (Shah et al., 2008):

$$M_{H_2} = \rho_{H_2} h\phi(1 - S_w), \tag{6.2}$$

where M_{H2} is the mass of H_2 per unit area of the basaltic rock, ρ_{H2} is the H_2 density, S_w is the residual water saturation, and ϕ is the porosity of the basaltic rock.

The column height decreases with pressure and temperature (Fig. 6-4), implying that lower volumes of H_2 can be stored in basaltic rocks located in hotter and higher pressure formations (e.g. deeper formations). For instance, at 308 K, H_2 column height decreased from 2141 m to 1316 m when pressure increased from 5 MPa to 20 MPa. However, at 343 K, it decreased from 1660 m to 928 m for the same increase in pressure. It is also seen that the H_2 column height is more than CO_2 column height (both basalts, Fig. 6-4), implying that basaltic rocks may store more H_2 than CO_2. To find the reason for this, we should assess all the affecting parameters in Equation (6.1) (r has been assumed to be the same for both H_2 and CO_2 systems). For instance, at 308 K and 5 MPa, γ, cos θ_r and $\Delta\rho$ for H_2 system were 73 mN/m (Hosseini et al., 2022d), 0.86 (from this study) and 1037 kg/m^3 (Kunz and Wagner, 2012, Al Ghafri et al., 2012), respectively. However, at 298 K and 5 MPa, γ, cos θ_r and $\Delta\rho$ for CO_2 system of WAB were 42 mN/m (Sarmadivaleh et al., 2015), 0.76 (Al-Yaseri et al., 2021b) and 867 kg/m^3 (Georgiadis et al., 2010), respectively. Thus, all three parameters (γ, cos θ_r and $\Delta\rho$) for H_2 are higher than for CO_2, implying that the higher column height for the H_2 system is due to the higher values of γ and cos θ_r compared to the CO_2 system. It is worth noting that the WAB has lower CO_2 column height due to its higher contact angle compared to the Icelandic Carbfix basalt.

Furthermore, the column height decreases with organic surface concentration (Fig. 6-5), suggesting that basaltic rocks with lower organic surface concentration may securely trap larger volumes of H_2. For instance, at 15 MPa and 323 K, the H_2 column height decreased from 918 m to 153 m when the concentration of stearic acid increased from 10^{-9} mol/L to 10^{-2} mol/L.

The error bars for the column heights shown in Fig. 6-4 and Fig. 6-5 were calculated by considering average standard deviation values of ± 0.2 mN/m for γ, ± 3 º for θ, and ± 0.15 kg/m^3 for $\Delta\rho$ and the pore throat radius of 29 nm. However, it is expected that the pore throat radius of the rock has large effect on the quantitative reliability of the column height. For example, if the pore throat radius is 5 nm, the column height will approximately be 6 times larger than when the pore throat size is 29 nm. Therefore, full-scale pore characterization of the rock is highly recommended to future research to reduce the uncertainty for the column height calculations (Hosseini et al., 2022c, Hosseini et al., 2021).

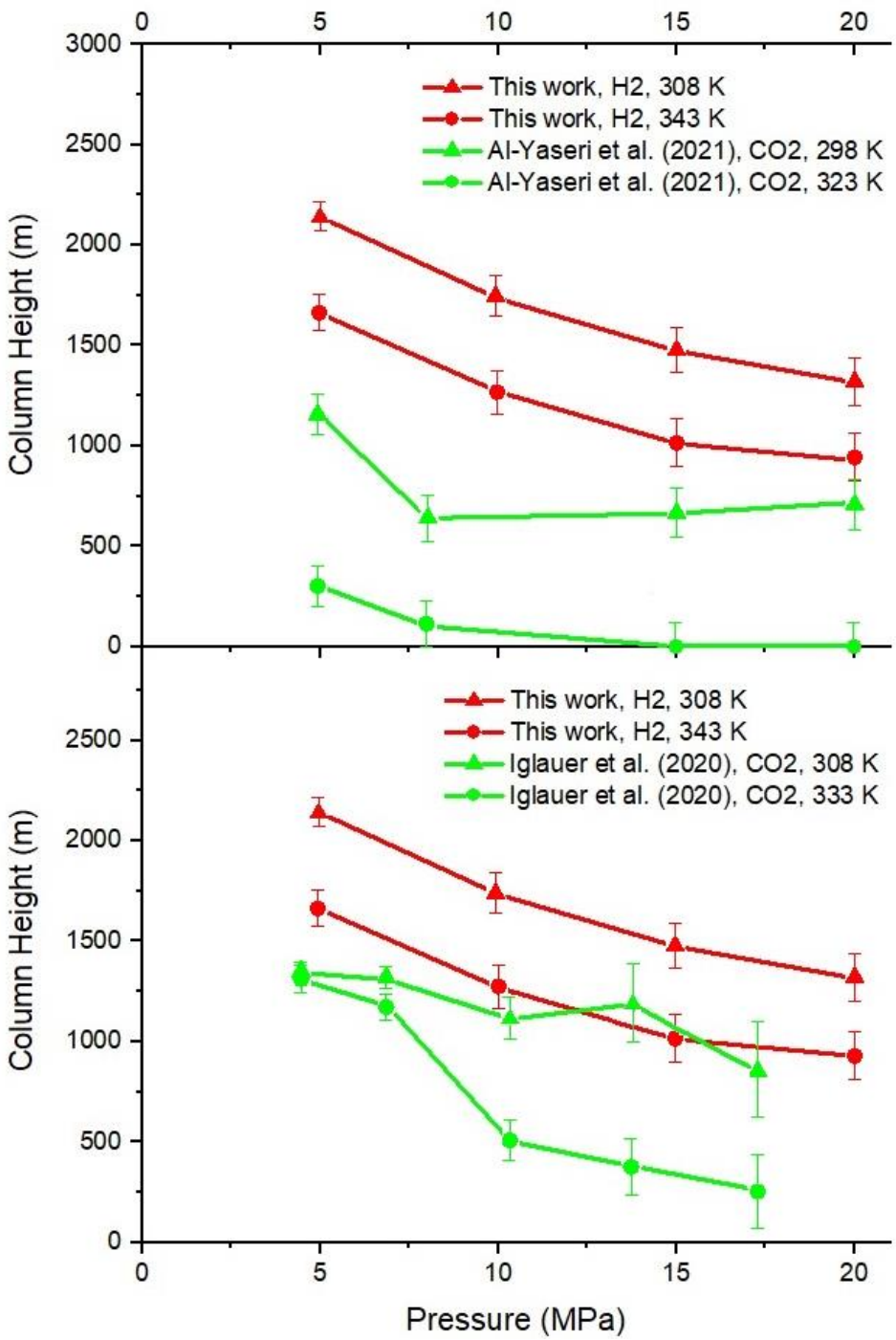

Fig. 6-4 H_2 column height (red lines) as a function of pressure and temperature, and comparison with CO_2 column height (green lines) of Western Australian basalt (top) and Icelandic Carbfix basalt (bottom).

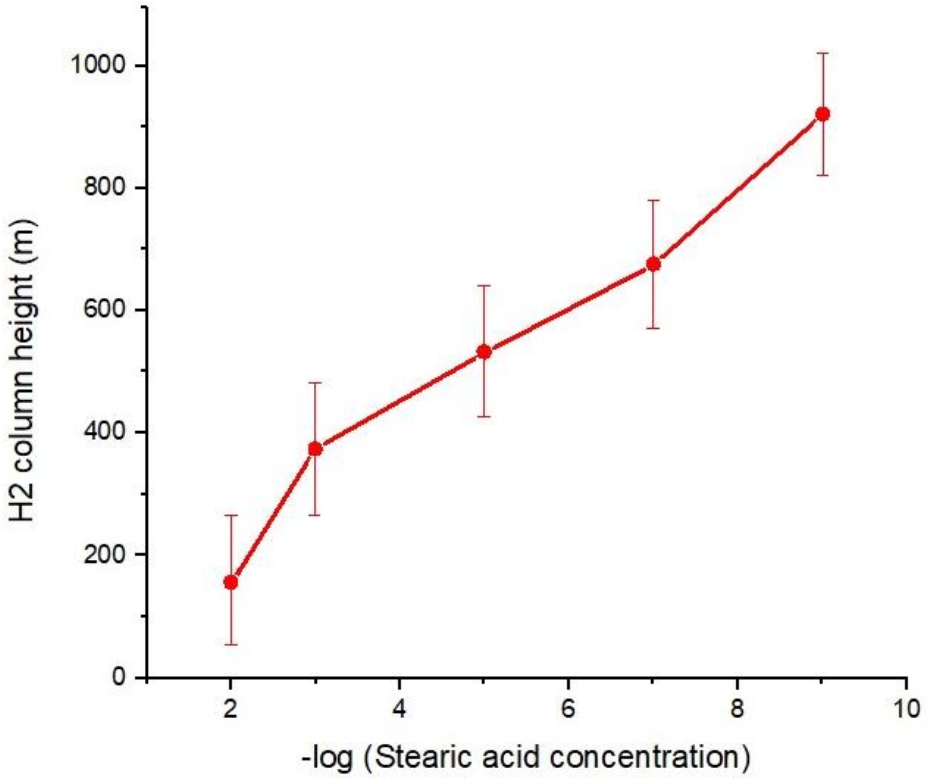

Fig. 6-5 H_2 column height in basalt as a function of organic surface concentration.

6.4 Conclusions

Recent studies have shown that basaltic rocks are promising candidates for CO_2 storage (Al-Yaseri et al., 2021b, Gislason et al., 2010, Iglauer et al., 2020, Matter et al., 2007, McGrail et al., 2017). However, the suitability of these rocks for H_2 storage has not been effectively evaluated in the literature. The wettability is a key parameter for H_2 geo-storage process, especially in controlling the gas flow rate during injection/production of hydrogen, fluid-flow behavior and containment security (Blunt, 2017, Jha et al., 2021, Arif et al., 2016d, Iglauer, 2017). Moreover, the wettability data for basalt-H_2-brine is scarce in the literature. Therefore, we measured this parameter for basalt-H_2-brine system at geo-storage conditions. It is concluded that the basalts are strongly water-wet (e.g. at low pressure) to weakly water-wet (e.g. at high pressure) in the presence of H_2. Thus, H_2 column heights which can be safely stored in basalts were obtained at geo-storage conditions, suggesting them as highly favorable candidates for H_2 storage. However, the possible presence of organic matter in basalts should also be taken into account as its presence may

significantly influence the wettability. For example, the increased H_2 wettability of basalts with organic acid concentration led to a decrease in H_2 column height, although all the measured contact angles were lower than 90º even at high stearic acid concentration. Moreover, under the same geo-storage conditions, more H_2 volume can be safely stored in basaltic rocks compared to CO_2 as the contact angles in H_2 system are lower than the CO_2 system. While the influence of mineralogy, as assessed through XRD analysis, on wettability was taken into account, it is recommended to enhance understanding by obtaining the spatial distribution of mineralogy in the basaltic rock sample. This can be achieved through imaging the rock surface using scanning electron microscopy (SEM), providing more accurate insights into how mineral distribution affects wettability. Thus, this work improves the understanding of basalt-H_2-brine system, which will aid in successful implementation of UHS in basaltic formations.

Chapter 7 Assessment of rock-hydrogen and rock-water interfacial tension in shale, evaporite and basaltic rocks

Published in *Journal of Natural Gas Science and Engineering*, Elsevier 2022, 106, 104743
DOI: https://doi.org/10.1016/j.jngse.2022.104743

Abstract

Underground hydrogen storage (UHS) is a distinguished method for reducing anthropogenic greenhouse gases (GHGs) and meeting global energy demand. One of the important parameters for subsurface storage of gas is rock-fluid interfacial tension ($\gamma_{rock\text{-}fluid}$) as gas injection and production rate, spread and flow in porous media, storage capacity, and containment security can be derived by this parameter. Moreover, it is one of the factors responsible for the wettability alteration in caprocks and basaltic rocks. However, it is impossible to experimentally measure $\gamma_{rock\text{-}fluid}$. Moreover, $\gamma_{rock\text{-}fluid}$ data for rock/H_2/water systems in various shales, evaporite, and basaltic formations at geo-storage conditions are scarce in the literature. Thus, advancing and receding contact angles data were used to theoretically compute it at various pressures, temperatures, and shale-TOC by the combination of Young's equation and Neumann's equation of state. For all the rocks evaluated in this study, it was found that $\gamma_{rock\text{-}gas}$ decreased with pressure, temperature, and shale-TOC. Also, $\gamma_{rock\text{-}water}$ decreased with temperature but increased with shale-TOC, assuming that it remained constant with pressure. Thus, this work provides a deep understanding of wetting characteristics at various rock/H_2/water systems, leading to a better investigation of hydrogen storage beneath shales, evaporite, and basaltic formations.

Keywords

Rock-gas interfacial tension, rock-water interfacial tension, hydrogen geo-storage, shale, evaporite, basalt.

7.1 Introduction

Nowadays, climate change or global warming resulting from human-caused greenhouse gases (GHGs) emissions is a serious concern for human life (Wilcox et al., 2020, Bernstein et al., 2008, Anderson et al., 2016, Cassia et al., 2018, Hoel and Kverndokk, 1996, Ali et al., 2022a). Moreover, non-renewable fossil fuels such as oil, gas, and coal as the main sources of energy will finally run out due to increased global energy demand and consumption (Srivastav et al., 2014, Palmer, 2019, Helm, 2016, Michaelides, 2017). Thus, countries are finding reliable solutions for a healthy environment and enough fuel to guarantee the sustainability of human life and activities in the future (Henrich et al., 2015, Kanwal et al., 2022, Henry, 2010). One of the solutions that has recently attracted attention throughout the world is the large-scale hydrogen economy (Moradi and Groth, 2019, Tarkowski, 2019, Zivar et al., 2021, Lankof and Tarkowski, 2020, Iglauer et al., 2021b). Hydrogen (H_2) as a clean fuel is a good substitute for fossil fuels, which is produced via various methods (Chen et al., 2020, Mohanty et al., 2021, Kumar and Himabindu, 2019, Wang et al., 2021, Arribas et al., 2018, Boretti et al., 2021, Cao et al., 2020, Shayan et al., 2018). However, large-scale hydrogen storage has been a serious problem due to the cost and safety issues (Lemieux et al., 2020, Zhang et al., 2016). One effective solution to this challenge is underground hydrogen storage (UHS) (Pfeiffer and Bauer, 2015, Iglauer, 2022). During the UHS process, hydrogen is injected into caverns artificially made in thick underground salt formations (Caglayan et al., 2020, Ozarslan, 2012) or other porous geological formations (e.g. depleted hydrocarbon reservoirs (Hemme and Van Berk, 2018, Pfeiffer and Bauer, 2015), coal seams (Keshavarz et al., 2022, Iglauer et al., 2022), and deep saline aquifers (Hassannayebi et al., 2019, Sáinz-García et al., 2017)). The hydrogen can then be withdrawn again when the need arises (Heinemann et al., 2021).

To prevent hydrogen from upward migration, an impermeable layer known as caprock (e.g., shale or evaporite with low permeability ($<10^{-21}$ m^2) and porosity (Hangx et al., 2011)) is required to seal the permeable reservoir rock. Moreover, basaltic rocks have recently been recommended as an unconventional medium for hydrogen storage (Hosseini et al., 2022b). In this regard, the wetting and interface characteristics of the rock/hydrogen/water system are critical parameters for gas geo-storage, which control gas storage capability and capillary sealing efficiency of caprocks (safe immobilization of gas beneath the caprocks) (Crotogino et al., 2010, Broseta et al., 2012, Hosseini et al., 2022c). The hydrogen wettability of minerals/rocks at geo-storage conditions (e.g.

quartz (Iglauer et al., 2021b), mica (Ali et al., 2021d), clay (Al-Yaseri et al., 2021c), calcite (Hosseini et al., 2022e), shale and evaporite (Hosseini et al., 2022c), and basalt (Hosseini et al., 2022b)) has been recently reported in the literature. However, these studies which are based on wetting characteristics of the minerals/rocks have not investigated the rock/fluid interfacial tension (IFT). Rock-gas interfacial tension ($\gamma_{rock\text{-}gas}$), rock-water interfacial tension ($\gamma_{rock\text{-}water}$), and water-gas interfacial tension ($\gamma_{water\text{-}gas}$) are three interface characteristics that determine the wetting characteristics in a rock/gas/water system (Young, 1805, Al-Yaseri et al., 2022b, N. Yekeen, 2022). Among these three interfacial tensions, $\gamma_{water\text{-}gas}$ is the only one that can be experimentally quantified, however, there is no independent experimental technique to quantify $\gamma_{rock\text{-}gas}$ and $\gamma_{rock\text{-}water}$ as there is no mobility at the rock interface (Li and Neumann, 1992, Abdulelah et al., 2021). Consequently, numerical/theoretical techniques are required to compute the rock-fluid interfacial tensions.

Unfortunately, $\gamma_{rock\text{-}fluid}$ for rock/H_2/water systems under geo-storage conditions has rarely been reported in the literature. The Neumann's equations of state were firstly applied to determine surface tensions of low energy solids from contact angles (Neumann et al., 1974). A few studies have recently computed $\gamma_{rock\text{-}fluid}$ via combination of the Young-Laplace equation and Neumann's equations of state. Pan et al. (2021) (Pan et al., 2021a) reported rock-gas and rock-water interfacial tensions for quartz/basalt-H_2-water systems at $T \leq 343$ K and $p \leq 20$ MPa. They showed that rock-water interfacial tension increased with organic acid concentration. However, rock-H_2 interfacial tension decreased with pressure, temperature, and organic acid concentration. Ali et al. (2022) (Ali et al., 2022b) reported rock-gas and rock-water interfacial tensions for mica-H_2-water systems at $p \leq 20$ MPa and $T \leq 343$ K. They found that rock-gas interfacial tension decreased with organic acid concentration, alkyl chain length, and pressure, but increased with nano-alumina concentration. More recently, (N. Yekeen, 2022) predicted rock-gas interfacial tension for clay/H_2/water systems. They found that clay minerals showed higher values of interfacial tension with H_2 compared to N_2 and CO_2. They also reported that kaolinite showed higher values of interfacial tension with H_2 among the clay minerals, although the differences are negligible.

However, there is a clear paucity of rock-fluid interfacial tension ($\gamma_{rock\text{-}fluid}$) data for rock/$H_2$/water systems in different shale, evaporite, and basaltic formations at geological conditions. Moreover, the subsurface rocks (specially shales, evaporite, and basaltic rocks studied in this work) do not

consist of only one mineral (which has been considered as benchmark in the previous works). Hence, the related structural storage capacities of shale, evaporite, and basaltic rocks are still unknown. Thus, we applied advancing and receding contact angles in the Neumann's equations of state to calculate rock-fluid interfacial tensions for rock/H_2/water systems in different shale, evaporite, and basaltic formations at geological conditions. This work thus gives essential information for the successful fulfillment of the UHS beneath caprocks and basaltic formations.

7.2 Methodology

The focus of this study is to calculate rock-hydrogen and rock-water interfacial tensions using the contact angle and liquid-gas interfacial tension data from literature (Hosseini et al., 2022d, Hosseini et al., 2022c, Hosseini et al., 2022b). The equilibrium contact angle (θ_e) for a solid/gas/water system is related to solid-gas interfacial tension (γ_{sg}), solid-water interfacial tension (γ_{sw}), and water-gas interfacial tension (γ_{wg}) as follows (Young, 1805):

$$\cos\theta_e = \frac{\gamma_{sg} - \gamma_{sw}}{\gamma_{wg}}. \tag{7.1}$$

To calculate the θ_e, the experimental receding (θ_r) and advancing (θ_a) contact angles data taken from (Hosseini et al., 2022c) were used. Table 7-1 gives the calculated θ_e and water-gas interfacial tension data at various temperatures and pressures for shale/H_2/water, oil shale/H_2/water, evaporite/H_2/water, and basalt/H_2/water systems. Tadmor's empirical technique was used to calculate θ_e (Tadmor, 2004):

$$\theta_e = \arccos\left(\frac{\eta_a \cos\theta_a + \eta_r \cos\theta_r}{\eta_a + \eta_r}\right), \tag{7.2}$$

where η_a and η_r are calculated as follows:

$$\eta_a = \left(\frac{\sin^3\theta_a}{\cos^3\theta_a - 3\cos\theta_a + 2}\right)^{1/3}, \tag{7.3}$$

$$\eta_r = \left(\frac{\sin^3 \theta_r}{\cos^3 \theta_r - 3\cos \theta_r + 2} \right)^{1/3}. \tag{7.4}$$

Neumann's equation of state was then applied for the calculation of rock-hydrogen and rock-water interfacial tensions at geo-storage conditions, which can be expressed for γ_{sg}, $\gamma_{sw,}$ and γ_{wg} as follows (Neumann et al., 1974, Li and Neumann, 1992):

$$f(\gamma_{sg}, \gamma_{sw}, \gamma_{wg}) = 0. \tag{7.5}$$

According to the reformed Neumann's equation of state proposed by (Ameri et al., 2013), γ_{sg} and γ_{sw} can be derived by the combination of the geometric means of solid/liquid cohesion works as follows:

$$\gamma_{sg} = \gamma_{sw} + \gamma_{wg} - 2\sqrt{\gamma_{sw}\gamma_{wg}} \left[1 - \beta \left(\gamma_{sw} - \gamma_{wg} \right)^2 \right], \tag{7.6}$$

$$\gamma_{sw} = \gamma_{sg} + \gamma_{wg} - 2\sqrt{\gamma_{sg}\gamma_{wg}} \left[1 - \beta \left(\gamma_{sg} - \gamma_{wg} \right)^2 \right], \tag{7.7}$$

where β is a constant. The combination of Eq. (7.1) and Eq. (7.6) derives:

$$\cos \theta_e = 1 - 2\sqrt{\frac{\gamma_{sw}}{\gamma_{wg}}} \left[1 - \beta \left(\gamma_{wg} - \gamma_{sw} \right)^2 \right]. \tag{7.8}$$

Thus, a nonlinear fit of input parameters ($\cos \theta_e$ and γ_{wg}) given in Table 7-1 is used to determine the fitting parameters (β and γ_{sw}), e.g. Table 7-2. While γ_{sg} and γ_{wg} depend on temperature and pressure, γ_{sw} is assumed to be independent of pressure (Ameri et al., 2013, Neumann et al., 1974). When the values of β and γ_{sw} are known, γ_{sg} can then be computed using Eq. (7.1) or Eq. (7.6).

Table 7-1 Input parameters (cos θ_e and γ_{wg}) required for the calculation of the fitting parameters (β and γ_{sw}) at various T and p for different rock/H_2/water systems (data taken from (Hosseini et al., 2022d, Hosseini et al., 2022b, Hosseini et al., 2022c), see Chapters 3, 5 and 6).

System	TOC (wt %)	rock composition from XRD	T (K)	p (MPa)	cos θ_e	γ_{wg} (mN/m)
shale A/H_2/water	0.08	quartz (28 wt %), dolomite (3 wt %), calcite (58 wt %), muscovite-illite (8 wt %), chlorite (2 wt %), hematite (1 wt %)	298	5	0.91	75.06
				10	0.85	74.29
				15	0.78	73.53
				20	0.71	72.76
			353	5	0.96	63.67
				10	0.93	63.15
				15	0.89	62.63
				20	0.87	62.11
shale B/H_2/water	0.1	quartz (30 wt %), kaolinite (7 wt %), siderite (6 wt %), muscovite-illite (33 wt %), chlorite (16 wt %), anatase (1 wt %), albite (4 wt %), potassium feldspar (1 wt %), goethite (2 wt %)	298	5	0.96	75.06
				10	0.92	74.29
				15	0.88	73.53
				20	0.84	72.76
			353	5	0.99	63.67
				10	0.98	63.15
				15	0.96	62.63
				20	0.95	62.11
shale C/H_2/water	0.09	quartz (25 wt %), chlorite (20 wt %), siderite (2 wt %), muscovite-illite (27 wt %), amorphous (10 wt %), anatase (1 wt %), albite (10 wt %), smectite group (5 wt %)	298	5	0.97	75.06
				10	0.96	74.29
				15	0.95	73.53
				20	0.94	72.76
			353	5	0.99	63.67
				10	0.98	63.15
				15	0.98	62.63
				20	0.97	62.11
evaporite/H_2/water	0.01	anhydrite (1 wt %), gypsum (99 wt %)	298	5	0.98	75.06
				10	0.98	74.29
				15	0.97	73.53
				20	0.97	72.76
			353	5	0.99	63.67
				10	0.99	63.15
				15	0.99	62.63
				20	0.98	62.11
basalt/H_2/water	0.05	Anorthite (55 wt %), Augite (25 wt %), Orthoclase (16 wt %), Lizardite (4 wt %)	308	5	0.86	73.05
				10	0.69	72.33
				15	0.60	71.61
				20	0.53	70.88
			343	5	0.70	66.02
				10	0.53	65.46

				15	0.42	64.89
				20	0.39	64.32
oil shale A/H_2/water	4.95	pyrite (6 wt %), calcite (28 wt %), dolomite (30 wt %), quartz (12 wt %), potassium feldspar (4 wt %), illite (15 wt %), amorphous (5 wt %)	323	5	0.68	70.04
				15	0.47	68.73
oil shale B/H_2/water	14	pyrite (3 wt %), calcite (56 wt %), dolomite (3 wt %), quartz (9 wt %), potassium feldspar (4 wt %), gypsum (1 wt %), amorphous (20 wt %), clay mineral (4 wt %)	323	5	0.33	70.04
				15	0.11	68.73

Table 7-2 Fitting parameters (β and γ_{sw}) for different rock/H_2/water systems at various temperatures.

System	T (K)	β	γ_{sw} (mN/m)
shale A/H_2/water	298	0.000866	42.12
	353	0.000584	23.01
shale B/H_2/water	298	0.000439	28.17
	353	0.000305	6.97
shale C/H_2/water	298	0.000189	4.46
	353	0.00025	1.69
evaporite/H_2/water	298	0.000173	1.42
	353	0.000243	0.66
basalt/H_2/water	308	0.00228	51.16
	343	0.0036	53.01
oil shale A/H_2/water	323	0.00594	57.92
oil shale B/H_2/water	323	0.01819	63.54

7.3 Results and discussion

The rock-fluid interfacial tension in caprocks plays a key role in their structural sealing potentials during UHS (Hosseini et al., 2022c, Ali et al., 2022b). This key factor can be influenced by many geo-storage conditions. For example, pressure, temperature, and TOC are parameters which are expected to change significantly with formation depth (Tiab and Donaldson, 2015). The caprocks have also clearly different mineralogy (Hosseini et al., 2022c). Thus, in this study, $\gamma_{rock\text{-}fluid}$ was specially investigated as a function of some real geo-storage conditions such as pressure, temperature, TOC, and mineralogy (based on data taken from our previously published works (Hosseini et al., 2022d, Hosseini et al., 2022b, Hosseini et al., 2022c)).

7.3.1 Influence of pressure and temperature on rock-fluid interfacial tension of rock/H_2/water system

For all the rock/H_2/water systems, θ_e increased with pressure (decrease in water wettability at constant temperature), Table 7-1. This is because the inter-particle energy between rock and gas increases with pressure (Iglauer et al., 2012). However, rock-gas interfacial tension ($\gamma_{rock\text{-}gas}$) decreased with pressure (Figure 7-1). For example, at 298.15 K, $\gamma_{shale\ A\text{-}H2}$ declined by 16 mN/m (110.31 mN/m to 94.02 mN/m) when pressure increased from 5 MPa to 20 MPa, Figure 7-1a. Similarly, at 308.15 K and the same pressure increase, $\gamma_{basalt\text{-}H2}$ declined by 25 mN/m (115.64 mN/m to 90.58 mN/m), Figure 7-1d. However, at 298.15 K and with the same pressure increase, $\gamma_{evaporite\text{-}H2}$ had a lower decrease from 75.12 mN/m to 71.65 mN/m, Figure 7-1e. The decrease in $\gamma_{rock\text{-}gas}$ with pressure is confirmed by the literature data (e.g. (Al-Yaseri et al., 2021a, Arif et al., 2016b, Pan et al., 2020a, Pan et al., 2021a, Dickson et al., 2006)). This trend is attributed to the reduction in difference between cohesive energy density (CED, an intermolecular interaction energy) of gas and CED of rock at elevated pressure (Arif et al., 2016b). While the CED of rock is larger than that of gas and does not change with pressure, the CED of the gas increases with pressure and comes close to the CED of rock. This reduction in gas/rock CEDs difference results in a favorable interaction between the gas and rock (as a strong energy surface such as rock tends to reduce its energy by adsorption of gas (Tripp and Combes, 1998)), thus $\gamma_{rock\text{-}gas}$ decreases with pressure (Dickson et al., 2006). This favorable interaction between H_2 and rock with pressure can

also be attributed to the increase in gas density and its tendency to be adsorbed on the rock surface. However, as the change in water density with pressure is not considerable (water is incompressible), the variation of intermolecular forces between rock and water is negligible, resulting in a very low change in $\gamma_{rock\text{-}water}$ with pressure. Based on Equation (7.1), cos θ_e increases with $\gamma_{rock\text{-}gas}$, but decreases with $\gamma_{rock\text{-}water}$ and $\gamma_{water\text{-}gas}$. Thus, the variation in the interfacial tensions with pressure can be interpreted by the variation in cos θ_e. For all the rocks studied in this work, the decrease in cos θ_e with pressure at a constant temperature is related to the reduction in $\gamma_{rock\text{-}gas}$. However, the decrease in cos θ_e is not related to $\gamma_{water\text{-}gas}$ and $\gamma_{rock\text{-}water}$ because $\gamma_{water\text{-}gas}$ slightly decreases and $\gamma_{rock\text{-}water}$ is assumed to be constant with pressure (e.g., see Fig. 7-2 for shale A/H_2/water system). This implies that $\gamma_{rock\text{-}gas}$ is the main parameter influenced by the variation in wettability with pressure in the rocks.

For shale/H_2/water and evaporite/H_2/water systems, θ_e decreased with temperature (due to the decrease in gas density and thus the intermolecular forces and interfacial energy between gas and rock). However, for the basalt/H_2/water system, θ_e increased with temperature (due to breaking hydrogen bonds between water molecules and silanol groups on the basalt surface). For all the rock/H_2/water systems, $\gamma_{rock\text{-}gas}$ decreased with temperature. For instance, at 10 MPa, $\gamma_{shale\ A\text{-}H2}$ declined by 23 mM/m (104.94 mN/m - 81.57 mN/m) when the temperature increased from 298.15 K to 353.15 K, Figure 7-1a. Similarly, at 10 MPa when the temperature increased from 308.15 K to 343.15 K, $\gamma_{basalt\text{-}H2}$ declined by 17 mN/m (103.05 mN/m to 85.82 mN/m), Figure 7-1d. However, at the same conditions, $\gamma_{evaporite\text{-}H2}$ had a lower decrease by 11 mN/m (74.02 mN/m to 63.20 mN/m), Figure 7-1e. The decrease in $\gamma_{rock\text{-}H2}$ with temperature is consistent with (Pan et al., 2021a, Ali et al., 2022b). However, some studies (e.g., (Arif et al., 2016b, Ali et al., 2022b, Abdulelah et al., 2021)) showed that $\gamma_{rock\text{-}CO2}$ increases with temperature, implying that the effect of temperature on $\gamma_{rock\text{-}gas}$ depends on the gas type (Ali et al., 2022b). This may be due to the different thermodynamic properties such as diffusion mechanisms (Kubica and Wolinska-Grabczyk, 2015) or different molecular properties such as quadrupole moment (which is strong in CO_2 compared to H_2) (Buckingham and Longuet-Higgins, 1968) with temperature between the gases. For shale/H_2/water and evaporite/H_2/water systems, $\gamma_{rock\text{-}water}$ decreased with temperature. For instance, $\gamma_{shale\ A\text{-}water}$ declined by 19 mN/m (42.12 mN/m to 23.01 mN/m), when the temperature increased from 298.15 K to 353.15 K, Table 7-2. This decrease in $\gamma_{rock\text{-}water}$ with the same increase in temperature was also obtained for the evaporite/H_2/water system, although it was very smooth (1.42 mN/m to 0.66

mN/m). However, for the basalt/H_2/water system, water molecules are desorbed from the basalt surface, implying that the effect of temperature on $\gamma_{rock\text{-}water}$ depends on the rock type (Pan et al., 2021a). For example, the different behavior in $\gamma_{rock\text{-}water}$ with temperature between basalt and evaporite (or shale) is explained by breaking hydrogen bonds between silanol groups (OH functional groups) on the basalt surface and water with temperature (analogous to quartz/H_2/water system (Janczuk and Zdziennicka, 1994, Chen et al., 2015a)). Thus $\gamma_{basalt\text{-}water}$ increases accordingly. The variation in the interfacial tensions with temperature can be interpreted by the variation in cos θ_e. For all the rocks, the increase in cos θ_e with the temperature at constant pressure is related to the reduction in $\gamma_{water\text{-}gas}$ and $\gamma_{rock\text{-}water}$ ($\gamma_{rock\text{-}gas}$ which is in the numerator of Equation (7.1) also decreases with temperature, thus, it is not effective in the increase in cos θ_e). This implies that $\gamma_{water\text{-}gas}$ and $\gamma_{rock\text{-}water}$ are the main parameters influenced by the variation in wettability with temperature in the rocks (e.g., see Fig. 7-2 for shale A/H_2/water system).

7.3.2 Influence of TOC on rock-fluid interfacial tension of shale/H_2/water systems

It is widely reported in the literature that the wetting characteristics and interfacial phenomena of geological formations (especially caprocks) can be considerably affected by the presence of organic matter (Arif et al., 2017a, Ali et al., 2022c, Lundegard and Kharaka, 1994, Akob et al., 2015). As the presence of organic matter in subsurface rocks is inevitable, we thus analyzed the effect of TOC on $\gamma_{shale\text{-}fluid}$. As can be seen from Table 7-1, θ_e increased with TOC. At the test pressure range and constant temperature, $\gamma_{shale\text{-}water}$ increased with TOC, Figure 7-3a. For instance, at 323.15 K, $\gamma_{shale\text{-}water}$ increased from 38.1 mN/m to 63.54 mN/m when TOC increased from 0.08 wt % to 14 wt %. This is consistent with (Pan et al., 2021a) and attributed to the increased hydrophobicity of the rock surface (surface de-wetting) with TOC (Arif et al., 2017a), where repulsed water molecules need more energy for spreading on the rock surface, which increases $\gamma_{shale\text{-}water}$. However, $\gamma_{shale\text{-}gas}$ decreased with TOC, Figure 7-3b. At 323.15 K and 5 MPa, $\gamma_{shale\text{-}gas}$ decreased from 103.26 mN/m to 86.85 mN/m when TOC increased from 0.08 wt % to 14 wt %. This decrease is also confirmed by (Pan et al., 2021a) and attributed to less energy needed for gas molecules to spread on the rock surface when hydrophobicity increases with TOC. The variation in the interfacial tensions with shale-TOC can be interpreted by the variation in cos θ_e. For oil shales, the decrease in cos θ_e with TOC at constant pressure and temperature is related to the

reduction in $\gamma_{rock\text{-}gas}$ and increase in $\gamma_{rock\text{-}water}$, while $\gamma_{water\text{-}gas}$ is constant (Fig. 7-4). It implies that $\gamma_{rock\text{-}gas}$ and $\gamma_{rock\text{-}water}$ are the main parameters influenced by the variation in wettability with TOC in oil shales.

7.3.3 Influence of mineralogy on rock-fluid interfacial tension of rock/H_2/water systems

The rock mineralogy of shales plays a crucial role in determining the wetting characteristics and therefore, significantly affecting the rock-fluid interfacial tension. For example, various minerals including quartz, calcite, feldspars, mica (e.g., muscovite), and clays (e.g., illite, chlorite, and kaolinite) can be found in the structure of shales (Hosseini et al., 2022c). Thus, the rock-fluid interfacial tension can be considerably affected by the mineral dominance, specifically in low-TOC rocks. As the wettability of the high-TOC shales (oil shales) is significantly influenced by their TOC (Hosseini et al., 2022c), their rock-fluid interfacial tensions are also influenced by their TOC (Fig. 7-3). For example, the high $\gamma_{rock\text{-}fluid}$ of shale A compared to that of shale B and shale C can be explained by the calcite dominance (58%, Table 7-1) in the mineralogy as calcite has high hydrophobicity. Also, clay + mica dominance in shale B is more than that in shale C, resulting in more $\gamma_{rock\text{-}fluid}$ in shale B (Pan et al., 2020c). Analogous to shale A, calcite is the dominant mineral for oil shale B (56%), making both more H_2-wet than other rocks. However, the higher $\gamma_{rock\text{-}water}$ of oil shales compared to that of other low-TOC rocks is also attributed to the remarkable difference in TOC. The high $\gamma_{rock\text{-}fluid}$ of basalt is also attributed to the higher content of plagioclase minerals which leads to a more hydrophobic rock. The evaporite sample (99% gypsum) and shale C have low $\gamma_{rock\text{-}water}$, implying that water molecules need low energy for spreading on the surfaces of these rocks to make them water-wet. Thus, the evaporite and shale C have more sealing efficiency than other rocks (Hosseini et al., 2022c).

In this study, the effect of some geo-storage conditions such as pressure, temperature, shale-TOC, and mineralogy on $\gamma_{rock\text{-}fluid}$ was investigated. However, these parameters may not cover all the real conditions for subsurface geological formations. For example, subsurface rocks such as caprocks have different mineralogy or wetting characteristics which may significantly affect the $\gamma_{rock\text{-}fluid}$ (Arif et al., 2016b). Thus, exact determination of the mineralogy using XRD analysis is essential for the assessment of the $\gamma_{rock\text{-}fluid}$. Other important parameters for real storage conditions are brine salinity (which can reach very high concentration) and ion type (which can be monovalent such as

Na^+, K^+, Cl^- or divalent such as Ca^{2+}, Mg^{2+}, CO_3^{2-}, SO_4^{2-}) as these parameters affect the wettability and $\gamma_{fluid\text{-}fluid}$ (Chen et al., 2017) thus the $\gamma_{rock\text{-}fluid}$. For example, the ions concentration needed for making a neutral surface increases with salinity (reduced surface polarity, e.g. (Arif et al., 2016a)), resulting in decrease in van der Waals forces between water and rock, which leads to higher $\gamma_{rock\text{-}water}$ (e.g. (Arif et al., 2016b)). As all data required for the $\gamma_{rock\text{-}fluid}$ calculation were taken from our previously published works (Hosseini et al., 2022d, Hosseini et al., 2022b, Hosseini et al., 2022c), we specially analyzed the effect of pressure, temperature, TOC, and mineralogy on $\gamma_{rock\text{-}fluid}$ (note that there was no literature data for ion type, valence and salinity for hydrogen system of the studied rocks). Thus, the effect of other parameters such as salinity and ion type can be potentially investigated in future research. These analyses help characterize the optimal conditions required for successful UHS.

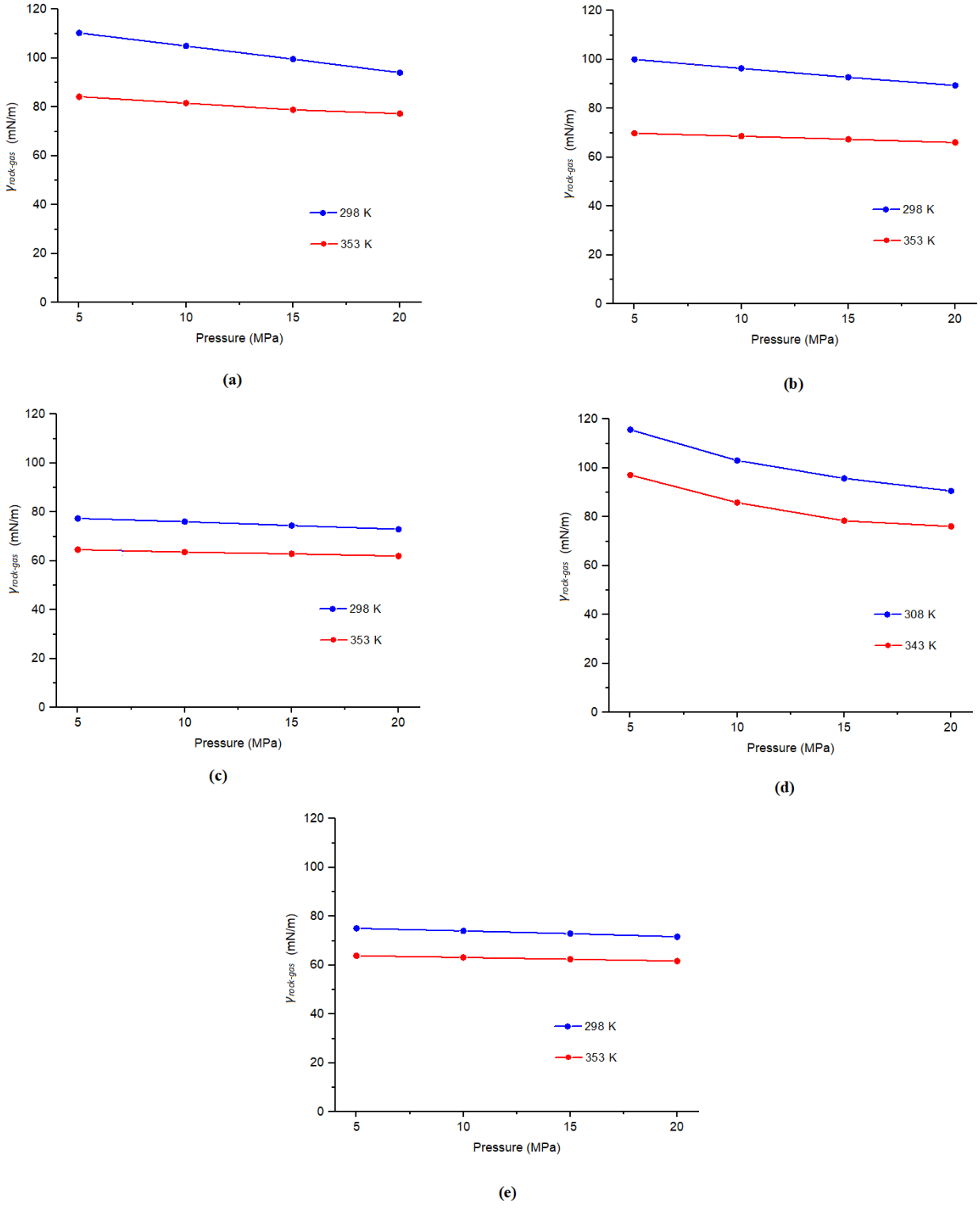

Fig. 7-1 Influence of temperature and pressure on rock-gas interfacial tension. (a) shale A/H_2/water, (b) shale B/H_2/water, (c) shale C/H_2/water, (d) basalt/H_2/water, and (d) evaporite/H_2/water.

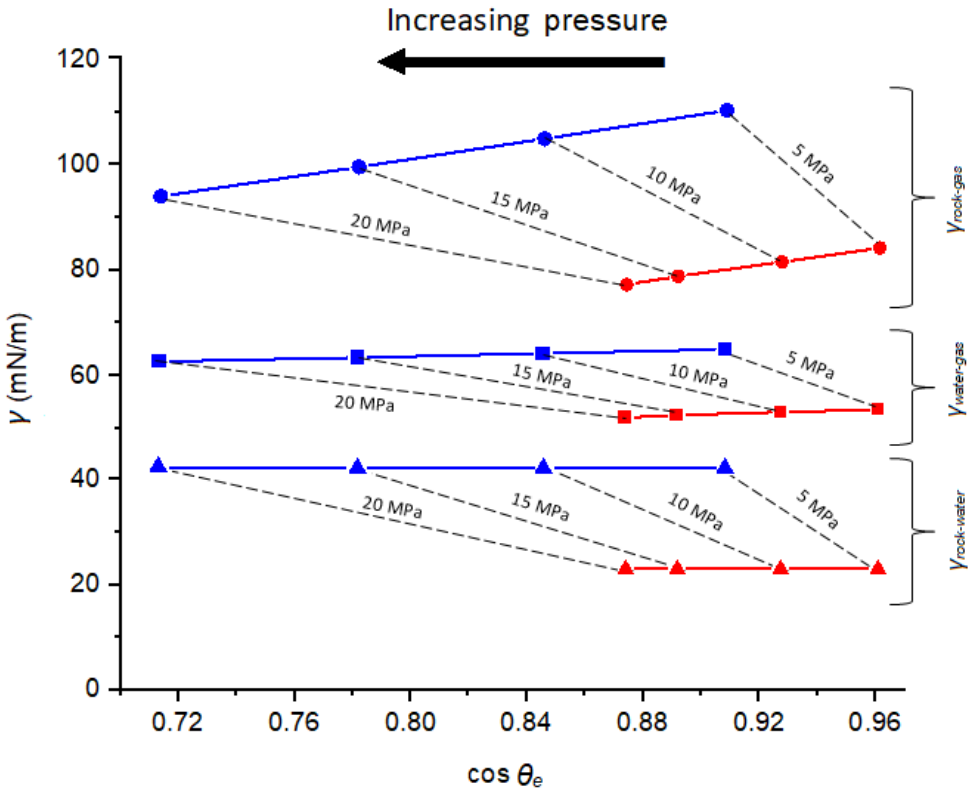

Fig. 7-2 Investigation of the main interfacial tensions influenced by the variation in wettability with pressure and temperature for shale A/H_2/water system. The blue and red lines show temperatures of 298 K and 353 K, respectively.

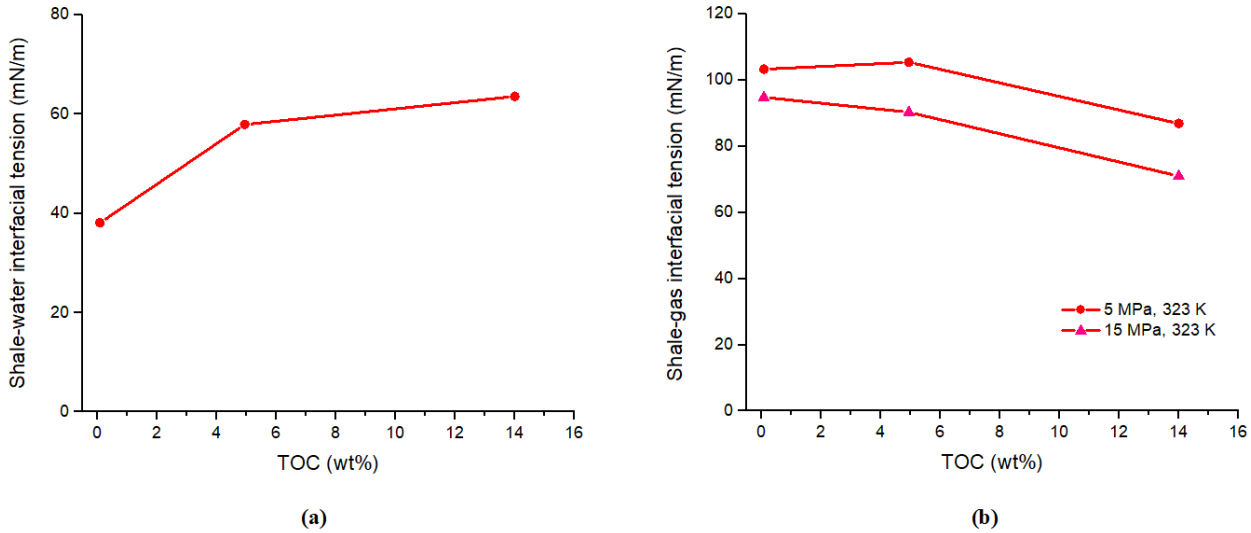

Fig. 7-3 Influence of TOC on shale-fluid interfacial tensions. (a) $\gamma_{shale\text{-}water}$ and (b) $\gamma_{shale\text{-}gas}$.

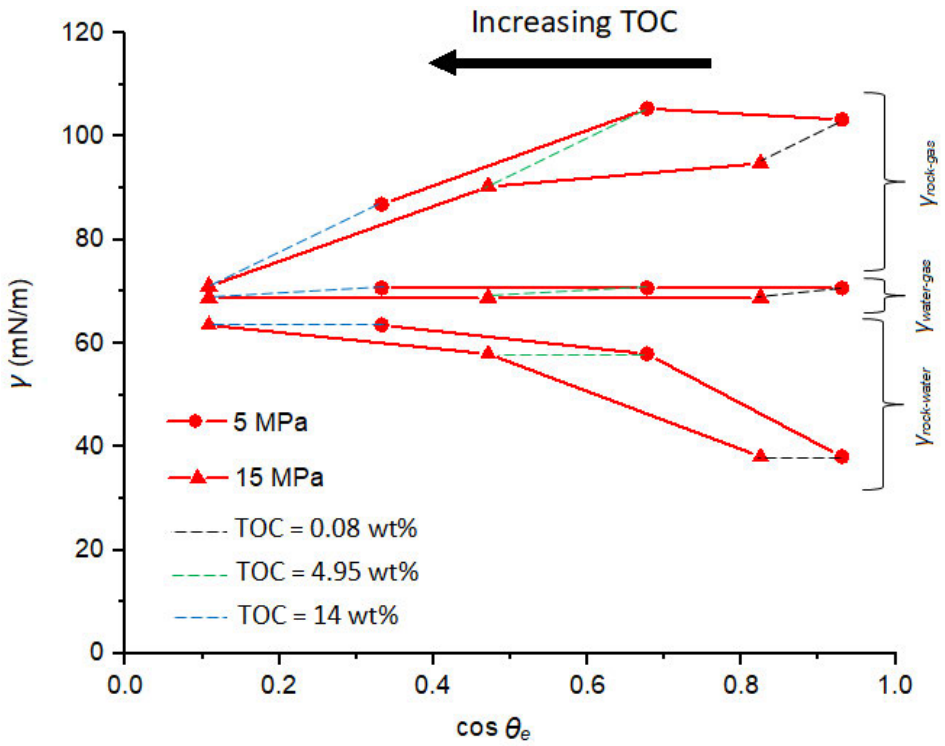

Fig. 7-4 Investigation of the main interfacial tensions influenced by the variation in wettability with shale-TOC.

7.4 Conclusions

One of the critical parameters for UHS is $\gamma_{rock\text{-}fluid}$ which controls gas storage capacity (Iglauer et al., 2015b, Ali et al., 2022b, Ali et al., 2021d), injection and production rate (Jha et al., 2021), spreading and flow in porous media (Al-Khdheeawi et al., 2017a, Al-Khdheeawi et al., 2017b), and containment security (Arif et al., 2016b). For example, as water-wet caprocks exhibit higher $\gamma_{rock\text{-}gas}$, they have strong H_2-storage potential (structural storage) due to the high tendency of H_2 in sticking to the rock (Iglauer et al., 2015a). However, there is no experimental technique for measuring the $\gamma_{rock\text{-}fluid}$ (Butt et al., 2013), resulting in the paucity of $\gamma_{rock\text{-}fluid}$ data for shale, evaporite, and basaltic rocks in the literature. Thus, $\gamma_{rock\text{-}fluid}$ for these rocks at geo-storage conditions was mathematically calculated by the combination of Young's equation and Neumann's equation of state. The results showed that $\gamma_{rock\text{-}gas}$ decreased with pressure, temperature, and shale-TOC. $\gamma_{rock\text{-}gas}$ is the main parameter influenced by the variation in wettability with pressure (in all rocks) and shale-TOC. Thus, gas molecules can easily wet the shale, evaporite, and basaltic rocks

with high pressure and high shale-TOC values (unfavorable conditions for sealing H_2). Moreover, $\gamma_{rock\text{-}water}$ decreased with temperature but increased with shale-TOC, indicating that hot rocks with low shale-TOC values may provide ideal conditions for hydrogen geo-storage sealing capacity. We conclude that $\gamma_{rock\text{-}fluid}$ data for various geo-storage conditions (such as pressure, temperature, and shale-TOC) is crucial for accurate estimation of gas storage capacity in UHS projects beneath caprocks and basaltic formations.

Chapter 8 Calcite-fluid interfacial tension: H_2 and CO_2 geological storage in carbonates

Published in *Energy & Fuels*, ACS Publications 2023, 37, 8, 5986–5994
DOI: https://doi.org/10.1021/acs.energyfuels.3c00399

Abstract

Underground hydrogen storage (UHS) and CO_2 geological storage (CGS) are two outstanding techniques for meeting universal energy demand and reducing anthropogenic greenhouse gases (GHGs). In this context, calcite-fluid interfacial tension ($\gamma_{calcite\text{-}fluid}$) is a critical parameter for gas storage in carbonate formations as it drives fluids spreading and flow in porous media, gas injection/withdrawal rate, gas storage capacity, and containment safety. Moreover, it is one of the factors responsible for the wettability alteration in carbonates. However, there is a scarcity of $\gamma_{calcite\text{-}fluid}$ data (e.g., $\gamma_{calcite\text{-}gas}$ and $\gamma_{calcite\text{-}water}$ for carbonate/gas/water systems) at geological conditions in the literature. Additionally, there is no independent experimental method to measure $\gamma_{rock\text{-}fluid}$, thus advancing and receding contact angles are often used to calculate it by the combination of Neumann's equation of state and Young's equation. We, therefore, theoretically calculated $\gamma_{calcite\text{-}fluid}$ as a function of the main geological parameters, including temperature, pressure, organic acid concentration, and salinity for calcite/H_2/water and calcite/CO_2/water systems. We recognized that $\gamma_{calcite\text{-}gas}$ decreased with pressure, salinity, and organic acid concentration but increased with temperature. Also, a slight increase in $\gamma_{calcite\text{-}water}$ with organic acid concentration and salinity was noticed at (15 MPa, 323.15 K) and (10 MPa, 323.15 K), respectively. However, the $\gamma_{calcite\text{-}water}$ slightly decreased with temperature by assuming that it remained constant with pressure. Furthermore, the values for $\gamma_{calcite\text{-}fluid}$ for H_2/brine system were more than that for CO_2/brine system. This work thus provides a deep understanding of wetting characteristics at calcite/H_2/water and calcite/CO_2/water interfaces and leads to a better investigation of H_2/CO_2 storage in carbonate formations.

Keywords

Calcite-gas interfacial tension, calcite-water interfacial tension, H_2 and CO_2 geo-storage, carbonates, contact angle

8.1 Introduction

The large-scale hydrogen economy might one day attain great value throughout the world which can provide a solution for mitigating human-caused emissions of greenhouse gases and meeting the increased worldwide energy need (Zivar et al., 2021, Caglayan et al., 2020, Lankof and Tarkowski, 2020, Lemieux et al., 2020). Hydrogen is produced via different methods like electrolysis, methane bi-reforming, biomass gasification, and solar thermochemistry (Arribas et al., 2018, Boretti et al., 2021, Cao et al., 2020, Chen et al., 2020, Kumar and Himabindu, 2019, Shayan et al., 2018, Wang et al., 2021). However, its storage at the surface is very complex due to its volatility and compressibility. An effective solution to this issue can be underground hydrogen storage (UHS), where hydrogen is injected into a geo-storage site [e.g., depleted hydrocarbon reservoirs, coal seams, and deep saline aquifers (Hassannayebi et al., 2019, Hemme and Van Berk, 2018, Aslannezhad et al., 2023)] and withdrawn again when the need arises. CO_2 geological storage (CGS) is a procedure where CO_2 is injected into a geo-storage site (e.g. one of the above-mentioned sites) for limiting anthropogenic greenhouse gas emissions and also for enhanced hydrocarbon recovery (Boot-Handford et al., 2014, Ettehadtavakkol et al., 2014, Metz et al., 2005, Blunt et al., 1993). Moreover, CO_2 has been proposed to be injected as cushion gas for the hydrogen retrieval at peak demand times (Iglauer et al., 2021b, Aslannezhad et al., 2023).

In this setting, the wetting characteristics of the rock/gas/water system drives the ability to spread gas across the formation and immobilize it beneath a caprock via containment security (Crotogino et al., 2010, Broseta et al., 2012). Recently, a few studies have reported the hydrogen wettability of minerals at geo-storage conditions (e.g., quartz (Hashemi et al., 2021b, Iglauer et al., 2021b), mica (Ali et al., 2021d, Ali et al., 2022c), clay (Al-Yaseri et al., 2021c), and calcite (Hosseini et al., 2022e)). However, these studies are based on wetting characteristics where information for rock/fluid interfacial tension (IFT) has not been investigated before. According to the Young-Laplace equation, contact angle for a solid/gas/water system is related to solid-gas interfacial

tension (γ_{sg}), solid-water interfacial tension (γ_{sw}), and water-gas interfacial tension (γ_{wg}) as follows (Young, 1805):

$$\cos\theta = \frac{\gamma_{sg} - \gamma_{sw}}{\gamma_{wg}}. \tag{8.1}$$

Thus, these three interfacial tensions are integral parts to measure the wettability, which need to be experimentally determined. Unlike γ_{wg} which can be measured experimentally (e.g., (Kashefi et al., 2016, Li et al., 2012a)), there is no independent experimental method to measure γ_{sg} and γ_{sw} (due to lack of mobility at rock interface; e.g., (Li and Neumann, 1992)). Notably, most of contact angle systems for wettability measurements are made of stainless steel material and it is shown in previous studies that metal embrittlement occurs due to hydrogen gas, which can cause leakages in the system (Lord, 2009, Zivar et al., 2021). Therefore, mathematical/theoretical methods such as Dickson et al.'s method (Dickson et al., 2006) and Neumann's equation of state (Neumann et al., 1974) are needed to be used for the calculation of γ_{sg} and γ_{sw} (Neumann et al., 1974). The technique developed by (Dickson et al., 2006) is complicated as it needs many surface interfacial tension components (e.g., hydrogen bonding, dispersion force, quadrupole interactions, and dipole interactions) for all three phase (rock/gas/water) to calculate γ_{sg} and γ_{sw} (Binks and Clint, 2002, Fowkes, 1963). However, the reformed version of the Neumann's equation of state (Ameri et al., 2013) combined with the Young-Laplace equation calculates γ_{sg} and γ_{sw} using the advancing/receding contact angle and fluid/fluid interfacial tension data.

A few studies have used the Young-Laplace equation and Neumann's equations of state to compute $\gamma_{rock\text{-}fluid}$ at gas geo-storage conditions. For example, (Ameri et al., 2013) reported $\gamma_{sandstone\text{-}CO2}$ at $p \leq 16$ MPa and $T = 318$ K. (Kaveh et al., 2016) calculated $\gamma_{shale\text{-}water}$ at $p \leq 15$ MPa and $T = 318$ K. (Arif et al., 2016b) computed $\gamma_{rock\text{-}CO2}$ and $\gamma_{rock\text{-}water}$ for quartz, mica, and coal at $p \leq 20$ MPa and $T \leq 343$ K. (Pan et al., 2020a) calculated $\gamma_{quartz\text{-}CH4}$, $\gamma_{quartz\text{-}CO2}$, and $\gamma_{quartz\text{-}water}$ at $p \leq 20$ MPa and $T \leq 353$ K. Furthermore, (Pan et al., 2021a) reported quartz/basalt-H_2, quartz/basalt-CO_2, quartz-CH_4, and quartz-water interfacial tensions at $T \leq 343$ K and $p \leq 20$ MPa. Moreover, (Al-Yaseri et al., 2021a) calculated shale-CO_2 interfacial tension at $p \leq 20$ MPa and $T = 343$ K. Also, (Ali et al., 2022b) reported $\gamma_{mica\text{-}CO2}$, $\gamma_{mica\text{-}H2}$, and $\gamma_{mica\text{-}water}$ at $p \leq 20$ MPa and $T \leq 343$ K. More recently,

(Hosseini et al., 2022a) assessed $\gamma_{rock\text{-}H2}$ and $\gamma_{rock\text{-}water}$ for shale, evaporite and basaltic rocks at $p \leq$ 20 MPa and $T \leq 353$ K.

Unfortunately, there is a clear paucity of data for rock-fluid interfacial tension ($\gamma_{rock\text{-}fluid}$) in carbonate formations at geological conditions. Thus, based on the available data, we calculated $\gamma_{calcite\text{-}H2}$, $\gamma_{calcite\text{-}CO2,}$ and $\gamma_{calcite\text{-}water}$ as a function of pressure, temperature, salinity, and organic acid concentration for calcite/H_2/water and calcite/CO_2/water systems via Neumann's equations of state using advancing and receding contact angles. This work thus gives essential information for the successful fulfillment of the UHS and CGS in carbonates.

8.2 Methodology

8.2.1. Calculation

First, we applied experimental receding (θ_r) and advancing (θ_a) contact angles data (taken from (Hosseini et al., 2022e) and (Arif et al., 2017a), see Fig. 8-1 for a schematic of the contact angle system; note a detailed description of the system with procedure for the measurements was given in our previous studies (Hosseini et al., 2022b, Hosseini et al., 2022c, Hosseini et al., 2022e)) to compute the equilibrium contact angle (θ_e) given in Tables 8-1, 8-3, and 8-4 using Tadmor's empirical technique defined as follows (Tadmor, 2004):

$$\theta_e = \arccos\left(\frac{\eta_a \cos\theta_a + \eta_r \cos\theta_r}{\eta_a + \eta_r}\right), \tag{8.2}$$

where η_a and η_r are calculated as follows:

$$\eta_a = \left(\frac{\sin^3\theta_a}{\cos^3\theta_a - 3\cos\theta_a + 2}\right)^{1/3}, \tag{8.3}$$

$$\eta_r = \left(\frac{\sin^3\theta_r}{\cos^3\theta_r - 3\cos\theta_r + 2}\right)^{1/3}. \tag{8.4}$$

Neumann's equation of state was then applied for the calculation of calcite-gas and calcite-water interfacial tensions at geo-storage conditions, which can be expressed for γ_{sg}, $\gamma_{sw,}$ and γ_{wg} as follows (Neumann et al., 1974, Li and Neumann, 1992):

$$f(\gamma_{sg},\gamma_{sw},\gamma_{wg})=0. \tag{8.5}$$

According to the reformed Neumann's equation of state proposed by (Ameri et al., 2013), γ_{sg} and γ_{sw} can be derived by the combination of the geometric means of solid/liquid cohesion works as follows:

$$\gamma_{sg}=\gamma_{sw}+\gamma_{wg}-2\sqrt{\gamma_{sw}\gamma_{wg}}\left[1-\beta\left(\gamma_{sw}-\gamma_{wg}\right)^2\right], \tag{8.6}$$

$$\gamma_{sw}=\gamma_{sg}+\gamma_{wg}-2\sqrt{\gamma_{sg}\gamma_{wg}}\left[1-\beta\left(\gamma_{sg}-\gamma_{wg}\right)^2\right], \tag{8.7}$$

where β is a constant. The combination of Eq. (8.1) and Eq. (8.6) derives:

$$\cos\theta_e=1-2\sqrt{\frac{\gamma_{sw}}{\gamma_{wg}}}\left[1-\beta\left(\gamma_{wg}-\gamma_{sw}\right)^2\right]. \tag{8.8}$$

Thus, a nonlinear fit of input parameters ($\cos\theta_e$ and γ_{wg}) given in Tables 8-1, 8-3, and 8-4 is used to determine the fitting parameters (β and γ_{sw}), e.g. Table 8-2. While γ_{sg} and γ_{wg} depend on temperature, pressure, organic acid concentration and salinity, γ_{sw} is assumed to be independent of pressure (Ameri et al., 2013, Neumann et al., 1974). Notably, γ_{wg} data for H_2/water and CO_2/water were taken from (Hosseini et al., 2022d) and (Arif et al., 2016a, Georgiadis et al., 2010, Sarmadivaleh et al., 2015), respectively. When the values of β and γ_{sw} are known, γ_{sg} can then be computed using Eq. (8.1) or Eq. (8.6). Fig. 8-2 shows a simple flowchart for the calculation of $\gamma_{rock\text{-}fluid}$. The average standard deviation of the $\gamma_{rock\text{-}fluid}$ calculations based on the contact angle experimental errors was ±2 mN/m.

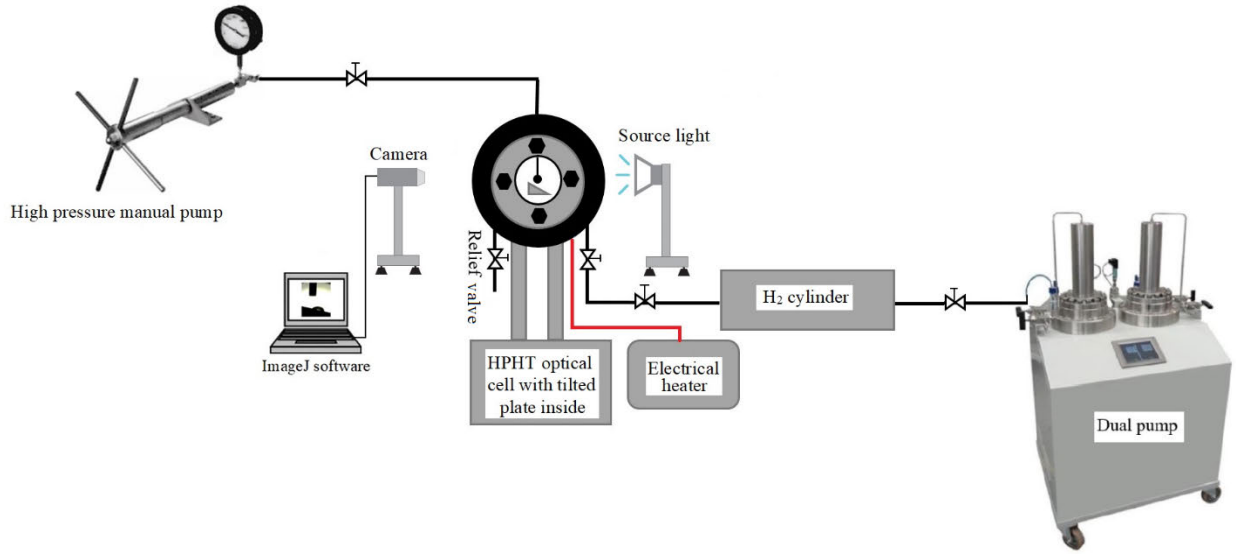

Fig. 8-1 Schematic of the high-pressure high-temperature (HPHT) experimental setup for contact angle measurements (Hosseini et al., 2022b, Hosseini et al., 2022c, Hosseini et al., 2022d).

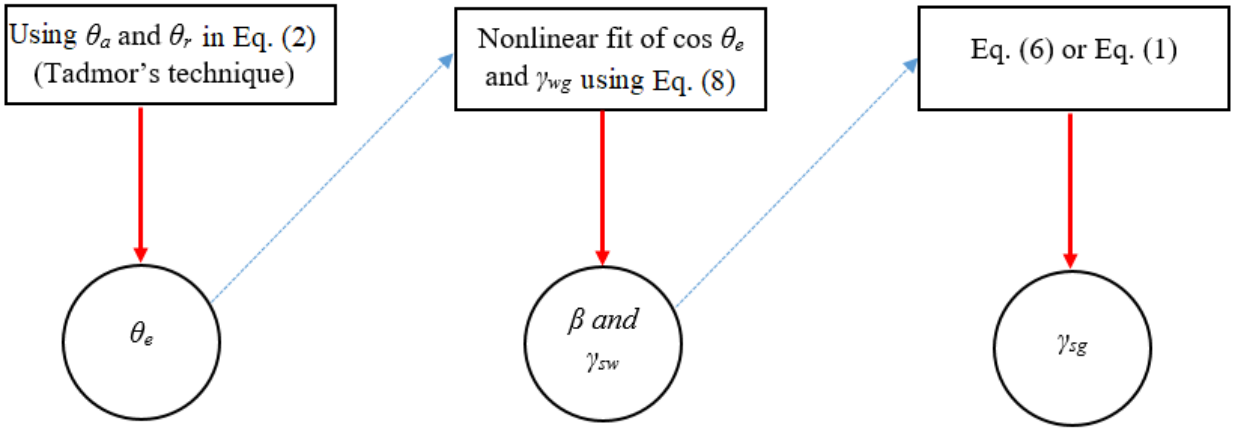

Fig. 8-2 A simple flowchart for the calculation of $\gamma_{rock\text{-}fluid}$ using the combination of Neumann's equation of state and Young-Laplace equation.

8.2.2 Validation

It is notable that the calculated values of $\gamma_{rock\text{-}fluid}$ were applied to predict θ using Eq. (8.1). Thus, the predicted θ was compared with the experimental θ to validate the model results (Tables 8-1, 8-3, and 8-4). The results show that there is good match between the calculated and experimental

contact angles, implying the correctness of the methodology applied in this work for reproducing the original experimental θ. The root mean square error (RMSE) for the results was 3º.

Table 8-1 Data needed for calculating the fitting parameters (β and γ_{sw}) and predicting contact angle at various temperatures and pressures for calcite/H_2/water and calcite/CO_2/water systems.

Calcite/H_2/DI-water					Calcite/CO_2/DI-water				
T (K)	p (MPa)	γ_{wg} (mN/m)[a]	Experimental θ (°)[b]	Predicted θ (°)	T (K)	p (MPa)	γ_{wg} (mN/m)[c]	Experimental θ (°)[d]	Predicted θ (°)
298	5	74	63	66	298	5	40	77	76
	10	73	75	72		10	28	89	91
	15	72	78	78		15	23	99	100
	20	72	82	83		20	21	104	103
323	5	69	49	51	323	5	49	33	31
	10	68	61	58		10	36	63	65
	15	67	64	64		15	29	78	78
	20	67	70	70		20	26	85	84
353	5	62	33	37	343	5	52	22	26
	10	62	53	48		10	43	39	36
	15	61	55	56		15	36	44	44
	20	61	63	64		20	27	49	50

[a]Taken from (Hosseini et al., 2022d), see Chapter 3

[b]Taken from (Hosseini et al., 2022e), see Chapter 4

[c]Taken from (Arif et al., 2016a, Georgiadis et al., 2010, Sarmadivaleh et al., 2015)

[d]Taken from (Arif et al., 2017a)

Table 8-2 Results of β for calcite/H_2/water and calcite/CO_2/water systems at various temperatures.

Calcite/H_2/DI-water		Calcite/CO_2/DI-water	
T (K)	β	T (K)	β
298	0.00237	298	0.00016
323	0.00291	323	0.00047
353	0.00609	343	0.00026

Table 8-3 Data needed for calculating the fitting parameters (β and γ_{sw}) and predicting contact angle at T = 323 K, p = 15 MPa and different salinities for calcite/H_2/water and calcite/CO_2/water systems.

Calcite/H_2/water				Calcite/CO_2/water			
m (mol/kg)	γ_{wg} (mN/m)[a]	Experimental θ (°)[b]	Predicted θ (°)	m (mol/kg)	γ_{wg} (mN/m)[c]	Experimental θ (°)[d]	Predicted θ (°)
0	67	67	67	0	32	78	78
1.05	69	69	68	0.85	33	79	78
3.15	71	71	70	1.71	35	84	80
4.95	74	74	71	2.57	36	88	81
				3.42	37	89	81

[a]Taken from (Hosseini et al., 2022d)

[b]Taken from (Hosseini et al., 2022e)

[c]Taken from (Arif et al., 2016a, Georgiadis et al., 2010, Sarmadivaleh et al., 2015)

[d]Taken from (Arif et al., 2017a)

Table 8-4 Data needed for calculating the fitting parameters (β and γ_{sw}) and predicting contact angle at T = 323 K, p = 10 MPa and different organic surface concentrations for calcite/H_2/water and calcite/CO_2/water systems.

Calcite/H_2/water				Calcite/CO_2/water			
c (mol/L)	γ_{wg} (mN/m)[a]	Experimental θ (°)[b]	Predicted θ (°)	c (mol/L)	γ_{wg} (mN/m)[c]	Experimental θ (°)[d]	Predicted θ (°)
10^{-2}	68	113	113	10^{-2}	36	127	127
10^{-3}	68	109	109	10^{-3}	36	120	122
10^{-5}	68	100	102	10^{-5}	36	114	118
10^{-7}	68	85	88	10^{-7}	36	101	96
10^{-9}	68	72	77	10^{-9}	36	87	89

[a]Taken from (Hosseini et al., 2022d)

[b]Taken from (Hosseini et al., 2022e)

[c]Taken from (Arif et al., 2016a, Georgiadis et al., 2010, Sarmadivaleh et al., 2015)

[d]Taken from (Arif et al., 2017a)

8.3 Results and discussion

There are various thermophysical parameters such as pressure, temperature and salinity which can vary underground (Hosseini, 2016, Hosseini, 2018, Hosseini et al., 2014) and significantly affect the $\gamma_{rock\text{-}fluid}$ (Arif et al., 2016b, Arif et al., 2017a). Moreover, the presence of organic matters in subsurface rocks can severely affect the wetting characteristics and interfacial phenomena, where reductive conditions ensue (Iglauer et al., 2021b). Because subsurface rocks have an organic matter to some extent (various alkyl chain lengths, i.e., small to long chains (Ali et al., 2022c)) we analyzed the influence of stearic acid C_{18} (which is commonly found in the geological formations (Akob et al., 2015, Hosseini et al., 2022b, Lundegard and Kharaka, 1994)) concentration on $\gamma_{rock\text{-}fluid}$. It is notable that fluids equilibration time and rock surface roughness are two important experimental factors which can also affect the $\gamma_{rock\text{-}fluid}$ by changing interface and wetting characteristics of the rock-fluid and fluid-fluid systems (e.g., $\gamma_{fluid\text{-}fluid}$ can be affected by the fluids equilibration time (Hosseini et al., 2022d), while contact angle can be affected by both the fluids equilibration time and rock surface roughness (Hosseini et al., 2022e)). However, the data used in this study shows that adequate time was given to the rock-fluid and fluid-fluid systems to reach equilibrium at the desired test conditions (e.g., see (Hosseini et al., 2022d, Hosseini et al., 2022e)). Also, the used samples were carefully polished to minimize the effect of rock surface roughness on the contact angle (i.e., all surface roughness values were < 1 μm, see (Arif et al., 2017a, Hosseini et al., 2022e)); note that a surface roughness of < 1 μm does not significantly affect the contact angle measurements (Al-Yaseri et al., 2016, Marmur, 2006). Thus, at the time of the experiments, the effects of these two factors on the measurements were minimized.

In the following, the effect of each thermophysical parameter and organic surface concentration on $\gamma_{rock\text{-}fluid}$ is discussed.

8.3.1 Influence of pressure on $\gamma_{rock\text{-}fluid}$ of unaged calcite sample

The equilibrium contact angle increased with increase in pressure (due to the increased inter-particle energy between rock and gas, Table 8-1). For both H_2/water and CO_2/water systems, rock-gas interfacial tension ($\gamma_{rock\text{-}gas}$) decreased when pressure increased at constant temperatures (Fig. 8-3). For example, at 323.15 K, $\gamma_{rock\text{-}H2}$ declined from 97.1 mN/m to 75.1 mN/m once pressure was

raised from 5 MPa to 20 MPa. Similarly, at 323.15 K and the same pressure conditions, $\gamma_{rock\text{-}CO2}$ declined from 48.7 mN/m to 9.6 mN/m. The literature data (e.g. (Arif et al., 2016b, Pan et al., 2021a, Dickson et al., 2006, Pan et al., 2020a, Al-Yaseri et al., 2021a, Abdulelah et al., 2021)) confirms this trend which is explained by the decrease in the difference of gas/rock cohesive energy densities (CEDs) at elevated pressure (due to the increase in CED of the gas, which comes close to the CED of rock), which leads to the favorable interaction between the gas and rock (Dickson et al., 2006). Notably, $\gamma_{rock\text{-}water}$ is considered to be constant as the water density does not have a significant effect due to an increase in pressure, resulting in a negligible variation of intermolecular forces between rock and water with pressure. However, in reality, it is expected that the rock-water interactions change with pressure as gas solubility in water increases with pressure (El-Maghraby et al., 2012). In case of CO_2 system, pH decreases due to increased solubility with pressure (Adamczyk et al., 2009), which can affect the interface and wetting characteristics of rock/fluid systems (Xie et al., 2018).

Also, $\gamma_{rock\text{-}CO2}$ is more than $\gamma_{rock\text{-}H2}$ because CO_2 has more density compared to H_2 (Ali et al., 2021d, Iglauer et al., 2021b, Al-Yaseri et al., 2016). For instance, the densities of H_2 and CO_2 at (20 MPa and 323.15 K) are 13.5 kg/m^3 and 785.2 kg/m^3, respectively (Leachman et al., 2009, Span and Wagner, 1996). A similar difference in $\gamma_{rock\text{-}gas}$ between CO_2/water and H_2/water systems was also observed for quartz and basaltic rock (Pan et al., 2021a).

8.3.2 Influence of temperature on $\gamma_{rock\text{-}fluid}$ of unaged calcite sample

The equilibrium contact angle decreased with temperature (due to the decreased intermolecular forces and interfacial energy between gas and rock, Table 8-1). Figure 8-4 gives the results of unaged calcite-water interfacial tension for both H_2/water and CO_2/water systems at various temperatures. For each system, the $\gamma_{rock\text{-}water}$ declined with temperature rise. For instance, the $\gamma_{rock\text{-}water}$ for H_2/water system declined from 57 mN/m to 50.30 mN/m once temperature was raised from 298 K to 353 K. Similarly, the rock-water interfacial tension for CO_2/water system decreased from 8.30 mN/m to 1.30 mN/m by increasing temperature from 298 K to 343 K. The literature data (e.g. for mica/CO_2 and coal/CO_2 (Arif et al., 2016b)) confirms this trend. It is notable that for quartz/gas/water systems, water molecules are desorbed from quartz surface (due to the breaking of hydrogen bonds between silanol groups and water) with temperature (Janczuk and Zdziennicka,

1994, Chen et al., 2015a), and thus $\gamma_{quartz\text{-}water}$ increases accordingly (Arif et al., 2016b, Pan et al., 2020a, Pan et al., 2021a).

For both H_2/water and CO_2/water systems, $\gamma_{rock\text{-}gas}$ increased with temperature (Fig. 8-3). For instance, when temperature was increased from 298 K to 353 K at 15 MPa, $\gamma_{rock\text{-}H2}$ rose from 71.5 mN/m to 85.1 mN/m. Similarly, $\gamma_{rock\text{-}CO2}$ increased from 4.6 mN/m to 26.3 mN/m once temperature was raised from 298 K to 343 K at 15 MPa. This increase is compatible with quartz/CO_2, mica/CO_2, and coal/CO_2 interfacial tensions (Arif et al., 2016b, Pan et al., 2020a) but inconsistent with quartz/H_2 and quartz/CH_4 interfacial tensions (Pan et al., 2021a), implying that the influence of temperature on $\gamma_{rock\text{-}gas}$ depends on the gas type. The increase in rock-gas interfacial tensions with increase in temperature is attributed to the fact that the CED of gas decreases with increase in temperature (Barton, 2017), whereas the CED of rock is assumed to remain steady with increase in temperature (Kittel and McEuen, 2018). This causes a rise in the difference between gas and rock CEDs at elevated temperatures and a less favorable interaction between the gas and rock (Dickson et al., 2006), resulting in the decrease in adsorption capacity with temperature due to the increase in kinetic energy and diffusion rate of gas (Perera et al., 2011, Sakurovs et al., 2007, Arif et al., 2016c). It is notable that when the temperature increases, the decrease in CO_2 density is more than that in H_2 density, leading to more decrease in intermolecular interactions and more increase in $\gamma_{rock\text{-}gas}$ in CO_2/water system compared to H_2/water system (Van Oss et al., 1986).

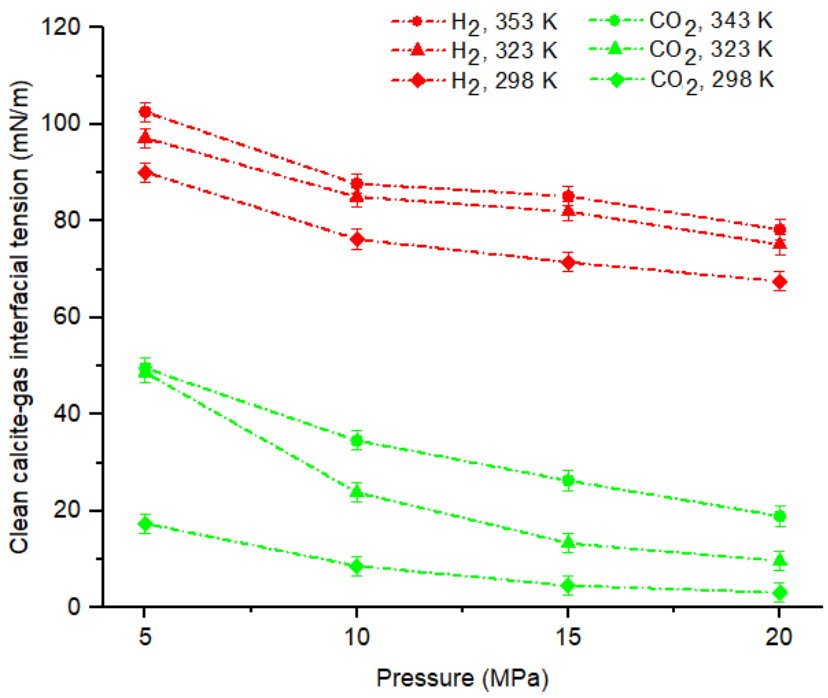

Fig. 8-3 Influence of temperature and pressure on unaged calcite-gas IFTs.

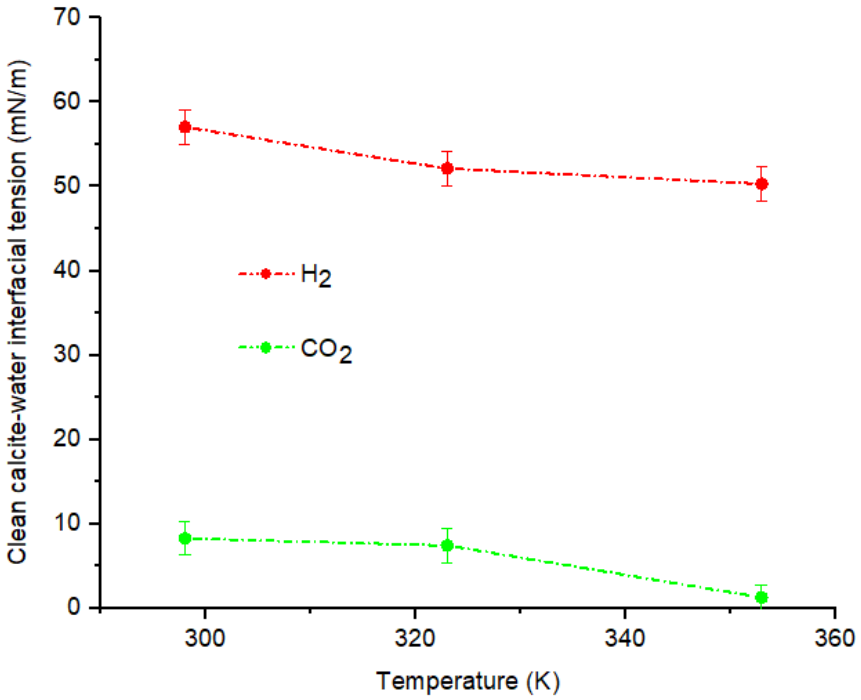

Fig. 8-4 Influence of temperature on unaged calcite-water IFTs.

8.3.3 Influence of salinity on $\gamma_{rock\text{-}fluid}$ of unaged calcite sample

The equilibrium contact angle increased with increase in salinity (*m*) due to the reduced surface polarity, Table 8-3. Moreover, the unaged calcite-brine interfacial tension slightly increased with salinity for both H_2/water and CO_2/water systems at constant temperature and pressure, Fig. 8-5. At the temperature of 323.15 K and pressure of 15 MPa, the $\gamma_{rock\text{-}water}$ for H_2/water system went up from 50 mN/m to 57.15 mN/m once salinity was raised by 4.95 mol/kg. Similarly, at the same temperature and pressure, the $\gamma_{rock\text{-}water}$ for CO_2/water system increased from 7.11 mN/m to 12.76 mN/m once salinity was raised from 0 mol/kg to 3.42 mol/kg (this salinity range was taken from (Arif et al., 2016b)). The literature data (e.g. mica/CO_2 (Arif et al., 2016b) and sandstone/CO_2 (Ameri et al., 2013)) confirms this trend. The concentration of ions required for making a neutral surface increases with salinity (reduced surface polarity, e.g. (Arif et al., 2016a, Iglauer, 2017)). As a result, van der Waals forces (weak intermolecular forces for attracting molecules to each other (Van Oss et al., 1986)) between rock and water decrease, which leads to higher rock-water interfacial tensions.

For H_2/water system, $\gamma_{rock\text{-}gas}$ decreased very slightly but remained constant for CO_2/water system with salinity at constant temperature and pressure, Fig. 8-6. At 15 MPa and 323.15 K, $\gamma_{rock\text{-}H2}$ declined from 76.84 mN/m to 73.89 mN/m once salinity was raised by 4.95 mol/kg (this salinity range was taken from (Hosseini et al., 2022d)), thus a decrease of only 3 mN/m with salinity. At the same pressure and temperature, when salinity was raised from 0 mol/kg to 3.42 mol/kg, $\gamma_{rock\text{-}CO2}$ remained constant (~ 13.5 mN/m), consistent with (Arif et al., 2016b) and implying that salinity does not have a considerable effect on the $\gamma_{rock\text{-}gas}$.

It is notable that apart from salinity, the ion type (which can be monovalent such as K^+, Na^+, Cl^- or divalent such as SO_4^{2-}, CO_3^{2-}, Mg^{2+}, Ca^{2+}) can also be another influencing factor on $\gamma_{calcite\text{-}fluid}$ as it affects the wettability and $\gamma_{fluid\text{-}fluid}$ (Chen et al., 2017). However, in this study, the effect of ion type on $\gamma_{calcite\text{-}fluid}$ was not analyzed as the required data for its calculation is not available in literature. Thus, the effect of ion type on $\gamma_{fluid\text{-}fluid}$ can be potentially investigated in future research.

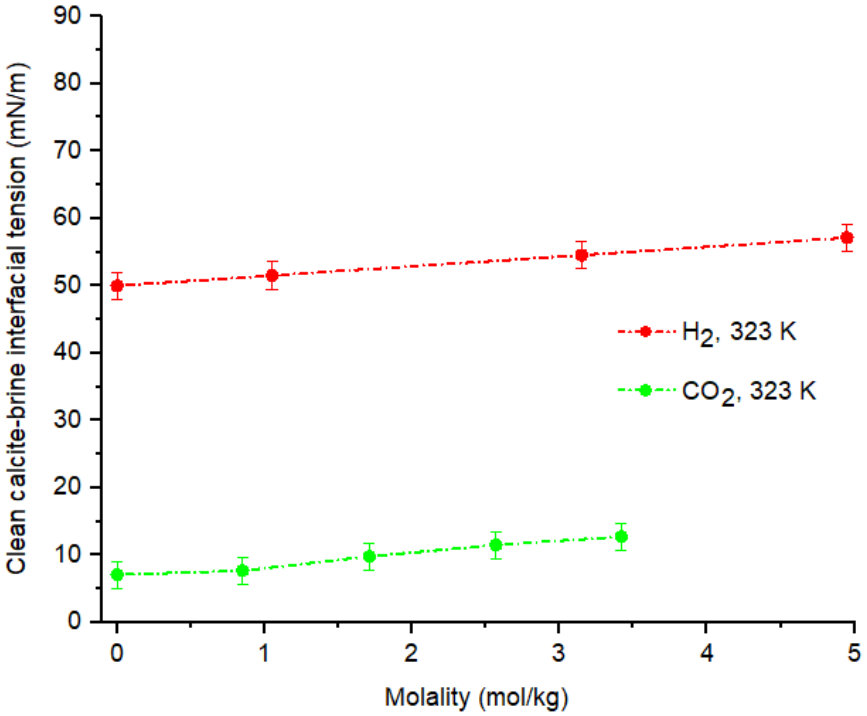

Fig. 8-5 Influence of salinity on unaged calcite-brine IFTs at 15 MPa and 323.15 K.

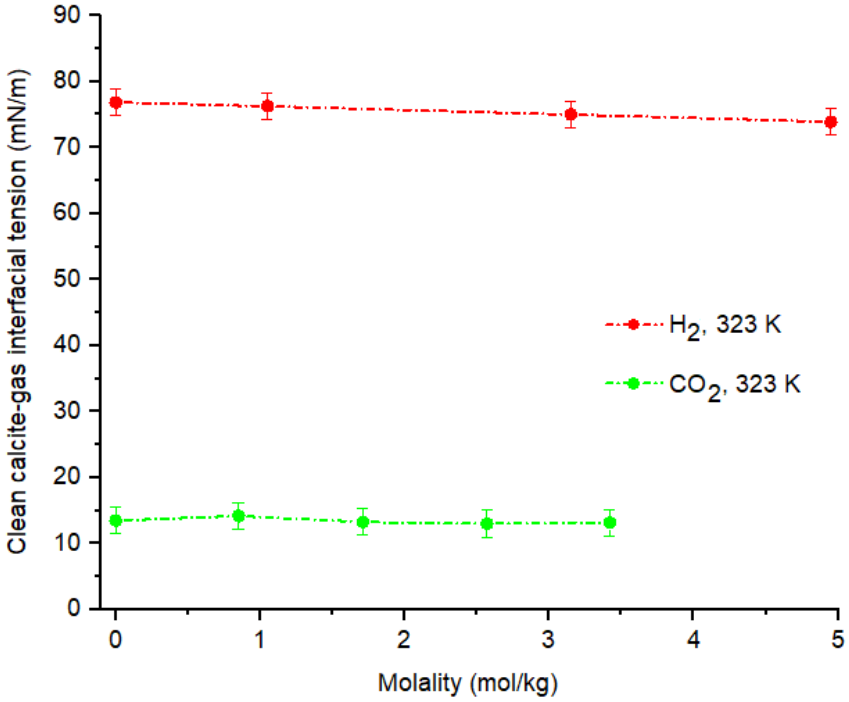

Fig. 8-6 Influence of salinity on unaged calcite-gas IFTs at 15 MPa and 323.15 K.

8.3.4 Influence of organic matters on $\gamma_{rock\text{-}fluid}$ of organic-aged calcite sample

With increasing the acid concentration (*c*), the equilibrium contact angle increased due to the increased hydrophobicity of the rock surface, Table 8-4. For both H_2/water and CO_2/water systems, organic aged calcite-water interfacial tension slightly rose with *c* at constant pressure and temperature, Fig. 8-7. At 323.15 K and 10 MPa, when *c* was raised from 10^{-9} mol/L to 10^{-2} mol/L, the $\gamma_{rock\text{-}water}$ for H_2/water system went up from 51 mN/m to 56.10 mN/m. Similarly, at the same temperature, pressure, and increase in stearic acid concentration, the $\gamma_{rock\text{-}water}$ for CO_2/water system increased from 10.13 mN/m to 18.81 mN/m. The literature data (e.g. quartz/H_2 and quartz/CO_2 (Pan et al., 2021a)) confirms this trend as the rock surface hydrophobicity rises due to the adsorbed organic molecules on the surface (Abramov et al., 2019, Iglauer et al., 2021b, Ali et al., 2022c). Therefore, repulsed water molecules need more energy to spread on the rock surface (increase in $\gamma_{rock\text{-}water}$).

However, for both H_2/water and CO_2/water systems, $\gamma_{rock\text{-}gas}$ decreased with organic acid concentration (Fig. 8-8). At 323.15 K and 10 MPa, $\gamma_{rock\text{-}H2}$ declined from 71.77 mN/m to 29.26 mN/m once acid concentration was raised from 10^{-9} mol/L to 10^{-2} mol/L. Similarly, at the same temperature, pressure, and increase in stearic acid concentration, the $\gamma_{rock\text{-}gas}$ for CO_2/water system decreased from 19.22 mN/m to 9.43 mN/m. This decrease is also confirmed by the literature data (e.g. quartz/H_2 and quartz/CO_2 (Pan et al., 2021a)) and is because gas molecules need less energy to spread on the rock surface when hydrophobicity increases with organic acid concentration.

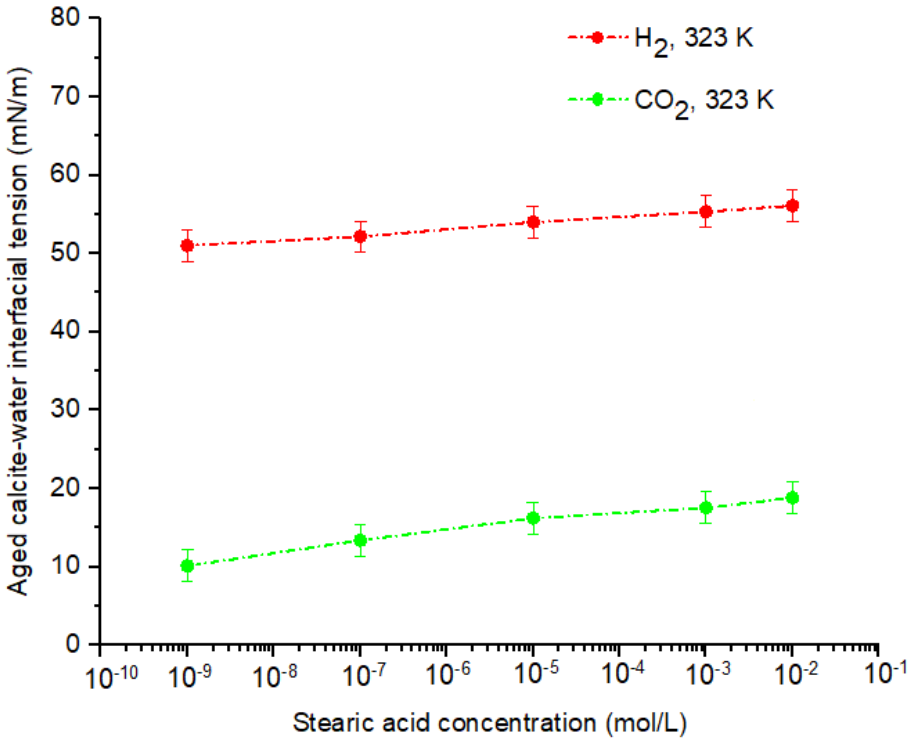

Fig. 8-7 Effect of organic matters on organic aged calcite-water IFTs at 10 MPa and 323.15 K.

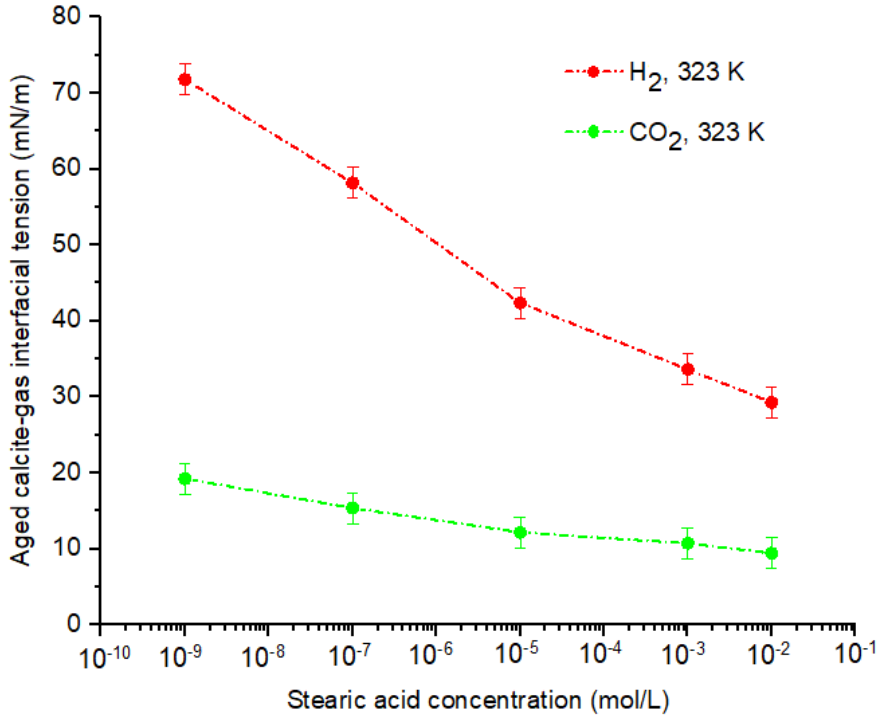

Fig. 8-8 Influence of organic matter on organic aged calcite-gas IFTs at 10 MPa and 323.15 K.

8.4 Implications

One of the key surface properties controlling the gas storage capacity in geological formations is wettability which is influenced by dynamic intermolecular interactions and affects the ability of fluid adsorption on a rock surface in the presence of another fluid (De Gennes, 1985). Unlike the contact angle (θ) and γ_{wg} given in Equation (8.1), the rock-fluid interfacial tensions ($\gamma_{rock\text{-}fluid}$) cannot be experimentally measured (Butt et al., 2013). However, $\gamma_{rock\text{-}fluid}$ can be computed via indirect methods such as Neumann's equations of state (Neumann et al., 1974) and molecular dynamic simulation (Good and Girifalco, 1960). Therefore, the reported $\gamma_{rock\text{-}fluid}$ in this study is significantly important to accurately evaluate gas storage capacity in UHS and CGS projects in carbonate formations. For example, a water-wet calcite-rich rock has high structural storage capacity due to its high $\gamma_{rock\text{-}gas}$ (the high tendency of rock to hold gas in pores (Arif et al., 2016d)). Moreover, $\gamma_{rock\text{-}fluids}$ are integral parameters for the evaluation of wettability at geo-storage conditions. For instance, for a calcite-rich rock, cos θ decreases with increase in pressure at a constant temperature due to the reduction in γ_{sg} (γ_{wg} slightly decreases but γ_{sw} assumed to be constant with pressure), implying that γ_{sg} is the main parameter influenced by wettability alteration with pressure in carbonates. However, cos θ increases with temperature (due to the increase in γ_{sg} and decrease in γ_{wg} and γ_{sw}) but decreases with salinity (due to the decrease in γ_{sg} and increase in γ_{wg} and γ_{sw}), implying that all three interfacial tensions expressed in Eq. (8.1) (γ_{sg}, γ_{sw}, γ_{wg}) are influenced by wettability alteration with temperature and salinity in geological formations (e.g., carbonates). Furthermore, the diverse wetting behavior of calcite caused by the presence of organic acid influences on the behavior of $\gamma_{rock\text{-}fluid}$. For example, for a water-wet calcite-rich rock with low organic acid concentration where cos $\theta > 0$, γ_{sg} is greater than γ_{sw}. However, for a gas-wet calcite-rich rock with high organic acid concentration where cos $\theta < 0$, γ_{sg} is lower than γ_{sw} (γ_{wg} is constant). This implies that γ_{sg} and γ_{sw} are the main parameters influenced by wettability variation with organic surface concentration in carbonates.

It is worth noting that the applied technique is quite straightforward, and the results can be easily validated with the experimental contact angle data. Thus, although the technique was applied only on calcite as a proxy for carbonates, it can also be used on other carbonate minerals (e.g., dolomite) or a carbonate rock with mixed mineralogy (e.g., calcite + dolomite) if the contact angle data is

available. Thus, the calculations on other carbonate minerals can be potentially investigated in future research.

8.5 Conclusions

$\gamma_{rock\text{-}fluid}$ is a critical parameter for UHS and CGS in carbonates as it controls fluids spreading and flow in porous media, gas storage capacity, and containment safety. However, there is a paucity of $\gamma_{rock\text{-}fluid}$ data for carbonates in the literature, specifically due to technical limitations for measuring it via experimental methods. Thus, we necessarily used Neumann's equations of state to calculate $\gamma_{rock\text{-}fluid}$ for carbonates at geo-storage conditions. The key findings of the study are as follows:

1. $\gamma_{rock\text{-}gas}$ decreased with pressure, salinity, and organic surface concentration but increased with temperature, implying that gas molecules can easily wet the rock surfaces at carbonate reservoirs with high pressure, high brine salinity, and high organic concentration (favorable conditions for adsorption trapping due to increased affinity of the gas and rock but unfavorable conditions for structural trapping in carbonates), whereas hot carbonate reservoirs could provide ideal conditions for structural trapping (unfavorable for adsorption trapping).

2. Two slight increase trends in $\gamma_{rock\text{-}water}$ with organic acid concentration at (323.15 K and 10 MPa) and salinity at (323.15 K and 15 MPa) were observed.

3. $\gamma_{rock\text{-}gas}$ for calcite/H_2/brine system was more than that for calcite/CO_2/brine system, indicating that at similar geo-storage conditions, CO_2 can more easily occupy small pores (more adsorption trapping) but be less structurally stored in carbonates compared to H_2 as CO_2-wettability of carbonates is always more than H_2-wettability of carbonates.

We conclude that $\gamma_{rock\text{-}fluid}$ (solid surface energy) data can effectively help optimize wettability dependence on gas geological storage conditions such as pressure, temperature, organic acid concentration and salinity, which will aid in accurate estimation of gas storage capacity in UHS and CGS projects in carbonate formations.

Chapter 9 Hydrogen-wettability alteration of Indiana limestone in the presence of organic acids and nanofluid

Published in *International Journal of Hydrogen Energy*, Elsevier 2023, 48, 90, 35220-35228
DOI: https://doi.org/10.1016/j.ijhydene.2023.05.292

Abstract

This study focuses on the wettability alteration (changing from a hydrophobic state to a hydrophilic state) of Indiana limestone for hydrogen (H_2) geological storage. We examine the effect of hexanoic acid C_6, lauric acid C_{12}, and stearic acid C_{18}, on the wettability of Indiana limestone at ambient (298 K and 0.1 MPa) and reservoir (323 K and 8.27 MPa) conditions. The effects of silica nanofluids (silica with deionized water) at various concentrations (0.1 wt%, 0.25 wt%, and 0.5 wt%) on the wettability reversal of stearic-aged samples were tested at ambient and reservoir conditions. The results revealed increased H_2-wetness (hydrophobicity) of the rock exposed to these organic acids in reservoir conditions. However, this hydrophobicity significantly decreased with the nanofluid treatment of the stearic-aged samples. This wettability reversal may increase the H_2 storage capacity and containment security and lead to successful large-scale geological storage operations if H_2 residual trapping is minimized. Thus, this chapter provides important information on one of the factors responsible for the wettability alteration in carbonates.

Keywords

Silica nanoparticles, organic acids, wettability alteration, hydrogen geological storage, Indiana limestone

9.1 Introduction

Underground hydrogen storage (UHS) is a prominent solution for mitigating fossil fuel greenhouse gas emissions, while balancing energy supply and demand (Hassanpouryouzband et al., 2020, Tarkowski, 2019, Isfehani et al., 2023). Porous rocks (e.g., depleted hydrocarbon reservoirs (Lemieux et al., 2019, Pfeiffer and Bauer, 2015), coal seams (Sedev et al., 2022, Iglauer et al., 2022), deep saline aquifers (Hassannayebi et al., 2019, Sáinz-García et al., 2017, Hosseini et al., 2022d)), artificial underground spaces (e.g., salt caverns (Lankof and Tarkowski, 2020)), or basaltic formations (Hosseini et al., 2022b) are potential UHS storage sites with vast storage capacities, guaranteeing uninterrupted energy supply at a commercial scale.

For UHS, wettability of sedimentary (e.g., carbonate and sandstone) and igneous (e.g., basalt) rocks is a crucial parameter which determines H_2 storage capacity, containment security and H_2 flow patterns (Hosseini et al., 2022e, Iglauer et al., 2015a, Iglauer et al., 2015b, Zeng et al., 2022). For example, water-wet rock has favorable conditions for gas storage, enabling high storage capacities and containment safety (Hosseini et al., 2022a). Specifically, mobility and residual trapping of H_2 strongly depend on the rock wettability (Iglauer et al., 2015a).

It has been shown that H_2 rock-wettability is strongly affected (in a detrimental way) by the presence of organic acids (Abramov et al., 2019, Akob et al., 2015, Ali et al., 2020a, Al-Yaseri et al., 2022a, Lundegard and Kharaka, 1994). These organic acids (carboxylic or fatty acids) can be present in subsurface rocks due to various factors, including microbial activity, organic matter decomposition, and diagenetic processes (Jardine et al., 1989, Madsen and Ida, 1998, Kvenvolden, 1967). When organic acids come into contact with the reservoir rock, they can induce chemical reactions and alter the surface properties of the rock (Barth and Bjørlykke, 1993). These alterations can result in changes in wettability, shifting the balance between hydrophilic and hydrophobic conditions (Ali et al., 2020a). Various organic acids (different alkyl chain length) can affect wettability, depending on various factors, including the acid concentration, rock mineralogy, and temperature (Mwangi et al., 2018).

Additionally, the introduction of nanofluid, which consists of nanoparticles dispersed in a base fluid, typically water or oil, has been investigated as a potential method for modifying the wettability of various rock (Al-Anssari et al., 2017, Al-Anssari et al., 2016, Ali et al., 2021a, Ali

et al., 2020b, Hirasaki and Zhang, 2004, Nasralla and Nasr-El-Din, 2014a). These nanoparticles can be engineered from various materials, including silica, alumina, titanium dioxide, and carbon nanotubes, among others (Hussein et al., 2013, Chen et al., 2018). When introduced to reservoir rocks, nanofluids can significantly alter the rock's surface properties, leading to changes in wettability behavior and subsequently affecting fluid flow characteristics (Aminnaji et al., 2015, Giraldo et al., 2013, Gupta and Mohanty, 2011, Mohammed and Babadagli, 2015). It is important to note that the effectiveness of nanofluids in wettability improvement depends on several factors, including the nanoparticle concentration, fluid composition, temperature, and reservoir rock characteristics (Nazari Moghaddam et al., 2015).

Although some scholars have previously examined the impact of organic acids on H_2 wettability in caprock and sandstone (e.g. (Ali et al., 2022c, Ali et al., 2021c)), this effect has not been specifically investigated in the context of a carbonate reservoir rock, such as Indiana limestone (which possesses favorable petrophysical properties and thus has the potential to serve as a reservoir rock for H_2 storage, resulting in high storage capacity (El-Maghraby and Blunt, 2013)). Additionally, the influence of nanofluids on reversing the hydrogen wettability of Indiana limestone, which contains organic components, remains unexplored.

Hence, in this study, we assessed the effects of organic acids and silica nanofluids on limestone H_2 wettability; the results of this study therefore aids in the industrial-scale implementation of a hydrogen economy.

9.2 Experimental methodology

9.2.1 Materials and preparation

Indiana limestone (retrieved from the Salem Formation in Indiana with Mississippian age (Churcher et al., 1991), composed of 97.07 wt% calcite, 1.2 wt% magnesite, 0.68 wt% alumina, 0.8 wt% silica, 0.12 wt% iron oxide, 0.13 wt% water and loss (Owens, 2009), provided by Ward's Natural Science, substrate dimensions = 1 × 1 × 0.4 cm) were used for the tests. To minimize the effect of surface roughness on the contact angle measurements (see below), we polished the surface of the substrates uniformly using 600- and 1200-grit sandpaper, and, to remove contaminants from the rock surface, the substrates were washed with acetone and wiped by ultra-pure nitrogen (purity

≥ 99.9 mol%, BOC). The substrates were then dried in an oven at 333 K for 60 min, and further cleaned in an air plasma (DiemerYocto instrument) for 15 min to remove residual organic contaminants on the surface (Iglauer et al., 2014). Hydrogen gas (H_2, purity ≥ 99.9 mol%, BOC) and brine (2 wt% NaCl + 1 wt% KCl, purities ≥ 0.99 mol fraction, from Scharlab in deionized (DI) water with an electrical conductivity of 0.02 mS/cm from David Gray) here used as fluid phases. Furthermore, three organic acids (purity ≥ 99 mol%, from Sigma Aldrich, i.e. hexanoic acid (liquid phase with the chemical formula $C_6H_{12}O_2$ and a molar mass of 116.16 g/mol), lauric acid (solid phase with the chemical formula $C_{12}H_{24}O_2$ and a molar mass of 200.32 g/mol), and stearic acid (solid phase with the chemical formula $C_{18}H_{36}O_2$ and a molar mass of 284.48 g/mol), were used for preparing 10^{-2} mol/L acid/n-decane solutions. The limestone samples were submerged in the organic acid solutions (one in hexanoic acid solution, one in lauric acid solution, and three in stearic acid solution) and aged for a week in an oven at 333 K to simulate real geological rocks exposed to formation fluid over geological times (Davis, 1982, Kleber et al., 2015, Ulrich et al., 1988, Zullig and Morse, 1988).

Silica nanoparticles (silicon dioxide, SiO_2, purity ≥ 99 mol%, white powder with a density of 2.6 g/cm^3 and particle size of 20 to 25 nm, insoluble in water, from Sigma Aldrich) were used to formulate three different nanofluids (0.1 wt%, 0.25 wt%, and 0.5 wt% nanoparticles in DI water). An ultrasonic homogenizer (frequency = 20 kHz) was used to homogenize nanofluids for 15 min (as nanoparticles cannot be homogeneously dispersed in DI water by magnetic stirring (Mahdi Jafari et al., 2006)). The substrates were submerged in nanofluids (in the stated concentrations) for 10 h in an oven at 333 K to improve wettability of the organic-acid-aged samples.

9.2.2. Measurements

9.2.2.1 Nanofluid pH and zeta potential measurements

Nanofluid pH was measured with a pH meter (with a resolution of 0.01 pH units, Ohaus, Australia), and nanoparticle zeta potentials (accuracy = 0.12 µm.cm/V.s) and average particle size (accuracy = 0.2 %) were measured with a Malvern nano-zeta sizer instrument, Table 9-1. These values can be analyzed and interpreted to understand the surface charge and stability of the particles or surfaces. The sample was carefully loaded into a suitable cuvette provided by the instrument. The

cuvette was cleaned to remove any contaminants that could affect the measurement. The desired measurement parameters (e.g. measurement angle, laser intensity, and acquisition time) was set on the instrument. The cuvette was placed into the instrument, where an electric field was applied to the sample, causing the particles or surfaces to move. The movement was detected using laser Doppler electrophoresis, and the zeta potential was calculated based on the velocity of the particles and the electric field strength.

Table 9-1 Nanofluid pH, nanoparticle zeta potential, and average particle sizes measured.

Nanoparticle concentration (wt%)	pH	Zeta potential (mV)	Average particle-size agglomeration (nm)
0.1	7.66	-23.4	120.9
0.25	7.6	-20.8	324.4
0.5	7.56	-20.1	333.4

9.2.2.2 Surface roughness measurements

Surface roughness affects contact angle measurements and, consequently, the wettability of a surface (Marmur, 2006). Therefore, an atomic force microscope (model DSE 95–200 from Semilab) was used to measure the surface roughness of the clean and aged samples. Before conducting AFM imaging, it was necessary to appropriately prepare the rock sample. This typically entailed cleaning the pure sample's surface to eliminate any contaminants and ensuring its flatness and stability, thereby enabling accurate measurements. The AFM equipment was configured with the suitable imaging mode (here contact mode) and probe. The probe, typically comprising a sharp tip connected to a cantilever, scanned the rock surface. The AFM probe was placed in contact with the rock surface, and the scanner scanned the sample in a systematic pattern. During the scanning process, the probe detected the surface topography by observing the deflection of the cantilever. The acquired topographic image was analyzed using Nanosurf C3000 Version 3.8.8.12 software to extract quantitative roughness parameters.

9.2.2.3 Elemental surface composition

The elemental composition of the rock surface (for pure and aged substrates) was measured via energy dispersive spectroscopy (EDS, Oxford X-act SSD X-ray detector with Inca and Aztec software). EDS was used in conjunction with scanning electron microscopy (SEM) to provide visualization and characterization of the elemental composition of the rock surface. The rock sample was properly prepared for SEM-EDS analysis. This involved cutting, polishing, and mounting the sample on a suitable holder. The sample surface was cleaned (i.e. dust removal by air, washing by acetone and drying in an oven) and flattened to ensure accurate measurements. The prepared rock sample was placed inside the SEM chamber, and an electron beam was focused onto the surface of the sample. As the beam scanned the sample, it interacted with the atoms on the rock surface, resulting in the generation of secondary electrons and X-rays. The SEM instrument was equipped with EDS detectors that captured the characteristic X-rays emitted from the sample. These X-rays have specific energies corresponding to the elements present in the sample. The detected X-rays were transformed into a spectrum, which depicted the elemental composition of the rock surface. The spectrum was then subjected to analysis using Inca and Aztec software. By identifying and quantifying the elemental peaks in the spectrum, it was possible to determine the elemental composition and relative abundance on the rock surface.

9.2.2.4 Contact angle measurements

Contact angle measurements are a fast and proven technique to quantitatively and directly analyze the wettability of rock–fluid systems (Chiquet et al., 2007); commonly used is the tilted plate method for simultaneously measuring advancing and receding angles (Lander et al., 1993), which was also used here. Thus, Indiana limestone substrates were placed on a tilted plate (angle = 15º) inside a high-pressure and high-temperature cell. Two Teledyne D-500 pumps (accuracy of 689.47 Pa for pressure) were connected to the cell to charge H_2 gas or brine into the HPHT cell at the desired test pressure and an electrical heater was used to set the desired test temperature. Our previous studies described the experimental procedure in detail (Hosseini et al., 2022b, Hosseini et al., 2022c, Hosseini et al., 2022e, Ali et al., 2021a). Considering the relative standard uncertainties of 689.47 Pa for pressure and 1 K for temperature, the average standard deviation of the measurements was ±3º.

9.3 Results and discussion

In the following section, we first discuss the results of surface roughness and elemental composition. Then, we evaluated the effect of organic-acid alkyl chain length on H_2 wettability. Finally, we discuss how nanofluid treatment of the stearic-acid aged sample changed the H_2 wettability.

9.3.1 Evaluation of surface roughness

The results indicated an increase in surface roughness as the rock sample underwent different aging processes, Fig. 9-1. By comparing the color scales of three different scenarios, the surface roughness of the pure Indiana limestone was observed to lie within the brown range. However, the color shifted to a lighter shade of brown after aging the limestone with stearic acid and subsequently treating it with nanofluid. The initial surface roughness (pure Indiana limestone) was 289.7 nm which represents the baseline roughness of the pure rock sample before any modifications or treatments were applied. The aging process with stearic acid resulted in a slight increase in surface roughness (305.1 nm) compared to the pure rock sample. Stearic acid is a fatty acid that can adsorb onto the rock surface, forming a thin film or layer. This adsorption can introduce additional roughness to the surface, leading to a slight increase in the measured roughness (Ali et al., 2021a). The aging of the stearic-aged sample with silica nanofluid caused a more significant increase in surface roughness (372.6 nm) compared to the previous step. Silica nanofluids typically consist of suspended nanoparticles, which can deposit and adhere to the surface (Ehtesabi et al., 2015). The deposition of nanoparticles can result in the formation of clusters or agglomerates, thereby increasing the surface roughness more prominently (Al-Anssari et al., 2016, Ali et al., 2020b). It is important to note that all the surface roughness values were lower than 1 μm and consequently did not significantly affect contact angle (Al-Yaseri et al., 2016, Hosseini et al., 2022e).

However, the roughness values provided represent only the topographical changes on the surface and do not account for other potential alterations in chemical or physical properties induced by the aging processes. Further analysis and characterization techniques (e.g. elemental surface

composition) are necessary to fully understand the effects of these treatments on the rock surface, see section 9.3.2.

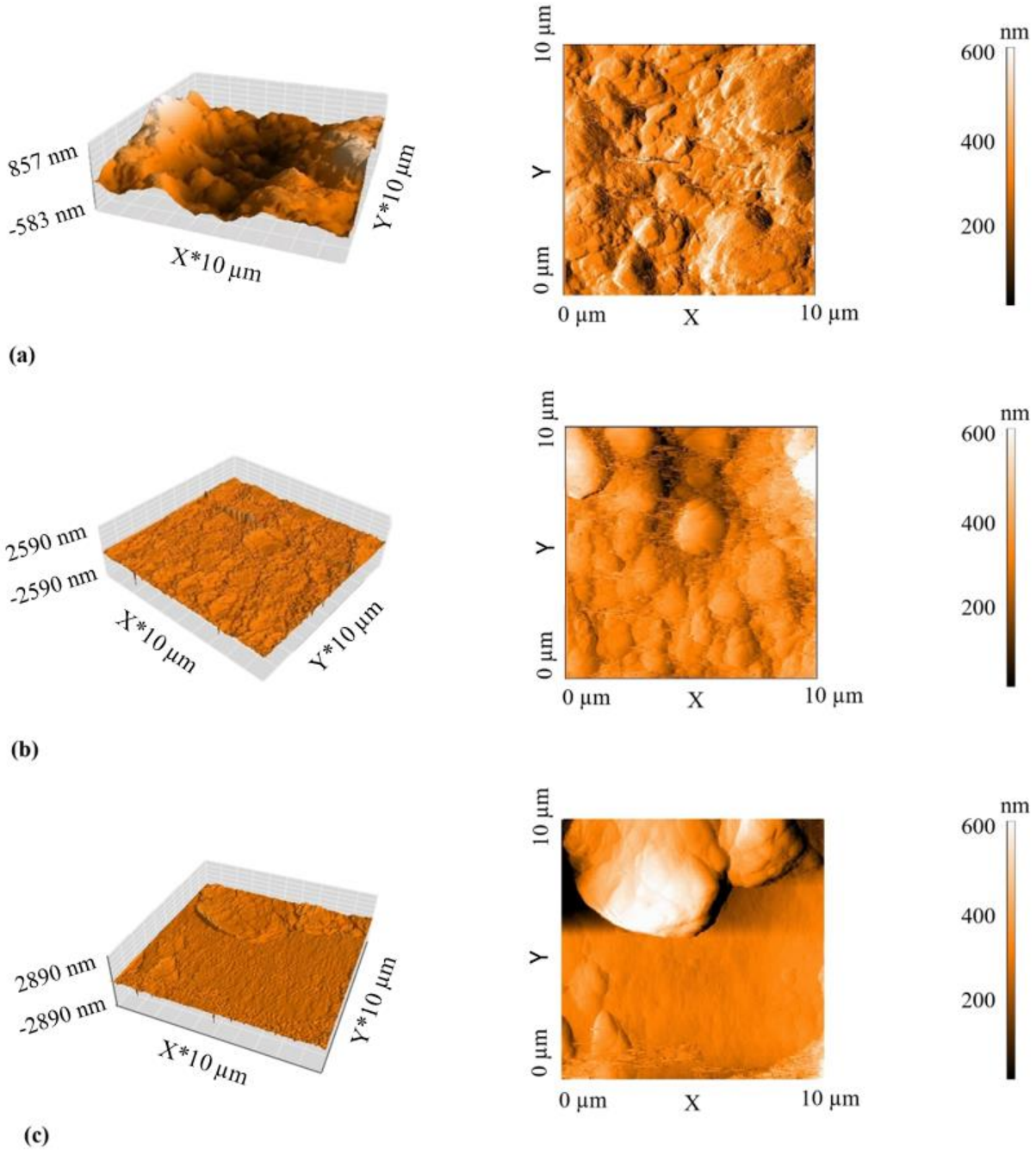

Fig. 9-1 Atomic force microscope images, (left) three-dimensional topography and (right) two-dimensional deflection signal, of (a) pure Indiana limestone, (b) Indiana limestone aged in stearic acid, and (c) Indiana limestone treated with silica nanofluid.

9.3.2 Evaluation of elemental surface composition

Aging with organic acids and nanofluids significantly changed the surface composition, Table 9-2 (compare also Fig. 9-2). For example, the surface carbon concentration increased from 14.27 to 65.29 wt% when the pure limestone was aged with 10^{-2} mol/L stearic acid. Stearic acid is an organic acid that contains carbon. During the aging process, the stearic acid likely adsorbed onto the surface of the limestone, increasing the carbon content on the surface (Jarrahian et al., 2012, Al-Shirawi et al., 2021). In addition, the surface silica concentration increased from 1.15 to 11.2 wt% when the organic-acid-aged sample was treated with 0.1 wt% SiO_2 nanofluid. The SiO_2 nanofluid contains silica nanoparticles that have a high affinity for binding to surfaces. When applied to the organic-acid-aged limestone sample, the silica nanoparticles likely adhered to the surface (e.g. (Bai et al., 2022, Afekare et al., 2020), see Fig. 9-2c), leading to an increased silica concentration (note: the SEM images shown in Fig. 9-2 are in a magnification factor of 2750x, i.e. a sample with 27.5 mm apparent size is imaged at 10 μm resolution).

Table 9-2 Elemental surface composition of pure and aged Indiana limestone samples.

Element	Pure limestone (wt%)	After aging with 10^{-2} mol/L stearic acid (wt%)	After treating the aged sample with 0.1 wt% SiO_2 nanofluid (wt%)
C	14.27	65.29	55.3
O	46.95	21.92	22.4
Na	0.32	0.2	0.5
Mg	0.31	0.09	0.9
Si	1.27	1.15	11.2
Cl	0.31	0.28	0.5
Ca	36.51	10.93	9.1
Fe	0.06	0.13	0.1

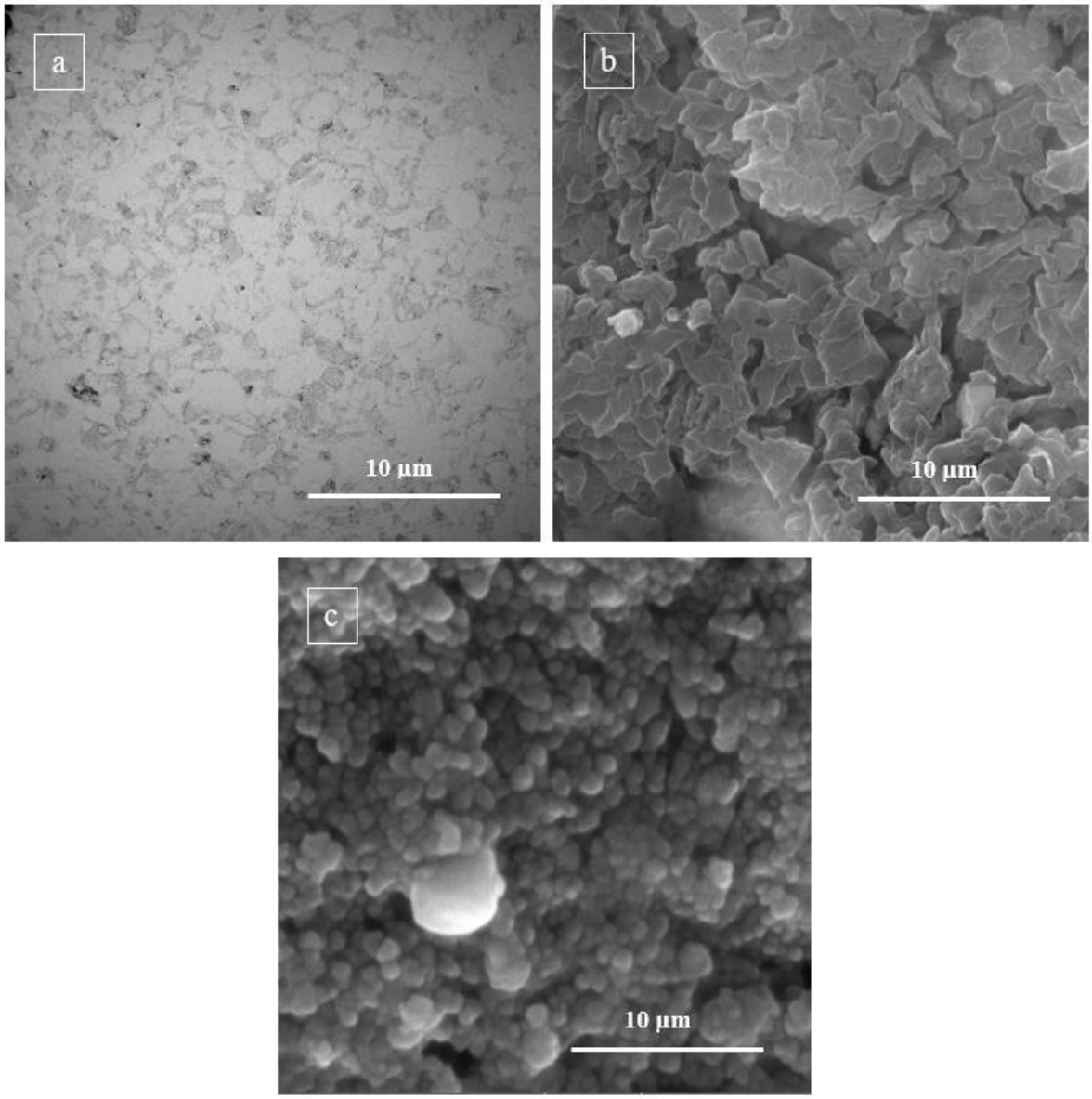

Fig. 9-2 SEM images (acquired via energy dispersive (EDS) technique) of Indiana limestone (at a magnification of 2750x): (a) pure, (b) after treatment with 10^{-2} mol/L stearic acid, and (c) aged, after treatment with 0.1 wt% SiO_2 nanofluid.

9.3.3 Effect of organic acids on hydrogen wettability of Indiana limestone

The pure Indiana limestone was strongly water-wet at ambient conditions (θ = 0º, at 298 K and 0.1 MPa), implying that the pore spaces which were initially filled with water will not be drained by H_2 unless a capillary entry pressure (p_{ce}) is overcome. For example, for a strongly water-wet

Indiana limestone with a mean pore radius of 1 µm (e.g., macro pores (Tawfik et al., 2019, Hosseini, 2016)), p_e = 0.15 MPa (calculated using the Young-Laplace relationship (Young, 1805) at ambient conditions) is required for H_2 to enter the pore space and displace water. When capillary pressure (p_c) increases, more H_2 enters the pore spaces, displacing water until an irreducible water saturation is achieved. This process requires more work as the surface free energy changes unfavorably (Morrow, 1970). Afterward, when p_c decreases, water spontaneously imbibes into the pore system (known as secondary imbibition (Leverett, 1941); note no more water imbibition occurs when p_c becomes zero), and this process does not require any work as the surface free energy changes favorably, indicating a strongly water-wet system (Schwartz, 1969). Moreover, the pure Indiana limestone was intermediate-wet (advancing (θ_a) = 71° and receding (θ_r) = 67°) at reservoir conditions (Fig. 9-3), consistent with the literature data (Ali et al., 2021a, Hosseini et al., 2022e). For this less hydrophilic state, H_2 enters the pore spaces at p_e = 0.05 MP which is lower than p_e in strongly water-wet state. Thus, the primary drainage process here is easier (smaller primary drainage curve) compared to the strongly water-wet state (Iglauer et al., 2015b). Another difference between these two wetting states is that unlike the strongly water-wet state, the secondary water imbibition occurs at both $p_c > 0$ and $p_c < 0$. Therefore, limited works are required to increase both H_2 and water saturations, indicating an intermediate-wet system (Purcell, 1950).

However, for the organic acid-aged samples, advancing and receding contact angles increased with increasing alkyl chain length (i.e. increasing organic-acid carbon number), implying a drastic increase in hydrophobicity of the rock surface (Ali et al., 2020b). For example, at ambient conditions, θ_a and θ_r increased from 58° to 105° and 55° to 101°, respectively, when the organic-acid carbon number on the rock surface increased from C_6 to C_{18}; similarly, at reservoir conditions, θ_a and θ_r increased from 94° to 131° and 81° to 113°, when carbon number increased from 6 to 18, Fig. 9-3. For the hydrophobic state ($\theta > 90^o$, where the rock is H_2-wet, e.g., when C_{18} exists in the Indiana limestone at both ambient and reservoir conditions), H_2 spontaneously enters the rock at $p_c = 0$ without any force (Iglauer et al., 2015b) and expels the water from the system, and this decrease in water saturation mostly occurs at $p_c = 0$, implying that minimal work is required to achieve the residual water saturation. In this case, water will imbibe into the system at $p_c < 0$ by applying force (Purcell, 1950). At such hydrophobic condition, H_2 is more mobile in the reservoir (Al-Khdheeawi et al., 2017a, Al-Khdheeawi et al., 2017b). Thus, the risk of UHS project in Indiana

limestone is higher when the rock is exposed to organic molecules (as expected in real geological formations (Hosseini et al., 2022e)).

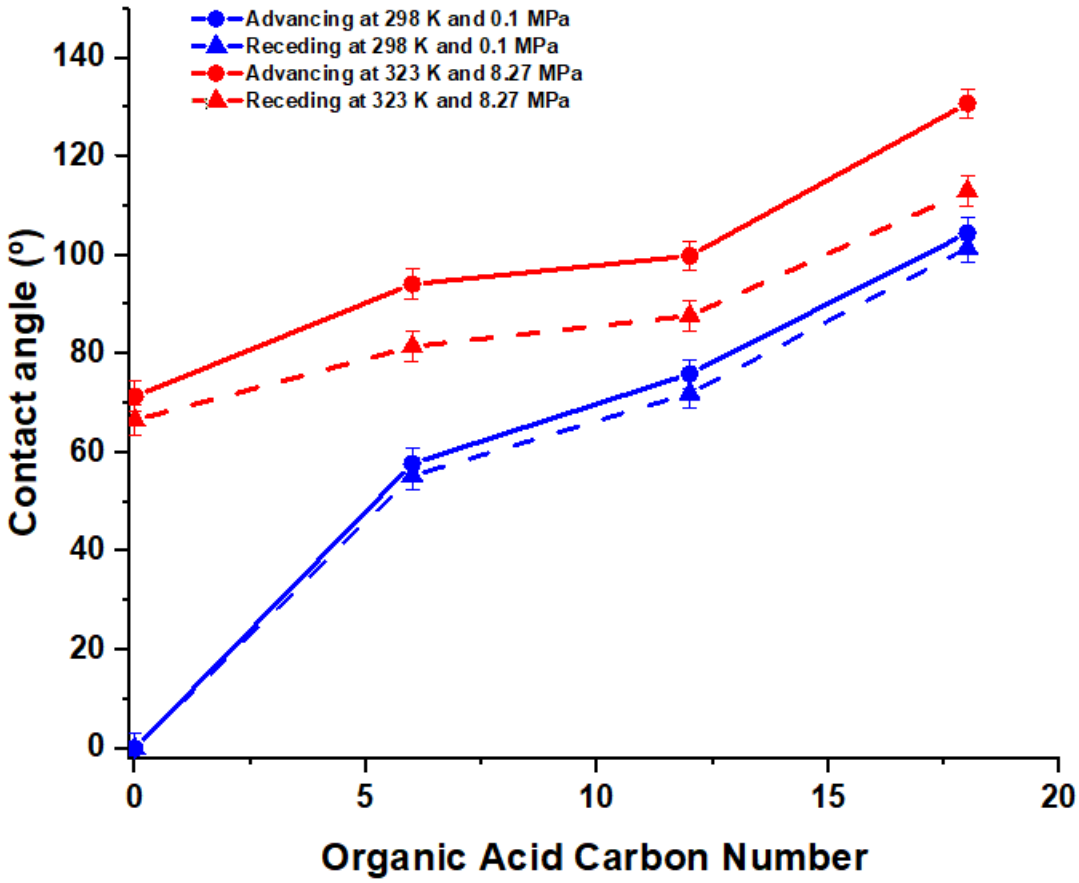

Fig. 9-3 Indiana limestone/H_2/brine advancing and receding water contact angles as a function of organic-acid carbon number.

9.3.4 Effect of nanofluids on hydrogen wettability of Indiana limestone

The stearic-acid aged Indiana limestone (which was initially hydrophobic, i.e. gas-wet, $\theta > 90^o$), became hydrophilic, i.e. water-wet, $\theta < 90^o$) after nanofluid treatment (Fig. 9-4), effectively reversing sample wettability (Ali et al., 2021a). For example, at 323 K and 8.27 MPa, the gas-wet surface (initially θ_a = 131° and θ_r = 113°) changed into a weakly water-wet surface (θ_a = 60° and

θ_r = 56°) after treatment with 0.1 wt% SiO_2 nanofluid and into a strongly-water wet surface (θ_a = 16° and θ_r = 11°) after treatment with 0.5 wt% SiO_2 nanofluid, indicating a decrease in H_2 mobility in Indiana limestone and thus de-risking the UHS projects. This effect of nanofluid treatment on wettability alteration of the rock is consistent with literature data on oil-wet carbonate rocks (Al-Anssari et al., 2016, Roustaei and Bagherzadeh, 2015).

Mechanistically, silica nanoparticles (which are hydrophilic due to the presence of Si-OH groups on the particle surfaces) adsorbed on the limestone surface (Table 9-2 and Fig. 9-2), (Wolthers et al., 2012, Kumar et al., 2020), which drastically increased limestone hydrophilicity (wettability alteration), consistent with (Ali et al., 2021a, Ali et al., 2020b, Al-Anssari et al., 2016, Keykhosravi et al., 2021). This wettability alteration, combined with a (small) reduction in the rock–fluid interfacial tension (e.g. (Jiang et al., 2017, Keykhosravi et al., 2021)) can be considered the principle mechanism for the wettability change observed. It is also important to note that the zeta potential could be a good index for assessing the surface charge of nanofluids and their stability (e.g., a lower zeta potential leads to low nanofluid stability, resulting in more precipitation of the particles (El-sayed et al., 2012), increasing particle-size agglomeration, Table 9-1).

Despite reducing the H_2 mobility, the nanofluid treatment increases the H_2 residual trapping (i.e., via the increase in water-wetness of the rock (Rahman et al., 2016, Al-Menhali and Krevor, 2016), see above), resulting in more H_2 loss which is unfavorable for UHS projects. It is worth highlighting that a monotonic relationship between initial and residual H_2 saturations is expected due to the increase in water-wetness of the rock (Tanino and Blunt, 2013, Spiteri et al., 2008).

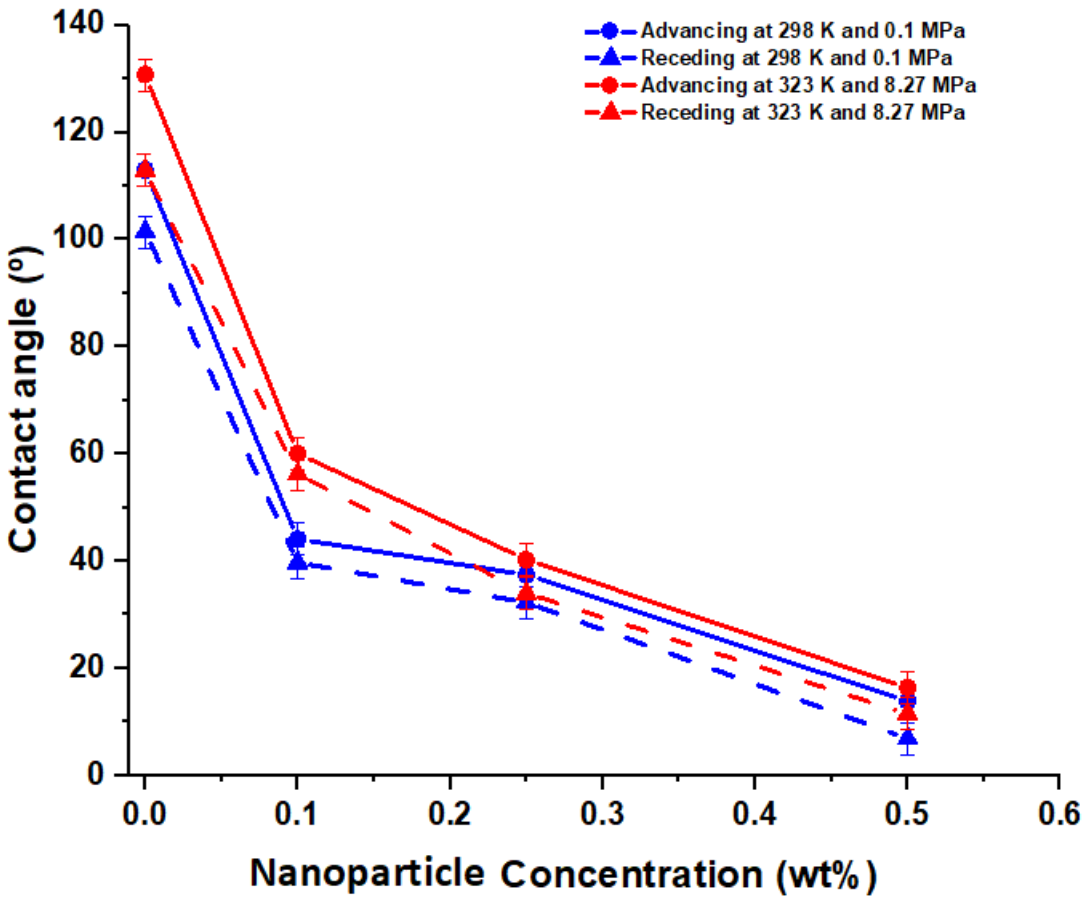

Fig. 9-4 Indiana limestone/H_2/brine advancing and receding water contact angles as a function of nanoparticle concentration in the used nanofluid.

9.4 Conclusions

The wettability alteration, the process of changing the surface properties of hydrophobic rocks to become more hydrophilic or water-wet, has been extensively studied in various fields such as CO_2 geological storage and hydrocarbon reservoirs. However, its applicability in UHS with the presence of organic matter has not been investigated. Organic molecules can adsorb on the rock surface under realistic geologic conditions, affecting rock wettability and H_2 storage capacity. Injecting nanoparticles into the organic-rich storage medium is a proposed solution to improve rock wettability, but there is a lack of data on the impact of organic molecules and nanofluids on carbonate rocks' H_2 wettability. This is significant as it aims to enhance the storage capacity and

recovery of H_2 while minimizing its leakage or loss in UHS projects. Thus, contact angle experiments were conducted to improve fundamental understanding in this area.

We found that at reservoir conditions (323 K and 8.27 MPa), the H_2 mobility increased in the presence of organic matter on the Indiana limestone rock surface, so that risky UHS project (i.e., H_2 leakage through the stearic acid-aged Indiana limestone) is highly possible. Moreover, all nano-aged samples displayed a decrease in the contact angles compared to the stearic-aged samples, so that θ_a and $\theta_r < 90^o$. This decrease was greater for high nanofluid concentrations. This wettability alteration resulted in decrease in H_2 mobility (de-risking UHS project), but increase in H_2 residual trapping (H_2 loss) which is unfavorable for UHS projects.

We conclude that the wettability alteration by nanofluids during UHS in Indiana limestome reservoir can have advantages and disadvantages. The planning of such experiment in the reservoir would be reasonable. However, the nanofluid concentration should be optimized, thereby maximizing the H_2 storage capacity and minimizing the risk points (i.e., H_2 leakage/loss).

Chapter 10 Streaming and zeta potentials of basalt as a function of pressure, temperature, salinity, and pH

Published in *Fuel*, Elsevier 2023, 351, 128996
DOI: https://doi.org/10.1016/j.fuel.2023.128996

Abstract

The electric surface charge of basalt in contact with filling fluids (e.g. water and CO_2) has broad range of applications in varied fields such as gas geological storage sites, geothermal systems, and hydrocarbon reservoirs. The surface charge at the interface between a solid surface (e.g. rock) and liquid (e.g. aqueous solution) can be quantified by the zeta potential, thus zeta potential measurement is a useful technique for interpreting wetting characteristics of rock-fluid systems and can be considered as one of the factors responsible for the wettability alteration in rocks. However, there is no data for zeta potentials for basaltic rocks in presence of aqueous solutions or how zeta potentials may be affected by pressure, temperature, salinity, or pH. Thus, streaming potential measurements were performed to determine the zeta potential of basaltic rocks in the presence of aqueous NaCl solution at pore pressures (1.72 MPa to 6.9 MPa), temperatures (298 K and 323 K), brine salinities (1 wt% NaCl to 3.5 wt% NaCl), and pH values (4 to 10). Also, the effects of mineralogy and CO_2-presence (dead and live brines) on the zeta potential were evaluated. The results showed that the zeta potential remained constant versus pressure, while it increased (became less negative) with increasing temperature and salinity, and decreased (became more negative) with increasing pH. This study provides key fundamental data and thus improves fundamental understanding of basalt-water-CO_2 interactions, thereby aiding in the improvement of various industrial applications, including gas geo-storage schemes and geothermal energy production.

Keywords

Zeta potential, streaming potential, basalt, dead brine, live brine, high pressure

10.1 Introduction

Basalt is the most common igneous rock in Earth's crust; it constitutes 67% of the ocean floor (with 2 – 4 kilometer thick layers), and covers 10% of the continents' surfaces (Gislason et al., 2010, Hosseini et al., 2022b, le Roex, 1998, Hosseini et al., 2022a). Such basaltic formations may form groundwater aquifers, geothermal reservoirs or hydrocarbon reservoirs (Wilcox et al., 2020, Schutter, 2003, Eidesgaard et al., 2019, Khadri and Moharir, 2016, Möller et al., 2016, Ystroem et al., 2020). However, while fluid flow through sedimentary rocks (e.g. carbonates or sandstones) has been widely investigated (e.g. (Orywall et al., 2017, Samaniego et al., 1992, Zhou et al., 2014, Zhou et al., 2021)), fluid flow through basaltic rocks is only poorly understood (Passarella, 2021). One key property related to such fluid flow is the streaming potential C (which is created when an electrolyte (here brine) flows through a stationary porous medium (here basalt) (Hunter, 2013, Sprunt et al., 1994)). C has a broad spectrum of important applications, including in enhanced hydrocarbon recovery, geothermal engineering, volcanology, drinking water production, hydraulic fracturing, CO_2 geo-sequestration (CGS) and H_2 geo-storage (e.g. (Collini et al., 2020, Hidayat et al., 2022a, Jackson et al., 2016, Leinov and Jackson, 2014, Mahani et al., 2017, Revil and Pezard, 1998)). C is related to the zeta potential (ζ) of the basalt, which is one of the main wettability-determinants and thus directly influences fluid flow through the basalt (e.g. (Awan et al., 2020, Arif et al., 2019, Luong and Rudolf, 2015)).

The ζ of sedimentary rocks has been widely investigated in the literature for various purposes. Regarding the influence of high salinity brines on ζ, (Singh et al., 2022), (Collini et al., 2020), (Cherubini et al., 2018), and (Al Mahrouqi et al., 2017) investigated carbonates, while (Walker and Glover, 2018), (Alarouj et al., 2021), and (Nasralla and Nasr-El-Din, 2014a) examined sandstone. The effect of elevated temperature on ζ for carbonates was studied by (Jackson et al., 2016), (Al Mahrouqi et al., 2017), and (Rodríguez and Araujo, 2006), while (Vinogradov and Jackson, 2015) investigated this effect for sandstone. In terms of conducting ζ measurements under multi-phase flow conditions, (Revil and Cerepi, 2004) conducted tests on carbonates, while (Sprunt et al., 1994) studied carbonates and sandstone. Additionally, (Alroudhan et al., 2016) investigated the impact of brine composition on ζ for carbonates, and (Thanh and Sprik, 2016) examined this effect for sandstone. The effect of brine pH on ζ for carbonates was examined by (Vdović and Bišćan, 1998), (Vdović, 2001), (Mahani et al., 2017), and (Chen et al., 2014). In the

case of sandstone, (Vinogradov and Jackson, 2015), (Alarouj et al., 2021), and (Hidayat et al., 2022a) investigated this effect.

However, ζ of volcanic rocks received only little attention. For example, (Jouniaux et al., 2000) measured the zeta potential of 11 andesitic volcanic samples with different permeabilities and concluded that the increase in permeability of basalt results in an increase in C. They attributed this variation to the reduction of rock's effective conductivity with permeability (note: C has inverse relation with the effective conductivity (e.g. (Ishido and Mizutani, 1981)), see section 10.2.3). In another study, (Hase et al., 2003) derived the zeta potential of various rocks from Aso volcano and found that basalt samples with low SiO_2 content and high isoelectric points (note: isoelectric point is the pH value where ζ equals zero (Reedijk and Poeppelmeier, 2013)) showed positive zeta potentials (ζ ranged from -20 to +20 mV). Moreover, (Aizawa et al., 2008) derived the zeta potential of 73 volcanic samples and found 9 samples with positive zeta potential, 11 samples with small values less than 10 mV, and the remaining samples with negative zeta potentials. There are also a few studies reporting ζ of the minerals which are commonly found in basaltic rocks, including augite (Tohry et al., 2021), olivine (Ucbas et al., 2014), labradorite (Dunning et al., 1982), albite (Vidyadhar and Rao, 2007), and microcline (Shehata and Nasr-El-Din, 2015). Under typical experimental conditions, most of these minerals have been found to exhibit negative zeta potentials.

Various thermophysical parameters, including pressure, temperature, brine salinity and composition (note that formation water always contains dissolved salts which can reach maximum saturation (Bjørlykke and Gran, 1994, Hosseini, 2016, Hosseini, 2018, Hosseini et al., 2014, Isfehani et al., 2023)), and brine pH can vary significantly in the underground (Hosseini et al., 2022e, Hosseini et al., 2022c), and this may significantly affect C and ζ (Hidayat et al., 2022b, Revil and Cerepi, 2004, Sprunt et al., 1994, Vinogradov and Jackson, 2011). However, the effects of these parameters on ζ of basaltic rock remains unknown.

In this study, we therefore examine the influence of pressure, temperature, pH value and brine salinity on ζ of a New Zealand basaltic rock sample. This also includes the effect of CO_2 (an acidic gas) added on ζ; this study will thus aid various important applications, including gas geo-storage (CO_2 and H_2) and geothermal projects.

10.2 Experimental methodology

10.2.1 Materials

A New Zealand basaltic core plug (petrophysical and mineralogical properties are listed in Table 10-1) was retrieved from Auckland Volcanic Field (AVF, depth = 74 m, age = 68.3 ka), New Zealand (Molloy et al., 2009). The sample contained labradorite ($(Na,Ca)_{1-2}Si_{3-2}O_8$), augite ($Ca(Fe,Mg)Si_2O_6$), olivine ($(Mg,Fe)_2SiO_4$), and nepheline ($(Na,K)AlSiO_4$) as main mineral components (Molloy et al., 2009) (compare Table 10-1). Furthermore, aqueous NaCl solutions ("dead brines") were prepared by dissolving NaCl salt (purity ≥ 99 mol% from Scharlab) in deionized (DI) water (electrical conductivity of 0.02 $mS.cm^{-1}$ from David Gray). Small amounts of NaOH (purity ≥ 99 mol% from Scharlab) and (aqueous) HCl (concentration of 10^{-3} mol/L and purity ≥ 99 mol% from Scharlab) were added for adjusting pH values (measured via a FiveGo pH meter, Mettler Toledo, accuracy of 0.01 pH units). Live brine was also prepared by dissolving CO_2 (purity > 99.9 mol% from BOC) in the dead brine at HPHT conditions, see below. The compositions of the produced brines (after core flooding, see also below) were analyzed via inductively coupled plasma (ICP) tests using a HORIBA Jobin Yvon® ULTIMA 2C instrument.

Table 10-1 Petrophysical and mineralogical properties of the basalt sample used in this study.

Property	Result	Unit
Mineralogy[1]	Labradorite (42), Augite (37.5), Olivine (11.9), Nepheline (8.6)	wt%
Core plug dimensions	Length = 5.2, Diameter = 3.8	cm
Porosity[2]	10 ± 1.0	%
Brine permeability[3]	4.6 ± 0.3	mD
Formation factor (F)[4]	61 ± 2	-

[1] Measured via X-ray diffraction (XRD, Bruker-AXS D8 instrument) analysis (Hosseini, 2018)

[2] Measured via UltraPoroPerm-910 from Core Laboratories

[3] Measured in core-flood apparatus (shown in Fig. 10-1). Permeability was measured at 10 MPa overburden pressure, and the error was obtained based on three different flow rates used at the same overburden pressure

[4] $F = \sigma_w/\sigma_{rw}$ is used when surface electrical conductivity is negligible for salinities > 0.1 M (as assumed here, see section 10.2.3) (Weller et al., 2013)

10.2.2 Experimental procedure

The streaming potential experiments were conducted using an HPHT core flooding system, Fig. 10-1. The core sample was cleaned with toluene and methanol to remove any impurities that could interfere with the flow or alter the surface properties. The core holder with the sample inside and associated electrodes on two sides was placed inside an oven with controlled temperature (accuracy of ±1° C). The core holder is made of polyether ether ketone (PEEK) which is a high-performance thermoplastic known for its excellent mechanical and chemical properties, making it suitable for use in experimental setups involving fluid flow and pressure (Al Mahrouqi et al., 2016). Using a PEEK core holder offers researchers several advantages, including resistance to chemicals, tolerance for high temperatures, strong mechanical properties, effective electrical insulation, and dimensional stability (Shakerian and Balcom, 2018). These benefits enhance the dependability and precision of streaming potential measurements conducted during core flooding experiments (Awan et al., 2022). The pumps (500D Hastelloy Teledyne ISCO pumps, flow rate resolution ~ 0.5% of setpoint, pressure resolution within 0.1% full scale) were used to apply an overburden pressure of 3.45 MPa and a pore back pressure of 1.72 MPa; brine was then injected through the sample at different flow rates (1 ml/min, 2 ml/min, and 3 ml/min) to equilibrate the rock core sample with the brine (note: the core sample was vacuumed before saturating it with brine to avoid air trapping). The back-pressure pump plays a crucial role in streaming core flooding experiments by providing controlled flow rate, representative sampling, continuous collection, and enhanced efficiency during the collection of brine or effluent fluid. The pressure control system (including pumps and pressure gauges) controls the flow rate and pressure of the brine flowing through the core. Two nonpolarizing Ag/AgCl electrodes are connected to a high impedance voltmeter to monitor the voltage of the brine. This brine flow through the rock resulted in pressure differential and voltage between the two sides of the core; and flow was continued until stable pressure differential and stable voltage were achieved. This was followed by a system relaxation (i.e. a static state without flow) and the associated static voltage (with zero pressure differential) was recorded. This process was repeated for different pore pressures (up to 6.9 MPa) and overburden pressures (up to 10.34 MPa) at the prescribed temperatures (note that the effective stress, i.e. the difference between overburden and pore back pressures was set to a constant 3.45 MPa (Awan et al., 2022)). All the pressure and voltage values were recorded and analyzed by a data acquisition system.

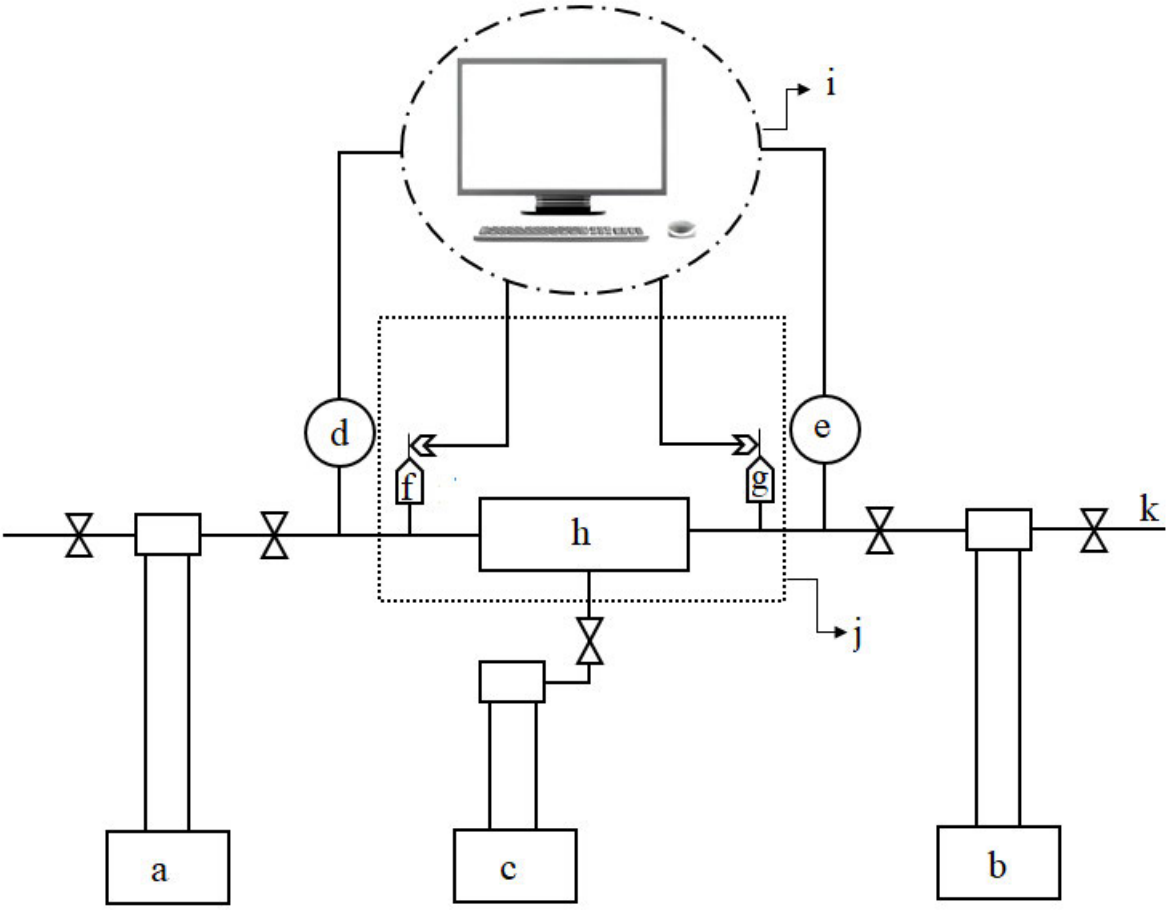

Fig. 10-1 Experimental apparatus for streaming potential measurements used in this study: (a) ISCO pump (flow rate accuracy of 0.5% of setpoint, pressure accuracy within 0.1% full scale) for injecting brine, (b) ISCO back-pressure pump for collecting brine, (c) ISCO pump for applying overburden pressure, (d) high precision pressure transducer (Keller-Druck, 0.1% accuracy) for monitoring the inlet pressure, (e) high precision pressure transducer for monitoring the outlet pressure, (f) nonpolarizing Ag/AgCl electrode (accuracy 0.15%) at injection side, (g) nonpolarizing Ag/AgCl electrode at collection side, (h) core holder, (i) data acquisition system, (j) oven, (k) effluent collection line.

10.2.3 Data analysis

The associated streaming potential coupling coefficient (C_{sp}) and zeta potential (ζ_{sp}) were calculated with the paired stabilization method described in (Vinogradov and Jackson, 2011); thus (Hidayat et al., 2022b):

$$C_{sp} = \frac{\Delta V}{\Delta P}, \tag{10.1}$$

where ΔV is the stabilized voltage (in mV) and ΔP is the stabilized pressure differential (in MPa). Note that C_{sp} is therefore the slope of stabilized ΔV plotted versus stabilized ΔP (for varying flow rates, here 1 ml/min, 2 ml/min, and 3 ml/min) at constant pH, brine salinity (S), overburden pressure, pore back pressure (p), and temperature (T) (Vinogradov et al., 2010). Figure 10-2 shows an example of how C_{sp} was determined at p = 3.45 MPa, T = 323 K, S = 1 wt% NaCl, and brine pH = 7.

The conductivity of a core saturated with water (σ_{rw}) can be calculated using the differential effective medium (DEM) theory (Sen et al., 1981, Sen, 1984):

$$\sigma_{rw} = \frac{\sigma_w}{F}\left(\frac{1-\sigma_s/\sigma_w}{1-\sigma_s/\sigma_{rw}}\right)^m, \tag{10.2}$$

where σ_w is the water conductivity (here obtained from (Sen and Goode, 1992)), F is the formation factor, σ_s is the rock surface conductivity, and m is the cementation exponent. Assuming that the effect of surface conductivity is negligible (when compared to the bulk fluid conductivity – i.e. no additional conductivity occurs in the vicinity of the charged interface and the effective conductivity equals the fluid conductivity, resulting in a constant F for all single-phase experiments (Hase et al., 2003)), which is justified as higher ionic strength (typically for salinities > 0.1 M if the rock contains minerals other than clays (Weller et al., 2013)), the following equation is obtained (Li et al., 2016):

$$F = \frac{\sigma_w}{\sigma_{rw}}. \tag{10.3}$$

Thus, ζ_{sp} could be obtained via the classical Helmholtz-Smoluchowski equation (Jouniaux and Pozzi, 1995):

$$\zeta_{sp} = \frac{\mu_w \sigma_w C_{sp}}{\varepsilon_w}, \tag{10.4}$$

where μ_w is the dynamic brine viscosity (here obtained from (Saunders et al., 2012)), $\mathcal{E}_w$ is the brine permittivity (here obtained from (Saunders et al., 2012)), and C_{sp} is obtained from Equation (1), see above. The average standard deviation of C_{sp} and ζ_{sp} were ±0.3 mV/MPa and ±2.5 mV based on replicate measurements.

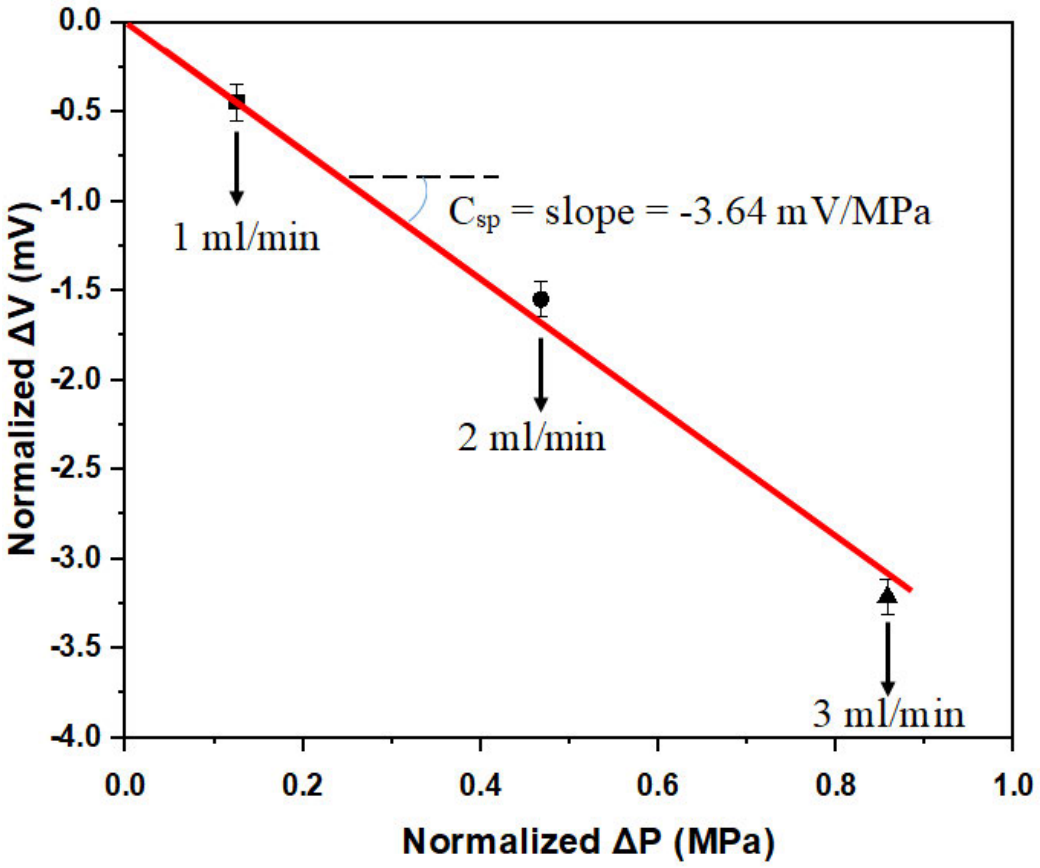

Fig. 10-2. C_{sp} (curve slope) determined via plotting ΔV versus ΔP (for 1 ml/min, 2 ml/min, and 3 ml/min brine flow rates) at 3.45 MPa, 323 K, 1 wt% NaCl brine salinity at pH = 7.

10.3 Results and discussion

All measured C are given in Table 10-2 and Fig. 10-3. In the following, the effect of each thermophysical parameter is discussed in detail.

Table 10-2 Streaming and zeta potentials measured for basalt.

Brine	p, MPa	T, K	S, wt% NaCl	pH[1]	pH[2]	C, mV/MPa	ζ, mV
Dead	1.72	298	1	7.0	7.1	-9.6	-23.3
Dead	3.45	298	1	7.0	7.3	-9.5	-23.1
Dead	5.17	298	1	7.0	7.4	-9.1	-22.0
Dead	6.9	298	1	7.0	7.3	-9.2	-22.3
Dead	1.72	323	1	7.0	7.0	-3.2	-8.2
Dead	3.45	323	1	7.0	7.1	-3.6	-9.3
Dead	5.17	323	1	7.0	7.3	-3.6	-9.1
Dead	6.9	323	1	7.0	7.2	-3.3	-8.6
Dead	5.17	323	1	4.0	6.4	-1.4	-3.7
Dead	5.17	323	1	8.5	7.4	-4.8	-12.3
Dead	5.17	323	1	10.0	7.9	-6.6	-16.9
Dead	5.17	323	1.8	7.0	7.0	-2.0	-8.2
Dead	5.17	323	2.6	7.0	7.1	-0.7	-4.6
Dead	5.17	323	3.5	7.0	7.2	-0.1	-0.7
Live	5.17	323	1	7.0	5.8	-2.5	-6.3

[1] injected brine at atmospheric condition

[2] collected brine at atmospheric condition

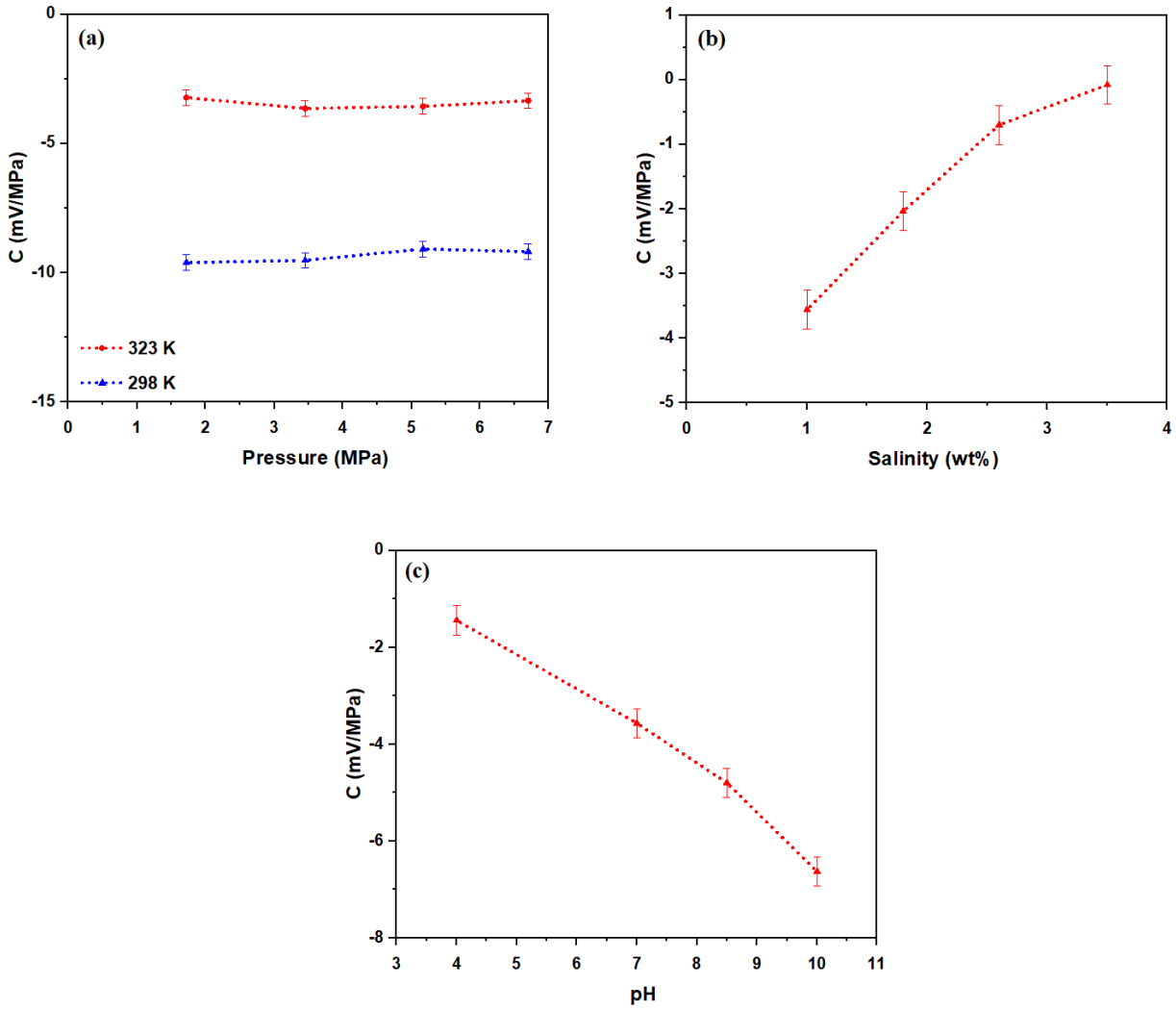

Fig. 10-3 Streaming potential C of basalt as a function of various thermophysical parameters: (a) effect of pressure and temperature, (b) effect of NaCl concentration (measured at 5.17 MPa and 323 K for dead brine), and (c) effect of pH value of the brine (measured at 1 wt% NaCl concentration, 5.17 MPa, and 323 K for dead brine).

10.3.1 Effects of pressure and temperature

Basaltic rock can be found at shallow (near to surface) or deep (i.e. up to 200 km) depth, resulting in a wide range of pore pressures existing in the rock (Cas and Simmons, 2018). However, for CGS and geothermal purposes, the ideal production depth lies within 200 to 1000 m underground depth (mostly due to limitations/complications in drilling operations, including slow penetration

rate, drill bit and string stuck due to pressure differential between wellbore mud pressure and pore pressure, wellbore collapse, among others (Millett et al., 2016)). Thus, in this study, we examined a pressure range of 1.72 MPa to 6.9 MPa to mimic realistic underground pressures for gas geo-storage purposes (Hosseini et al., 2022b).

Dead brine C did not change with pore pressure (at constant temperature, salinity and pH), Table 10-2 and Fig. 10-3. Moreover, ζ remained constant when pore pressure increased from 1.72 MPa to 6.9 MPa (at constant temperature), Fig. 10-4; this behavior was also observed for sandstone (e.g. (Hidayat et al., 2022a, Hidayat et al., 2022b)) and carbonates (e.g. (Rodríguez and Araujo, 2006)); note that for dead brine at constant salinity (here 1 wt% NaCl) and constant temperature (here 298 or 323 K), μ_w, σ_w, and $\mathcal{E}_w$ and also pH remained constant (Saunders et al., 2012, Hidayat et al., 2022b, Vinogradov et al., 2018). However, it was found by (Hidayat et al., 2022b) that for live brine (where pH decreased with increase in pore pressure due to increased CO_2 dissolution, reaction with water and associated increased acidity, e.g. (Iglauer, 2011, Peng et al., 2013, Adamczyk et al., 2009)), ζ increased with pore pressure due to protonation of functional surface groups on the rock (e.g. (Hidayat et al., 2022b, Karunarathne et al., 2022, Stumm and Morgan, 2012, Vinogradov and Jackson, 2015, Vinogradov et al., 2018)). This observation significantly impacts the wettability of CO_2-basalt (which increases with pressure, consistent with the more hydrophobic rock surface characteristics (Al-Yaseri et al., 2021b, Iglauer et al., 2020)). The increase in CO_2-basalt wettability with increase in pressure can also be attributed to the increased intermolecular forces between basalt and CO_2 (Iglauer et al., 2012).

Furthermore, C and ζ increased with temperature (decrease in $|C|$ and $|\zeta|$). For example, when temperature increased from 298 K to 323 K at 5.17 MPa, C and ζ changed from -9.1 mV/MPa to -3.6 mV/MPa and from -22 mV to -9.1 mV, respectively. This result is again similar to the responses observed for sandstone (e.g. (Hidayat et al., 2022b, Vinogradov et al., 2018, Vinogradov and Jackson, 2015)) and carbonates (e.g. (Al Mahrouqi et al., 2016, Al Mahrouqi et al., 2017, Rodríguez and Araujo, 2006)), and is attributed to the decrease in pH when temperature increases at low ionic strength (Note that this is caused by dissociation of water molecules which are more vibrated and ionized at higher temperature, resulting in an increase in hydronium ions and consequently an acidic behavior), (Ross and Behringer, 2019, Vinogradov et al., 2018). Moreover, $\mathcal{E}_w$ and μ_w decreased with temperature, while σ_w increased with temperature (i.e. by increasing

temperature from 298 K to 323 K, σ_w increased from 17.83 mS/m to 27.29 mS/mv (see Eq. (9) in (Sen and Goode, 1992)), while $\mathcal{E}_w$ decreased from 6.64 × 10^{-10} F/m to 5.96 × 10^{-10} F/m (see Eq. (A-3) in (Saunders et al., 2012)) and μ_w decreased from 9.02 × 10^{-4} Pa.s to 5.58 × 10^{-4} Pa.s (see Eq. (A-9) in (Saunders et al., 2012)) for dead brine (with a salinity of 1 wt% NaCl at 5.17 MPa). Thus, based on Equation (4), μ_w and C are the most significant parameters affecting ζ and leading to its increase with temperature. We also conclude that the increase in CO_2 wettability with temperature (for the basalt/CO_2/brine system, e.g. (Al-Yaseri et al., 2021b, Iglauer et al., 2020)) can at least partially be attributed to the decrease in $|\zeta|$ with increasing temperature, see Fig. 10-4.

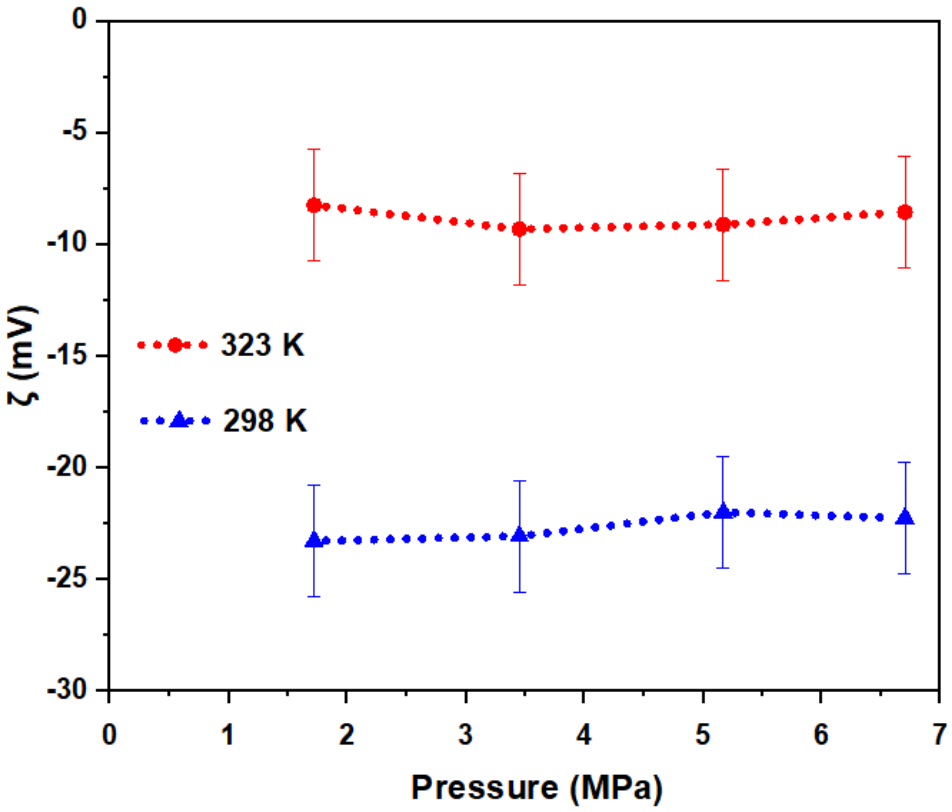

Fig. 10-4 Zeta potential of the dead brine-basalt system as a function of pore pressure and temperature (measured at 1 wt% NaCl and pH = 7).

10.3.2 Effect of salinity

C and ζ increased with salinity, Fig. 10-5; for example, when salinity increased from 1 wt% NaCl to 3.5 wt% NaCl at 5.7 MPa and 323 K, C increased from -3.6 mV/MPa to -0.1 mV/MPa, while ζ changed from -9.1 mV to -0.7 mV. However, ζ remained negative over the whole salinity range tested. Such a decrease in $|\zeta|$ with increasing salinity was also reported for sandstone (e.g. (Walker and Glover, 2018, Vinogradov et al., 2010, Alarouj et al., 2021, Awan et al., 2022, Nasralla and Nasr-El-Din, 2014b)) and carbonates (e.g. (Al Mahrouqi et al., 2017, Collini et al., 2020, Cherubini et al., 2018)), albeit anomalies regarding the salinity dependence of ζ have also been reported for sandstone (e.g. (Li et al., 2018, Hidayat et al., 2022b)); those anomalies were attributed to other minerals such as chlorites, montmorillonite, mica, feldspars, and ilmenite contained in the sandstone (Shehata and Nasr-El-Din, 2015). Mechanistically this ρ-s response implies that alterations in the electrical resistivity (ρ) of the rock are related to the compression of the electric double layer and the subsequent surface charge (s) shielding (i.e. the negative surface charge of basalt is shielded by the cations of the dissolved salt; note that as the double layer compresses, the ions in the diffuse layer move closer to the surface, leading to increased shielding of the surface charges on the basalt (Al-Yaseri et al., 2016, Arif et al., 2017a)), which results in a more electrically neutral surface. Moreover, $\mathcal{E}_w$, decreased with salinity, but μ_w and σ_w increased with salinity. For example, when salinity increased from 1 wt% NaCl to 3.5 wt% NaCl (at p = 5.17 MPa and T = 323 K), σ_w increased from 27.28 mS/m to 83.08 mS/m, while $\mathcal{E}_w$ slightly decreased from 5.96×10^{-10} F/m to 5.36×10^{-10} F/m and μ_w slightly increased from 5.58×10^{-4} Pa.s to 5.77×10^{-4} Pa.s (for the latter three parameters dead brine with 1 wt% NaCl salinity was considered). Thus, based on Equation (4), C is the most significant parameter which reduces $|\zeta|$ when salinity increases. Consequently, CO_2 wettability increases with salinity for basalt due to the decrease in $|\zeta|$ with increasing salinity, see Fig. 10-5.

Divalent ions found in salts such as Mg^{2+} and Ca^{2+} exhibit stronger electrostatic interactions with the surface of the basaltic rock when compared to monovalent ions such as K^+ and Na^+ (Gopani et al., 2021, Salgın et al., 2012). These interactions lead to a decrease in the magnitude of the zeta potential (Yukselen-Aksoy and Kaya, 2011). Moreover, certain salts, such as Na_2CO_3, KOH, $(NH_4)_2SO_4$ and KHP have the ability to alter the pH of the brine (Xu et al., 2013, Alhakimi et al., 2003). These pH changes impact the zeta potential of basaltic rocks (Walker and Glover, 2018).

In the presence of hydroxyl ions (OH^-), creating alkaline conditions (e.g. by Na_2CO_3 and KOH), the zeta potential becomes more negative (Kovalchuk and Zozulynets, 2021). Conversely, the presence of hydrogen ions (H^+), leading to acidic conditions (e.g. by $(NH_4)_2SO_4$ and KHP), leads to less negative zeta potentials (Gislason et al., 2014), see also section 10.3.3.

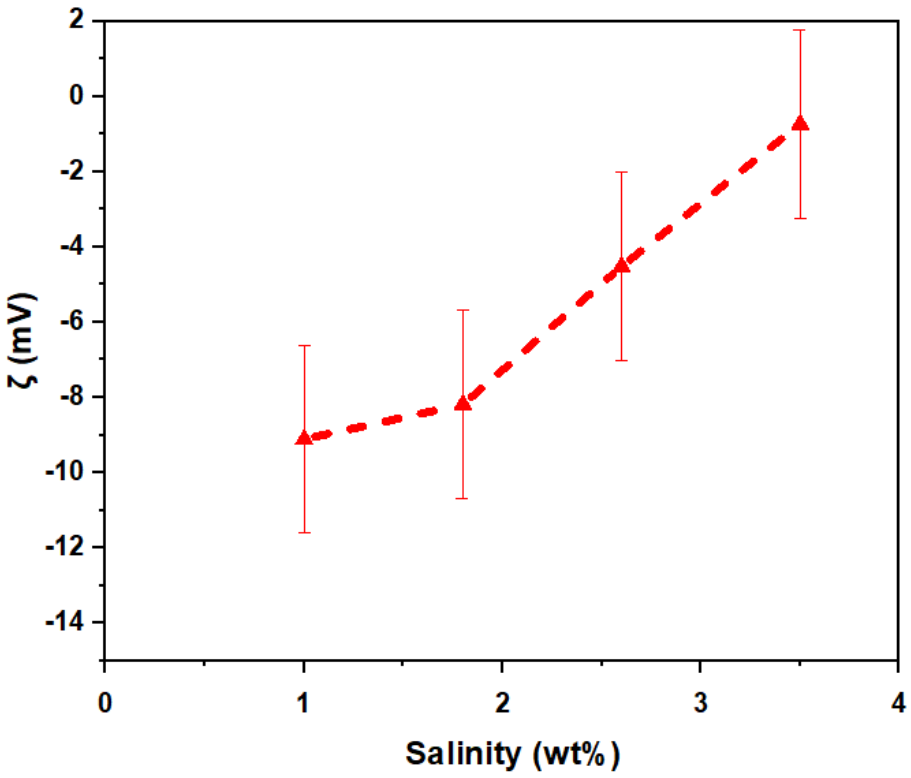

Fig. 10-5 Basalt zeta potential as a function of NaCl concentration in the dead brine (measured at p =5.17 MPa, T = 323 K and pH = 7).

10.3.3 Effect of pH value

In case of CGS, the pH value of the pore fluid in the basalt can vary significantly, from relatively low (pH = 3-4 (Galeczka et al., 2013, Gislason et al., 2014, Rogers et al., 2006, Kaszuba and Janecky, 2009)) to high (pH = 8-11, due to the basic nature of basalt which contains 45 to 55% silica (i.e. mafic minerals, plagioclase feldspars and feldspathoid minerals, e.g. (Gudbrandsson et al., 2011)). Here, C and ζ increased strongly with decreasing pH, as expected (consistent with data

reported (Hidayat et al., 2022b, Walker and Glover, 2018, Shehata and Nasr-El-Din, 2015, Alarouj et al., 2021, Vinogradov and Jackson, 2015) for sandstone and (Farooq et al., 2011, Saw and Mandal, 2020, Vdović, 2001, Vdović and Bišćan, 1998, Mahani et al., 2017) for carbonates), and due to protonation of surface function groups (compare reaction schemes 10-1 and 10-2, Fig. 10-6); for instance, C increased from -6.6 mV/MPa to -1.4 mV/MPa and ζ increased from -16.9 mV to -3.7 mV when pH decreased from 10 to 4 (moving pH away from point of zero charge or PZC = 3.5 for basalt (Anda et al., 2015)). Again, ζ remained negative over the whole pH range tested here, consistent with literature data (reported for other minerals, e.g. (Vinogradov et al., 2018, Hidayat et al., 2022b, Walker and Glover, 2018)). Overall alkaline components in the basalt (e.g. calcium, magnesium, sodium and potassium which create pH > 7, (Bell et al., 2003, Kovalchuk and Zozulynets, 2021)) reduce the surface potential (i.e. render it more negative, by adding OH^- ions onto the rock surface (i.e. via deprotonation reaction, see Scheme 10-2) while the acidic components (e.g. iron and aluminum which create pH < 7, (Gislason et al., 2014, Snæbjörnsdóttir et al., 2014)) increase ζ by adding protons (H^+) onto the rock surface (i.e. via a protonation reaction, see Scheme 10-1).

In addition, in CGS, dissolution trapping is a major storage mechanism, and generally CO_2 mixes with H_2O around the edges of the injected CO_2 plume which (see above) creates acidic live brine (Riaz et al., 2006, Iglauer, 2011, Raza et al., 2022, El-Maghraby et al., 2012, Al-Khdheeawi et al., 2017a). Thus, we conducted one test for 1 ml/min, 2 ml/min, and 3 ml/min brine flow rates with live brine (1 wt% NaCl brine equilibrated with CO_2 at 5.17 MPa and 323 K) and compared the result with that of dead brine (at the same test pressure and temperature). Now, while C was -3.6 mV/MPa and ζ was -9.1 mV for dead brine (pH = 7.3 for produced brine at atmospheric condition, see Table 10-2), C = -2.5 mV/MPa and ζ = -6.33 mV were measured for live brine (pH = 5.8 for produced brine at atmospheric condition, see Table 10-2). This higher ζ for live brine is consistent with our results in terms of the effects of pH on ζ, see above, and it is also consistent with (Hidayat et al., 2022a, Hidayat et al., 2022b) where they tested these effects on San Saba sandstone sample at 4.5 to 10 MPa and 298 to 313 K and compared their results with Fontainebleau sample at the same experimental conditions.

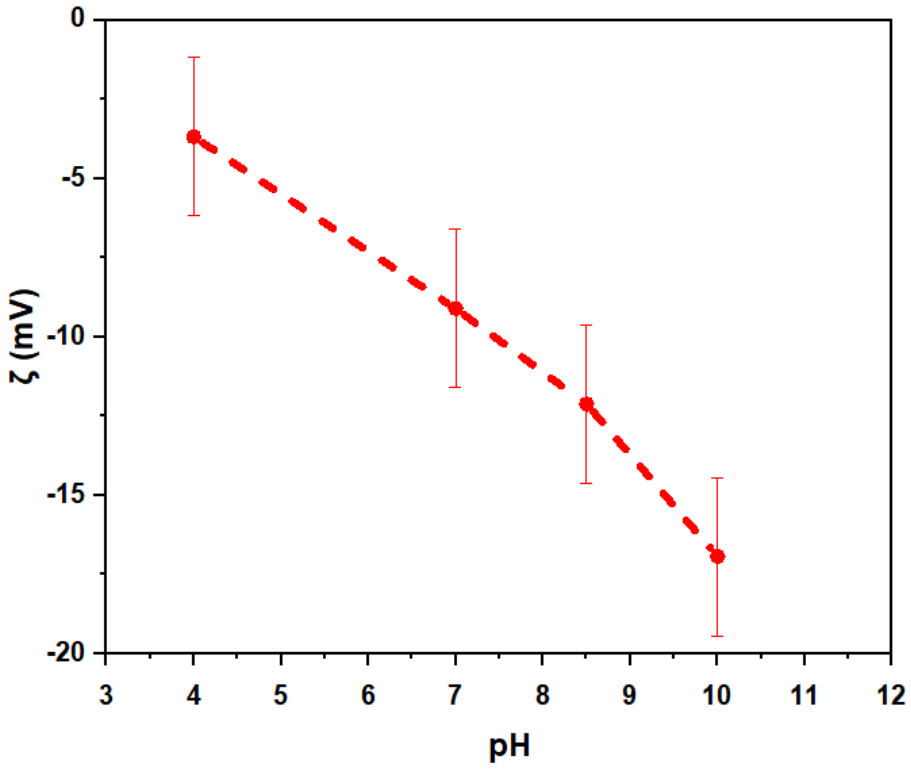

Fig. 10-6 Zeta potential of basalt as a function of pH value of the brine (measured at 1 wt% NaCl concentration, 5.17 MPa and 323 K).

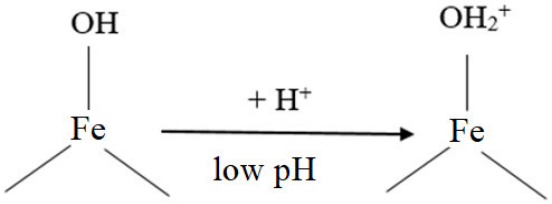

Scheme 10-1 Protonation of FeOH surface group.

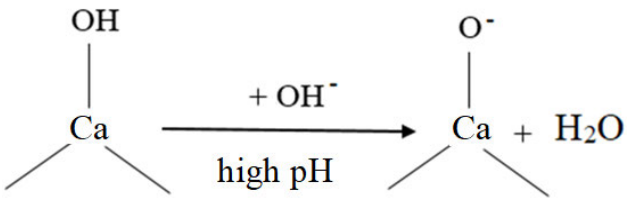

Scheme 10-2 Deprotonation of CaOH surface group.

10.3.4 Effect of rock mineralogy

Rock mineralogy significantly affects ζ (Awan et al., 2022), and it has been suggested that ζ can be estimated as a weighted average of the zeta potentials of all minerals in the rock (Alarouj et al., 2021). Consequently, ζ of the rock is mostly determined by the ζ of the dominant minerals in that

rock (Hidayat et al., 2022b). For example, in the basalt studied here, the dominant minerals were labradorite and augite (constituting a total of 79.5 wt% of the rock, see Table 10-1); thus, it is expected that ζ of the basalt is mostly affected by ζ of these two minerals.

Augite (a pyroxene mineral which constitutes 37.5 wt% of the basalt) tends to exhibit a negative zeta potential, under typical experimental conditions (Dunning et al., 1982). This is primarily attributed to the presence of negatively charged surface groups or sites (e.g. silicate groups) on its surface. These silicate groups can undergo ionization in an aqueous environment, resulting in the release of OH^- ions or other negatively charged species (Hair, 1975). Under neutral to alkaline pH conditions, the dissociation of silicate groups on the augite surface contributes to a net negative charge (Zhuravlev, 1987). Tohry et al. (2021) (Tohry et al., 2021) found that ζ of hematite is more negative than that of augite ($|\zeta_{augite}| < |\zeta_{hematite}|$). Moreover, Forbes and Franks (2013) (Forbes and Franks, 2013) found that ζ of quartz is more negative than that of hematite ($|\zeta_{hematite}| < |\zeta_{quartz}|$). We, thus, expect that ζ of quartz should be more negative than that of augite ($|\zeta_{augite}| < |\zeta_{quartz}|$).

Similarly, the zeta potentials of labradorite (a plagioclase feldspar which constitutes 42 wt% of the basalt) and nepheline (a feldspathoid mineral which constitutes 8.6 wt% of the basalt) are negative under typical experimental conditions (Dunning et al., 1982, Rudolph and Peuker, 2014), indicating their propensity to attract and interact with positively charged species (cations) in the surrounding solution. This can be attributed to the presence of charged surface groups on the mineral surfaces, which are usually derived from the dissociation of OH groups on the surface of the minerals (Hair, 1975).

Despite augite, labradorite and nepheline which tend to exhibit negative ζ, olivine (a magnesium iron silicate which constitutes 11.9 wt% of the basalt) has positive ζ at pH = 5 to 7 (Ucbas et al., 2014), resulting in an increase in ζ for basalt.

Overall, ζ of quartz is found to be more negative than that of the dominant minerals in the basalt, such as labradorite (e.g. as shown in (Walker and Glover, 2018) compared to (Dunning et al., 1982)) and augite (as mentioned above). Additionally, ζ of olivine is positive. Therefore, based on these findings, we can conclude that in a macro-scale, ζ_{quartz} is more negative than ζ_{basalt}. It is also important to note that since the SiO_2 content in basalt (i.e. 52 wt%) is less than that of quartz (Le Bas and Streckeisen, 1991), ζ_{quartz} is more negative than ζ_{basalt} (Hase et al., 2003), which is

consistent with literature results (e.g. (Fan et al., 2020, Forbes and Franks, 2013, Zhou et al., 2020)) and our result in this study (e.g. see Figs. 10-4, 10-5 and 10-6 for basalt and sandstone). Consequently, more gas wettability of basalt/gas/brine system is expected compared to that of quartz/gas/brine system (e.g. (Iglauer, 2017, Iglauer et al., 2020, Hosseini et al., 2022b)) due to less $|\zeta|$ in the basalt.

Table 10-3 lists concentrations of the main cations in the dead and live effluents. In this regard, identification of the dissolved Na is impossible as it is hard to distinguish between Na in NaCl aqueous solution and the dissolved Na. However, it is clearly seen a significant increase in concentration of Ca and carbonate ($CaCO_3$) mineral and a non-significant increase in concentration of Fe and K by the live brine (pH = 5.8) compared to the dead brine (pH = 7.3), implying more dissolution of the minerals by the live brine. This shows the impact of a pH < 7 environment on the mineral dissolution, where divalent cations (e.g. Mg^{2+}, Ca^{2+}, and Fe^{2+}) are released into the solution (Park and Fan, 2004, Goldberg et al., 2008) (note that the dissolution rate of basalt is a function of pH and temperature (Gislason and Oelkers, 2003)). The release of Ca^{2+} cations as an alkali component of the basalt reduces the pH of the system, implying the less negative zeta potential with the live brine compared to the dead brine. It is notable that high concentration of the divalent cations can enhance the rate of carbon mineralization (Flaathen, 2009), indicating that the studied basalt can be a good host rock for mineral trapping of CO_2. Furthermore, the permeability and porosity of the basaltic host rock can be increased due to the more mineral dissolution through the live brine (Kanakiya et al., 2017), resulting in an increase in the streaming potential coupling coefficient, consistent with (Jouniaux et al., 2000).

Table 10-3 Concentrations of the main cations in the dead and live brines.

Element	Unit	Live brine	Dead brine
Ca	mg/L	1.1	< 0.5
Mg	mg/L	< 0.5	< 0.5
K	mg/L	2.0	1.9
Na	mg/L	3800	3800
Fe	µg/L	19	< 10
Hardness as $CaCO_3$*	mg/L	4.9	< 3.0

*The released Ca^{2+} cations into the solution can react with dissolved CO_2 to form carbonate ($CaCO_3$) mineral (Raza et al., 2022).

10.4 Conclusions

The electric surface charge of basaltic rocks saturated with geo-fluids (e.g. water, CO_2 and H_2) has many applications in various fields such as CO_2 and H_2 geological storage sites, hydrocarbon reservoirs, and geothermal systems (Collini et al., 2020, Hidayat et al., 2022a, Jackson et al., 2016, Revil and Pezard, 1998). Therefore, the zeta potential of a basaltic rock (saturated with aqueous NaCl solutions) was deduced from streaming potential measurement and the effects of pore pressure, temperature, salinity, rock mineralogy and pH were reported for the first time. The key findings of the study are as follows:

- ζ was negative at all thermophysical conditions examined in this study; the ζ of dead brine remained constant versus pore pressure (as the pH value did not change). However, ζ strongly increased when CO_2 was added (and pH decreased significantly, live brine); thus the magnitude of ζ decreased with pore pressure when CO_2 was present, implying an increase in CO_2 wettability with pore pressure, and consistent with independent contact angle measurements (e.g. (Al-Yaseri et al., 2021b, Iglauer et al., 2020)).

- ζ increased (attained less negative values) with increasing temperature (implying an increase in CO_2 wettability with temperature, consistent with literature (Al-Yaseri et al., 2021b, Al-Yaseri and Jha, 2021, Hosseini et al., 2022b, Iglauer et al., 2020)) and salinity, but decreased (became more negative) with increasing pH.

- Pore pressure, temperature and salt type have an indirect impact on the ζ via impact on pH, while the pH value strongly affects ζ (Hidayat et al., 2022a, Thanh and Sprik, 2016, Walker and Glover, 2018).

- The ζ_{basalt} measured in this study is less negative than $\zeta_{sandstone}$ reported in the literature (i.e. ζ_{basalt} = -9.53 mV/MPa and $\zeta_{sandstone}$ = -15.7 mV/MPa at p = 3.45 MPa, T = 298 K, pH = 7 and S = 1 wt% NaCl were obtained, e.g. (Hidayat et al., 2022a)).

The fundamental results reported in this study are relevant for many applications, including gas geo-storage (CO_2 and H_2), subsurface flow pattern interpretation and geothermal projects.

Chapter 11 Conclusions and future outlook

11.1 Conclusions

This thesis presents fundamental data on the wetting characteristics and interfaces of rock/H_2/brine systems at UHS conditions. The IFT between H_2 and brine was determined using pendant drop technique. The hydrogen wettability for calcite, caprocks, basalt and Indiana limestone was measured using advancing and receding contact angle measurements. The obtained contact angle and IFT data were then utilized to theoretically calculate the rock-fluid IFT by combining Young's equation and Neumann's equation of state. A wide range of experimental conditions were investigated, including pressure (0.1 MPa to 20 MPa), temperature (298 K to 353 K), and brine salinity (0 $mol.kg^{-1}$ to 4.95 $mol.kg^{-1}$). The study also analyzed the implications of wettability and interfacial tension on UHS process. Overall, the findings contribute to a better understanding of interface and wetting characteristics of various rock/H_2/brine systems and their influences on predicting H_2 storage capacity and containment security. The key findings of this research can be summarized as follows:

a) H_2-brine interfacial tension

As $\gamma_{H2\text{-}brine}$ considerably affects the capillary pressure, the linear variation of $\gamma_{H2\text{-}brine}$ with reservoir conditions, such as pressure, temperature, and salinity, influences the capillary pressure variations. The variations in the capillary pressure are more pronounced for temperature and salinity, as $\gamma_{H2\text{-}brine}$ exhibited significant changes with these two variables compared to pressure. As a result, it is anticipated that the pore-network upscaled functions utilized in reservoir-scale modelling would be sensitive to reservoir conditions.

b) Wettability of rock/H_2/brine systems

- The optimal conditions for reducing the risks associated with H_2 storage projects in calcite-rich carbonate formations involve high temperatures, low salinity, low pressures, and low organic surface concentration. However, it should be noted that even with intermediate wettability at low organic surface concentration, safe storage cannot be guaranteed. Comparing our findings with previously published studies on quartz/H_2/brine and mica/H_2/brine indicates that calcite-rich formations pose a higher risk for H_2 storage projects compared to other formations under geological conditions. Therefore, it is crucial to assess the influencing parameters accurately in order to ensure the success of H_2 geo-storage projects in carbonate formations.

- The capillary sealing efficiency in caprocks declined under all geo-storage conditions, whereas in oil shales, it increased with temperature. While both γ and θ declined with increase in temperature, the impact of γ (decrease in $\gamma\cos\theta$) was more significant than that of θ for clean caprocks, resulting in a reduction in capillary sealing efficiency as temperature increased. However, in the case of oil shales with high TOC, the effect of θ (increase in $\gamma\cos\theta$) was more dominant than γ, leading to an increase in capillary sealing efficiency as temperature increased.

- The presence of organic acid concentration resulted in enhanced H_2-wettability of basalts, leading to a decrease in the height of the H_2 column. However, even at high concentrations of stearic acid, all measured contact angles remained below 90 degrees. Furthermore, under identical geo-storage conditions, basaltic rocks can safely accommodate a larger volume of H_2 compared to CO_2, as the contact angles observed in the H_2 system are lower than those in the CO_2 system.

c) Factors responsible for the wettability alteration

- The rock-H_2 IFT for shale, evaporite and basaltic rocks decreased as pressure, temperature, and shale-TOC increased. Among these factors, the rock-H_2 IFT was primarily influenced by changes in wettability caused by pressure and shale-TOC. This indicates that under

high-pressure and high-shale-TOC conditions, gas molecules can easily wet the rocks, which is detrimental to effective sealing of H_2 during geo-storage. Furthermore, rock-water IFT increased with increasing shale-TOC but decreased with increasing temperature. This suggests that hot rocks with low shale-TOC values may offer optimal conditions for maximizing the sealing capacity of hydrogen during geo-storage. Thus, obtaining rock-fluid IFT data under various geo-storage conditions, including temperature, pressure, and shale-TOC, is crucial for accurately estimating the H_2 storage capacity in UHS projects beneath caprocks and basaltic formations.

- The calcite-H_2 IFT decreased with increasing brine salinity, pressure, and organic concentration, while it increased with temperature. This suggests that under high-pressure, high-brine salinity, and high-organic concentration conditions, gas molecules readily wet the surfaces of carbonate rocks. These conditions are favorable for adsorption trapping, as the affinity between gas and rock increases. However, they are unfavorable for structural trapping in carbonates. On the other hand, hot calcite-rich rocks offer ideal conditions for structural trapping but are less favorable for adsorption trapping. There were two slight increasing trends observed for calcite-water IFT: one with organic acid concentration (at 10 MPa and 323.15 K) and the other with salinity (at 15 MPa and 323.15 K). Furthermore, calcite-H_2 IFT was higher than calcite-CO_2 IFT. This indicates that, under similar geo-storage conditions, CO_2 has a higher tendency to occupy small pores, resulting in more adsorption trapping. However, CO_2 is less structurally stored in carbonates compared to H_2. This is due to the consistently higher wettability of carbonates by CO_2 compared to H_2.

- Under reservoir conditions of 323 K and 8.27 MPa, the presence of organic matter on the surface of Indiana limestone led to an increase in H_2 mobility. This increased mobility raises concerns about the potential risks associated with UHS projects in Indiana limestone, specifically the possibility of H_2 leakage through the rock containing organic matter. Furthermore, all samples treated with nanoparticles exhibited a decrease in H_2-wettability. This alteration in wettability led to a reduction in H_2 mobility, which can reduce the risks associated with UHS projects. However, it also resulted in an increase in H_2 residual trapping, which is unfavorable for UHS projects as it can lead to H_2 loss. In conclusion,

the wettability alteration caused by nanofluids during UHS in Indiana limestone reservoirs can have both advantages and disadvantages. Therefore, it would be reasonable to plan experiments involving nanofluids in the reservoir. However, it is crucial to optimize the concentration of nanofluids to maximize H_2 storage capacity while minimizing the risk factors such as H_2 leakage or loss.

- Across all examined thermophysical conditions in this study, ζ for basalt consistently exhibited negative values. ζ of dead brine remained unaffected by pore pressure as the pH value remained constant. However, the presence of CO_2 (live brine) led to a significant decrease in pH, resulting in a strong increase in ζ. This indicates that the magnitude of ζ decreased with increasing pore pressure when CO_2 was present, suggesting an augmentation in gas wettability as pore pressure increased. This finding is consistent with existing literature. Furthermore, ζ increased (attaining less negative values) with rising temperature, indicating an increase in gas wettability with higher temperature. This finding is also consistent with existing literature. Similarly, an increase in salinity also resulted in an increase in ζ. However, ζ decreased (becoming more negative) with higher pH levels. Pore pressure, temperature, and salt type indirectly influence ζ through their impact on pH. The pH value, in turn, strongly affects ζ. Comparing the measured ζ of basalt in this study to the reported ζ of sandstone in literature, it was observed that ζ of basalt is less negative than that of sandstone under similar experimental conditions.

11.2 Recommendations

Although this study extensively gathered interface and wetting characteristics data for different significant rock/H_2/brine systems, there remain unaddressed gaps and limitations. Therefore, the future research direction can be outlined as follows:

- Existing extensive datasets examining the impact of salinity on interface and wetting properties during the UHS processes have primarily utilized NaCl and KCl salts for making

solutions as representatives of formation brine. However, it is important to note that in actual reservoir conditions, formation brine comprises a mixture of monovalent, divalent, and occasionally trivalent ions. Therefore, future studies should prioritize additional research that takes into account the admixture of brine, as it would provide a more accurate representation of typical reservoir conditions. The effect of different ion types can also be potentially investigated in future research.

- In this research, the wettability data was collected following a brief equilibration period between the phases due to limited time for collecting the extensive datasets. Nevertheless, it is worth considering that hydrogen might interact with various rock minerals over an extended period of storage, resulting in mineral dissolution or precipitation. Such interactions can have a substantial impact on wettability, and consequently long-term effects on storage capacity and containment security. Hence, it is recommended to subject the rock samples to the tested fluids for an extended duration to mimic real storage conditions and compare the wettability results before and after exposure.

- The present study investigates some subjective organic acids and their respective concentrations to establish benchmarks for scientific advancements. However, it should be noted that the actual composition of organic acids may vary, and conducting accurate analyses on real geological samples would provide more comprehensive insights and detailed understanding.

- In this study, the application of silica nanofluid was utilized as a method to modify the wettability of the rock. It is recommended to examine the effect of other nanoparticles such as zinc oxide, aluminium oxide, magnesium oxide, zirconium oxide and iron oxide on wetting characteristics of subsurface rocks.

- Assessing the long-term stability and compatibility of nanofluids with reservoir conditions is a pivotal aspect of research in the context of hydrogen wettability. It entails studying how nanofluids behave within subsurface rock formations over extended timeframes and

under varying temperature and pressure conditions representative of real reservoir environments. Investigating the persistence of nanofluid-induced alterations in wettability and their potential impact on reservoir performance is crucial for determining the practical viability of nanofluids in subsurface applications. Furthermore, long-term stability assessments can shed light on the durability and sustainability of nanofluid-based wettability control strategies, which are essential considerations for their successful implementation in subsurface energy exploration and production.

- The influence of nanofluid on wettability was solely examined using Indiana limestone as the storage rock. It is advisable to conduct tests with nanofluid on sealing rock (without affecting the wettability of the storage formation) to determine the most suitable nanofluid concentration.

- The contact angle measurements employed in this study predominantly reflect surface chemistry under in-situ conditions. Consequently, it is advisable to complement these findings with other qualitative methods such as capillary pressure curve analysis and evaluation of relative permeability. The incorporation of these supplementary methods would yield a more holistic understanding of the intricate wetting characteristics within the pore matrix. Furthermore, given that Underground Hydrogen Storage (UHS) involves cyclic procedures encompassing both hydrogen imbibition (storage) and drainage (extraction) processes, it is essential to consider wettability for both phases. The data presented here is exclusively derived under specific in-situ conditions representative of hydrogen storage in reservoirs. Hence, to capture dynamic wettability throughout both storage and extraction processes, it is recommended to conduct hydrogen core flooding experiments. This approach could contribute to predicting and comprehending wetting transitions and interface stability during the entirety of the storage and extraction processes.

- The prediction of structural storage capacity using the interface and wetting characteristics of the rock-fluids systems only offers an initial approximation of storage heights, assuming the rock behaves like a simple capillary tube. However, in reality, the pore morphology of

rocks is much more intricate. To overcome this limitation, a more sophisticated coreflooding setup can directly estimate the capillary entry pressure of H_2, providing a more accurate assessment. Moreover, it is required to develop detailed pore-scale models to simulate the interface and wetting characteristics of rock-H_2-brine systems. These models could incorporate realistic rock geometries, surface properties, and fluid behavior to better understand the interplay between rock surfaces, hydrogen, and brine at geo-storage conditions.

- The pore structure of caprocks, particularly shales, is a crucial factor that significantly influences sealing efficiency. This structure varies considerably based on thermal evolution, different lithofacies, and structural conditions. Additionally, the presence of shale micro-fractures plays a significant role in assessing sealing efficiency. In this study, we made assumptions about two representative pore sizes when analyzing the capillary sealing efficiency in caprocks. However, for future research aiming to enhance our understanding of sealing efficiency, it is necessary to conduct comprehensive pore and micro-fracture characterization of caprocks using advanced techniques such as X-ray tomography, infrared spectroscopy, and neutron scattering (NS). These techniques can shed light on the influence of nanoconfinement on the wetting behavior of rock-H_2-brine systems, involving the study of wetting properties in nanoporous or nanoscale-confined rock materials and their interactions with H_2 and brine. Furthermore, it is essential to carefully examine the effects of maturity, connectivity, and distribution of organic matter on caprock wettability and, consequently, capillary sealing.

- In order to investigate the impact of shale-TOC on shale H_2-wettability, various samples with different TOC levels were tested, sourced from different locations. However, it is recommended to test multiple shale samples extracted from different depths of a single shale layer, as TOC can vary within the layer itself, consequently influencing wettability.

- In the calculation of rock-fluid IFT using Neumann's equation of state, it is assumed that the rock-brine IFT does not change with pressure. However, in reality, the rock-brine IFT

can change with pressure if any changes in dissolution and pH occur with pressure. Thus, this effect should be considered in future research.

- It is necessary to use molecular dynamics simulations or other atomistic modelling approaches to elucidate the mechanisms governing wetting behavior, interfacial tension, and adsorption phenomena in rock-H_2-brine systems.

- Using reservoir simulation is a robust approach to validate the findings of this thesis, particularly concerning estimated hydrogen column height at a field scale. To ensure this validation, it is essential to calibrate the simulation model meticulously to mimic the actual geological and wettability conditions. Incorporating real field data, conducting sensitivity analyses, historical performance matching, and scenario analyses are critical steps to confirm the model's reliability and to assess the sensitivity of the findings to varying parameters.

- Further scientific research is necessary to achieve a profound understanding of the concepts, theories, objectives, and methods pertaining to thermodynamics in geological porous media.

- It is recommended to implement large-scale field investigations, integrated reservoir modelling, and the consideration of geological heterogeneity to understand evolving flow patterns, optimal well placement and production strategies based on data given in this study, and the exploration of enhanced recovery methods.

References

ABAD, A. V. & DODDS, P. E. 2020. Green hydrogen characterisation initiatives: Definitions, standards, guarantees of origin, and challenges. *Energy Policy,* 138**,** 111300.

ABDULELAH, H., AL-YASERI, A., ALI, M., GIWELLI, A., NEGASH, B. M. & SARMADIVALEH, M. 2021. CO2/Basalt's interfacial tension and wettability directly from gas density: Implications for Carbon Geo-sequestration. *Journal of Petroleum Science and Engineering,* 204**,** 108683.

ABRAMOV, A., KESHAVARZ, A. & IGLAUER, S. 2019. Wettability of fully hydroxylated and alkylated (001) α-quartz surface in carbon dioxide atmosphere. *The Journal of Physical Chemistry C,* 123**,** 9027-9040.

ADAMCZYK, K., PRÉMONT-SCHWARZ, M., PINES, D., PINES, E. & NIBBERING, E. T. 2009. Real-time observation of carbonic acid formation in aqueous solution. *Science,* 326**,** 1690-1694.

ADAMSON, A. W. & GAST, A. P. 1967. *Physical chemistry of surfaces*, Interscience publishers New York.

AFEKARE, D., GUPTA, I. & RAO, D. 2020. Nanoscale investigation of silicon dioxide nanofluids and implications for enhanced oil recovery–An atomic force microscope study. *Journal of Petroleum Science and Engineering,* 191**,** 107165.

AGGELOPOULOS, C., ROBIN, M. & VIZIKA, O. 2011. Interfacial tension between CO2 and brine (NaCl+ CaCl2) at elevated pressures and temperatures: The additive effect of different salts. *Advances in Water Resources,* 34**,** 505-511.

AIZAWA, K., UYESHIMA, M. & NOGAMI, K. 2008. Zeta potential estimation of volcanic rocks on 11 island arc-type volcanoes in Japan: Implication for the generation of local self-potential anomalies. *Journal of Geophysical Research: Solid Earth,* 113.

AKHONDZADEH, H., KESHAVARZ, A., AL-YASERI, A. Z., ALI, M., AWAN, F. U. R., WANG, X., YANG, Y., IGLAUER, S. & LEBEDEV, M. 2020. Pore-scale analysis of coal cleat network evolution through liquid nitrogen treatment: A Micro-Computed Tomography investigation. *International Journal of Coal Geology,* 219**,** 103370.

AKHONDZADEH, H., KESHAVARZ, A., AWAN, F. U. R., ALI, M., AL-YASERI, A., LIU, C., YANG, Y., IGLAUER, S., GUREVICH, B. & LEBEDEV, M. 2021. Liquid nitrogen fracturing efficiency as a function of coal rank: A multi-scale tomographic study. *Journal of Natural Gas Science and Engineering,* 95**,** 104177.

AKITT, J. 1973. Proton chemical shift and hydration of the hydronium ion in aqueous acids. *Journal of the Chemical Society, Dalton Transactions***,** 49-52.

AKOB, D. M., COZZARELLI, I. M., DUNLAP, D. S., ROWAN, E. L. & LORAH, M. M. 2015. Organic and inorganic composition and microbiology of produced waters from Pennsylvania shale gas wells. *Applied Geochemistry,* 60**,** 116-125.

AL-ANSSARI, S., ALI, M., MEMON, S., BHATTI, M. A., LAGAT, C. & SARMADIVALEH, M. 2020. Reversible and irreversible adsorption of bare and hybrid silica nanoparticles onto carbonate surface at reservoir condition. *Petroleum,* 6**,** 277-285.

AL-ANSSARI, S., ARIF, M., WANG, S., BARIFCANI, A., LEBEDEV, M. & IGLAUER, S. 2017. Wettability of nano-treated calcite/CO2/brine systems: Implication for enhanced CO2 storage potential. *International Journal of Greenhouse Gas Control,* 66**,** 97-105.

AL-ANSSARI, S., BARIFCANI, A., WANG, S., MAXIM, L. & IGLAUER, S. 2016. Wettability alteration of oil-wet carbonate by silica nanofluid. *Journal of colloid and interface science,* 461**,** 435-442.

AL-BAZALI, T. M., ZHANG, J., CHENEVERT, M. E. & SHARMA, M. M. Measurement of the sealing capacity of shale caprocks. SPE annual technical conference and exhibition, 2005. OnePetro.

AL-KHDHEEAWI, E. A., MAHDI, D. S., ALI, M., IGLAUER, S. & BARIFCANI, A. Reservoir scale porosity-permeability evolution in sandstone due to CO2 geological storage. Proceedings of the 15th Greenhouse Gas Control Technologies Conference, 2021. 15-18.

AL-KHDHEEAWI, E. A., VIALLE, S., BARIFCANI, A., SARMADIVALEH, M. & IGLAUER, S. 2017a. Impact of reservoir wettability and heterogeneity on CO2-plume migration and trapping capacity. *International Journal of Greenhouse Gas Control,* 58**,** 142-158.

AL-KHDHEEAWI, E. A., VIALLE, S., BARIFCANI, A., SARMADIVALEH, M. & IGLAUER, S. 2017b. Influence of injection well configuration and rock wettability on CO2 plume behaviour and CO2 trapping capacity in heterogeneous reservoirs. *Journal of Natural Gas Science and Engineering,* 43**,** 190-206.

AL-MENHALI, A. S. & KREVOR, S. 2016. Capillary trapping of CO2 in oil reservoirs: Observations in a mixed-wet carbonate rock. *Environmental science and technology,* 50**,** 2727-2734.

AL-MUKAINAH, H., AL-YASERI, A., YEKEEN, N., AL HAMAD, J. & MAHMOUD, M. 2022. Wettability of shale–brine–H2 system and H2-brine interfacial tension for assessment of the sealing capacities of shale formations during underground hydrogen storage. *Energy Reports,* 8**,** 8830-8843.

AL-RUBAYE, A., AL-YASERI, A., ALI, M. & BEN MAHMUD, H. 2021. Characterization and analysis of naturally fractured gas reservoirs based on stimulated reservoir volume and petro-physical parameters. *Journal of Petroleum Exploration and Production,* 11**,** 639-649.

AL-SHIRAWI, M., KARIMI, M. & AL-MAAMARI, R. S. 2021. Impact of carbonate surface mineralogy on wettability alteration using stearic acid. *Journal of Petroleum Science and Engineering,* 203**,** 108674.

AL-YASERI, A., ABDULELAH, H., YEKEEN, N., ALI, M., NEGASH, B. M. & ZHANG, Y. 2021a. Assessment of CO2/shale interfacial tension. *Colloids Surfaces A: Physicochemical Engineering Aspects,* 627**,** 127118.

AL-YASERI, A., ALI, M., ALI, M., TAHERI, R. & WOLFF-BOENISCH, D. 2021b. Western Australia basalt-CO2-brine wettability at geo-storage conditions. *Journal of colloid and interface science,* 603**,** 165-171.

AL-YASERI, A., ESTEBAN, L., GIWELLI, A., SAROUT, J., LEBEDEV, M. & SARMADIVALEH, M. 2022a. Initial and residual trapping of hydrogen and nitrogen in Fontainebleau sandstone using nuclear magnetic resonance core flooding. *International Journal of Hydrogen Energy,* 47**,** 22482-22494.

AL-YASERI, A. & JHA, N. K. 2021. On hydrogen wettability of basaltic rock. *Journal of Petroleum Science and Engineering,* 200**,** 108387.

AL-YASERI, A., WOLFF-BOENISCH, D., FAUZIAH, C. A. & IGLAUER, S. 2021c. Hydrogen wettability of clays: Implications for underground hydrogen storage. *International Journal of Hydrogen Energy,* 46**,** 34356-34361.

AL-YASERI, A., YEKEEN, N., ALI, M., PAL, N., VERMA, A., ABDULELAH, H., HOTEIT, H. & SARMADIVALEH, M. 2022b. Effect of organic acids on CO2-rock and water-rock

interfacial tension: Implications for CO2 geo-storage. *Journal of Petroleum Science and Engineering,* 214**,** 110480.

AL-YASERI, A., YEKEEN, N., MAHMOUD, M., KAKATI, A., XIE, Q. & GIWELLI, A. 2022c. Thermodynamic characterization of H2-brine-shale wettability: Implications for hydrogen storage at subsurface. *International Journal of Hydrogen Energy,* 47**,** 22510-22521.

AL-YASERI, A. Z., LEBEDEV, M., BARIFCANI, A. & IGLAUER, S. 2016. Receding and advancing (CO2+ brine+ quartz) contact angles as a function of pressure, temperature, surface roughness, salt type and salinity. *The Journal of Chemical Thermodynamics,* 93**,** 416-423.

AL-YASERI, A. Z., ROSHAN, H., LEBEDEV, M., BARIFCANI, A. & IGLAUER, S. 2016. Dependence of quartz wettability on fluid density. *Geophysical Research Letters,* 43**,** 3771-3776.

AL GHAFRI, S., MAITLAND, G. C. & TRUSLER, J. M. 2012. Densities of aqueous MgCl2 (aq), CaCl2 (aq), KI (aq), NaCl (aq), KCl (aq), AlCl3 (aq), and (0.964 NaCl+ 0.136 KCl)(aq) at temperatures between (283 and 472) K, pressures up to 68.5 MPa, and molalities up to 6 mol· kg–1. *Journal of Chemical and Engineering Data,* 57**,** 1288-1304.

AL MAHROUQI, D., VINOGRADOV, J. & JACKSON, M. D. 2016. Temperature dependence of the zeta potential in intact natural carbonates. *Geophysical Research Letters,* 43**,** 11,578-11,587.

AL MAHROUQI, D., VINOGRADOV, J. & JACKSON, M. D. 2017. Zeta potential of artificial and natural calcite in aqueous solution. *Advances in Colloid and Interface Science,* 240**,** 60-76.

ALANAZI, A., YEKEEN, N., ALI, M., ALI, M., ABU-MAHFOUZ, I. S., KESHAVARZ, A., IGLAUER, S. & HOTEIT, H. 2023. Influence of organics and gas mixing on hydrogen/brine and methane/brine wettability using Jordanian oil shale rocks: Implications for hydrogen geological storage. *Journal of Energy Storage,* 62**,** 106865.

ALAROUJ, M., COLLINI, H. & JACKSON, M. D. 2021. Positive Zeta Potential in Sandstones Saturated With Natural Saline Brine. *Geophysical Research Letters,* 48**,** e2021GL094306.

ALHAKIMI, G., STUDNICKI, L. H. & AL-GHAZALI, M. 2003. Photocatalytic destruction of potassium hydrogen phthalate using TiO2 and sunlight: application for the treatment of industrial wastewater. *Journal of Photochemistry and Photobiology A: Chemistry,* 154**,** 219-228.

ALI, M., AFTAB, A., ARAIN, Z.-U.-A., AL-YASERI, A., ROSHAN, H., SAEEDI, A., IGLAUER, S. & SARMADIVALEH, M. 2020a. Influence of organic acid concentration on wettability alteration of cap-rock: implications for CO2 trapping/storage. *ACS Applied Materials & Interfaces,* 12**,** 39850-39858.

ALI, M., AFTAB, A., AWAN, F. U. R., AKHONDZADEH, H., KESHAVARZ, A., SAEEDI, A., IGLAUER, S. & SARMADIVALEH, M. 2021a. CO2-wettability reversal of cap-rock by alumina nanofluid: Implications for CO2 geo-storage. *Fuel Processing Technology,* 214**,** 106722.

ALI, M., AL-ANSSARI, S., ARIF, M., BARIFCANI, A., SARMADIVALEH, M., STALKER, L., LEBEDEV, M. & IGLAUER, S. 2019a. Organic acid concentration thresholds for ageing of carbonate minerals: Implications for CO2 trapping/storage. *Journal of colloid and interface science,* 534**,** 88-94.

ALI, M., ARIF, M., SAHITO, M. F., AL-ANSSARI, S., KESHAVARZ, A., BARIFCANI, A., STALKER, L., SARMADIVALEH, M. & IGLAUER, S. 2019b. CO2-wettability of

sandstones exposed to traces of organic acids: Implications for CO2 geo-storage. *International Journal of Greenhouse Gas Control,* 83**,** 61-68.

ALI, M., AWAN, F. U. R., ALI, M., AL-YASERI, A., ARIF, M., SÁNCHEZ-ROMÁN, M., KESHAVARZ, A. & IGLAUER, S. 2021b. Effect of humic acid on CO2-wettability in sandstone formation. *Journal of Colloid and Interface Science,* 588**,** 315-325.

ALI, M., JHA, N. K., AL-YASERI, A., ZHANG, Y., IGLAUER, S. & SARMADIVALEH, M. 2021c. Hydrogen wettability of quartz substrates exposed to organic acids; Implications for hydrogen geo-storage in sandstone reservoirs. *Journal of Petroleum Science and Engineering,* 207**,** 109081.

ALI, M., JHA, N. K., PAL, N., KESHAVARZ, A., HOTEIT, H. & SARMADIVALEH, M. 2022a. Recent advances in carbon dioxide geological storage, experimental procedures, influencing parameters, and future outlook. *Earth-Science Reviews,* 225**,** 103895.

ALI, M., PAN, B., YEKEEN, N., AL-ANSSARI, S., AL-ANAZI, A., KESHAVARZ, A., IGLAUER, S. & HOTEIT, H. 2022b. Assessment of wettability and rock-fluid interfacial tension of caprock: Implications for hydrogen and carbon dioxide geo-storage. *International Journal of Hydrogen Energy,* 47**,** 14104-14120.

ALI, M., SAHITO, M. F., JHA, N. K., MEMON, S., KESHAVARZ, A., IGLAUER, S., SAEEDI, A. & SARMADIVALEH, M. 2020b. Effect of nanofluid on CO2-wettability reversal of sandstone formation; implications for CO2 geo-storage. *Journal of colloid and interface science,* 559**,** 304-312.

ALI, M., YEKEEN, N., PAL, N., KESHAVARZ, A., IGLAUER, S. & HOTEIT, H. 2021d. Influence of pressure, temperature and organic surface concentration on hydrogen wettability of caprock; implications for hydrogen geo-storage. *Energy Reports,* 7**,** 5988-5996.

ALI, M., YEKEEN, N., PAL, N., KESHAVARZ, A., IGLAUER, S. & HOTEIT, H. 2022c. Influence of organic molecules on wetting characteristics of mica/H2/brine systems: Implications for hydrogen structural trapping capacities. *Journal of Colloid and Interface Science,* 608**,** 1739-1749.

ALMEIDA, B. & TELO DA GAMA, M. 1989. Surface tension of simple mixtures: comparison between theory and experiment. *The Journal of Physical Chemistry,* 93**,** 4132-4138.

ALPASLAN, D., ERSEN DUDU, T. & AKTAS, N. 2023. Synthesis of poly (ginger oil) organo particles as a metal free catalysis and their use in hydrogen production from sodium borohydride methanolysis. *Journal of Polymers and the Environment,* 31**,** 1191-1201.

ALROUDHAN, A., VINOGRADOV, J. & JACKSON, M. 2016. Zeta potential of intact natural limestone: Impact of potential-determining ions Ca, Mg and SO4. *Colloids and Surfaces A: Physicochemical and Engineering Aspects,* 493**,** 83-98.

AMERI, A., KAVEH, N. S., RUDOLPH, E., WOLF, K. H., FARAJZADEH, R. & BRUINING, J. 2013. Investigation on interfacial interactions among crude oil–brine–sandstone rock–CO2 by contact angle measurements. *Energy and fuels,* 27**,** 1015-1025.

AMINNAJI, M., FAZELI, H., BAHRAMIAN, A., GERAMI, S. & GHOJAVAND, H. 2015. Wettability alteration of reservoir rocks from liquid wetting to gas wetting using nanofluid. *Transport in Porous Media,* 109**,** 201-216.

AMOTT, E. 1959. Observations relating to the wettability of porous rock. *Transactions of the AIME,* 216**,** 156-162.

ANDA, M., SHAMSHUDDIN, J. & FAUZIAH, C. 2015. Improving chemical properties of a highly weathered soil using finely ground basalt rocks. *Catena,* 124**,** 147-161.

ANDERSON, T. R., HAWKINS, E. & JONES, P. D. 2016. CO2, the greenhouse effect and global warming: from the pioneering work of Arrhenius and Callendar to today's Earth System Models. *Endeavour,* 40**,** 178-187.

ANDERSON, W. 1986. Wettability literature survey-part 2: Wettability measurement. *Journal of petroleum technology,* 38**,** 1246-1262.

APLIN, A. C., MATENAAR, I. F., MCCARTY, D. K. & VAN DER PLUIJM, B. A. 2006. Influence of mechanical compaction and clay mineral diagenesis on the microfabric and pore-scale properties of deep-water Gulf of Mexico mudstones. *Clays and Clay Minerals,* 54**,** 500-514.

ARGAUD, M. J. Predicting the interfacial tension of brine/gas (or condensate) systems. European Core Analysis Symposium, 1992. 14-16.

ARIF, M., ABU-KHAMSIN, S. A. & IGLAUER, S. 2019. Wettability of rock/CO2/brine and rock/oil/CO2-enriched-brine systems: Critical parametric analysis and future outlook. *Advances in colloid and interface science,* 268**,** 91-113.

ARIF, M., AL-YASERI, A. Z., BARIFCANI, A., LEBEDEV, M. & IGLAUER, S. 2016a. Impact of pressure and temperature on CO2–brine–mica contact angles and CO2–brine interfacial tension: Implications for carbon geo-sequestration. *Journal of colloid & interface science,* 462**,** 208-215.

ARIF, M., BARIFCANI, A. & IGLAUER, S. 2016b. Solid/CO2 and solid/water interfacial tensions as a function of pressure, temperature, salinity and mineral type: Implications for CO2-wettability and CO2 geo-storage. *International Journal of Greenhouse Gas Control,* 53**,** 263-273.

ARIF, M., BARIFCANI, A., LEBEDEV, M. & IGLAUER, S. 2016c. CO2-wettability of low to high rank coal seams: Implications for carbon sequestration and enhanced methane recovery. *Fuel,* 181**,** 680-689.

ARIF, M., BARIFCANI, A., LEBEDEV, M. & IGLAUER, S. 2016d. Structural trapping capacity of oil-wet caprock as a function of pressure, temperature and salinity. *International Journal of Greenhouse Gas Control,* 50**,** 112-120.

ARIF, M., LEBEDEV, M., BARIFCANI, A. & IGLAUER, S. 2017a. CO2 storage in carbonates: Wettability of calcite. *International Journal of Greenhouse Gas Control,* 62**,** 113-121.

ARIF, M., LEBEDEV, M., BARIFCANI, A. & IGLAUER, S. 2017b. Influence of shale-total organic content on CO2 geo-storage potential. *Geophysical Research Letters,* 44**,** 8769-8775.

ARIF, M., ZHANG, Y. & IGLAUER, S. 2021. Shale wettability: Data sets, challenges, and outlook. *Energy & Fuels,* 35**,** 2965-2980.

ARMITAGE, P., WORDEN, R., FAULKNER, D., APLIN, A., BUTCHER, A. & ILIFFE, J. 2010. Diagenetic and sedimentary controls on porosity in Lower Carboniferous fine-grained lithologies, Krechba field, Algeria: A petrological study of a caprock to a carbon capture site. *Marine and Petroleum Geology,* 27**,** 1395-1410.

ARRIBAS, L., GONZÁLEZ-AGUILAR, J. & ROMERO, M. 2018. Solar-driven thermochemical water-splitting by cerium oxide: determination of operational conditions in a directly irradiated fixed bed reactor. *Energies,* 11**,** 2451.

ASLANNEZHAD, M., ALI, M., KALANTARIASL, A., SAYYAFZADEH, M., YOU, Z., IGLAUER, S. & KESHAVARZ, A. 2023. A review of hydrogen/rock/brine interaction: Implications for Hydrogen Geo-storage. *Progress in Energy and Combustion Science,* 95**,** 101066.

AWAN, F. U. R., AL-YASERI, A., AKHONDZADEH, H., IGLAUER, S. & KESHAVARZ, A. 2022. Influence of mineralogy and surfactant concentration on zeta potential in intact sandstone at high pressure. *Journal of Colloid and Interface Science,* 607**,** 401-411.

AWAN, F. U. R., KESHAVARZ, A., AKHONDZADEH, H., AL-ANSSARI, S., AL-YASERI, A., NOSRATI, A., ALI, M. & IGLAUER, S. 2020. Stable dispersion of coal fines during hydraulic fracturing flowback in coal seam gas reservoirs—an experimental study. *Energy and Fuels,* 34**,** 5566-5577.

BAI, Y., PU, C., LI, X., HUANG, F., LIU, S., LIANG, L. & LIU, J. 2022. Performance evaluation and mechanism study of a functionalized silica nanofluid for enhanced oil recovery in carbonate reservoirs. *Colloids and Surfaces A: Physicochemical and Engineering Aspects,* 652**,** 129939.

BALAT, M. 2008. Possible methods for hydrogen production. *Energy Sources, Part A: Recovery, Utilization, and Environmental Effects,* 31**,** 39-50.

BARTH, T. & BJØRLYKKE, K. 1993. Organic acids from source rock maturation: generation potentials, transport mechanisms and relevance for mineral diagenesis. *Applied Geochemistry,* 8**,** 325-337.

BARTON, A. F. 2017. *CRC handbook of solubility parameters and other cohesion parameters*, Routledge.

BAUER, S., PFEIFFER, T., BOOCKMEYER, A., DAHMKE, A. & BEYER, C. 2015. Quantifying induced effects of subsurface renewable energy storage. *Energy Procedia,* 76**,** 633-641.

BELL, D. R., ROSSMAN, G. R., MALDENER, J., ENDISCH, D. & RAUCH, F. 2003. Hydroxide in olivine: A quantitative determination of the absolute amount and calibration of the IR spectrum. *Journal of Geophysical Research: Solid Earth,* 108.

BERNSTEIN, L., BOSCH, P., CANZIANI, O., CHEN, Z., CHRIST, R. & RIAHI, K. 2008. IPCC, 2007: climate change 2007: synthesis report. IPCC.

BHANDARI, R. & SHAH, R. R. 2021. Hydrogen as energy carrier: techno-economic assessment of decentralized hydrogen production in Germany. *Renewable Energy,* 177**,** 915-931.

BICO, J., THIELE, U. & QUÉRÉ, D. 2002. Wetting of textured surfaces. *Colloids and Surfaces A: Physicochemical and Engineering Aspects,* 206**,** 41-46.

BINIWALE, R. B., RAYALU, S., DEVOTTA, S. & ICHIKAWA, M. 2008. Chemical hydrides: a solution to high capacity hydrogen storage and supply. *International Journal of Hydrogen Energy,* 33**,** 360-365.

BINKS, B. P. & CLINT, J. H. 2002. Solid wettability from surface energy components: relevance to Pickering emulsions. *Langmuir,* 18**,** 1270-1273.

BISCAY, F., GHOUFI, A., LACHET, V. & MALFREYT, P. 2009. Monte Carlo calculation of the methane-water interfacial tension at high pressures. *The Journal of chemical physics,* 131.

BJØRLYKKE, K. & GRAN, K. 1994. Salinity variations in North Sea formation waters: Implications for large-scale fluid movements. *Marine and Petroleum Geology,* 11**,** 5-9.

BLUNT, M., FAYERS, F. J. & ORR JR, F. M. 1993. Carbon dioxide in enhanced oil recovery. *Energy Conversion & Management,* 34**,** 1197-1204.

BLUNT, M. J. 2017. *Multiphase flow in permeable media: A pore-scale perspective*, Cambridge University Press.

BONGIORNO, V. & DAVIS, H. T. 1975. Modified van der Waals theory of fluid interfaces. *Physical Review A,* 12**,** 2213.

BOOT-HANDFORD, M. E., ABANADES, J. C., ANTHONY, E. J., BLUNT, M. J., BRANDANI, S., MAC DOWELL, N., FERNÁNDEZ, J. R., FERRARI, M.-C., GROSS, R. & HALLETT, J. P. 2014. Carbon capture and storage update. *Energy & Environmental Science,* 7**,** 130-189.

BORETTI, A., NAYFEH, J. & AL-MAAITAH, A. 2021. Hydrogen production by solar thermochemical water-splitting cycle via a beam down concentrator. *Frontiers in Energy Research,* 9**,** 116.

BORYSENKO, A., CLENNELL, B., SEDEV, R., BURGAR, I., RALSTON, J., RAVEN, M., DEWHURST, D. & LIU, K. 2009. Experimental investigations of the wettability of clays and shales. *Journal of Geophysical Research: Solid Earth,* 114.

BROSETA, D., TONNET, N. & SHAH, V. 2012. Are rocks still water-wet in the presence of dense CO2 or H2S? *Geofluids,* 12**,** 280-294.

BUCKINGHAM, A. & LONGUET-HIGGINS, H. 1968. The quadrupole moments of dipolar molecules. *Molecular Physics,* 14**,** 63-72.

BUSCH, A., ALLES, S., GENSTERBLUM, Y., PRINZ, D., DEWHURST, D. N., RAVEN, M. D., STANJEK, H. & KROOSS, B. M. 2008. Carbon dioxide storage potential of shales. *International journal of greenhouse gas control,* 2**,** 297-308.

BUTT, H.-J., GRAF, K. & KAPPL, M. 2013. *Physics and chemistry of interfaces*, John Wiley & Sons.

CABALLERO, B., TRUGO, L. & FINGLAS, P. 2003. Encyclopedia of food sciences and nutrition: Volumes 1-10.

CAGLAYAN, D. G., WEBER, N., HEINRICHS, H. U., LINßEN, J., ROBINIUS, M., KUKLA, P. A. & STOLTEN, D. 2020. Technical potential of salt caverns for hydrogen storage in Europe. *International Journal of Hydrogen Energy,* 45**,** 6793-6805.

CAHN, J. W. & HILLIARD, J. E. 1958. Free energy of a nonuniform system. I. Interfacial free energy. *The Journal of chemical physics,* 28**,** 258-267.

CANADELL, J. G., LE QUÉRÉ, C., RAUPACH, M. R., FIELD, C. B., BUITENHUIS, E. T., CIAIS, P., CONWAY, T. J., GILLETT, N. P., HOUGHTON, R. & MARLAND, G. 2007. Contributions to accelerating atmospheric CO2 growth from economic activity, carbon intensity, and efficiency of natural sinks. *Proceedings of the national academy of sciences,* 104**,** 18866-18870.

CAO, L., IRIS, K., XIONG, X., TSANG, D. C., ZHANG, S., CLARK, J. H., HU, C., NG, Y. H., SHANG, J. & OK, Y. S. 2020. Biorenewable hydrogen production through biomass gasification: A review and future prospects. *Environmental research,* 186**,** 109547.

CARLES, P., BACHAUD, P., LASSEUR, E., BERNE, P. & BRETONNIER, P. 2010. Confining properties of carbonated Dogger caprocks (Parisian Basin) for CO2 storage purpose. *il & Gas Science and Technology–Revue de l'Institut Français du Pétrole,* 65**,** 461-472.

CAS, R. A. & SIMMONS, J. M. 2018. Why deep-water eruptions are so different from subaerial eruptions. *Frontiers in Earth Science,* 6**,** 198.

CASSIA, R., NOCIONI, M., CORREA-ARAGUNDE, N. & LAMATTINA, L. 2018. Climate change and the impact of greenhouse gasses: CO2 and NO, friends and foes of plant oxidative stress. *Frontiers in plant science,* 9**,** 273.

CHAPMAN, W. G., GUBBINS, K. E., JACKSON, G. & RADOSZ, M. 1989. SAFT: Equation-of-state solution model for associating fluids. *Fluid Phase Equilibria,* 52**,** 31-38.

CHAUDHARY, K., BAYANI CARDENAS, M., WOLFE, W. W., MAISANO, J. A., KETCHAM, R. A. & BENNETT, P. C. 2013. Pore-scale trapping of supercritical CO2 and the role of grain wettability and shape. *Geophysical Research Letters,* 40**,** 3878-3882.

CHEN, A. F., ADZMI, M. A., ADAM, A., OTHMAN, M. F., KAMARUZZAMAN, M. K. & MRWAN, A. G. 2018. Combustion characteristics, engine performances and emissions of a diesel engine using nanoparticle-diesel fuel blends with aluminium oxide, carbon nanotubes and silicon oxide. *Energy Conversion and Management,* 171**,** 461-477.

CHEN, C., CHAI, Z., SHEN, W., LI, W. & SONG, Y. 2017. Wettability of supercritical CO2–brine–mineral: The effects of ion type and salinity. *Energy & Fuels,* 31**,** 7317-7324.

CHEN, C., WAN, J., LI, W. & SONG, Y. 2015a. Water contact angles on quartz surfaces under supercritical CO2 sequestration conditions: Experimental and molecular dynamics simulation studies. *International Journal of Greenhouse Gas Control,* 42**,** 655-665.

CHEN, C., ZHANG, N., LI, W. & SONG, Y. 2015b. Water contact angle dependence with hydroxyl functional groups on silica surfaces under CO2 sequestration conditions. *Environmental science technology,* 49**,** 14680-14687.

CHEN, L., QI, Z., ZHANG, S., SU, J. & SOMORJAI, G. A. 2020. Catalytic hydrogen production from methane: A review on recent progress and prospect. *Catalysts,* 10**,** 858.

CHEN, L., ZHANG, G., WANG, L., WU, W. & GE, J. 2014. Zeta potential of limestone in a large range of salinity. *Colloids and Surfaces A: Physicochemical and Engineering Aspects,* 450**,** 1-8.

CHENG, W.-H., DE LA CALLE, A., ATWATER, H. A., STECHEL, E. B. & XIANG, C. 2021. Hydrogen from sunlight and water: A side-by-side comparison between photoelectrochemical and solar thermochemical water-splitting. *ACS Energy Letters,* 6**,** 3096-3113.

CHERUBINI, A., GARCIA, B., CEREPI, A. & REVIL, A. 2018. Streaming potential coupling coefficient and transport properties of unsaturated carbonate rocks. *Vadose Zone Journal,* 17**,** 1-12.

CHIQUET, P., BROSETA, D. & THIBEAU, S. 2007. Wettability alteration of caprock minerals by carbon dioxide. *Geofluids,* 7**,** 112-122.

CHOW, Y. F., ERIKSEN, D. K., GALINDO, A., HASLAM, A. J., JACKSON, G., MAITLAND, G. C. & TRUSLER, J. M. 2016a. Interfacial tensions of systems comprising water, carbon dioxide and diluent gases at high pressures: Experimental measurements and modelling with SAFT-VR Mie and square-gradient theory. *Fluid Phase Equilibria,* 407**,** 159-176.

CHOW, Y. F., MAITLAND, G. C. & TRUSLER, J. M. 2016b. Interfacial tensions of the (CO2+ N2+ H2O) system at temperatures of (298 to 448) K and pressures up to 40 MPa. *The Journal of Chemical Thermodynamics,* 93**,** 392-403.

CHOW, Y. F., MAITLAND, G. C. & TRUSLER, J. M. 2018. Interfacial tensions of (H2O+ H2) and (H2O+ CO2+ H2) systems at temperatures of (298–448) K and pressures up to 45 MPa. *Fluid Phase Equilibria,* 475**,** 37-44.

CHU, Y., WEI, Y., YUAN, X. & SHI, X. 2011. Bioconversion of wheat stalk to hydrogen by dark fermentation: effect of different mixed microflora on hydrogen yield and cellulose solubilisation. *Bioresource Technology,* 102**,** 3805-3809.

CHURCHER, P., FRENCH, P., SHAW, J. & SCHRAMM, L. Rock properties of Berea sandstone, Baker dolomite, and Indiana limestone. SPE international symposium on oilfield chemistry, 1991. OnePetro.

COLLINI, H., LI, S., JACKSON, M. D., AGENET, N., RASHID, B. & COUVES, J. 2020. Zeta potential in intact carbonates at reservoir conditions and its impact on oil recovery during controlled salinity waterflooding. *Fuel,* 266**,** 116927.

CORNELISSE, P., WIJTKAMP, M., PETERS, C. & DE SWAAN ARONS, J. 1998. Interfacial tensions of fluid mixtures with polar and associating components. *Fluid phase equilibria,* 150**,** 633-640.

COSTELLO, A., ABBAS, M., ALLEN, A., BALL, S., BELL, S., BELLAMY, R., FRIEL, S., GROCE, N., JOHNSON, A. & KETT, M. 2009. Managing the health effects of climate change: lancet and University College London Institute for Global Health Commission. *The lancet,* 373**,** 1693-1733.

CROTOGINO, F., DONADEI, S., BÜNGER, U. & LANDINGER, H. Large-scale hydrogen underground storage for securing future energy supplies. 18th World hydrogen energy conference, 2010. 37-45.

CUMICHEO, C., CARTES, M., SEGURA, H., MÜLLER, E. A. & MEJÍA, A. 2014. High-pressure densities and interfacial tensions of binary systems containing carbon dioxide+ n-alkanes:(n-dodecane, n-tridecane, n-tetradecane). *Fluid Phase Equilibria,* 380**,** 82-92.

DAHRAJ, N. U., ALI, M. & KHAN, M. N. End of linear flow time picking in long transient hydraulically fractured wells to correctly estimate the permeability, fracture half-length and original gas in place in liquid rich shales. SPE/PAPG Pakistan Section Annual Technical Conference, 2016. SPE, SPE-185303-MS.

DAKE, L. P. 1983. *Fundamentals of reservoir engineering,* Elsevier.

DANESH, A. 1998. *PVT and phase behaviour of petroleum reservoir fluids,* Elsevier.

DAVIS, J. A. 1982. Adsorption of natural dissolved organic matter at the oxide/water interface. *Geochimica et cosmochimica acta,* 46**,** 2381-2393.

DE GENNES, P.-G. 1985. Wetting: statics and dynamics. *Reviews of modern physics,* 57**,** 827.

DE LUCIA, M., PILZ, P., LIEBSCHER, A. & KÜHN, M. 2015. Measurements of H2 solubility in saline solutions under reservoir conditions: preliminary results from project H2STORE. *Energy Procedia,* 76**,** 487-494.

DEPKEN, J., DYCK, A., ROß, L. & EHLERS, S. 2022. Safety Considerations of Hydrogen Application in Shipping in Comparison to LNG. *Energies,* 15**,** 3250.

DICKSON, J. L., GUPTA, G., HOROZOV, T. S., BINKS, B. P. & JOHNSTON, K. P. 2006. Wetting phenomena at the CO2/water/glass interface. *Langmuir,* 22**,** 2161-2170.

DICKSON, M. H. & FANELLI, M. 2013. *Geothermal energy: utilization and technology,* Routledge.

DINCER, I. 2007. Environmental and sustainability aspects of hydrogen and fuel cell systems. *International Journal of Energy Research,* 31**,** 29-55.

DONALDSON, E. C. & ALAM, W. 2013. *Wettability,* Elsevier.

DRELICH, J., FANG, C. & WHITE, C. 2002. Measurement of interfacial tension in fluid-fluid systems. *Encyclopedia of surface and colloid science,* 3**,** 3158-3163.

DUNNING, J., HERREN, B., TIPPS, R. & SNYDER, R. 1982. Fractionation of mineral species by electrophoresis. *Journal of Geophysical Research: Solid Earth,* 87**,** 10781-10788.

EHTESABI, H., AHADIAN, M. M. & TAGHIKHANI, V. 2015. Enhanced heavy oil recovery using TiO2 nanoparticles: investigation of deposition during transport in core plug. *Energy & Fuels,* 29**,** 1-8.

EIDESGAARD, Ó., SCHOVSBO, N., BOLDREEL, L. & ÓLAVSDÓTTIR, J. 2019. Shallow geothermal energy system in fractured basalt: A case study from Kollafjørður, Faroe Islands, NE-Atlantic Ocean. *Geothermics,* 82**,** 296-314.

EL-MAGHRABY, R., PENTLAND, C., IGLAUER, S. & BLUNT, M. 2012. A fast method to equilibrate carbon dioxide with brine at high pressure and elevated temperature including solubility measurements. *The Journal of Supercritical Fluids,* 62**,** 55-59.

EL-MAGHRABY, R. M. & BLUNT, M. J. 2013. Residual CO2 trapping in Indiana limestone. *Environmental science and technology,* 47**,** 227-233.

EL-SAYED, G. M., KAMEL, M., MORSY, N. & TAHER, F. 2012. Encapsulation of nano Disperse Red 60 via modified miniemulsion polymerization. I. Preparation and characterization. *Journal of applied polymer science,* 125**,** 1318-1329.

ENDERS, S. & QUITZSCH, K. 1998. Calculation of interfacial properties of demixed fluids using density gradient theory. *Langmuir,* 14**,** 4606-4614.

ENERGY, E. C. D.-G. F. 2014. *EU Energy in Figures: Statistical Pocketbook,* Publications Office of the European Union.

EPELLE, E. I., OBANDE, W., UDOURIOH, G. A., AFOLABI, I. C., DESONGU, K. S., ORIVRI, U., GUNES, B. & OKOLIE, J. A. 2022. Perspectives and prospects of underground hydrogen storage and natural hydrogen. *Sustainable Energy and Fuels*.

ESFANDYARI, H., SARMADIVALEH, M., ESMAEILZADEH, F., ALI, M., IGLAUER, S. & KESHAVARZ, A. 2022. Experimental evaluation of rock mineralogy on hydrogen-wettability: Implications for hydrogen geo-storage. *Journal of Energy Storage,* 52**,** 104866.

ESPINOZA, D. N. & SANTAMARINA, J. C. 2010. Water-CO2-mineral systems: Interfacial tension, contact angle, and diffusion—Implications to CO2 geological storage. *Water resources research,* 46.

ESPINOZA, D. N. & SANTAMARINA, J. C. 2017. CO2 breakthrough—Caprock sealing efficiency and integrity for carbon geological storage. *International Journal of Greenhouse Gas Control,* 66**,** 218-229.

ETTEHADTAVAKKOL, A., LAKE, L. W. & BRYANT, S. L. 2014. CO2-EOR and storage design optimization. *International Journal of Greenhouse Gas Control,* 25**,** 79-92.

EVANS, R. 1979. The nature of the liquid-vapour interface and other topics in the statistical mechanics of non-uniform, classical fluids. *Advances in physics,* 28**,** 143-200.

FAN, G., WANG, L., CAO, Y. & LI, C. 2020. Collecting agent–mineral interactions in the reverse flotation of iron ore: a brief review. *Minerals,* 10**,** 681.

FAROKHPOOR, R., BJØRKVIK, B. J., LINDEBERG, E. & TORSÆTER, O. 2013. Wettability behaviour of CO2 at storage conditions. *International Journal of Greenhouse Gas Control,* 12**,** 18-25.

FAROOQ, U., TWEHEYO, M. T., SJÖBLOM, J. & ØYE, G. 2011. Surface characterization of model, outcrop, and reservoir samples in low salinity aqueous solutions. *Journal of Dispersion Science and Technology,* 32**,** 519-531.

FIROOZABADI, A. & RAMEY JR, H. J. 1988. Surface tension of water-hydrocarbon systems at reservoir conditions. *Journal of Canadian Petroleum Technology,* 27.

FISK, S. & WIDOM, B. 1969. Structure and free energy of the interface between fluid phases in equilibrium near the critical point. *The Journal of Chemical Physics,* 50**,** 3219-3227.

FLAATHEN, T. K. 2009. *Water-rock interaction during CO2 sequestration in basalt.* Université Paul Sabatier-Toulouse III.

FLEURY, M., PIRONON, J., LE NINDRE, Y.-M., BILDSTEIN, O., BERNE, P., LAGNEAU, V., BROSETA, D., PICHERY, T., FILLACIER, S. & LESCANNE, M. 2010. Evaluating sealing efficiency of caprocks for CO2 storage: an overview of the geocarbone-integrity program and results. *Oil & Gas Science and Technology–Revue de l'Institut Français du Pétrole,* 65**,** 435-444.

FORBES, E. & FRANKS, G. 2013. Selective separation of hematite from quartz by flotation using a temperature responsive polymer. *Iron Ore***,** 12-14.

FOWKES, F. M. 1963. Additivity of intermolecular forces at interfaces. i. determination of the contribution to surface and interfacial tensions of dispersion forces in various liquids1. *The Journal of Physical Chemistry,* 67**,** 2538-2541.

FREITAS, S. V., OLIVEIRA, M. B., QUEIMADA, A. J., PRATAS, M. J., LIMA, A. S. & COUTINHO, J. A. 2011. Measurement and prediction of biodiesel surface tensions. *Energy and Fuels*

25**,** 4811-4817.

FUJII, A., EBATA, T. & MIKAMI, N. 2002. Direct observation of weak hydrogen bonds in microsolvated phenol: Infrared spectroscopy of OH stretching vibrations of phenol− CO and− CO2 in S0 and D0. *The Journal of Physical Chemistry A,* 106**,** 10124-10129.

FUKUZAWA, K., WATANABE, K., YASUDA, K. & OHMURA, R. 2018. Interfacial tension measurements in the (CO2+ H2) gas mixture and water system at temperatures from 271.2 K to 280.2 K and pressures up to 7.0 MPa. *The Journal of Chemical Thermodynamics,* 119**,** 20-25.

FURMIDGE, C. 1962. Studies at phase interfaces. I. The sliding of liquid drops on solid surfaces and a theory for spray retention. *Journal of colloid science,* 17**,** 309-324.

FURNES, H. & STAUDIGEL, H. 1999. Biological mediation in ocean crust alteration: how deep is the deep biosphere? *Earth Planetary Science Letters,* 166**,** 97-103.

FURNES, H., STAUDIGEL, H., THORSETH, I. H., TORSVIK, T., MUEHLENBACHS, K. & TUMYR, O. 2001. Bioalteration of basaltic glass in the oceanic crust. *Geochemistry, Geophysics, Geosystems,* 2.

GABRIELLI, P., POLUZZI, A., KRAMER, G. J., SPIERS, C., MAZZOTTI, M. & GAZZANI, M. 2020. Seasonal energy storage for zero-emissions multi-energy systems via underground hydrogen storage. *Renewable and Sustainable Energy Reviews,* 121**,** 109629.

GALECZKA, I., WOLFF-BOENISCH, D. & GISLASON, S. 2013. Experimental studies of basalt-H2O-CO2 interaction with a high pressure column flow reactor: the mobility of metals. *Energy Procedia,* 37**,** 5823-5833.

GEORGIADIS, A., MAITLAND, G., TRUSLER, J. M. & BISMARCK, A. 2010. Interfacial tension measurements of the (H2O+ CO2) system at elevated pressures and temperatures. *Journal of Chemical and Engineering Data,* 55**,** 4168-4175.

GILBERT, B. C. & PARSONS, A. F. 2002. The use of free radical initiators bearing metal–metal, metal–hydrogen and non-metal–hydrogen bonds in synthesis. *Journal of the Chemical Society, Perkin Transactions 2***,** 367-387.

GIRALDO, J., BENJUMEA, P., LOPERA, S., CORTÉS, F. B. & RUIZ, M. A. 2013. Wettability alteration of sandstone cores by alumina-based nanofluids. *Energy & Fuels,* 27**,** 3659-3665.

GIRIFALCO, L. & GOOD, R. J. 1957. A theory for the estimation of surface and interfacial energies. I. Derivation and application to interfacial tension. *The Journal of Physical Chemistry,* 61**,** 904-909.

GISLASON, S. R., BROECKER, W., GUNNLAUGSSON, E., SNÆBJÖRNSDÓTTIR, S., MESFIN, K., ALFREDSSON, H., ARADOTTIR, E., SIGFUSSON, B., GUNNARSSON, I. & STUTE, M. 2014. Rapid solubility and mineral storage of CO2 in basalt. *Energy Procedia*, 63**,** 4561-4574.

GISLASON, S. R. & OELKERS, E. H. 2003. Mechanism, rates, and consequences of basaltic glass dissolution: II. An experimental study of the dissolution rates of basaltic glass as a function of pH and temperature. *Geochimica et Cosmochimica Acta,* 67**,** 3817-3832.

GISLASON, S. R. & OELKERS, E. H. 2014. Carbon storage in basalt. *Science,* 344**,** 373-374.

GISLASON, S. R., WOLFF-BOENISCH, D., STEFANSSON, A., OELKERS, E. H., GUNNLAUGSSON, E., SIGURDARDOTTIR, H., SIGFUSSON, B., BROECKER, W. S., MATTER, J. M. & STUTE, M. 2010. Mineral sequestration of carbon dioxide in basalt: A pre-injection overview of the CarbFix project. *International Journal of Greenhouse Gas Control,* 4**,** 537-545.

GODULA-JOPEK, A. 2015. *Hydrogen production: by electrolysis*, John Wiley & Sons.

GOLDBERG, D., ASTON, L., BONNEVILLE, A., DEMIRKANLI, I., EVANS, C., FISHER, A., GARCIA, H., GERRARD, M., HEESEMANN, M. & HNOTTAVANGE-TELLEEN, K. 2018. Geological storage of CO2 in sub-seafloor basalt: the CarbonSAFE pre-feasibility study offshore Washington State and British Columbia. *Energy Procedia,* 146**,** 158-165.

GOLDBERG, D. S., TAKAHASHI, T. & SLAGLE, A. L. 2008. Carbon dioxide sequestration in deep-sea basalt. *Proceedings of the National Academy of Sciences,* 105**,** 9920-9925.

GOMARI, K. R. & HAMOUDA, A. 2006. Effect of fatty acids, water composition and pH on the wettability alteration of calcite surface. *Journal of petroleum science engineering,* 50**,** 140-150.

GOOD, R. J. & GIRIFALCO, L. 1960. A theory for estimation of surface and interfacial energies. III. Estimation of surface energies of solids from contact angle data. *The Journal of Physical Chemistry,* 64**,** 561-565.

GOPALSAMY, K. & SUBRAMANIAN, V. 2014. Hydrogen storage capacity of alkali and alkaline earth metal ions doped carbon based materials: A DFT study. *International Journal of Hydrogen Energy*, 39**,** 2549-2559.

GOPANI, P. H., SINGH, N., SARMA, H. K., MATTEY, P. & SRIVASTAVA, V. R. 2021. Role of monovalent and divalent ions in low-salinity water flood in carbonate reservoirs: An integrated analysis through zeta potentiometric and simulation studies. *Energies,* 14**,** 729.

GOU, Q., XU, S., HAO, F., YANG, F., SHU, Z. & LIU, R. 2021. The effect of tectonic deformation and preservation condition on the shale pore structure using adsorption-based textural quantification and 3D image observation. *Energy,* 219**,** 119579.

GOU, Q., XU, S., HAO, F., YANG, F., ZHANG, B., SHU, Z., ZHANG, A., WANG, Y., LU, Y. & CHENG, X. 2019. Full-scale pores and micro-fractures characterization using FE-SEM, gas adsorption, nano-CT and micro-CT: A case study of the Silurian Longmaxi Formation shale in the Fuling area, Sichuan Basin, China. *Fuel,* 253**,** 167-179.

GRAETZ, J. 2009. New approaches to hydrogen storage. *Chemical Society Reviews,* 38**,** 73-82.

GRATE, J. W., DEHOFF, K. J., WARNER, M. G., PITTMAN, J. W., WIETSMA, T. W., ZHANG, C. & OOSTROM, M. 2012. Correlation of oil–water and air–water contact angles of diverse silanized surfaces and relationship to fluid interfacial tensions. *Langmuir,* 28**,** 7182-7188.

GROENENBERG, R., JUEZ-LARRE, J., GONCALVES MACHADO, C., WASCH, L., DIJKSTRA, H., WASSING, B., ORLIC, B., BRUNNER, L., VAN DER VALK, K. &

HAJONIDES VAN DER MEULEN, T. 2020. Techno-economic modelling of large-scale energy storage systems.
GUDBRANDSSON, S., WOLFF-BOENISCH, D., GISLASON, S. R. & OELKERS, E. H. 2011. An experimental study of crystalline basalt dissolution from 2⩽ pH⩽ 11 and temperatures from 5 to 75 C. *Geochimica et Cosmochimica Acta,* 75**,** 5496-5509.
GUGGENHEIM, E. A. 1945. The principle of corresponding states. *The Journal of Chemical Physics,* 13**,** 253-261.
GUILTINAN, E. J., CARDENAS, M. B., BENNETT, P. C., ZHANG, T. & ESPINOZA, D. N. 2017. The effect of organic matter and thermal maturity on the wettability of supercritical CO2 on organic shales. *International Journal of Greenhouse Gas Control,* 65**,** 15-22.
GUPTA, R. A. & MOHANTY, K. 2011. Wettability alteration mechanism for oil recovery from fractured carbonate rocks. *Transport in porous media,* 87**,** 635-652.
HAGHIGHI, O. M., ZARGAR, G., KHAKSAR MANSHAD, A., ALI, M., TAKASSI, M. A., ALI, J. A. & KESHAVARZ, A. 2020. Effect of environment-friendly non-ionic surfactant on interfacial tension reduction and wettability alteration; implications for enhanced oil recovery. *Energies,* 13**,** 3988.
HAIR, M. L. 1975. Hydroxyl groups on silica surface. *Journal of Non-Crystalline Solids,* 19**,** 299-309.
HALDAR, S. K. 2020. *Introduction to mineralogy and petrology,* Elsevier.
HANGX, S., SPIERS, C. & PEACH, C. 2011. The mechanical behavior of anhydrite and the effect of deformation on permeability development–Implications for caprock integrity during geological storage of CO2. *Energy Procedia,* 4**,** 5358-5363.
HANGX, S. J., SPIERS, C. J. & PEACH, C. J. 2010. Mechanical behavior of anhydrite caprock and implications for CO2 sealing capacity. *Journal of Geophysical Research: Solid Earth,* 115.
HARKINS, W. D. & BROWN, F. 1919. The determination of surface tension (free surface energy), and the weight of falling drops: the surface tension of water and benzene by the capillary height method. *Journal of the American Chemical Society,* 41**,** 499-524.
HARRIES, D. N., PASKEVICIUS, M., SHEPPARD, D. A., PRICE, T. E. C. & BUCKLEY, C. E. 2011. Concentrating solar thermal heat storage using metal hydrides. *Proceedings of the IEEE,* 100**,** 539-549.
HARTLAND, S. 2004. *Surface and interfacial tension: measurement, theory, and applications*, CRC Press.
HASE, H., ISHIDO, T., TAKAKURA, S., HASHIMOTO, T., SATO, K. & TANAKA, Y. 2003. ζ potential measurement of volcanic rocks from Aso caldera. *Geophysical Research Letters,* 30.
HASHEMI, L., BLUNT, M. & HAJIBEYGI, H. 2021a. Pore-scale modelling and sensitivity analyses of hydrogen-brine multiphase flow in geological porous media. *Scientific reports,* 11**,** 1-13.
HASHEMI, L., BOON, M., GLERUM, W., FARAJZADEH, R. & HAJIBEYGI, H. 2022. A comparative study for H2–CH4 mixture wettability in sandstone porous rocks relevant to underground hydrogen storage. *Advances in Water Resources,* 163**,** 104165.
HASHEMI, L., GLERUM, W., FARAJZADEH, R. & HAJIBEYGI, H. 2021b. Contact angle measurement for hydrogen/brine/sandstone system using captive-bubble method relevant for underground hydrogen storage. *Advances in Water Resources,* 154**,** 103964.

HASSANNAYEBI, N., AZIZMOHAMMADI, S., DE LUCIA, M. & OTT, H. 2019. Underground hydrogen storage: application of geochemical modelling in a case study in the Molasse Basin, Upper Austria. *Environmental Earth Sciences,* 78**,** 1-14.

HASSANPOURYOUZBAND, A., JOONAKI, E., EDLMANN, K. & HASZELDINE, R. S. 2021. Offshore geological storage of hydrogen: Is this our best option to achieve net-zero? *ACS Energy Letters,* 6**,** 2181-2186.

HASSANPOURYOUZBAND, A., JOONAKI, E., EDLMANN, K., HEINEMANN, N. & YANG, J. 2020. Thermodynamic and transport properties of hydrogen containing streams. *Scientific Data,* 7**,** 1-14.

HEINEMANN, N., ALCALDE, J., MIOCIC, J. M., HANGX, S. J., KALLMEYER, J., OSTERTAG-HENNING, C., HASSANPOURYOUZBAND, A., THAYSEN, E. M., STROBEL, G. J. & SCHMIDT-HATTENBERGER, C. 2021. Enabling large-scale hydrogen storage in porous media–the scientific challenges. *J Energy & Environmental Science,* 14**,** 853-864.

HELM, D. 2016. The future of fossil fuels—is it the end? *Oxford Review of Economic Policy,* 32**,** 191-205.

HEMME, C. & VAN BERK, W. 2018. Hydrogeochemical modeling to identify potential risks of underground hydrogen storage in depleted gas fields. *Applied Sciences,* 8**,** 2282.

HENRICH, E., DAHMEN, N., DINJUS, E. & SAUER, J. 2015. The role of biomass in a future world without fossil fuels. *Chemie Ingenieur Technik,* 87**,** 1667-1685.

HENRY, R. 2010. Evaluation of plant biomass resources available for replacement of fossil oil. *Plant biotechnology journal,* 8**,** 288-293.

HIDAYAT, M., SARMADIVALEH, M., DERKSEN, J., VEGA-MAZA, D., IGLAUER, S. & VINOGRADOV, J. 2022a. Zeta potential of CO2-rich aqueous solutions in contact with intact sandstone sample at temperatures of 23° C and 40° C and pressures up to 10.0 MPa. *Journal of Colloid and Interface Science,* 607**,** 1226-1238.

HIDAYAT, M., SARMADIVALEH, M., DERKSEN, J., VEGA-MAZA, D., IGLAUER, S. & VINOGRADOV, J. 2022b. Zeta potential of a natural clayey sandstone saturated with carbonated NaCl solutions at supercritical CO2 conditions. *Geophysical Research Letters,* 49**,** e2022GL099277.

HIGGS, S., DA WANG, Y., SUN, C., ENNIS-KING, J., JACKSON, S. J., ARMSTRONG, R. T. & MOSTAGHIMI, P. 2022. In-situ hydrogen wettability characterisation for underground hydrogen storage. *International Journal of Hydrogen Energy,* 47**,** 13062-13075.

HILDENBRAND, A. & KROOSS, B. 2003. CO2 migration processes in argillaceous rocks: pressure-driven volume flow and diffusion. *ournal of geochemical exploration,* 78**,** 169-172.

HIRASAKI, G. & ZHANG, D. L. 2004. Surface chemistry of oil recovery from fractured, oil-wet, carbonate formations. *Spe Journal,* 9**,** 151-162.

HOEL, M. & KVERNDOKK, S. 1996. Depletion of fossil fuels and the impacts of global warming. *Resource energy economics,* 18**,** 115-136.

HONG, W. Y. 2022. A techno-economic review on carbon capture, utilisation and storage systems for achieving a net-zero CO2 emissions future. *Carbon Capture Science & Technology***,** 100044.

HOSSEINI, M. 2016. Estimation of mean pore-size using formation evaluation and Stoneley slowness. *Journal of Natural Gas Science and Engineering,* 33**,** 898-907.

HOSSEINI, M. 2018. Formation evaluation of a clastic gas reservoir: presentation of a solution to a fundamentally difficult problem. *Journal of geophysics and engineering,* 15**,** 2418-2432.
HOSSEINI, M., ALI, M., FAHIMPOUR, J., KESHAVARZ, A. & IGLAUER, S. 2022a. Assessment of rock-hydrogen and rock-water interfacial tension in shale, evaporite and basaltic rocks. *Journal of Natural Gas Science and Engineering***,** 104743.
HOSSEINI, M., ALI, M., FAHIMPOUR, J., KESHAVARZ, A. & IGLAUER, S. 2022b. Basalt-H2-brine wettability at geo-storage conditions: Implication for hydrogen storage in basaltic formations. *Journal of Energy Storage,* 52**,** 104745.
HOSSEINI, M., ARIF, M., KESHAVARZ, A. & IGLAUER, S. 2021. Neutron scattering: A subsurface application review. *Earth-Science Reviews,* 221**,** 103755.
HOSSEINI, M., FAHIMPOUR, J., ALI, M., KESHAVARZ, A. & IGLAUER, S. 2022c. Capillary Sealing Efficiency Analysis of Caprocks: Implication for Hydrogen Geological Storage. *Energy & Fuels,* 36**,** 4065–4075.
HOSSEINI, M., FAHIMPOUR, J., ALI, M., KESHAVARZ, A. & IGLAUER, S. 2022d. H2−brine interfacial tension as a function of salinity, temperature, and pressure; implications for hydrogen geo-storage. *Journal of Petroleum Science and Engineering,* 213**,** 110441.
HOSSEINI, M., FAHIMPOUR, J., ALI, M., KESHAVARZ, A. & IGLAUER, S. 2022e. Hydrogen wettability of carbonate formations: Implications for hydrogen geo-storage. *Journal of Colloid and Interface Science,* 614**,** 256-266.
HOSSEINI, M., JAVAHERIAN, A. & MOVAHED, B. 2014. Determination of permeability index using Stoneley slowness analysis, NMR models, and formation evaluations: a case study from a gas reservoir, south of Iran. *Journal of Applied Geophysics,* 109**,** 80-87.
HOSSEINI, S. E. & BUTLER, B. 2020. An overview of development and challenges in hydrogen powered vehicles. *International Journal of Green Energy,* 17**,** 13-37.
HOU, J., LIN, S., ZHANG, M. & LI, W. 2023. Salinity, temperature and pressure effect on hydrogen wettability of carbonate rocks. *International Journal of Hydrogen Energy,* 48**,** 11303-11311.
HRIBAR, B., SOUTHALL, N. T., VLACHY, V. & DILL, K. A. 2002. How ions affect the structure of water. *Journal of the American Chemical Society,* 124**,** 12302-12311.
HSIANG, S. M., BURKE, M. & MIGUEL, E. 2013. Quantifying the influence of climate on human conflict. *Science,* 341**,** 1235367.
HUANG, S. H. & RADOSZ, M. 1990. Equation of state for small, large, polydisperse, and associating molecules. *Industrial and Engineering Chemistry Research,* 29**,** 2284-2294.
HUNTER, R. J. 2013. *Zeta potential in colloid science: principles and applications*, Academic press.
HUSSEIN, A. M., BAKAR, R. A., KADIRGAMA, K. & SHARMA, K. 2013. Experimental measurements of nanofluids thermal properties. *International Journal of Automotive and Mechanical Engineering,* 7**,** 850-863.
IGLAUER, S. 2011. *Dissolution trapping of carbon dioxide in reservoir formation brine-a carbon storage mechanism*, INTECH Open Access Publisher London, UK.
IGLAUER, S. 2017. CO2–water–rock wettability: variability, influencing factors, and implications for CO2 geostorage. *Accounts of chemical research,* 50**,** 1134-1142.
IGLAUER, S. 2018. Optimum storage depths for structural CO2 trapping. *International Journal of Greenhouse Gas Control,* 77**,** 82-87.
IGLAUER, S. 2022. Optimum geological storage depths for structural H2 geo-storage. *Journal of Petroleum Science and Engineering,* 212**,** 109498.

IGLAUER, S., ABID, H., AL-YASERI, A. & KESHAVARZ, A. 2021a. Hydrogen Adsorption on Sub-Bituminous Coal: Implications for Hydrogen Geo-Storage. *Geophysical Research Letters,* 48**,** e2021GL092976.

IGLAUER, S., AKHONDZADEH, H., ABID, H., PALUSZNY, A., KESHAVARZ, A., ALI, M., GIWELLI, A., ESTEBAN, L., SAROUT, J. & LEBEDEV, M. 2022. Hydrogen flooding of a coal core: effect on coal swelling. *Geophysical Research Letters,* 49**,** e2021GL096873.

IGLAUER, S., AL-YASERI, A. Z. & WOLFF-BOENISCH, D. 2020. Basalt-CO2-brine wettability at storage conditions in basaltic formations. *International Journal of Greenhouse Gas Control,* 102**,** 103148.

IGLAUER, S., AL-YASERI, A. Z., REZAEE, R. & LEBEDEV, M. 2015a. CO2 wettability of caprocks: Implications for structural storage capacity and containment security. *Geophysical Research Letters,* 42**,** 9279-9284.

IGLAUER, S., ALI, M. & KESHAVARZ, A. 2021b. Hydrogen Wettability of Sandstone Reservoirs: Implications for Hydrogen Geo-Storage. *Geophysical Research Letters,* 48**,** e2020GL090814.

IGLAUER, S., MATHEW, M. & BRESME, F. 2012. Molecular dynamics computations of brine–CO2 interfacial tensions and brine–CO2–quartz contact angles and their effects on structural and residual trapping mechanisms in carbon geo-sequestration. *Journal of colloid and interface science,* 386**,** 405-414.

IGLAUER, S., PENTLAND, C. & BUSCH, A. 2015b. CO2 wettability of seal and reservoir rocks and the implications for carbon geo-sequestration. *Water Resources Research,* 51**,** 729-774.

IGLAUER, S., SALAMAH, A., SARMADIVALEH, M., LIU, K. & PHAN, C. 2014. Contamination of silica surfaces: Impact on water–CO2–quartz and glass contact angle measurements. *International Journal of Greenhouse Gas Control,* 22**,** 325-328.

ISFEHANI, Z. D., SHEIDAIE, A., HOSSEINI, M., FAHIMPOUR, J., IGLAUER, S. & KESHAVARZ, A. 2023. Interfacial tensions of (brine+ H2+ CO2) systems at gas geo-storage conditions. *Journal of Molecular Liquids***,** 121279.

ISHIDO, T. & MIZUTANI, H. 1981. Experimental and theoretical basis of electrokinetic phenomena in rock-water systems and its applications to geophysics. *Journal of Geophysical Research: Solid Earth,* 86**,** 1763-1775.

JACKSON, M. D., AL-MAHROUQI, D. & VINOGRADOV, J. 2016. Zeta potential in oil-water-carbonate systems and its impact on oil recovery during controlled salinity water-flooding. *Scientific reports,* 6**,** 1-13.

JACKSON, M. D., VALVATNE, P. H. & BLUNT, M. J. 2005. Prediction of wettability variation within an oil/water transition zone and its impact on production. *SPE Journal,* 10**,** 185-195.

JAIN, I. 2009. Hydrogen the fuel for 21st century. *International journal of hydrogen energy,* 34**,** 7368-7378.

JANCZUK, B. & ZDZIENNICKA, A. 1994. A study on the components of surface free energy of quartz from contact angle measurements. *Journal of materials science,* 29**,** 3559-3564.

JANDER, J. H., SCHMIDT, P. S., GIRAUDET, C., WASSERSCHEID, P., RAUSCH, M. H. & FRÖBA, A. P. J. I. J. O. H. E. 2021. Hydrogen solubility, interfacial tension, and density of the liquid organic hydrogen carrier system diphenylmethane/dicyclohexylmethane. 46**,** 19446-19466.

JARDINE, P., MCCARTHY, J. & WEBER, N. 1989. Mechanisms of dissolved organic carbon adsorption on soil. *Soil Science Society of America Journal,* 53**,** 1378-1385.

JARRAHIAN, K., SEIEDI, O., SHEYKHAN, M., SEFTI, M. V. & AYATOLLAHI, S. 2012. Wettability alteration of carbonate rocks by surfactants: a mechanistic study. *Colloids and Surfaces A: Physicochemical and Engineering Aspects,* 410**,** 1-10.

JHA, N. K., AL-YASERI, A., GHASEMI, M., AL-BAYATI, D., LEBEDEV, M. & SARMADIVALEH, M. 2021. Pore scale investigation of hydrogen injection in sandstone via X-ray micro-tomography. *International Journal of Hydrogen Energy,* 46**,** 34822-34829.

JHA, N. K., IGLAUER, S., BARIFCANI, A., SARMADIVALEH, M. & SANGWAI, J. S. 2019. Low-salinity surfactant nanofluid formulations for wettability alteration of sandstone: role of the SiO2 nanoparticle concentration and divalent cation/SO42–ratio. *Energy and Fuels,* 33**,** 739-746.

JHA, N. K., LEBEDEV, M., IGLAUER, S., ALI, M., ROSHAN, H., BARIFCANI, A., SANGWAI, J. S. & SARMADIVALEH, M. 2020. Pore scale investigation of low salinity surfactant nanofluid injection into oil saturated sandstone via X-ray micro-tomography. *Journal of Colloid and Interface Science,* 562**,** 370-380.

JIANG, L., CHEN, Z., ALI, S. F., ZHANG, J., CHEN, Y. & CHEN, S. 2022. Storing carbon dioxide in deep unmineable coal seams for centuries following underground coal gasification. *Journal of Cleaner Production,* 378**,** 134565.

JIANG, R., LI, K. & HORNE, R. A mechanism study of wettability and interfacial tension for EOR using silica nanoparticles. SPE Annual Technical Conference and Exhibition, 2017. OnePetro.

JONES, D., HEAD, I., GRAY, N., ADAMS, J., ROWAN, A., AITKEN, C., BENNETT, B., HUANG, H., BROWN, A. & BOWLER, B. 2008. Crude-oil biodegradation via methanogenesis in subsurface petroleum reservoirs. *Nature,* 451**,** 176-180.

JOUNIAUX, L., BERNARD, M. L., ZAMORA, M. & POZZI, J. P. 2000. Streaming potential in volcanic rocks from Mount Pelée. *Journal of Geophysical Research: Solid Earth,* 105**,** 8391-8401.

JOUNIAUX, L. & POZZI, J. P. 1995. Streaming potential and permeability of saturated sandstones under triaxial stress: Consequences for electrotelluric anomalies prior to earthquakes. *Journal of Geophysical Research: Solid Earth,* 100**,** 10197-10209.

JUNG, J.-W. & WAN, J. 2012. Supercritical CO2 and ionic strength effects on wettability of silica surfaces: Equilibrium contact angle measurements. *Energy and Fuels,* 26**,** 6053-6059.

KANAANI, M., SEDAEE, B. & ASADIAN-PAKFAR, M. 2022. Role of cushion gas on underground hydrogen storage in depleted oil reservoirs. *Journal of Energy Storage,* 45**,** 103783.

KANAKIYA, S., ADAM, L., ESTEBAN, L., ROWE, M. C. & SHANE, P. 2017. Dissolution and secondary mineral precipitation in basalts due to reactions with carbonic acid. *Journal of Geophysical Research: Solid Earth,* 122**,** 4312-4327.

KANG, S. M., FATHI, E., AMBROSE, R. J., AKKUTLU, I. Y. & SIGAL, R. F. 2011. Carbon dioxide storage capacity of organic-rich shales. *Spe Journal,* 16**,** 842-855.

KANNAH, R. Y., KAVITHA, S., KARTHIKEYAN, O. P., KUMAR, G., DAI-VIET, N. V. & BANU, J. R. 2021. Techno-economic assessment of various hydrogen production methods–A review. *Bioresource technology,* 319**,** 124175.

KANWAL, S., MEHRAN, M. T., HASSAN, M., ANWAR, M., NAQVI, S. R. & KHOJA, A. H. 2022. An integrated future approach for the energy security of Pakistan: Replacement of

fossil fuels with syngas for better environment and socio-economic development. *Renewable Sustainable Energy Reviews,* 156**,** 111978.
KARUNARATHNE, C. I., AL-YASERI, A. Z., KESHAVARZ, A. & IGLAUER, S. 2022. Effect of Inorganic Acid Concentration on Sandstone Surface Chemistry Examined via Nuclear Magnetic Resonance. *The Journal of Physical Chemistry C,* 126**,** 10863-10871.
KASHEFI, K., PEREIRA, L. M., CHAPOY, A., BURGASS, R. & TOHIDI, B. 2016. Measurement and modelling of interfacial tension in methane/water and methane/brine systems at reservoir conditions. *Fluid Phase Equilibria,* 409**,** 301-311.
KASZUBA, J. P. & JANECKY, D. R. 2009. Geochemical impacts of sequestering carbon dioxide in brine formations. *Carbon sequestration and its role in the global carbon cycle,* 183**,** 239-248.
KAVEH, N. S., BARNHOORN, A. & WOLF, K.-H. 2016. Wettability evaluation of silty shale caprocks for CO2 storage. *International Journal of Greenhouse Gas Control,* 49**,** 425-435.
KAYA, A. & YUKSELEN, Y. 2005. Zeta potential of clay minerals and quartz contaminated by heavy metals. *Canadian Geotechnical Journal,* 42**,** 1280-1289.
KENARD JR, R. 1962. Steam methane reforming for hydrogen production. *World Pet.,* 33.
KESHAVARZ, A., ABID, H., ALI, M. & IGLAUER, S. 2022. Hydrogen diffusion in coal: Implications for hydrogen geo-storage. *Journal of Colloid and Interface Science,* 608**,** 1457-1462.
KEYKHOSRAVI, A., VANANI, M. B., DARYASAFAR, A. & AGHAYARI, C. 2021. Comparative study of different enhanced oil recovery scenarios by silica nanoparticles: an approach to time-dependent wettability alteration in carbonates. *Journal of Molecular Liquids,* 324**,** 115093.
KHADRI, S. & MOHARIR, K. 2016. Characterization of aquifer parameter in basaltic hard rock region through pumping test methods: a case study of Man River basin in Akola and Buldhana Districts Maharashtra India. *Modeling Earth Systems and Environment,* 2**,** 1-18.
KHAN, A., REDELIUS, P. & KRINGOS, N. 2014. Surface energy measurements and wettability investigation of different minerals and bitumen for cold asphalts. *Paper,* 933**,** 1-5.
KITTEL, C. & MCEUEN, P. 2018. *Introduction to solid state physics*, John Wiley & Sons.
KLEBER, M., EUSTERHUES, K., KEILUWEIT, M., MIKUTTA, C., MIKUTTA, R. & NICO, P. S. 2015. Mineral–organic associations: formation, properties, and relevance in soil environments. *Advances in agronomy,* 130**,** 1-140.
KLELL, M. 2010. Storage of hydrogen in the pure form. *Handbook of hydrogen storage: new materials for future energy storage***,** 1.
KNORR, W. 2009. Is the airborne fraction of anthropogenic CO2 emissions increasing? *Geophysical research letters,* 36.
KONDEPUDI, D. K. 2008. *Introduction to modern thermodynamics*, Wiley Chichester.
KONTOGEORGIS, G. M., MICHELSEN, M. L., FOLAS, G. K., DERAWI, S., VON SOLMS, N. & STENBY, E. H. 2006a. Ten years with the CPA (Cubic-Plus-Association) equation of state. Part 1. Pure compounds and self-associating systems. *Industrial and engineering chemistry research,* 45**,** 4855-4868.
KONTOGEORGIS, G. M., MICHELSEN, M. L., FOLAS, G. K., DERAWI, S., VON SOLMS, N. & STENBY, E. H. 2006b. Ten years with the CPA (Cubic-Plus-Association) equation of state. Part 2. Cross-associating and multicomponent systems. *Industrial and Engineering Chemistry Research,* 45**,** 4869-4878.

KORTE, C., MANDT, T. & BERGHOLZ, T. Y. 2016. Physics of Hydrogen. *Hydrogen Science and Engineering: Materials, Processes, Systems and Technology***,** 563-600.

KOVALCHUK, O. & ZOZULYNETS, V. Study of influence of alkaline component type on pH value and properties of alkali activated concretes containing basalt rock. E3S Web of Conferences, 2021. EDP Sciences, 07001.

KREVOR, S., BLUNT, M. J., BENSON, S. M., PENTLAND, C. H., REYNOLDS, C., AL-MENHALI, A. & NIU, B. 2015. Capillary trapping for geologic carbon dioxide storage–From pore scale physics to field scale implications. *International Journal of Greenhouse Gas Control,* 40**,** 221-237.

KUBICA, P. & WOLINSKA-GRABCZYK, A. 2015. Correlation between cohesive energy density, fractional free volume, and gas transport properties of poly (ethylene-co-vinyl acetate) materials. *International Journal of Polymer Science,* 2015.

KUMAR, S., TIWARI, R., HUSEIN, M., KUMAR, N. & YADAV, U. 2020. Enhancing the performance of HPAM polymer flooding using nano CuO/nanoclay blend. *Processes,* 8**,** 907.

KUMAR, S. S. & HIMABINDU, V. 2019. Hydrogen production by PEM water electrolysis–A review. *Materials Science for Energy Technologies,* 2**,** 442-454.

KUNZ, O. & WAGNER, W. 2012. The GERG-2008 wide-range equation of state for natural gases and other mixtures: an expansion of GERG-2004. *Journal of chemical and engineering data,* 57**,** 3032-3091.

KVENVOLDEN, K. A. 1967. Normal fatty acids in sediments. *Journal of the American Oil Chemists' Society,* 44**,** 628-636.

KWOK, D. Y. & NEUMANN, A. W. 1999. Contact angle measurement and contact angle interpretation. *Advances in colloid and interface science,* 81**,** 167-249.

LAI, C.-Y., COZZOLINO, M., DIAMANTI, M. V., AL HASSAN, S. & CHIESA, M. 2015. Underlying mechanism of time dependent surface properties of calcite (CaCO3): A baseline for investigations of reservoirs wettability. *The Journal of Physical Chemistry C,* 119**,** 29038-29043.

LANDER, L. M., SIEWIERSKI, L. M., BRITTAIN, W. J. & VOGLER, E. A. 1993. A systematic comparison of contact angle methods. *Langmuir,* 9**,** 2237-2239.

LANKOF, L. & TARKOWSKI, R. 2020. Assessment of the potential for underground hydrogen storage in bedded salt formation. *International Journal of Hydrogen Energy,* 45**,** 19479-19492.

LAW, B. E. & CURTIS, J. 2002. Introduction to unconventional petroleum systems. *AAPG bulletin,* 86**,** 1851-1852.

LE BAS, M. & STRECKEISEN, A. L. 1991. The IUGS systematics of igneous rocks. *Journal of the Geological Society,* 148**,** 825-833.

LE QUÉRÉ, C., MORIARTY, R., ANDREW, R. M., CANADELL, J. G., SITCH, S., KORSBAKKEN, J. I., FRIEDLINGSTEIN, P., PETERS, G. P., ANDRES, R. J. & BODEN, T. A. 2015. Global carbon budget 2015. *Earth System Science Data,* 7**,** 349-396.

LE ROEX, A. 1998. Mid-ocean ridge basalt (MORB). *Geochemistry. Encyclopedia of Earth Science*.

LEACHMAN, J. W., JACOBSEN, R. T., PENONCELLO, S. & LEMMON, E. W. 2009. Fundamental equations of state for parahydrogen, normal hydrogen, and orthohydrogen. *Journal of Physical and Chemical Reference Data,* 38**,** 721-748.

LEE, S.-T. & CHIEN, M. A new multicomponent surface tension correlation based on scaling theory. SPE Improved Oil Recovery Conference?, 1984. SPE, SPE-12643-MS.
LEINOV, E. & JACKSON, M. 2014. Experimental measurements of the SP response to concentration and temperature gradients in sandstones with application to subsurface geophysical monitoring. *Journal of Geophysical Research: Solid Earth,* 119**,** 6855-6876.
LEMIEUX, A., SHARP, K. & SHKARUPIN, A. 2019. Preliminary assessment of underground hydrogen storage sites in Ontario, Canada. *International Journal of Hydrogen Energy,* 44**,** 15193-15204.
LEMIEUX, A., SHKARUPIN, A. & SHARP, K. 2020. Geologic feasibility of underground hydrogen storage in Canada. *International Journal of Hydrogen Energy,* 45**,** 32243-32259.
LEROY, P., LASSIN, A., AZAROUAL, M. & ANDRÉ, L. 2010. Predicting the surface tension of aqueous 1: 1 electrolyte solutions at high salinity. *Geochimica et Cosmochimica Acta,* 74**,** 5427-5442.
LEVERETT, M. 1941. Capillary behavior in porous solids. *Transactions of the AIME,* 142**,** 152-169.
LEVIN, D. B. & CHAHINE, R. 2010. Challenges for renewable hydrogen production from biomass. *International Journal of Hydrogen Energy,* 35**,** 4962-4969.
LI, D. & NEUMANN, A. 1992. Equation of state for interfacial tensions of solid-liquid systems. *Advances in Colloid and Interface Science,* 39**,** 299-345.
LI, S., COLLINI, H. & JACKSON, M. D. 2018. Anomalous zeta potential trends in natural sandstones. *Geophysical Research Letters,* 45**,** 11,068-11,073.
LI, S., DONG, M., LI, Z., HUANG, S., QING, H. & NICKEL, E. 2005. Gas breakthrough pressure for hydrocarbon reservoir seal rocks: implications for the security of long-term CO2 storage in the Weyburn field. *Geofluids,* 5**,** 326-334.
LI, S., LEROY, P., HEBERLING, F., DEVAU, N., JOUGNOT, D. & CHIABERGE, C. 2016. Influence of surface conductivity on the apparent zeta potential of calcite. *Journal of colloid and interface science,* 468**,** 262-275.
LI, X.-S., LIU, J.-M. & FU, D. 2008. Investigation of interfacial tensions for carbon dioxide aqueous solutions by perturbed-chain statistical associating fluid theory combined with density-gradient theory. *Industrial and engineering chemistry research,* 47**,** 8911-8917.
LI, X., BOEK, E., MAITLAND, G. C. & TRUSLER, J. M. 2012a. Interfacial Tension of (Brines+ CO2):(0.864 NaCl+ 0.136 KCl) at Temperatures between (298 and 448) K, Pressures between (2 and 50) MPa, and Total Molalities of (1 to 5) mol· kg–1. *Journal of Chemical & Engineering Data,* 57**,** 1078-1088.
LI, X., BOEK, E. S., MAITLAND, G. C. & TRUSLER, J. M. 2012b. Interfacial Tension of (Brines+ CO2): CaCl2 (aq), MgCl2 (aq), and Na2SO4 (aq) at Temperatures between (343 and 423) K, Pressures between (2 and 50) MPa, and Molalities of (0.5 to 5) mol· kg–1. *Journal of Chemical Engineering Data,* 57**,** 1369-1375.
LI, Y., CHEN, J.-Q., YANG, J.-H., LIU, J.-S. & TONG, W.-S. 2021. Determination of shale macroscale modulus based on microscale measurement: A case study concerning multiscale mechanical characteristics. *Petroleum Science*.
LI, Y. & TAGHIZADEH-HESARY, F. 2022. The economic feasibility of green hydrogen and fuel cell electric vehicles for road transport in China. *Energy Policy,* 160**,** 112703.
LI, Y., WANG, Z., PAN, Z., NIU, X., YU, Y. & MENG, S. 2019a. Pore structure and its fractal dimensions of transitional shale: A cross-section from east margin of the Ordos Basin, China. *Fuel,* 241**,** 417-431.

LI, Y., YANG, J., PAN, Z., MENG, S., WANG, K. & NIU, X. 2019b. Unconventional natural gas accumulations in stacked deposits: a discussion of upper paleozoic coal-bearing strata in the east margin of the ordos basin, China. *Acta Geologica Sinica-English Edition,* 93**,** 111-129.

LIU, A. & LIU, S. 2023. Hydrogen sorption and diffusion in coals: Implications for hydrogen geo-storage. *Applied Energy,* 334**,** 120746.

LÓPEZ-CHÁVEZ, E., GARCIA-QUIROZ, A., PEÑA-CASTAÑEDA, Y. A., DIAZ-GONGORA, J. A., DE LANDA CASTILLO-ALVARADO, F. & CARBELLIDO, W. R. 2020. Modeling and simulation of the adsorption and storage of hydrogen in calcite rock oil fields. *Journal of Molecular Modeling,* 26**,** 1-14.

LORD, A. S. 2009. Overview of geologic storage of natural gas with an emphasis on assessing the feasibility of storing hydrogen. Sandia National Laboratories (SNL), Albuquerque, NM, and Livermore, CA ….

LORD, A. S., KOBOS, P. H. & BORNS, D. J. 2014. Geologic storage of hydrogen: Scaling up to meet city transportation demands. *International Journal of Hydrogen Energy,* 39**,** 15570-15582.

LUBITZ, W. & TUMAS, W. 2007. Hydrogen: an overview. *Chemical reviews,* 107**,** 3900-3903.

LUBOŃ, K. & TARKOWSKI, R. 2023. The influence of the first filling period length and reservoir level depth on the operation of underground hydrogen storage in a deep aquifer. *International Journal of Hydrogen Energy,* 48**,** 1024-1042.

LUCONI, L., TUCI, G., GIAMBASTIANI, G., ROSSIN, A. & PERUZZINI, M. 2019. H2 production from lightweight inorganic hydrides catalyzed by 3d transition metals. *International Journal of Hydrogen Energy,* 44**,** 25746-25776.

LUIDOLD, S. & ANTREKOWITSCH, H. 2007. Hydrogen as a reducing agent: State-of-the-art science and technology. *Jom,* 59**,** 20-26.

LUNDEGARD, P. D. & KHARAKA, Y. K. 1994. Distribution and occurrence of organic acids in subsurface waters. *Organic acids in geological processes.* Springer.

LUONG, D. T. & RUDOLF, S. 2015. Zeta potential measurement using streaming potential in porous media. *VNU Journal of Science: Mathematics-Physics,* 31.

MA, L., SLATER, T., DOWEY, P. J., YUE, S., RUTTER, E. H., TAYLOR, K. G. & LEE, P. D. 2018. Hierarchical integration of porosity in shales. *Scientific reports,* 8**,** 1-14.

MACLEOD, D. 1923. On a relation between surface tension and density. *Transactions of the Faraday Society,* 19**,** 38-41.

MADSEN, L. & IDA, L. 1998. Adsorption of carboxylic acids on reservoir minerals from organic and aqueous phase. *SPE Reservoir Evaluation & Engineering,* 1**,** 47-51.

MAHANI, H., KEYA, A. L., BERG, S. & NASRALLA, R. 2017. Electrokinetics of carbonate/brine interface in low-salinity waterflooding: Effect of brine salinity, composition, rock type, and pH on?-potential and a surface-complexation model. *Spe Journal,* 22**,** 53-68.

MAHDI JAFARI, S., HE, Y. & BHANDARI, B. 2006. Nano-emulsion production by sonication and microfluidization—a comparison. *International journal of food properties,* 9**,** 475-485.

MAHESAR, A. A., ALI, M., SHAR, A. M., MEMON, K. R., MOHANTY, U. S., AKHONDZADEH, H., TUNIO, A. H., IGLAUER, S. & KESHAVARZ, A. 2020a. Effect of cryogenic liquid nitrogen on the morphological and petrophysical characteristics of tight gas sandstone rocks from kirthar fold belt, Indus Basin, Pakistan. *Energy and Fuels,* 34**,** 14548-14559.

MAHESAR, A. A., SHAR, A. M., ALI, M., TUNIO, A. H., UQAILLI, M. A., MOHANTY, U. S., AKHONDZADEH, H., IGLAUER, S. & KESHAVARZ, A. 2020b. Morphological and petro physical estimation of eocene tight carbonate formation cracking by cryogenic liquid nitrogen; a case study of Lower Indus basin, Pakistan. *Journal of Petroleum Science and Engineering,* 192**,** 107318.

MALLANTS, D., MARIVOET, J. & SILLEN, X. 2001. Performance assessment of the disposal of vitrified high-level waste in a clay layer. *Journal of Nuclear Materials,* 298**,** 125-135.

MAN, Y., YANG, S., XIANG, D., LI, X. & QIAN, Y. 2014. Environmental impact and techno-economic analysis of the coal gasification process with/without CO2 capture. *Journal of cleaner production,* 71**,** 59-66.

MANCIU, M. & RUCKENSTEIN, E. 2003. Specific ion effects via ion hydration: I. Surface tension. *Advances in colloid and interface science,* 105**,** 63-101.

MARMUR, A. 2006. Soft contact: measurement and interpretation of contact angles. *Soft Matter,* 2**,** 12-17.

MASSOUDI, R. & KING JR, A. 1974. Effect of pressure on the surface tension of water. Adsorption of low molecular weight gases on water at 25. deg. *The Journal of Physical Chemistry,* 78**,** 2262-2266.

MATTER, J. M., TAKAHASHI, T. & GOLDBERG, D. 2007. Experimental evaluation of in situ CO2-water-rock reactions during CO2 injection in basaltic rocks: Implications for geological CO2 sequestration. *Geochemistry, Geophysics, Geosystems,* 8.

MATZEN, M. J., ALHAJJI, M. H. & DEMIREL, Y. 2015. Technoeconomics and sustainability of renewable methanol and ammonia productions using wind power-based hydrogen.

MCGRAIL, B. P., SCHAEF, H. T., SPANE, F. A., HORNER, J. A., OWEN, A. T., CLIFF, J. B., QAFOKU, O., THOMPSON, C. J. & SULLIVAN, E. C. 2017. Wallula Basalt pilot demonstration project: post-injection results and conclusions. *Energy Procedia,* 114**,** 5783-5790.

MEMON, K. R., ALI, M., AWAN, F. U. R., MAHESAR, A. A., ABBASI, G. R., MOHANTY, U. S., AKHONDZADEH, H., TUNIO, A. H., IGLAUER, S. & KESHAVARZ, A. 2021. Influence of cryogenic liquid nitrogen cooling and thermal shocks on petro-physical and morphological characteristics of Eagle Ford shale. *Journal of Natural Gas Science and Engineering,* 96**,** 104313.

MEMON, K. R., MAHESAR, A. A., ALI, M., TUNIO, A. H., MOHANTY, U. S., AKHONDZADEH, H., AWAN, F. U. R., IGLAUER, S. & KESHAVARZ, A. 2020. Influence of cryogenic liquid nitrogen on petro-physical characteristics of mancos shale: an experimental investigation. *Energy and Fuels,* 34**,** 2160-2168.

METZ, B., DAVIDSON, O., DE CONINCK, H., LOOS, M. & MEYER, L. 2005. *IPCC special report on carbon dioxide capture and storage,* Cambridge: Cambridge University Press.

MICHAELIDES, E. E. 2017. A new model for the lifetime of fossil fuel resources. *Natural Resources Research,* 26**,** 161-175.

MIDILLI, A., KUCUK, H., TOPAL, M. E., AKBULUT, U. & DINCER, I. 2021. A comprehensive review on hydrogen production from coal gasification: Challenges and Opportunities. *International Journal of Hydrogen Energy,* 46**,** 25385-25412.

MILLETT, J., WILKINS, A., CAMPBELL, E., HOLE, M., TAYLOR, R., HEALY, D., JERRAM, D., JOLLEY, D., PLANKE, S. & ARCHER, S. 2016. The geology of offshore drilling through basalt sequences: Understanding operational complications to improve efficiency. *Marine and Petroleum Geology,* 77**,** 1177-1192.

MIOCIC, J., HEINEMANN, N., EDLMANN, K., SCAFIDI, J., MOLAEI, F. & ALCALDE, J. 2023. Underground hydrogen storage: A review. *Geological Society, London, Special Publications,* 528**,** SP528-2022-88.

MIQUEU, C., MENDIBOURE, B., GRACIAA, A. & LACHAISE, J. 2008. Petroleum mixtures: An efficient predictive method for surface tension estimations at reservoir conditions. *Fuel,* 87**,** 612-621.

MIQUEU, C., MIGUEZ, J. M., PINEIRO, M. M., LAFITTE, T. & MENDIBOURE, B. 2011. Simultaneous application of the gradient theory and Monte Carlo molecular simulation for the investigation of methane/water interfacial properties. *The Journal of Physical Chemistry B,* 115**,** 9618-9625.

MIRCHI, V., DEJAM, M. & ALVARADO, V. 2022. Interfacial tension and contact angle measurements for hydrogen-methane mixtures/brine/oil-wet rocks at reservoir conditions. *International Journal of Hydrogen Energy,* 47**,** 34963-34975.

MOHAMMED, M. & BABADAGLI, T. 2015. Wettability alteration: A comprehensive review of materials/methods and testing the selected ones on heavy-oil containing oil-wet systems. *Advances in colloid and interface science,* 220**,** 54-77.

MOHANTY, U. S., ALI, M., AZHAR, M. R., AL-YASERI, A., KESHAVARZ, A. & IGLAUER, S. 2021. Current advances in syngas (CO+ H2) production through bi-reforming of methane using various catalysts: A review. *International Journal of Hydrogen Energy,* 46**,** 32809-32845.

MÖLLER, P., ROSENTHAL, E., INBAR, N. & MAGRI, F. 2016. Hydrochemical considerations for identifying water from basaltic aquifers: The Israeli experience. *Journal of Hydrology: Regional Studies,* 5**,** 33-47.

MOLLOY, C., SHANE, P. & AUGUSTINUS, P. 2009. Eruption recurrence rates in a basaltic volcanic field based on tephra layers in maar sediments: implications for hazards in the Auckland volcanic field. *Geological Society of America Bulletin,* 121**,** 1666-1677.

MORADI, R. & GROTH, K. M. 2019. Hydrogen storage and delivery: Review of the state of the art technologies and risk and reliability analysis. *International Journal of Hydrogen Energy,* 44**,** 12254-12269.

MORI, D. & HIROSE, K. 2009. Recent challenges of hydrogen storage technologies for fuel cell vehicles. *International journal of hydrogen energy,* 34**,** 4569-4574.

MORROW, N. R. 1970. Physics and thermodynamics of capillary action in porous media. *Industrial and Engineering Chemistry,* 62**,** 32-56.

MORROW, N. R. 1975. The effects of surface roughness on contact: angle with special reference to petroleum recovery. *Journal of Canadian Petroleum Technology,* 14.

MOSS, B., BABACAN, O., KAFIZAS, A. & HANKIN, A. 2021. A review of inorganic photoelectrode developments and reactor scale-up challenges for solar hydrogen production. *Advanced Energy Materials,* 11**,** 2003286.

MUHAMMED, N. S., HAQ, B., AL SHEHRI, D., AL-AHMED, A., RAHMAN, M. M. & ZAMAN, E. 2022. A review on underground hydrogen storage: Insight into geological sites, influencing factors and future outlook. *Energy Reports,* 8**,** 461-499.

MUHAMMED, N. S., HAQ, M. B., AL SHEHRI, D. A., AL-AHMED, A., RAHMAN, M. M., ZAMAN, E. & IGLAUER, S. 2023. Hydrogen storage in depleted gas reservoirs: A comprehensive review. *Fuel,* 337**,** 127032.

MÜLLER, E. A. & MEJÍA, A. S. 2014. Resolving discrepancies in the measurements of the interfacial tension for the CO2+ H2O mixture by computer simulation. *The journal of physical chemistry letters,* 5**,** 1267-1271.

MWANGI, P., BRADY, P. V., RADONJIC, M. & THYNE, G. 2018. The effect of organic acids on wettability of sandstone and carbonate rocks. *Journal of Petroleum Science and Engineering,* 165**,** 428-435.

N. YEKEEN, A. A.-Y., B. MAMO NEGASH, M. ALI, A. GIWELLI, L. ESTEBAN, J. SAROUT 2022. Clay-Hydrogen and Clay-Cushion Gas Interfaial Tensions: Implications for Hydrogen Storage. *International Journal of Hydrogen Energy*.

NASRALLA, R. A. & NASR-EL-DIN, H. A. 2014a. Double-layer expansion: is it a primary mechanism of improved oil recovery by low-salinity waterflooding? *SPE Reservoir Evaluation and Engineering,* 17**,** 49-59.

NASRALLA, R. A. & NASR-EL-DIN, H. A. 2014b. Impact of cation type and concentration in injected brine on oil recovery in sandstone reservoirs. *Journal of Petroleum Science and Engineering,* 122**,** 384-395.

NATIONAL OCEANIC AND ATMOSPHERIC ADMINISTRATION, G. M. L. (n.d.). Trends in atmospheric carbon dioxide. Retrieved May 2, 2023, from https://gml.noaa.gov/ccgg/trends/.

NAZARAHARI, M. J., MANSHAD, A. K., ALI, M., ALI, J. A., SHAFIEI, A., SAJADI, S. M., MORADI, S., IGLAUER, S. & KESHAVARZ, A. 2021. Impact of a novel biosynthesized nanocomposite (SiO2@ Montmorilant@ Xanthan) on wettability shift and interfacial tension: Applications for enhanced oil recovery. *Fuel,* 298**,** 120773.

NAZARI MOGHADDAM, R., BAHRAMIAN, A., FAKHROUEIAN, Z., KARIMI, A. & ARYA, S. 2015. Comparative study of using nanoparticles for enhanced oil recovery: wettability alteration of carbonate rocks. *Energy & Fuels,* 29**,** 2111-2119.

NAZIR, H., MUTHUSWAMY, N., LOUIS, C., JOSE, S., PRAKASH, J., BUAN, M. E., FLOX, C., CHAVAN, S., SHI, X. & KAURANEN, P. 2020a. Is the H2 economy realizable in the foreseeable future? Part II: H2 storage, transportation, and distribution. *International Journal of Hydrogen Energy,* 45**,** 20693-20708.

NAZIR, H., MUTHUSWAMY, N., LOUIS, C., JOSE, S., PRAKASH, J., BUAN, M. E., FLOX, C., CHAVAN, S., SHI, X. & KAURANEN, P. 2020b. Is the H2 economy realizable in the foreseeable future? Part III: H2 usage technologies, applications, and challenges and opportunities. *International Journal of Hydrogen Energy,* 45**,** 28217-28239.

NEUMANN, A., GOOD, R., HOPE, C. & SEJPAL, M. 1974. An equation-of-state approach to determine surface tensions of low-energy solids from contact angles. *Journal of colloid and interface science,* 49**,** 291-304.

NILSSEN, H., FREDHEIM, A., SOLBRAA, E. & KVAMME, B. Theoretical prediction of interfacial tensions for hydrocarbon mixtures with gradient theory in combination with Peng-Robinson equation of state. Proc. Offshore Technol. Conf., Society of Petroleum Engineers, 2010.

NINO-AMEZQUITA, O. G., ENDERS, S., JAEGER, P. T. & EGGERS, R. 2010. Measurement and prediction of interfacial tension of binary mixtures. *Industrial and Engineering Chemistry Research,* 49**,** 592-601.

NORDHOLM, S., JOHNSON, M. & FREASIER, B. 1980. Generalized van der Waals theory. III. The prediction of hard sphere structure. *Australian Journal of Chemistry,* 33**,** 2139-2150.

OKEKE, O. & OKOGBUE, C. 2011. Shales: A review of their classifications, properties and importance to the petroleum industry. *Global Journal of Geological Sciences,* 9**,** 75-83.
OLDENBURG, C. M. 2003. Carbon dioxide as cushion gas for natural gas storage. *Energy & Fuels,* 17**,** 240-246.
OLIVEIRA, M., COUTINHO, J. & QUEIMADA, A. 2011. Surface tensions of esters from a combination of the gradient theory with the CPA EoS. *Fluid phase equilibria,* 303**,** 56-61.
OLIVEIRA, M., MARRUCHO, I., COUTINHO, J. & QUEIMADA, A. 2008. Surface tension of chain molecules through a combination of the gradient theory with the CPA EoS. *Fluid Phase Equilibria,* 267**,** 83-91.
ORYWALL, P., DRÜPPEL, K., KUHN, D., KOHL, T., ZIMMERMANN, M. & EICHE, E. 2017. Flow-through experiments on the interaction of sandstone with Ba-rich fluids at geothermal conditions. *Geothermal Energy,* 5**,** 1-24.
OWENS, J. 2009. Indiana Limestone Handbook, Indiana Limestone Institute of America. Inc.
OZARSLAN, A. 2012. Large-scale hydrogen energy storage in salt caverns. *International Journal of Hydrogen Energy,* 37**,** 14265-14277.
PACHAURI, R. K., ALLEN, M. R., BARROS, V. R., BROOME, J., CRAMER, W., CHRIST, R., CHURCH, J. A., CLARKE, L., DAHE, Q. & DASGUPTA, P. 2014. *Climate change 2014: synthesis report. Contribution of Working Groups I, II and III to the fifth assessment report of the Intergovernmental Panel on Climate Change*, Ipcc.
PALLAS, N. & HARRISON, Y. 1990. An automated drop shape apparatus and the surface tension of pure water. *Colloids and Surfaces,* 43**,** 169-194.
PALMER, G. 2019. Renewables rise above fossil fuels. *Nature Energy,* 4**,** 538-539.
PAN, B., GONG, C., WANG, X., LI, Y. & IGLAUER, S. 2020a. The interfacial properties of clay-coated quartz at reservoir conditions. *Fuel,* 262**,** 116461.
PAN, B., LI, Y., WANG, H., JONES, F. & IGLAUER, S. 2018. CO2 and CH4 wettabilities of organic-rich shale. *Energy & Fuels,* 32**,** 1914-1922.
PAN, B., LI, Y., ZHANG, M., WANG, X. & IGLAUER, S. 2020b. Effect of total organic carbon (TOC) content on shale wettability at high pressure and high temperature conditions. *Journal of Petroleum Science and Engineering,* 193**,** 107374.
PAN, B., YIN, X. & IGLAUER, S. 2020c. A review on clay wettability: From experimental investigations to molecular dynamics simulations. *Advances in Colloid and Interface Science***,** 102266.
PAN, B., YIN, X. & IGLAUER, S. 2021a. Rock-fluid interfacial tension at subsurface conditions: Implications for H2, CO2 and natural gas geo-storage. *International Journal of Hydrogen Energy,* 46**,** 25578-25585.
PAN, B., YIN, X., JU, Y. & IGLAUER, S. 2021b. Underground hydrogen storage: Influencing parameters and future outlook. *Advances in Colloid and Interface Science,* 294**,** 102473.
PANFILOV, M., GRAVIER, G. & FILLACIER, S. Underground storage of H2 and H2-CO2-CH4 mixtures. ECMOR X-10th European conference on the mathematics of oil recovery, 2006. European Association of Geoscientists & Engineers, cp-23-00003.
PARK, A.-H. A. & FAN, L.-S. 2004. CO2 mineral sequestration: physically activated dissolution of serpentine and pH swing process. *Chemical Engineering Science,* 59**,** 5241-5247.
PARKINSON, B., TABATABAEI, M., UPHAM, D. C., BALLINGER, B., GREIG, C., SMART, S. & MCFARLAND, E. 2018. Hydrogen production using methane: Techno-economics of decarbonizing fuels and chemicals. *International Journal of Hydrogen Energy,* 43**,** 2540-2555.

PASSARELLA, M. 2021. *Basalt-fluid interactions at subcritical and supercritical conditions: An experimental study.* Open Access Te Herenga Waka-Victoria University of Wellington.
PENG, C., CRAWSHAW, J. P., MAITLAND, G. C., TRUSLER, J. M. & VEGA-MAZA, D. 2013. The pH of CO2-saturated water at temperatures between 308 K and 423 K at pressures up to 15 MPa. *The Journal of Supercritical Fluids,* 82**,** 129-137.
PENTLAND, C. H., EL-MAGHRABY, R., IGLAUER, S. & BLUNT, M. J. 2011. Measurements of the capillary trapping of super-critical carbon dioxide in Berea sandstone. *Geophysical Research Letters,* 38.
PEREIRA, L. M., CHAPOY, A., BURGASS, R., OLIVEIRA, M. B., COUTINHO, J. A. & TOHIDI, B. 2016. Study of the impact of high temperatures and pressures on the equilibrium densities and interfacial tension of the carbon dioxide/water system. *The Journal of Chemical Thermodynamics,* 93**,** 404-415.
PERERA, M. 2023. A review of underground hydrogen storage in depleted gas reservoirs: Insights into various rock-fluid interaction mechanisms and their impact on the process integrity. *Fuel,* 334**,** 126677.
PERERA, M., RANJITH, P., CHOI, S., BOUAZZA, A., KODIKARA, J. & AIREY, D. 2011. A review of coal properties pertinent to carbon dioxide sequestration in coal seams: with special reference to Victorian brown coals. *Environmental earth sciences,* 64**,** 223-235.
PFEIFFER, W. 2017. *Hydrogen energy storage in porous geological formations-Investigation of storage dimensioning, induced effects and monitoring methods.*
PFEIFFER, W. T. & BAUER, S. 2015. Subsurface porous media hydrogen storage–scenario development and simulation. *Energy Procedia,* 76**,** 565-572.
PICHLER, M. Underground sun storage results and outlook. EAGE/DGMK joint workshop on underground storage of hydrogen, 2019. European Association of Geoscientists & Engineers, 1-4.
PIERCE, E., CARMONA, F. & AMIRFAZLI, A. 2008. Understanding of sliding and contact angle results in tilted plate experiments. *Colloids and Surfaces A: Physicochemical and Engineering Aspects,* 323**,** 73-82.
PORTARAPILLO, M. & DI BENEDETTO, A. 2021. Risk assessment of the large-scale hydrogen storage in salt caverns. *Energies,* 14**,** 2856.
POSER, C. I. & SANCHEZ, I. C. 1979. Surface tension theory of pure liquids and polymer melts. *Journal of Colloid and Interface Science,* 69**,** 539-548.
PRINCEN, H., ZIA, I. & MASON, S. 1967. Measurement of interfacial tension from the shape of a rotating drop. *Journal of colloid and interface science,* 23**,** 99-107.
PURCELL, W. 1950. Interpretation of capillary pressure data. *Journal of Petroleum Technology,* 2**,** 11-12.
QUEIMADA, A., ROLO, L., CAÇO, A., MARRUCHO, I., STENBY, E. H. & COUTINHO, J. 2006. Prediction of viscosities and surface tensions of fuels using a new corresponding states model. *Fuel,* 85**,** 874-877.
RAAD, S. M. J., LEONENKO, Y. & HASSANZADEH, H. 2022. Hydrogen storage in saline aquifers: Opportunities and challenges. *Renewable and Sustainable Energy Reviews,* 168**,** 112846.
RAAD, S. M. J., RANJBAR, E., HASSANZADEH, H. & LEONENKO, Y. 2023. Hydrogen-brine mixture PVT data for reservoir simulation of hydrogen storage in deep saline aquifers. *International Journal of Hydrogen Energy,* 48**,** 696-708.

RAHMAN, T., LEBEDEV, M., BARIFCANI, A. & IGLAUER, S. 2016. Residual trapping of supercritical CO2 in oil-wet sandstone. *Journal of colloid and interface science,* 469**,** 63-68.

RAHMSTORF, S. 2007. A semi-empirical approach to projecting future sea-level rise. *Science,* 315**,** 368-370.

RAMACHANDRAN, R. & MENON, R. K. 1998. An overview of industrial uses of hydrogen. *International journal of hydrogen energy,* 23**,** 593-598.

RAZA, A., GLATZ, G., GHOLAMI, R., MAHMOUD, M. & ALAFNAN, S. 2022. Carbon mineralization and geological storage of CO2 in basalt: Mechanisms and technical challenges. *Earth-Science Reviews,* 229**,** 104036.

REEDIJK, J. & POEPPELMEIER, K. 2013. Comprehensive inorganic chemistry II: from elements to applications. *V1 Main-Group Elem., Incl. Noble Gases V2 Transition Elem., Lanthanides and Actinides V3 Bioinorganic Fundam. and Appl.: Metals in Nat. Living Syst. and Metals in Toxicology and Med. V4 Solid-State Mater., Incl. Ceramics and Minerals V5 Porous Mater. and Nanomaterials V6 Homogeneous Catal. Appl. V7 Surf. Inorganic Chem. and Heterog. Catal. V8 Coord. and Organometallic Chem. V9 Theory and Methods.* Elsevier Ltd.

REN, N., GUO, W., LIU, B., CAO, G. & DING, J. 2011. Biological hydrogen production by dark fermentation: challenges and prospects towards scaled-up production. *Current opinion in biotechnology,* 22**,** 365-370.

REN, N., WANG, A., CAO, G., XU, J. & GAO, L. 2009. Bioconversion of lignocellulosic biomass to hydrogen: potential and challenges. *Biotechnology advances,* 27**,** 1051-1060.

REVIL, A. & CEREPI, A. 2004. Streaming potentials in two-phase flow conditions. *Geophysical research letters,* 31.

REVIL, A. & PEZARD, P. 1998. Streaming electrical potential anomaly along faults in geothermal areas. *Geophysical Research Letters,* 25**,** 3197-3200.

REZAEYAN, A., TABATABAEI-NEJAD, S. A., KHODAPANAH, E. & KAMARI, M. 2015. A laboratory study on capillary sealing efficiency of Iranian shale and anhydrite caprocks. *Marine and Petroleum Geology,* 66**,** 817-828.

RIAHI, K., GRÜBLER, A. & NAKICENOVIC, N. 2007. Scenarios of long-term socio-economic and environmental development under climate stabilization. *Technological Forecasting & Social Change,* 74**,** 887-935.

RIAZ, A., HESSE, M., TCHELEPI, H. & ORR, F. 2006. Onset of convection in a gravitationally unstable diffusive boundary layer in porous media. *Journal of Fluid Mechanics,* 548**,** 87-111.

ROBINSON, D. B. & PENG, D.-Y. 1978. *The characterization of the heptanes and heavier fractions for the GPA Peng-Robinson programs,* Gas processors association.

RODRÍGUEZ, K. & ARAUJO, M. 2006. Temperature and pressure effects on zeta potential values of reservoir minerals. *Journal of Colloid and Interface Science,* 300**,** 788-794.

ROGERS, K. L., NEUHOFF, P. S., PEDERSEN, A. K. & BIRD, D. K. 2006. CO2 metasomatism in a basalt-hosted petroleum reservoir, Nuussuaq, West Greenland. *Lithos,* 92**,** 55-82.

ROSS, E. & BEHRINGER, D. 2019. Changes in temperature, pH, and salinity affect the sheltering responses of Caribbean spiny lobsters to chemosensory cues. *Scientific Reports,* 9**,** 1-11.

ROUSTAEI, A. & BAGHERZADEH, H. 2015. Experimental investigation of SiO2 nanoparticles on enhanced oil recovery of carbonate reservoirs. *Journal of Petroleum Exploration & Production Technology,* 5**,** 27-33.

ROWLINSON, J. S. 1979. Translation of JD van der Waals'"The thermodynamik theory of capillarity under the hypothesis of a continuous variation of density". *Journal of Statistical Physics,* 20**,** 197-200.

RUDOLPH, M. & PEUKER, U. A. 2014. Mapping hydrophobicity combining AFM and Raman spectroscopy. *Minerals Engineering,* 66**,** 181-190.

SAHIMI, M. & TAYLOR, B. N. 1991. Surface tension of binary liquid–vapor mixtures: A comparison of mean-field and scaling theories. *The Journal of chemical physics,* 95**,** 6749-6761.

SÁINZ-GARCÍA, A., ABARCA, E., RUBÍ, V. & GRANDIA, F. 2017. Assessment of feasible strategies for seasonal underground hydrogen storage in a saline aquifer. *International Journal of Hydrogen Energy,* 42**,** 16657-16666.

SAKINTUNA, B., LAMARI-DARKRIM, F. & HIRSCHER, M. 2007. Metal hydride materials for solid hydrogen storage: a review. *International journal of hydrogen energy,* 32**,** 1121-1140.

SAKUROVS, R., DAY, S., WEIR, S. & DUFFY, G. 2007. Application of a modified Dubinin− Radushkevich equation to adsorption of gases by coals under supercritical conditions. *Energy and fuels,* 21**,** 992-997.

SAKUROVS, R. & LAVRENCIC, S. 2011. Contact angles in CO2-water-coal systems at elevated pressures. *International Journal of Coal Geology,* 87**,** 26-32.

SALGıN, S., SALGıN, U. & BAHADıR, S. 2012. Zeta potentials and isoelectric points of biomolecules: the effects of ion types and ionic strengths. *International Journal of Electrochemical Science,* 7**,** 12404-12414.

SAMANIEGO, V., CHILINGARIAN, G., MAZZULLO, S. & RIEKE, H. 1992. Chapter 10 Fluid Flow Through Carbonate Rock Systems. Carbonate Reservoir Characterization: A Geologic-Engineering Analysis. Part I. Elsevier, NewYork.

SANCHEZ, I. C. 2013. *Physics of polymer surfaces and interfaces*, Butterworth-Heinemann.

SARAJI, S., GOUAL, L., PIRI, M. & PLANCHER, H. 2013a. Wettability of sc-CO2/water/quartz systems: Simultaneous measurement of contact angle and interfacial tension at reservoir conditions. *Langmuir,* 29**,** 6856-6866.

SARAJI, S., GOUAL, L., PIRI, M. J. C., PHYSICOCHEMICAL, S. A. & ASPECTS, E. 2013b. Dynamic adsorption of asphaltenes on quartz and calcite packs in the presence of brine films. *Colloids and Surfaces A: Physicochemical and Engineering Aspects,* 434**,** 260-267.

SARAVANAN, A., KUMAR, P. S., ARON, N. S. M., JEEVANANTHAM, S., KARISHMA, S., YAASHIKAA, P., CHEW, K. W. & SHOW, P. L. 2022. A review on bioconversion processes for hydrogen production from agro-industrial residues. *International Journal of Hydrogen Energy,* 47**,** 37302-37320.

SARI, A., AL MASKARI, N. S., SAEEDI, A. & XIE, Q. 2020. Impact of surface roughness on wettability of oil-brine-calcite system at sub-pore scale. *Journal of Molecular Liquids,* 299**,** 112107.

SARMA, S. J., BRAR, S. K., SYDNEY, E. B., LE BIHAN, Y., BUELNA, G. & SOCCOL, C. R. 2012. Microbial hydrogen production by bioconversion of crude glycerol: A review. *International Journal of Hydrogen Energy,* 37**,** 6473-6490.

SARMADIVALEH, M., AL-YASERI, A. Z. & IGLAUER, S. 2015. Influence of temperature and pressure on quartz–water–CO2 contact angle and CO2–water interfacial tension. *Journal of colloid and interface science,* 441**,** 59-64.

SAUER, B. B. & DEE, G. T. 1994. Studies of polymer, copolymer, and associating liquids by melt surface tension methods and Cahn-Hilliard density-gradient theory. *Journal of colloid and interface science,* 162**,** 25-35.
SAUNDERS, J., JACKSON, M., GULAMALI, M., VINOGRADOV, J. & PAIN, C. 2012. Streaming potentials at hydrocarbon reservoir conditions. *Geophysics,* 77**,** E77-E90.
SAW, R. K. & MANDAL, A. 2020. A mechanistic investigation of low salinity water flooding coupled with ion tuning for enhanced oil recovery. *RSC advances,* 10**,** 42570-42583.
SAXENA, R., SEAL, D., KUMAR, S. & GOYAL, H. 2008. Thermo-chemical routes for hydrogen rich gas from biomass: a review. *Renewable and Sustainable Energy Reviews,* 12**,** 1909-1927.
SCHUTTER, S. R. 2003. Occurrences of hydrocarbons in and around igneous rocks. *Geological Society, London, Special Publications,* 214**,** 35-68.
SCHWARTZ, A. M. 1969. Capillarity-theory and practice. *Industrial and Engineering Chemistry,* 61**,** 10-21.
SEDEV, R., AKHONDZADEH, H., ALI, M., KESHAVARZ, A. & IGLAUER, S. 2022. Contact angles of a brine on a bituminous coal in compressed hydrogen. *Geophysical Research Letters,* 49**,** e2022GL098261.
SELLEY, R. C., COCKS, L. R. M. & PLIMER, I. R. 2005. *Encyclopedia of geology*, Elsevier Academic.
SEN, P., SCALA, C. & COHEN, M. 1981. A self-similar model for sedimentary rocks with application to the dielectric constant of fused glass beads. *Geophysics,* 46**,** 781-795.
SEN, P. N. 1984. Grain shape effects on dielectric and electrical properties of rocks. *Geophysics,* 49**,** 586-587.
SEN, P. N. & GOODE, P. A. 1992. Influence of temperature on electrical conductivity on shaly sands. *Geophysics,* 57**,** 89-96.
SEYITOGLU, S., DINCER, I. & KILICARSLAN, A. 2017. Energy and exergy analyses of hydrogen production by coal gasification. *International Journal of Hydrogen Energy,* 42**,** 2592-2600.
SHAH, V., BROSETA, D., MOURONVAL, G. & MONTEL, F. 2008. Water/acid gas interfacial tensions and their impact on acid gas geological storage. *International Journal of Greenhouse Gas Control,* 2**,** 594-604.
SHAKERIAN, M. & BALCOM, B. 2018. An MR/MRI compatible core holder with the RF probe immersed in the confining fluid. *Journal of Magnetic Resonance,* 286**,** 36-41.
SHARIAT, A., MOORE, R. G., MEHTA, S. A., VAN FRAASSEN, K. C., NEWSHAM, K. E. & RUSHING, J. A. Laboratory measurements of CO2-H2O interfacial tension at HP/HT conditions: Implications for CO2 sequestration in deep aquifers. Carbon management technology conference, 2012. CMTC, CMTC-150010-MS.
SHAYAN, E., ZARE, V. & MIRZAEE, I. 2018. Hydrogen production from biomass gasification; a theoretical comparison of using different gasification agents. *Energy Conversion management,* 159**,** 30-41.
SHEHATA, A. M. & NASR-EL-DIN, H. A. Zeta potential measurements: Impact of salinity on sandstone minerals. SPE International Symposium on Oilfield Chemistry, 2015. OnePetro.
SHI, J. & DURUCAN, S. 2005. CO2 storage in deep unminable coal seams. *Oil and gas science and technology,* 60**,** 547-558.
SHI, Z., JESSEN, K. & TSOTSIS, T. T. 2020. Impacts of the subsurface storage of natural gas and hydrogen mixtures. *International Journal of Hydrogen Energy,* 45**,** 8757-8773.

SHUKLA, R., RANJITH, P., HAQUE, A. & CHOI, X. 2010. A review of studies on CO2 sequestration and caprock integrity. *Fuel,* 89**,** 2651-2664.
SINGH, L. & WAHID, Z. A. 2015. Methods for enhancing bio-hydrogen production from biological process: a review. *Journal of Industrial and Engineering Chemistry,* 21**,** 70-80.
SINGH, N., GOPANI, P. H., SARMA, H. K., MATTEY, P., NEGI, D. S., SRIVASTAVA, V. R. & LUXBACHER, T. 2022. Charging behaviour at the carbonate rock-water interface in low-salinity waterflooding: Estimation of zeta potential in high-salinity brines. *The Canadian Journal of Chemical Engineering,* 100**,** 1226-1234.
SLOWINSKI JR, E. J., GATES, E. E. & WARING, C. E. 1957. The effect of pressure on the surface tensions of liquids. *The Journal of Physical Chemistry,* 61**,** 808-810.
SNÆBJÖRNSDÓTTIR, S. Ó., WIESE, F., FRIDRIKSSON, T., ÁRMANSSON, H., EINARSSON, G. M. & GISLASON, S. R. 2014. CO2 storage potential of basaltic rocks in Iceland and the oceanic ridges. *Energy Procedia,* 63**,** 4585-4600.
SOAVE, G. 1972. Equilibrium constants from a modified Redlich-Kwong equation of state. *Chemical engineering science,* 27**,** 1197-1203.
SOLEYMANZADEH, A., RAHMATI, A., YOUSEFI, M. & ROSHANI, B. 2021. Theoretical and experimental investigation of effect of salinity and asphaltene on IFT of brine and live oil samples. *Journal of Petroleum Exploration and Production,* 11**,** 769-781.
SORGULU, F. & DINCER, I. 2018. A renewable source based hydrogen energy system for residential applications. *International Journal of Hydrogen Energy,* 43**,** 5842-5851.
SPAN, R. & WAGNER, W. 1996. A new equation of state for carbon dioxide covering the fluid region from the triple-point temperature to 1100 K at pressures up to 800 MPa. *Journal of physical and chemical reference data,* 25**,** 1509-1596.
SPITERI, E. J., JUANES, R., BLUNT, M. J. & ORR, F. M. 2008. A new model of trapping and relative permeability hysteresis for all wettability characteristics. *Spe Journal,* 13**,** 277-288.
SPRUNT, E. S., MERCER, T. B. & DJABBARAH, N. F. 1994. Streaming potential from multiphase flow. *Geophysics,* 59**,** 707-711.
SRIVASTAV, D., SINGH, A. P. & KUMAR, A. 2014. Fossil fuels running out: Third generation micro algal biofuels showing light of hope. *Open Access Library Journal,* 1**,** 1-10.
STALKER, L., VARMA, S., VAN GENT, D., HAWORTH, J. & SHARMA, S. 2013. South West Hub: a carbon capture and storage project. *Australian Journal of Earth Sciences,* 60**,** 45-58.
STANDNES, D. C. & AUSTAD, T. 2003. Wettability alteration in carbonates: Interaction between cationic surfactant and carboxylates as a key factor in wettability alteration from oil-wet to water-wet conditions. *Colloids Surfaces A: Physicochemical Engineering Aspects,* 216**,** 243-259.
STAUFFER, C. E. 1965. The measurement of surface tension by the pendant drop technique. *The journal of physical chemistry,* 69**,** 1933-1938.
STETSON, N., MCWHORTER, S. & AHN, C. 2016. Introduction to hydrogen storage. *Compendium of hydrogen energy.* Elsevier.
STIEGEL, G. J. & RAMEZAN, M. 2006. Hydrogen from coal gasification: An economical pathway to a sustainable energy future. *International journal of coal geology,* 65**,** 173-190.
STUMM, W. & MORGAN, J. J. 2012. *Aquatic chemistry: chemical equilibria and rates in natural waters,* John Wiley & Sons.
SUGDEN, S. 1924. VI.—The variation of surface tension with temperature and some related functions. *Journal of the Chemical Society, Transactions,* 125**,** 32-41.

SUTTON, R. P. An improved model for water-hydrocarbon surface tension at reservoir conditions. SPE Annual Technical Conference and Exhibition?, 2009. SPE, SPE-124968-MS.
SWAIN, P. S. & LIPOWSKY, R. 1998. Contact angles on heterogeneous surfaces: A new look at Cassie's and Wenzel's laws. *Langmuir,* 14**,** 6772-6780.
TADMOR, R. 2004. Line energy and the relation between advancing, receding, and young contact angles. *Langmuir,* 20**,** 7659-7664.
TAKACH, M., SARAJLIĆ, M., PETERS, D., KROENER, M., SCHULDT, F. & VON MAYDELL, K. 2022. Review of hydrogen production techniques from water using renewable energy sources and its storage in salt caverns. *Energies,* 15**,** 1415.
TANINO, Y. & BLUNT, M. 2013. Laboratory investigation of capillary trapping under mixed-wet conditions. *Water Resources Research,* 49**,** 4311-4319.
TARKOWSKI, R. 2019. Underground hydrogen storage: Characteristics and prospects. *Renewable and Sustainable Energy Reviews,* 105**,** 86-94.
TARKOWSKI, R. & ULIASZ-MISIAK, B. 2022. Towards underground hydrogen storage: A review of barriers. *Renewable & Sustainable Energy Reviews,* 162**,** 112451.
TAWFIK, M., KARPYN, Z. & JOHNS, R. Multiscale study of chemically-tuned waterflooding in carbonate rocks using micro-computed tomography. IOR 2019–20th European Symposium on Improved Oil Recovery, 2019. EAGE Publications BV, 1-23.
TCP-TASK#42, H. 2023. Underground Hydrogen Storage: Technology Monitor Report.
TEMPLETON, C. C. & RODGERS, J. C. 1967. Solubility of anhydrite in several aqueous salt solutions between 250. degree. and 325. degree. *Journal of Chemical and Engineering Data,* 12**,** 536-547.
THANH, L. D. & SPRIK, R. 2016. Zeta potential in porous rocks in contact with monovalent and divalent electrolyte aqueous solutions. *Geophysics,* 81**,** D303-D314.
TIAB, D. & DONALDSON, E. C. 2015. *Petrophysics: theory and practice of measuring reservoir rock and fluid transport properties,* Gulf professional publishing.
TOHRY, A., DEHGHAN, R., ZAREI, M. & CHELGANI, S. C. 2021. Mechanism of humic acid adsorption as a flotation separation depressant on the complex silicates and hematite. *Minerals Engineering,* 162**,** 106736.
TONNET, N., MOURONVAL, G., CHIQUET, P. & BROSETA, D. 2011. Petrophysical assessment of a carbonate-rich caprock for CO2 geological storage purposes. *Energy Procedia,* 4**,** 5422-5429.
TRIPP, C. & COMBES, J. 1998. Chemical modification of metal oxide surfaces in supercritical CO2: The interaction of supercritical CO2 with the adsorbed water layer and the surface hydroxyl groups of a silica surface. *Langmuir,* 14**,** 7348-7352.
TRUEMAN, C., RODGERS, K., MCLELLAN, I. & HURSTHOUSE, A. 2019. Geochemistry: inorganic. *Encyclopedia of Analytical Science: Reference Module in Chemistry, Molecular Sciences and Chemical Engineering.* Elsevier Limited.
TUNEGA, D., BENCO, L., HABERHAUER, G., GERZABEK, M. H. & LISCHKA, H. 2002. Ab initio molecular dynamics study of adsorption sites on the (001) surfaces of 1: 1 dioctahedral clay minerals. *The Journal of Physical Chemistry B,* 106**,** 11515-11525.
TUNEGA, D., GERZABEK, M. H. & LISCHKA, H. 2004. Ab initio molecular dynamics study of a monomolecular water layer on octahedral and tetrahedral kaolinite surfaces. *The Journal of Physical Chemistry B,* 108**,** 5930-5936.

TÜRKE, A., MÉNEZ, B. & BACH, W. 2018. Comparing biosignatures in aged basalt glass from North Pond, Mid-Atlantic Ridge and the Louisville Seamount Trail, off New Zealand. *Plos one,* 13**,** e0190053.

TURNER, J. A. 2004. Sustainable hydrogen production. *Science,* 305**,** 972-974.

TUROŃ, K. 2020. Hydrogen-powered vehicles in urban transport systems–current state and development. *Transportation Research Procedia,* 45**,** 835-841.

UCBAS, Y., BOZKURT, V., BILIR, K. & IPEK, H. 2014. Concentration of chromite by means of magnetic carrier using sodium oleate and other reagents. *Physicochemical Problems of Mineral Processing,* 50.

UGARTE, E. R. & SALEHI, S. 2022. A review on well integrity issues for underground hydrogen storage. *Journal of Energy Resources Technology,* 144.

ULRICH, H. J., STUMM, W. & COSOVIC, B. 1988. Adsorption of aliphatic fatty acids on aquatic interfaces. Comparison between two model surfaces: the mercury electrode and δ-Al2O3 colloids. *Environmental science & technology,* 22**,** 37-41.

VAN OSS, C., GOOD, R. & CHAUDHURY, M. 1986. The role of van der Waals forces and hydrogen bonds in "hydrophobic interactions" between biopolymers and low energy surfaces. *Journal of colloid & Interface Science,* 111**,** 378-390.

VAN ROOIJEN, W., HABIBI, P., XU, K., DEY, P., VLUGT, T., HAJIBEYGI, H. & MOULTOS, O. 2023. Interfacial Tensions, Solubilities, and Transport Properties of the H2/H2O/NaCl System: A Molecular Simulation Study. *Journal of Chemical and Engineering Data,* .

VDOVIĆ, N. 2001. Electrokinetic behaviour of calcite—the relationship with other calcite properties. *Chemical Geology,* 177**,** 241-248.

VDOVIĆ, N. & BIŠĆAN, J. 1998. Electrokinetics of natural and synthetic calcite suspensions. *Colloids and Surfaces A: Physicochemical and Engineering Aspects,* 137**,** 7-14.

VIDYADHAR, A. & RAO, K. H. 2007. Adsorption mechanism of mixed cationic/anionic collectors in feldspar-quartz flotation system. *Journal of Colloid and Interface Science,* 306**,** 195-204.

VINOGRADOV, J., JAAFAR, M. & JACKSON, M. 2010. Measurement of streaming potential coupling coefficient in sandstones saturated with natural and artificial brines at high salinity. *Journal of Geophysical Research: Solid Earth,* 115.

VINOGRADOV, J. & JACKSON, M. 2011. Multiphase streaming potential in sandstones saturated with gas/brine and oil/brine during drainage and imbibition. *Geophysical Research Letters,* 38.

VINOGRADOV, J. & JACKSON, M. D. 2015. Zeta potential in intact natural sandstones at elevated temperatures. *Geophysical Research Letters,* 42**,** 6287-6294.

VINOGRADOV, J., JACKSON, M. D. & CHAMEROIS, M. 2018. Zeta potential in sandpacks: Effect of temperature, electrolyte pH, ionic strength and divalent cations. *Colloids Surfaces A: Physicochemical and Engineering Aspects,* 553**,** 259-271.

WAGNER, W. & PRUß, A. 2002. The IAPWS formulation 1995 for the thermodynamic properties of ordinary water substance for general and scientific use. *Journal of physical and chemical reference data,* 31**,** 387-535.

WALKER, E. & GLOVER, P. 2018. Measurements of the relationship between microstructure, pH, and the streaming and zeta potentials of sandstones. *Transport in porous media,* 121**,** 183-206.

WAN, R. 2011. *Advanced well completion engineering*, Gulf professional publishing.

WANG, J., AN, Q., ZHAO, Y., PAN, G., SONG, J., HU, Q. & TAN, C.-W. 2023. Role of electrolytic hydrogen in smart city decarbonization in China. *Applied Energy,* 336**,** 120699.
WANG, M., WANG, G., SUN, Z., ZHANG, Y. & XU, D. 2019. Review of renewable energy-based hydrogen production processes for sustainable energy innovation. *Global Energy Interconnection,* 2**,** 436-443.
WANG, S., LU, A. & ZHONG, C.-J. 2021. Hydrogen production from water electrolysis: role of catalysts. *Nano Convergence,* 8**,** 1-23.
WANG, Z., ROBERTS, R., NATERER, G. & GABRIEL, K. 2012. Comparison of thermochemical, electrolytic, photoelectrolytic and photochemical solar-to-hydrogen production technologies. *International Journal of Hydrogen Energy,* 37**,** 16287-16301.
WATSON, M. N., DANIEL, R. F., TINGATE, P. R. & GIBSON-POOLE, C. M. 2005. CO2-related seal capacity enhancement in mudstones: Evidence from the pine lodge natural CO2 accumulation, Otway Basin, Australia. *Greenhouse Gas Control Technologies 7*. Elsevier.
WEGER, L. B., LEITAO, J. & LAWRENCE, M. G. 2021. Expected impacts on greenhouse gas and air pollutant emissions due to a possible transition towards a hydrogen economy in German road transport. *International journal of hydrogen energy,* 46**,** 5875-5890.
WEINAUG, C. F. & KATZ, D. L. 1943. Surface tensions of methane-propane mixtures. *Industrial Engineering Chemistry,* 35**,** 239-246.
WELLER, A., SLATER, L. & NORDSIEK, S. 2013. On the relationship between induced polarization and surface conductivity: Implications for petrophysical interpretation of electrical measurements. *Geophysics,* 78**,** D315-D325.
WENZEL, R. N. 1936. Resistance of solid surfaces to wetting by water. *Industrial and Engineering Chemistry,* 28**,** 988-994.
WILCOX, P. S., HONIAT, C., TRÜSSEL, M., EDWARDS, R. L. & SPÖTL, C. 2020. Exceptional warmth and climate instability occurred in the European Alps during the Last Interglacial period. *Communications Earth Environment,* 1**,** 1-6.
WINTERFELD, P., SCRIVEN, L. & DAVIS, H. 1978. An approximate theory of interfacial tensions of multicomponent systems: Applications to binary liquid-vapor tensions. *AIChE Journal,* 24**,** 1010-1014.
WOLLENWEBER, J., A ALLES, S., KRONIMUS, A., BUSCH, A., STANJEK, H. & KROOSS, B. M. 2009. Caprock and overburden processes in geological CO2 storage: An experimental study on sealing efficiency and mineral alterations. *Energy Procedia,* 1**,** 3469-3476.
WOLTHERS, M., DI TOMMASO, D., DU, Z. & DE LEEUW, N. H. 2012. Calcite surface structure and reactivity: molecular dynamics simulations and macroscopic surface modelling of the calcite–water interface. *Physical Chemistry Chemical Physics,* 14**,** 15145-15157.
WU, S. Calculation of interfacial tension in polymer systems. Journal of Polymer Science Part C: Polymer Symposia, 1971. Wiley Online Library, 19-30.
XIA, Y., YANG, Z. & ZHU, Y. 2013. Porous carbon-based materials for hydrogen storage: advancement and challenges. *Journal of Materials Chemistry A,* 1**,** 9365-9381.
XIE, Q., SARI, A., PU, W., CHEN, Y., BRADY, P. V., AL MASKARI, N. & SAEEDI, A. 2018. pH effect on wettability of oil/brine/carbonate system: Implications for low salinity water flooding. *Journal of Petroleum Science and Engineering,* 168**,** 419-425.
XU, S., GOU, Q., HAO, F., ZHANG, B., SHU, Z., LU, Y. & WANG, Y. 2020. Shale pore structure characteristics of the high and low productivity wells, Jiaoshiba shale gas field, Sichuan

Basin, China: Dominated by lithofacies or preservation condition? *Marine and Petroleum Geology,* 114**,** 104211.
XU, Z., ZHU, W., GONG, M. & ZHANG, H. 2013. Direct gasification of dewatered sewage sludge in supercritical water. Part 1: effects of alkali salts. *International Journal of Hydrogen Energy,* 38**,** 3963-3972.
YANG, D., GU, Y. & TONTIWACHWUTHIKUL, P. 2008. Wettability determination of the reservoir brine− reservoir rock system with dissolution of CO2 at high pressures and elevated temperatures. *Energy and Fuels,* 22**,** 504-509.
YEKEEN, N., AL-YASERI, A., NEGASH, B. M., ALI, M., GIWELLI, A., ESTEBAN, L. & SAROUT, J. 2022. Clay-hydrogen and clay-cushion gas interfacial tensions: Implications for hydrogen storage. *International Journal of Hydrogen Energy,* 47**,** 19155-19167.
YEKEEN, N., PADMANABHAN, E., ABDULELAH, H., IRFAN, S. A., OKUNADE, O. A., KHAN, J. A. & NEGASH, B. M. 2021. CO2/brine interfacial tension and rock wettability at reservoir conditions: A critical review of previous studies and case study of black shale from Malaysian formation. *Journal of Petroleum Science and Engineering,* 196**,** 107673.
YEKTA, A., MANCEAU, J.-C., GABOREAU, S., PICHAVANT, M. & AUDIGANE, P. 2018. Determination of hydrogen–water relative permeability and capillary pressure in sandstone: application to underground hydrogen injection in sedimentary formations. *Transport in Porous Media,* 122**,** 333-356.
YOUNG, T. 1805. III. An essay on the cohesion of fluids. *Philosophical transactions of the royal society of London***,** 65-87.
YSTROEM, L. H., NITSCHKE, F., HELD, S. & KOHL, T. 2020. A multicomponent geothermometer for high-temperature basalt settings. *Geothermal Energy,* 8**,** 1-21.
YU, H., WANG, Z., REZAEE, R., ZHANG, Y., HAN, T., ARIF, M. & JOHNSON, L. 2018. Porosity estimation in kerogen-bearing shale gas reservoirs. *Journal of Natural Gas Science and Engineering,* 52**,** 575-581.
YUKSELEN-AKSOY, Y. & KAYA, A. 2011. A study of factors affecting on the zeta potential of kaolinite and quartz powder. *Environmental Earth Sciences,* 62**,** 697-705.
ZENG, L., HOSSEINI, M., KESHAVARZ, A., IGLAUER, S., LU, Y. & XIE, Q. 2022. Hydrogen wettability in carbonate reservoirs: Implication for underground hydrogen storage from geochemical perspective. *International Journal of Hydrogen Energy,* 47**,** 25357-25366.
ZHANG, F., ZHAO, P., NIU, M. & MADDY, J. 2016. The survey of key technologies in hydrogen energy storage. *International journal of hydrogen energy,* 41**,** 14535-14552.
ZHAO, L., CAO, G.-L., WANG, A.-J., GUO, W.-Q., LIU, B.-F., REN, H.-Y., REN, N.-Q. & MA, F. 2012. Enhanced bio-hydrogen production by immobilized Clostridium sp. T2 on a new biological carrier. *International Journal of Hydrogen Energy,* 37**,** 162-166.
ZHOU, F., LIU, Q., LIU, X., LI, W., FENG, J. & CHI, R.-A. 2020. Surface electrical behaviors of apatite, dolomite, quartz, and phosphate ore. *Frontiers in Materials,* 7**,** 35.
ZHOU, X., KARIMI-FARD, M., DURLOFSKY, L. J. & AYDIN, A. 2014. Fluid flow through porous sandstone with overprinting and intersecting geological structures of various types. *Geological Society, London, Special Publications,* 374**,** 187-209.
ZHOU, X., ZHANG, Q., XING, H., LV, J., SU, H. & HUANG, Z. 2021. Numerical Study of Reactive Flow in Fractured Carbonate Rock. *Frontiers in Earth Science***,** 992.
ZHU, Q.-L. & XU, Q. 2015. Liquid organic and inorganic chemical hydrides for high-capacity hydrogen storage. *Energy and Environmental Science,* 8**,** 478-512.

ZHURAVLEV, L. 1987. Concentration of hydroxyl groups on the surface of amorphous silicas. *Langmuir,* 3**,** 316-318.

ZIVAR, D., KUMAR, S. & FOROOZESH, J. 2021. Underground hydrogen storage: A comprehensive review. *International Journal of Hydrogen Energy,* 46**,** 23436-23462.

ZULFIQAR, B., VOGEL, H., DING, Y., GOLMOHAMMADI, S., KÜCHLER, M., REUTER, D. & GEISTLINGER, H. 2020. The impact of wettability and surface roughness on fluid displacement and capillary trapping in 2-D and 3-D porous media: 2. Combined effect of wettability, surface roughness, and pore space structure on trapping efficiency in sand packs and micromodels. *Water Resources Research,* 56**,** e2020WR027965.

ZULLIG, J. J. & MORSE, J. W. 1988. Interaction of organic acids with carbonate mineral surfaces in seawater and related solutions: I. Fatty acid adsorption. *Geochimica et Cosmochimica Acta,* 52**,** 1667-1678.

ZUO, Y.-X. & STENBY, E. H. 1996a. Calculation of surface tensions of polar mixtures with a simplified gradient theory model. *Journal of chemical engineering of Japan,* 29**,** 159-165.

ZUO, Y.-X. & STENBY, E. H. 1996b. A linear gradient theory model for calculating interfacial tensions of mixtures. *Journal of colloid and interface science,* 182**,** 126-132.

ZUO, Y. X. & STENBY, E. H. 1997. Corresponding-states and parachor models for the calculation of interfacial tensions. *The Canadian Journal of Chemical Engineering,* 75**,** 1130-1137.

ZÜTTEL, A., REMHOF, A., BORGSCHULTE, A. & FRIEDRICHS, O. 2010. Hydrogen: the future energy carrier. *Philosophical Transactions of the Royal Society A: Mathematical, Physical & Engineering Sciences,* 368**,** 3329-3342.

Appendix

This appendix contains a signed statement of contribution from all contributors.

To Whom It May Concern,

I, *Mirhasan Hosseini*, contributed *as the first author* to the paper/publication entitled "*H_2− brine interfacial tension as a function of salinity, temperature, and pressure; implications for hydrogen geo-storage*".

[redacted]

I, as a Co-Author, endorse that this level of contribution by the Candidate indicated above is appropriate.

Jalal Fahimpour

[redacted]

Assistant Professor at Department of Petroleum Engineering, Amirkabir University of Technology, Tehran, Iran

---

Muhammad Ali

[redacted]

Researcher at Petroleum Engineering Discipline, School of Engineering, Edith Cowan University, 270 Joondalup Dr, Joondalup, WA, 6027, Australia

---

Alireza Keshavarz

[redacted]

Senior Lecturer at Petroleum Engineering Discipline, School of Engineering, Edith Cowan University, 270 Joondalup Dr, Joondalup, WA, 6027, Australia

---

[redacted]

Professor at Petroleum Engineering Discipline, School of Engineering, Edith Cowan University, 270 Joondalup Dr, Joondalup, WA, 6027, Australia

---

To Whom It May Concern,

I, *Mirhasan Hosseini*, contributed *as the first author* to the paper/publication entitled "*Hydrogen wettability of carbonate formations: Implications for hydrogen geo-storage*".

[redacted]

I, as a Co-Author, endorse that this level of contribution by the Candidate indicated above is appropriate.

Jalal Fahimpour

[redacted]

Assistant Professor at Department of Petroleum Engineering, Amirkabir University of Technology, Tehran, Iran

---

Muhammad Ali

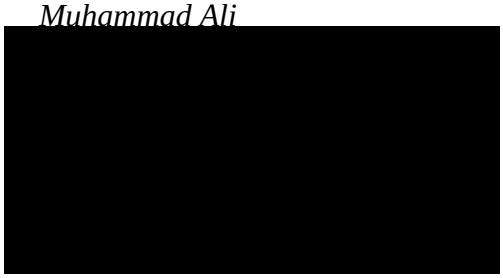

Researcher at Petroleum Engineering Discipline, School of Engineering, Edith Cowan University, 270 Joondalup Dr, Joondalup, WA, 6027, Australia

---

Alireza Keshavarz

Senior Lecturer at Petroleum Engineering Discipline, School of Engineering, Edith Cowan University, 270 Joondalup Dr, Joondalup, WA, 6027, Australia

---

Stefan Iglauer

Professor at Petroleum Engineering Discipline, School of Engineering, Edith Cowan University, 270 Joondalup Dr, Joondalup, WA, 6027, Australia

---

To Whom It May Concern,

I, *Mirhasan Hosseini*, contributed *as the first author* to the paper/publication entitled "*Capillary sealing efficiency analysis of caprocks: implication for hydrogen geological storage*".

[redacted]

I, as a Co-Author, endorse that this level of contribution by the Candidate indicated above is appropriate.

Jalal Fahimpour

[redacted]

Assistant Professor at Department of Petroleum Engineering, Amirkabir University of Technology, Tehran, Iran

---

Muhammad Ali

[redacted]

Researcher at Petroleum Engineering Discipline, School of Engineering, Edith Cowan University, 270 Joondalup Dr, Joondalup, WA, 6027, Australia

---

Alireza Keshavarz

[redacted]

Senior Lecturer at Petroleum Engineering Discipline, School of Engineering, Edith Cowan University, 270 Joondalup Dr, Joondalup, WA, 6027, Australia

---

Stefan Iglauer

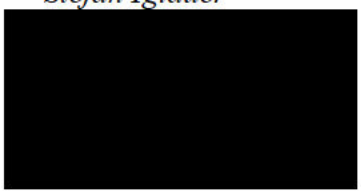

Professor at Petroleum Engineering Discipline, School of Engineering, Edith Cowan University, 270 Joondalup Dr, Joondalup, WA, 6027, Australia

---

To Whom It May Concern,

I, *Mirhasan Hosseini*, contributed *as the first author* to the paper/publication entitled "*Basalt-H_2-brine wettability at geo-storage conditions: Implication for hydrogen storage in basaltic formations*".

I, as a Co-Author, endorse that this level of contribution by the Candidate indicated above is appropriate.

Muhammad Ali

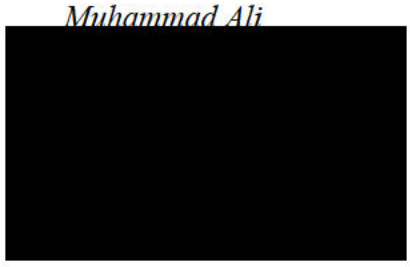

Researcher at Petroleum Engineering Discipline, School of Engineering, Edith Cowan University, 270 Joondalup Dr, Joondalup, WA, 6027, Australia

---

Jalal Fahimpour

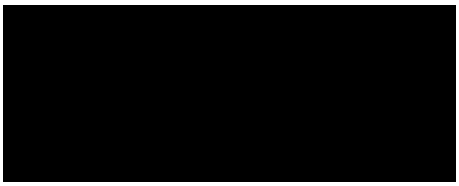

Assistant Professor at Department of Petroleum Engineering, Amirkabir University of Technology, Tehran, Iran

---

Alireza Keshavarz

Senior Lecturer at Petroleum Engineering Discipline, School of Engineering, Edith Cowan University, 270 Joondalup Dr, Joondalup, WA, 6027, Australia

---

Stefan Iglauer

Professor at Petroleum Engineering Discipline, School of Engineering, Edith Cowan University, 270 Joondalup Dr, Joondalup, WA, 6027, Australia

---

To Whom It May Concern,

I, *Mirhasan Hosseini*, contributed *as the first author* to the paper/publication entitled "*Assessment of rock-hydrogen and rock-water interfacial tension in shale, evaporite and basaltic rocks".*

I, as a Co-Author, endorse that this level of contribution by the Candidate indicated above is appropriate.

Muhammad Ali

Researcher at Petroleum Engineering Discipline, School of Engineering, Edith Cowan University, 270 Joondalup Dr, Joondalup, WA, 6027, Australia

---

Jalal Fahimpour

Assistant Professor at Department of Petroleum Engineering, Amirkabir University of Technology, Tehran, Iran

---

Alireza Keshavarz

Senior Lecturer at Petroleum Engineering Discipline, School of Engineering, Edith Cowan University, 270 Joondalup Dr, Joondalup, WA, 6027, Australia

---

Stefan Iglauer

[redacted]

Professor at Petroleum Engineering Discipline, School of Engineering, Edith Cowan University, 270 Joondalup Dr, Joondalup, WA, 6027, Australia

---

To Whom It May Concern,

I, *Mirhasan Hosseini*, contributed *as the first author* to the paper/publication entitled "*Calcite−Fluid Interfacial Tension: H_2 and CO_2 Geological Storage in Carbonates".*

[redacted]

I, as a Co-Author, endorse that this level of contribution by the Candidate indicated above is appropriate.

Muhammad Ali

[redacted]

Researcher at Petroleum Engineering Discipline, School of Engineering, Edith Cowan University, 270 Joondalup Dr, Joondalup, WA, 6027, Australia

---

Jalal Fahimpour

[redacted]

Assistant Professor at Department of Petroleum Engineering, Amirkabir University of Technology, Tehran, Iran

---

Alireza Keshavarz

Senior Lecturer at Petroleum Engineering Discipline, School of Engineering, Edith Cowan University, 270 Joondalup Dr, Joondalup, WA, 6027, Australia

---

Stefan Iglauer

Professor at Petroleum Engineering Discipline, School of Engineering, Edith Cowan University, 270 Joondalup Dr, Joondalup, WA, 6027, Australia

---

To Whom It May Concern,

I, *Mirhasan Hosseini*, contributed *as the first author* to the paper/publication entitled "*Hydrogen-wettability alteration of Indiana limestone in the presence of organic acids and nanofluid".*

I, as a Co-Author, endorse that this level of contribution by the Candidate indicated above is appropriate.

Rossen Sedev

[redacted]

Researcher at Petroleum Engineering Discipline, School of Engineering, Edith Cowan University, 270 Joondalup Dr, Joondalup, WA, 6027, Australia

---

Mujahid Ali

[redacted]

Researcher at Petroleum Engineering Discipline, School of Engineering, Edith Cowan University, 270 Joondalup Dr, Joondalup, WA, 6027, Australia

---

Muhammad Ali

[redacted]

Researcher at Petroleum Engineering Discipline, School of Engineering, Edith Cowan University, 270 Joondalup Dr, Joondalup, WA, 6027, Australia

---

Jalal Fahimpour

[redacted]

Assistant Professor at Department of Petroleum Engineering, Amirkabir University of Technology, Tehran, Iran

---

Alireza Keshavarz

[redacted]

Senior Lecturer at Petroleum Engineering Discipline, School of Engineering, Edith Cowan University, 270 Joondalup Dr, Joondalup, WA, 6027, Australia

---

[redacted]

Professor at Petroleum Engineering Discipline, School of Engineering, Edith Cowan University, 270 Joondalup Dr, Joondalup, WA, 6027, Australia

---

To Whom It May Concern,

I, *Mirhasan Hosseini*, contributed *as the first author* to the paper/publication entitled "*Streaming and zeta potentials of basalt as a function of pressure, temperature, salinity, and pH*".

[redacted]

I, as a Co-Author, endorse that this level of contribution by the Candidate indicated above is appropriate.

Faisal Ur Rahman Awan

[redacted]

Researcher at Petroleum Engineering Discipline, School of Engineering, Edith Cowan University, 270 Joondalup Dr, Joondalup, WA, 6027, Australia

---

Nilesh Kumar Jha

[redacted]

Researcher at Petroleum Engineering Discipline, School of Engineering, Edith Cowan University, 270 Joondalup Dr, Joondalup, WA, 6027, Australia

---

Alireza Keshavarz

[redacted]

Senior Lecturer at Petroleum Engineering Discipline, School of Engineering, Edith Cowan University, 270 Joondalup Dr, Joondalup, WA, 6027, Australia

---

Stefan Iglauer

[redacted]

Professor at Petroleum Engineering Discipline, School of Engineering, Edith Cowan University, 270 Joondalup Dr, Joondalup, WA, 6027, Australia